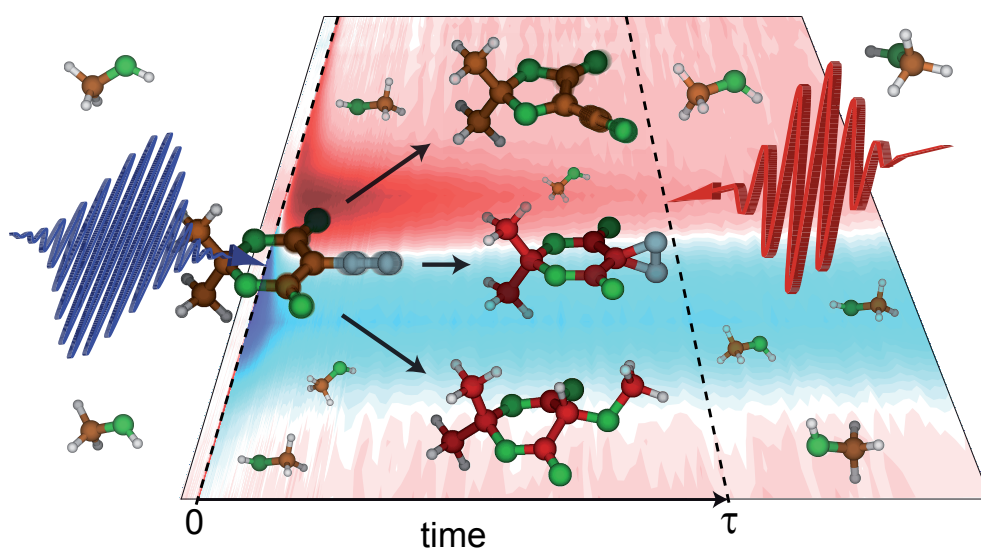# Uncovering photoinduced chemical reaction pathways
# in the liquid phase
# with ultrafast vibrational spectroscopy



**Dissertation zur Erlangung des
naturwissenschaftlichen Doktorgrades
der Julius-Maximilians-Universität
Würzburg**

vorgelegt von

Philipp Benjamin Rudolf

aus Regensburg

Würzburg 2014

Eingereicht am _____
bei der Fakultät für Chemie und Pharmazie

1. Gutachter: Prof. Dr. P. Nürnberger (Ruhr-Universität Bochum)
2. Gutachter:
der schriftlichen Arbeit

1. Prüfer: Prof. Dr. P. Nürnberger (Ruhr-Universität Bochum)
2. Prüfer:
3. Prüfer:
im öffentlichen Promotionskolloquium

Datum des öffentlichen Promotionskolloquiums: _____

Doktorurkunde ausgehändigt am: _____

# List of Publications

Parts of this work have been published in the following references:

Reference [1]:

P. Rudolf, J. Buback, J. Aulbach, P. Nuernberger, and T. Brixner,
*Ultrafast Multisequential Photochemistry of 5-Diazo Meldrum's Acid,*
J. Am. Chem. Soc. **132**, 15213-15222 (2010).


Reference [2]:

P. Rudolf, F. Kanal, J. Knorr, C. Nagel, J. Niesel, T. Brixner, U. Schatzschneider, and
P. Nuernberger,
*Ultrafast Photochemistry of a Manganese-Tricarbonyl CO-Releasing Molecule (CORM)*
*in Aqueous Solution,*
J. Phys. Chem. Lett. **4**, 596-602 (2013).


Reference [3]:

P. Rudolf, F. Kanal, D. Gehrig, J. Niesel, T. Brixner, U. Schatzschneider and P. Nuern-
berger,
*Femtosecond Mid-Infrared Study of the Aqueous Solution Photochemistry of a CO-*
*Releasing Molecule (CORM),*
In *Ultrafast Phenomena XVIII* (M. Chergui, A. Taylor, S. Cundiff, R. de Vivie-Riedle
and K. Yamagouchi, Eds.) EPJ Web of Conferences **41**, 05004 (2013).


Reference [4]:

J. Knorr, P. Rudolf, and P. Nuernberger,
*A comparative study on chirped-pulse upconversion and direct multichannel MCT detec-*
*tion,*
Optics Express **21**, 30693-30706 (2013).

The publications overleaf have partly been used in this dissertation. The following table
itemizes to what extent the different sections of the publications have been reused at
which position in this work. Concerning the figures, it is noted in the respective captions
whether it is a reprint or an adaptation from the corresponding publication.

| publication | usage | dissertation |
|---|---|---|
| Ref. [1] | | |
| pp. 1–2 | reproduced, modified, and extended | pp. 69–71 |
| pp. 2–3 | reproduced and modified | pp. 71–72 |
| pp. 3–7 | mainly reproduced, minor modifications and extensions | pp. 72–82 |
| pp. 7–9 | mainly reproduced, minor modifications and extensions | pp. 82–86 |
| pp. 9–10 | mainly reproduced, minor modifications and extensions | pp. 86–88 |
| Ref. [2] | | |
| pp. 1–2 | reproduced, modified, and extended | pp. 89–90 |
| pp. 2,4–6 | reproduced, modified, and extended | pp. 90–91 |
| pp. 2–5 | reproduced, modified, and extended | pp. 91–99 |
| p. 5 | reproduced, modified, and extended | pp. 99–100 |
| Ref. [3] | | |
| pp. 1–3 | modified and extended | pp. 89–100 |
| Ref. [4] | | |
| pp. 4–5 | modified | pp. 64–65 |
| pp. 5–14 | modified | pp. 107–115 |

# Contents

# 1 Introduction

*Mehr Licht!*
*(More light!)*

alleged last words of Johann W. v. Goethe, 1749-1832 [5]

From today's perspective, the invention and enhancement of light sources generating ultrashort coherent laser pulses with temporal durations ranging from picoseconds down to femtoseconds constitute the laying of the foundation stone for an extensive and prolific field of research: femtochemistry. With an instrumentation precise enough both to initiate photoexcitation processes in molecules and to monitor their outcome after ultrashort waiting times, science began to observe the breaking and formation of chemical bonds in real-time, i.e., to investigate photoinduced chemical reactions that typically emerge in the range of femtoseconds to picoseconds. Of course, the studying and exploitation of chemical reactions can look back on a long history. However, till the early eighties of the last century the existence of ephemeral transition states remained concealed, likewise their dynamic emergence and subsequent reorganization to form further intermediate states or stable photoproducts.

Proceeding from this basis, femtochemistry evolved to utilize various experimental configurations and techniques in order to unravel the photoinduced reaction characteristics of a multitude of compounds in differing microscopic environments, ranging from small isolated molecules in gas-phase experiments through large molecular systems like proteins in liquid surroundings to spacious systems embedded in condensed phase structures. Throughout the last decades, this entailed copious findings that convey an understanding of fundamental microscopic processes steering the living nature that we are part of. Findings that in turn permit instructive and sound predications about macroscopic phenomena. In this sense, it is of special interest to investigate compounds whose photoinduced reaction dynamics are integrated into a wider context, e.g., an established application in industrial procedures or a utilization conceivable in the near future in the field of life sciences.

One example for such a compound is 5-diazo Meldrum's acid (DMA). It is affiliated with the class of $\alpha$-diazocarbonyls that play a significant role for the production of electronic microchips and various other industrial chemistry procedures. The second molecular system under study in this thesis is a manganese-tricarbonyl CO-releasing molecule (CORM) dissolved in water. It also provides promising properties, as it has been shown to be tissue-selective and cytotoxic against cancer cells. To uncover the accordant reaction dynamics, within this thesis transient vibrational spectroscopy is employed. Thereby, the molecular sample is excited by an ultrashort pump pulse in the

spectral region that corresponds to the absorption characteristics of the system under investigation (predominantly in the ultraviolet (UV) spectral regime). At continuously varied waiting times up to several nanoseconds, an ultrashort probe pulse in the mid-infrared (MIR) spectral region monitors the reaction's development via changes in the vibrational signatures of all emerging photoproducts that are detectable at the respective waiting time within the tunable spectral coverage of the probe pulse. In addition, steady-state spectroscopic methods and quantum-chemical calculations within the framework of density functional theory (DFT) accomplish the investigations. Following this introduction, Chapter 2 introduces the theoretical concepts that provide a basic understanding of both the employed experimental techniques and the photoinduced molecular processes, including an introduction to DFT calculations.

During this thesis, considerable effort has been put into the installation, alignment, and improvement of a transient spectrometer, which mainly consists of a system delivering ultrashort laser pulses, devices to generate the pump and probe pulses, and a setup for the detection of the signals deriving from the photoinduced molecular reaction. Chapter 3 subsumes the employed instrumentation with respect to the subsequently presented experimental studies. In addition, some considerations from an experimenter's point of view are addressed that are meant to facilitate the inevitable adjustments of the instrumentation.

Building on this, Chapter 4 presents the unraveling of the light-induced multisequential reaction scheme of DMA in alcohol surrounding. Its rich photochemistry provides parallel reaction pathways with multiple consecutive intermediate states. The photoinduced loss of a diazo group accompanied by a reformation of the molecular structure to form ketene, known as Wolff rearrangement reaction, is a key property that makes $\alpha$-diazocarbonyls in general so useful as photoactive compounds in positive photoresists. The underlying mechanism has given rise to a long controversy. It either takes place in a concerted manner where the ketene is formed directly by losing the diazo group synchronously with the rearrangement, or in a stepwise fashion, where the ketene is formed via a carbene intermediate and a subsequent rearrangement. As well, both mechanisms can occur concurrently. Partly in conjunction with solvent molecules, further pathways emerge and branch to finally form four possible reaction outcomes. By femtosecond mid-infrared transient absorption spectroscopy covering several nanoseconds in combination with DFT calculations a coherent picture of the reaction scheme is deduced.

The second molecular system under study in this thesis is the $[Mn(CO)_3(tpm)]^+$ (tpm = tris(2-pyrazolyl)methane) CORM dissolved in water. In recent years, biological applications of CORMs, which may be utilized as an in-situ source for carbon monoxide, an endogenous gasotransmitter in the human body, have been demonstrated. Suitable compounds have to be stable in air and in water, soluble in water, and specific to particular tissues. Recently synthesized metal carbonyl complexes can act as dark-stable prodrugs under physiological conditions. One of them is the investigated manganese complex. This molecule undergoes photoinduced CO release following UV irradiation. Whereas the ultrafast dynamics of CO liberation in water-insoluble metal carbonyls has been studied for many compounds, the photolysis of CO in water-soluble CORMs with suitable properties for biological applications have so far only been studied on a

macroscopic scale and at irradiation times of several minutes. Using UV-pump–MIR-probe transient absorption spectroscopy with two different pump wavelengths supported by DFT as well as time dependent DFT (TDDFT) calculations, the primary processes of CO release are presented in Chapter 5. These are essential for a full understanding of the biological activity of CORMs.

The findings of both the studies on DMA and on the CORM segue into continuative experiments that are described in the outset of Chapter 6. On the one hand, the obtained knowledge related to the rich photochemistry of DMA, which provides several concomitant reactions pathways in alcohol environment, can facilitate the determining of an appropriate feedback signal for a quantum control experiment. In such an experiment, the population ratio between two parallel pathways could be steered by specifically tailored pump pulses. Therefore, preparative measurements with respect to the shaping and characterization of UV laser pulses are carried out and discussed in Section 6.1. On the other hand, the biological applications of the CORM inspire to initiate the CO loss via two simultaneously interacting visible (VIS) photons, instead of one UV photon that would be absorbed by biological tissue with harmful consequences to the organism. This gives rise to the implementation and testing of a setup for the recording of two-photon excitation spectra via an extended VIS-pump–MIR-probe spectroscopy experiment in addition to the UV-pump–MIR-probe instrumentation (see Sec. 6.2).

Since the detection of weak absorption-change signals in the MIR spectral region on the order of mOD or below concerns each time-resolved vibrational spectroscopy experiment, it seems beneficial to improve the spectral resolution and coverage of the standard detection with a HgCdTe (MCT) detector array. This can be done on the basis of chirped-pulse upconversion (CPU). Accordingly, the concluding part of Chapter 6 deals with a comparison between both detection schemes with respect to the accessible spectral bandwidths, the spectral samplings, and the occurring noise levels in the course of a transient absorption experiment.

# 2 Basic theoretical concepts

This chapter gives an introduction to the theoretical concepts behind the subsequently presented experiments. The latter mainly focus on the investigation of molecular processes in the course of photoinduced chemical reactions. This is the breaking or reformation of molecular bonds which can be monitored via changes in the vibrational motion of particular molecular subunits and functional groups. By nature this occurs on an ultrafast timescale in the range of femtoseconds to picoseconds which leads to the necessity for an instrument that enables one to observe such temporally short events: femtosecond laser pulses, the centerpiece of the experimental realizations and prerequisite for most observations in the following.

Therefore, this section begins with a mathematical description of femtosecond laser pulses as well as their spatial and temporal properties. In order to access different transitions of various molecules, laser pulses consisting of different colors in different spectral regions have to be generated and potentially even manipulated. The description of those nonlinear processes is followed by a depiction of the relevant molecular transitions within a photoinduced interaction. This theoretical background leads to an understanding of density functional theory (DFT) calculations, i.e., how to calculate and predict molecular ground state properties. The section is completed by an introduction of the central experimental method in this work, the pump–probe spectroscopy, the results of which also consist of coherent effects and vibrational relaxation processes, that accompany the signatures of chemical reaction dynamics.

## 2.1 Mathematical formalism of femtosecond laser pulses

Ultrashort laser pulses are one of the essential building blocks on the way to investigate photoinduced chemical reactions occurring on a femtosecond to picosecond timescale. Accordingly, a brief introduction to the mathematical formalism behind these light fields will be given. This is followed by an explanation of parameters that help to describe and understand laser pulses and on the basis of which handling in practice is facilitated. The content of this section falls back on classical textbooks [6–12], in which much more complete and thorough depictions to this subject and in the same way to this whole theoretical chapter can be found.

One can think of laser pulses as a superposition of electromagnetic waves with different oscillation frequencies (i.e., consisting of different colors), which add up constructively at a certain point in space within a certain time window. In a first approach, the duration of the emerging wave packet depends on the number of waves added up. It can be described by an electric field $\mathbf{E}(t, \mathbf{r})$ that obeys to the inhomogeneous wave equation for

isotropic, nonmagnetic media

$$-\nabla \times \left( \nabla \times \mathbf{E}(t, \mathbf{r}) \right) - \frac{1}{c^2} \frac{\partial^2}{\partial t^2} \mathbf{E}(t, \mathbf{r}) = \mu_0 \frac{\partial^2}{\partial t^2} \mathbf{P}(t, \mathbf{r}) \ , \tag{2.1}$$

with $c = 1/\sqrt{\varepsilon_0 \mu_0}$ being the speed of light in vacuum whereas $\mu_0$ and $\varepsilon_0$ represent the magnetic permeability and the permitivity of vacuum, respectively. Both quantities $\mathbf{E}(t, \mathbf{r})$ and the dielectric polarization $\mathbf{P}(t, \mathbf{r})$ show mutual interdependency, meaning that the electric field induces a polarization in a medium as well as the polarization retroacts to create an electromagnetic field.

Within the scope of this thesis a practically orientated simplification for $\mathbf{E}(t, \mathbf{r})$ is a separation into two parts:

$$\mathbf{E}(t, \mathbf{r}) \propto u^+(\mathbf{r}) \, \mathbf{E}^+(t, z) \ + \ \text{c.c..} \tag{2.2}$$

In this assumption the scalar $u^+(\mathbf{r})$ describes the transverse beam profile in space whereas $\mathbf{E}^+(t, z)$ contains information about the polarization and the temporal behaviour of the electric field with respect to the propagation along the z-axis. Although the electric field is real-valued, a complex representation (c.c. denotes the complex conjugate of the first term in Eq. (2.2)) often facilitates the mathematical treatment.

### 2.1.1 Temporal and spectral structure of $\mathbf{E}(t, \mathbf{r})$

To further describe the temporal properties of the electric field, it is valid to neglect the polarization and space dependence, thus obtaining $E(t)$ instead of $\mathbf{E}^+(t, z)$. Via the Fourier transform (indicated by $\mathcal{F}$ and $\mathcal{F}^{-1}$ for the inverse transformation, respectively) the corresponding field $E(\omega)$ as a function of frequency is obtained. Each field in both spaces can be described more precisely by means of a temporal or spectral phase and a temporal or spectral amplitude (i.e., the envelope of a laser pulse), so that in summary the following holds:

$$\mathcal{F}\left\{ E(t) \right\} = E(\omega) = \frac{1}{\sqrt{2\pi}} \int\limits_{-\infty}^{\infty} E(t) \, e^{-i\omega t} \mathrm{d}t = A(\omega) \, e^{-i\Phi(\omega)}, \tag{2.3}$$

$$\mathcal{F}^{-1}\left\{ E(\omega) \right\} = E(t) = \frac{1}{\sqrt{2\pi}} \int\limits_{-\infty}^{\infty} E(\omega) \, e^{i\omega t} \mathrm{d}\omega = A(t) \, e^{i\,\Phi(t)}. \tag{2.4}$$

Since the electric field is a real function in time, for its complex conjugated function $E^*(\omega)$ the symmetry relation $E(\omega) = E^*(-\omega)$ holds. Therefore, Eqs. (2.3) and (2.4) can be understood for exclusively positive frequencies as well.

The outcome of an experiment using ultrashort light fields often depends on certain characteristics of the applied laser pulses. To provide clarity about how to characterize and distinguish laser pulses it is beneficial to expand the introduced phases into Taylor series. As the spectral amplitude is centered around the carrier frequency $\omega_0$ while

the temporal shape is centered around time zero, the expansions with the according coefficients take the following forms:

$$\Phi(t) = \sum_{j=0}^{\infty} \frac{a_j}{j!} t^j, \text{ with } a_j = \left.\frac{\mathrm{d}^j \Phi(t)}{\mathrm{d}t^j}\right|_{t=0}, \tag{2.5}$$

$$\Phi(\omega) = \sum_{j=0}^{\infty} \frac{b_j}{j!} (\omega - \omega_0)^j, \text{ with } b_j = \left.\frac{\mathrm{d}^j \Phi(\omega)}{\mathrm{d}\omega^j}\right|_{\omega=\omega_0}. \tag{2.6}$$

Each Taylor coefficient provides certain information so that by dint of this representation various properties of a laser pulse can be discerned:

- Except for the sign, the zeroth-order coefficients in both the temporal and the frequency domain are identical and describe the position of the electric field oscillations relative to the pulse envelope. It is often referred to both coefficients as absolute phase or carrier-envelope phase (CEP). Short laser pulses consisting of only few cycles show differing behaviour in a light–matter interaction, depending on the CEP [13]. In the course of this thesis a lot more oscillations generate the laser pulses in use so that any CEP-sensitive effects will not be observed.

- In the temporal domain, the first-order coefficients represent the carrier frequency ($a_1 = \omega_0$). In the spectral domain $b_1$ shifts the whole laser pulse in time.

- Higher-order coefficients cause significant changes in the substructure of the electric field, leading to a temporal elongation of the pulse or to a decomposition into differently weighted subpulses, for instance. The former involves any phase function with $a_j \neq 0 \; \forall \; j \geqq 2$ or $b_j \neq 0 \; \forall \; j \geqq 2$ of even order and thus all kinds of chirp (with $a_2 \neq 0$ and $a_j = 0 \; \forall \; j \geqq 3$ one speaks of a linearly chirped pulse). For $b_j \neq 0 \; \forall \; j > 2$ of odd order, the pulse gets separated into a pulse sequence. A systematic illustration of the just briefly described phenomena is given in [8].

Hence, strongly depending on the phase function, two laser pulses with identical spectra can show completely different behavior in time. As in practice it is either unavoidable or wanted that an applied laser pulse interacts with matter (e.g., with crystals, glass or air), its phase function gets necessarily distorted during an experiment. It is common to assess these changes via the different orders of the Taylor expansion. Likewise it is an established procedure to manipulate laser pulses by tuning the different orders of phase separately with an appropriate device.

How the phase changes when a laser pulse traverses a medium is described with the help of the complex refractive index $\tilde{n}$ or the complex wave number $\tilde{k}$:

$$\tilde{n}(\omega) = n(\omega) - i\kappa(\omega), \text{ and } \tilde{k}(\omega) = \frac{\omega}{c}\tilde{n}(\omega). \tag{2.7}$$

The imaginary part $\kappa(\omega)$ is the extinction coefficient and describes absorption phenomena while the real part $n(\omega)$ incorporates refraction and dispersion. The absorptive part is neglected in the following, so that a laser pulse traveling through a dispersive medium of length L, gains additional phase of the form

$$\Phi(\omega, L) = k(\omega) \; L = \frac{\omega \; n(\omega)}{c} L. \tag{2.8}$$

Thereby the coefficients for the spectral phase in Eq. (2.6) can be expanded to

$$b_j = \frac{\mathrm{d}^j \Phi(\omega, L)}{\mathrm{d}\omega^j}\Big|_{\omega=\omega_0} = \frac{L}{c}\Big(j\frac{\partial^{j-1}n(\omega)}{\partial\omega^{j-1}} + \omega\frac{\partial^j n(\omega)}{\partial\omega^j}\Big)\Big|_{\omega=\omega_0}. \tag{2.9}$$

From this general description some frequently considered quantities can be derived. With a closer look at the first derivative

$$b_1 = \frac{L}{c}\Big(n(\omega) + \omega\frac{\mathrm{d}n(\omega)}{\mathrm{d}\omega}\Big)\Big|_{\omega=\omega_0} = \frac{L}{v_g(\omega_0)} = \tau_g(\omega_0), \text{ with} \tag{2.10}$$

$$v_g(\omega_0) = \Big(\frac{dk(\omega)}{d\omega}\Big|_{\omega=\omega_0}\Big)^{-1}, \tag{2.11}$$

one yields the group velocity $v_g(\omega_0)$ and the group delay $\tau_g(\omega_0)$. The former is the velocity with which the pulse propagates through material. The latter is the time, the peak of the envelope gets delayed while passing a medium. Further quantities are revealed by examining the second derivative. For instance the group delay dispersion (GDD)

$$\mathrm{GDD} = b_2 = \frac{L}{c}\Big(2\frac{\partial n(\omega)}{\partial\omega} + \omega\frac{\partial^2 n(\omega)}{\partial\omega^2}\Big)\Big|_{\omega=\omega_0} = \frac{\mathrm{d}\tau_g(\omega)}{\mathrm{d}\omega}\Big|_{\omega=\omega_0}, \tag{2.12}$$

and the group velocity dispersion (GVD)

$$\mathrm{GVD} = \frac{1}{c}\Big(2\frac{\partial n(\omega)}{\partial\omega} + \omega\frac{\partial^2 n(\omega)}{\partial\omega^2}\Big)\Big|_{\omega=\omega_0} = \frac{\mathrm{d}\big(\frac{1}{v_g(\omega)}\big)}{\mathrm{d}\omega}\Big|_{\omega=\omega_0}, \tag{2.13}$$

which is simply the GDD normalized to the length. The GVD is a criterion for the quantity of linear chirp that is added to a laser pulse owing to dispersion. Both parameters but especially the latter are customary to characterize different optical materials as well as their sometimes unwanted effects on traversing laser pulses.

Thinking of elongated laser pulses due to dispersion it appears beneficial to have a measure at hand to quantify the actual pulse duration and spectral width. This can be achieved via the temporal intensity which is the average of $E^2(t)$ during one optical cycle $T = 2\pi/\omega_0$:

$$I(t) = c\varepsilon_0 n\frac{1}{T}\int_{t-\frac{\pi}{\omega_0}}^{t+\frac{\pi}{\omega_0}} E^2(t')\mathrm{d}t' = 2c\varepsilon_0 nA(t)^2. \tag{2.14}$$

The spectral intensity can be expressed in an equivalent form: $I(\omega) = 2c\varepsilon_0 nA(\omega)^2$.

Here should be stated that this way of expressing $I(t)$ and $I(\omega)$ requires one simplification: the slowly varying envelope approximation (SVEA). This means that the bandwidth of a laser pulse is small in comparison to the carrier frequency ($\Delta\omega \ll \omega_0$). Or in other words, concerning the description of ultrashort laser pulses with the concept of the carrier frequency and a complex valued field envelope (including all nonlinear phase contributions $\varphi(t) = \Phi(t) - \omega_0 t$, i.e., $E(t) = A(t)\,e^{i\,\varphi(t)}\,e^{i\omega_0 t} = \hat{A}(t)\,e^{i\omega_0 t}$, the temporal variation of $\hat{A}(t)$ during one optical cycle $T = 2\pi/\omega_0$ should be small:

$$|\frac{\mathrm{d}}{\mathrm{d}t}\hat{A}(t)| \ll \omega_0|\hat{A}(t)|. \tag{2.15}$$

Since the duration of one optical cycle of a laser pulse in the visible spectral regime is in the range of 2 fs, which is much shorter than the pulses discussed in this thesis, the SVEA is valid.

Now, by means of the full width at half maximum (FWHM) of the according intensity function, the pulse duration $\Delta t$ as well as the aforementioned spectral bandwidth $\Delta\omega$ can be obtained:

$$\Delta\omega = \text{FWHM}\{I(\omega)\}, \qquad (2.16)$$
$$\Delta t = \text{FWHM}\{I(t)\}. \qquad (2.17)$$

Both parameters are not independently adjustable as the underlying fields are related to each other via a Fourier transformation. However, the product of Eqs. (2.16) and (2.17), which is called the time–bandwidth product, can reach a lower limit:

$$\Delta\omega\Delta t \geq 2\pi c_B. \qquad (2.18)$$

The equal sign holds for completely unchirped pulses, i.e., no expansion coefficients from Eqs. (2.5) and (2.6) appear for $j \geq 2$. Such bandwidth-, transform- or Fourier-limited pulses therefore are the shortest pulses that can be obtained from a given spectrum. The numerical constant $c_B$ depends on the particular pulse shape. For instance, in case of a Gaussian pulse shape it is $c_B = 2(\ln 2)/\pi = 0.441$ [9]. Other typical pulse shapes are the Lorentzian function or shapes that contain the hyperbolic secant function ($\text{sech}^2$).

So one should note that the quantifications given in Eqs. (2.16) and (2.17) are only reasonable for not too complicatedly composed pulse shapes but predominantly for bell-shaped pulse profiles. Considering for instance multi-pulse sequences or pulse shapes with slowly fading wings that span over a significant temporal or spectral range, the FWHM does no longer have substantial significance. In this case more accurate information on the pulse duration can be expected from a calculation of the appropriate second-order moment of the field distribution [9].

### 2.1.2 Spatial structure of $\mathbf{E}(t, \mathbf{r})$

In Eq. (2.2) the solution for the inhomogeneous wave equation has been separated. So far, a short description of $\mathbf{E}(t, \mathbf{r})$ in the time and frequency domain has been presented accompanied by implications due to dispersion effects. In the following a closer look at the transverse beam profile in space $u^+(\mathbf{r})$ shall be taken. The practical relevance is given for instance whenever one has to evaluate in which way (de-)focusing optics affect the spatial beam profile.

It is assumed that $u^+(\mathbf{r})$ varies slowly with $z$ as the fast oscillating part of the electric field along the $z$-direction is part of the exponential term in $\mathbf{E}(t, \mathbf{r})$. Furthermore, the paraxial approximation (small-angle approximation) is applied which means that owing to the finite beam width the transverse variations are small in comparison to typical propagation lengths [10]. Within this thesis, applicable solutions to the accordingly adjusted paraxial wave equation in vacuum are Gaussian beams in the $\text{TEM}_{00}$ (the
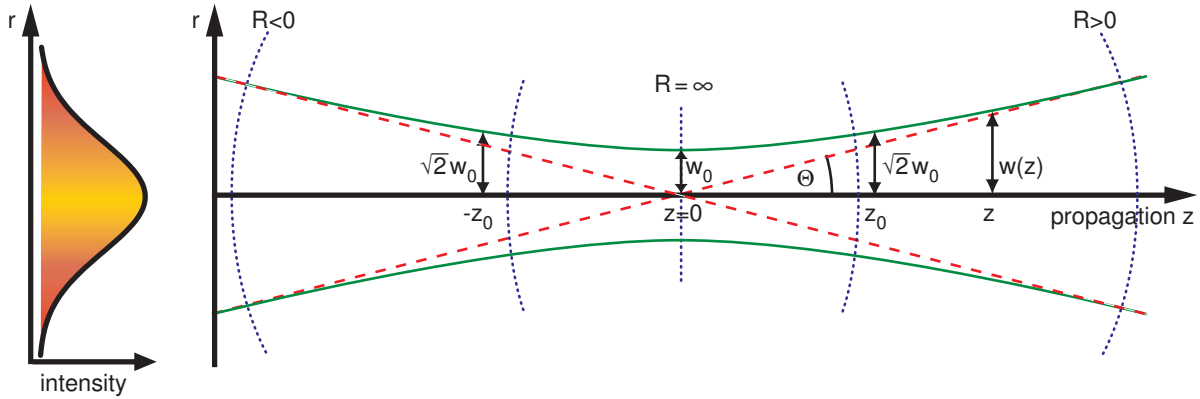
**Figure 2.1:** Propagation parameters of a Gaussian beam. Left: Intensity distribution of a Gaussian beam depending on the distance from the z-axis. Right: Paraxial beam propagation through the beam waist at $z = 0$. The dotted blue lines indicate the radii of curvature and the wavefront with respect to the propagation distance. The dashed red lines designate both the angle of divergence $\Theta$ and the linear increase of the beam size for large propagation distances; in the far field $R(z)$ becomes $z$. The continuous green hyperbolic lines indicate $w(z)$, the distances from the z-axis where the field amplitude is $1/e$ of the according on-axis value. At the Rayleigh length $z_0$, it is $w(z_0) = \sqrt{2}w_0$ [6, 14].

lowest order of transverse electromagnetic modes):

$$u^+(\mathbf{r}) = u_0 \frac{1}{\sqrt{1 + z^2/z_0^2}} \, e^{-i\psi(z)} \, e^{ik(x^2+y^2)/2R(z)} \, e^{-(x^2+y^2)/w^2(z)}, \tag{2.19}$$

with the beam waist of radius $w_0$ located at $z = 0$. Derived from this formula, Fig. 2.1 illustrates the basic propagation characteristics of a Gaussian beam [15] which are also elucidated in the following.

1.  The Rayleigh length $z_0 = \dfrac{\pi w_0^2}{\lambda}$. $\hfill(2.20)$

    Within the range $-z_0 \leq z \leq z_0$ the beam diameter $w(z) = w_0\sqrt{1 + z^2/z_0^2}$ stays in the limits $w_0 \leq w \leq \sqrt{2}w_0$. As long as the spot size of a Gaussian beam does not exceed this boundary (while traveling along realistic propagation distances) it is called a collimated beam. Equation (2.20) implies that this quantity is proportional to the lowest beam waist $w_0$. That means the tighter a beam is focused the shorter the Rayleigh range becomes and the sooner a beam gets uncollimated.

2.  The radius of curvature $R(z) = z + z_0^2/z$. $\hfill(2.21)$

    At the origin $z = 0$ the curvature is infinite, likewise at $z = \infty$, whereas in between it becomes $R(z) \approx z$ as it is equivalent to the curvature of spherical waves emerging from $z = 0$. From this it follows that the divergence angle $\Theta$ can be approximated with $\Theta \approx w(z)/z$ which leads to an approximated spot size $w(z) \approx z\lambda/(\pi w_0)$. This allows for an estimation of:

3. The focal beam waist $w_0 \approx \dfrac{f\lambda}{\pi w(f)}$. (2.22)

Provided that the spot size of an incoming collimated beam $w(f)$ is known as well as the focal length $f$ of an encountered lens or focusing mirror, Eq. (2.22) is a widespread tool to calculate the spot size at the focus position with sufficient accuracy.

## 2.2 Nonlinear optical processes

Starting once more from Eq. (2.1), so far the electromagnetic field $\mathbf{E}(t, \mathbf{r})$ has been explained in more detail. In this section the source term $\mathbf{P}(t, \mathbf{r})$ lies in the focus of consideration, and more precisely its nonlinear nature that creates a crucial precondition for many experiments in the following: the accessibility of laser pulses out of a wide spectral range spanned from ultraviolet (UV) wavelengths up to the mid-infrared (MIR) regime. These frequency conversion processes result from the exceptionally high peak intensities of ultrashort laser pulses in conjunction with suitable materials which show a noticeable nonlinear response to an incoming electric field.

### 2.2.1 Nonlinear polarization and phase matching

In a different way from classical electrodynamics where the dielectric polarization is described as a linear response of a medium to an electromagnetic field ($P(\omega) = \varepsilon_0 \chi(\omega) E(\omega)$, with the dielectric susceptibility $\chi(\omega)$), the treatment of ultrashort laser pulses demands to regard nonlinear contributions. Therefore, the polarization is expanded into higher orders of $E(\omega)$, while for simplification the spatial dependence is neglected [9, 12, 16, 17]:

$$\mathbf{P}(\omega) = \varepsilon_0 \sum_{j=1}^{\infty} \chi^{(j)}(\omega)\mathbf{E}(\omega)^j = \mathbf{P}^{(1)}(\omega) + \mathbf{P}^{(2)}(\omega) + \mathbf{P}^{(3)}(\omega) + \dots . \tag{2.23}$$

Due to the vectorial character of $\mathbf{E}(\omega)$ each dielectric susceptibility $\chi^{(j)}(\omega)$ is a tensor of $(j+1)$th rank so that Eq. (2.23) notated with indices reads

$$P_i = \varepsilon_0 \left[ \sum_{k=1}^{3} \chi^{(1)}_{ik} E_k + \sum_j \sum_k \chi^{(2)}_{i,j,k} E_j E_k + \dots \right]. \tag{2.24}$$

Thus the components $P_i$ ($i = x, y, z$) of the induced polarization are determined by two quantities: the polarization of the incoming electromagnetic field (i.e. the components $E_x$, $E_y$, $E_z$ that are nonzero) and the components of the susceptibility tensors, defined by symmetry properties of the interacting material. From a simplified microscopic perspective, under the influence of the incident wave packet oscillating dipole moments are induced that in turn generate new electromagnetic waves with frequencies defined by the dielectric polarization.

For illustration a simple and experimentally highly relevant example shall be given. If one considers the superposition of two waves $\mathbf{E} = \mathbf{E}_1 \cos(\omega_1 t + k_1 z) + \mathbf{E}_2 \cos(\omega_2 t + k_2 z)$

with frequencies $\omega_1$ and $\omega_2$, via the trigonometric identity $\cos^2 x = 1/2(1 + \cos 2x)$ the second-order term in Eq. (2.23) becomes

$$\begin{aligned} \mathbf{P}^{(2)}(\omega) =& \frac{1}{2}\varepsilon_0 \chi^{(2)} \left[ \mathbf{E}_1^2 + \mathbf{E}_2^2 + \mathbf{E}_1^2 \cos(2\omega_1 t) + \mathbf{E}_2^2 \cos(2\omega_2 t) \right] \\ &+ \varepsilon_0 \chi^{(2)} \left[ \mathbf{E}_1 \mathbf{E}_2 \cos(\omega_1 + \omega_2)t + \mathbf{E}_1 \mathbf{E}_2 \cos(\omega_1 - \omega_2)t \right], \end{aligned} \tag{2.25}$$

so that the nonlinear polarization $P^{(2)}(\omega)$ contains different contributions. In addition to a frequency independent term, it is composed of parts with $2\omega_1$ and $2\omega_2$ as well as of parts that oscillate with $(\omega_1 + \omega_2)$ and $(\omega_1 - \omega_2)$, implying that the induced dipoles emit light at new spectral positions. The various phenomena of frequency conversion will be described more in detail later in this section. From Eq. (2.25) one can extract furthermore that the radiated light has an intensity proportional to the square of the causing field amplitude:

$$I(2\omega) \propto I^2(\omega), \text{ and } I(\omega_1 \pm \omega_2) \propto I(\omega_1) \cdot I(\omega_2). \tag{2.26}$$

This explains that laser pulses are not only in use to achieve high time resolutions but also to provide the needed intensity for time-resolved spectroscopy experiments as described below.

It is the mere possibility to generate light with different wavelengths that has been described hitherto. To do so efficiently, another aspect has to be taken into account. For instance in case of a $\chi^{(2)}$-process as discussed above, where two frequencies form a new one, it is crucial to obey the conservation of energy and momentum:

$$\omega_3 = \omega_1 + \omega_2, \text{ and} \tag{2.27}$$

$$\mathbf{k_3} = \mathbf{k_1} + \mathbf{k_2} . \tag{2.28}$$

The latter is often referred to as the phase matching condition. Unless this condition is not met, every partial wave generated from one single dipole would be out of phase with respect to the majority of other sub-waves, resulting to a certain extent in destructive interference. So, again from a microscopic point of view, one has to ensure that the microscopic structure (e.g. the lattice in case of a crystal) is suitable and properly oriented with reference to the beam direction (represented by $\mathbf{k_1}$ and $\mathbf{k_2}$) of the original light fields. To further investigate this situation there is one aspect that has to be clarified. Under the assumption that absorption does not occur and a collinear geometry is considered ($\mathbf{k}_1 || \mathbf{k}_2 || \mathbf{k}_3$), the second part of Eq. (2.7) reformulates the phase matching condition to

$$\omega_3 n(\omega_3) = \omega_1 n(\omega_1) + \omega_2 n(\omega_2), \tag{2.29}$$

which, in conjunction with the conservation of energy (confer Eq. (2.27)), turns into

$$n(\omega_1) = n(\omega_2) = n(\omega_3). \tag{2.30}$$

Due to material dispersion this relation is usually rarely fulfilled. However, there are anisotropic crystals that have certain qualities to overcome this problem. Namely, uni-axial birefringent crystals, with uniaxial meaning that the crystal has *one* optical axis.

For propagation along the optical axis every polarization component of an incoming electric field encounters the same indices of refraction. For other propagation directions one distinguishes the ordinary and the extraordinary refractive indices $n_o(\omega)$ and $n_e(\omega)$. In case of a negative uniaxial crystal, it is $n_e(\omega) < n_o(\omega)$, the opposite holds in a positive uniaxial crystal. Whereas $n_o(\omega)$ remains constant and unaffected by the propagation direction, $n_e(\omega)$ depends on the angle $\theta$ between the wave vector $\mathbf{k}$ and the optical axis

$$n_e(\omega, \theta) = \frac{n_o(\omega) n_e(\omega, 90°)}{\sqrt{n_o(\omega)^2 \sin^2\theta + n_e(\omega, 90°)^2 \cos^2\theta}}, \qquad (2.31)$$

so that $n_e(\omega, \theta)$ is tunable between $n_e(\omega, 0°) = n_o(\omega)$ and $n_e(\omega, 90°) = n_e(\omega)$, whereby Eq. (2.30) can be satisfied for a specific frequency. The surrounding frequencies that build up a laser pulse experience a certain phase mismatch $\Delta k = k_3 - k_2 - k_1$ at the same time. The intensity of the generated light with frequency $\omega_3$ after passing a uniaxial birefringent crystal of length $L$ shows the following proportionality [12]:

$$I(\omega_3, L) \propto \frac{I(\omega_1) I(\omega_2) \omega_3^2}{n(\omega_1) n(\omega_2) n(\omega_3)} L^2 \operatorname{sinc}^2\left(\frac{\Delta k L}{2}\right). \qquad (2.32)$$

The wavevector mismatch is fully characterized by the $\operatorname{sinc}^2$-dependence. If broad spectra are intended to be converted an increasing mismatch is unavoidable, hence the crystal length has to be reduced in order to compensate for it.

In practice, one differentiates between particular types of phase matching, depending on the (linear) polarizations of the incoming and the outgoing laser beams. For three laser beams there exist eight ($2^3$) possible combinations, albeit usually the first two cases are predominantly in use: Type I phase matching connotes that both incoming fields have parallel polarizations while the generated wave is orthogonally polarized. In a type II phase matching process, the incident waves are orthogonally polarized as defined by [18].

### 2.2.2 Frequency conversion processes

For a versatile applicability, femtosecond laser pulses have to be available in different spectral regions depending on the molecular system under investigation. Commonly, an experiment begins with the generation of the fundamental light around 800 nm by dint of a Titanium–Sapphire (Ti:Sa) oscillator (see Chapter 3), which is the origin of any further laser pulses at different wavelengths produced via subsequent frequency conversion processes. After the theoretical background to this topic has been given in the previous section, this passage summarizes the conversion processes that have been de facto in use within the scope of this work.

#### $\chi^{(2)}$-processes: SFG, DFG, OPA

For these processes the second-order response $\chi^{(2)}$ of a medium to highly intensive femtosecond laser pulses is exploited. The materials that are eligible have to be anisotropic like birefringent crystals, with $\beta$-bariumborate (BBO) in the visible spectral regime and
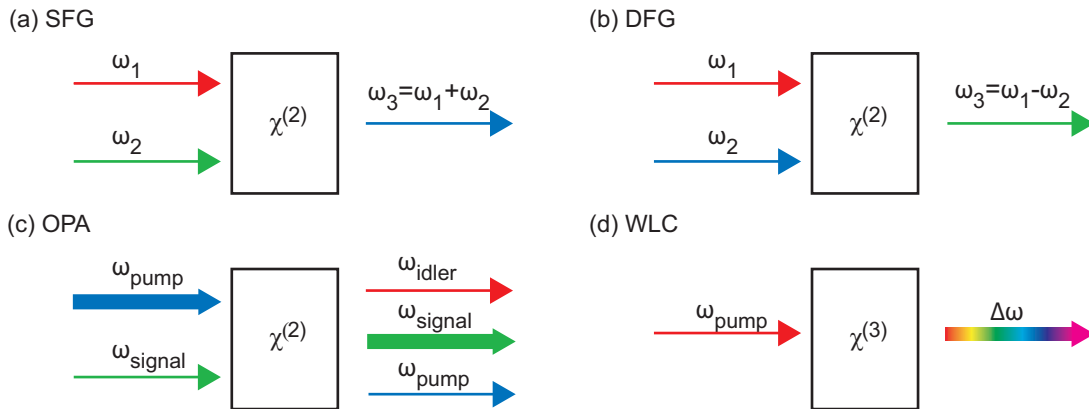
**Figure 2.2:** Frequency conversion processes that exert second- and third-order susceptibilities $\chi^{(2)}$ and $\chi^{(3)}$: (a) sum frequency generation (SFG) which is the generalization of second harmonic generation (SHG) for $\omega_1 = \omega_2$. (b) Difference frequency generation (DFG). (c) Optical parametric amplification (OPA) which is also a DFG process but in this case the energy transfer from the pump beam to the signal pulse is emphasized. (d) Generation of a white-light continuum (WLC), alias supercontinuum. The colors denote a suitable possibility concerning the order of wavelengths within the according frequency mixing process.

silverthiogallate ($AgGaS_2$) for the MIR region being particularly relevant in the context of this thesis. Elsewise, isotropic or centrosymmetric media show in general inversion symmetry which leads to vanishing even-order susceptibilities [15, 19], thus making them unusable for the following processes that are depicted in Fig. 2.2.

As described in Eq. (2.25) two laser pulses oscillating with central frequencies $\omega_1$ and $\omega_2$ generate a new light field centered around $\omega_3$, providing that an appropriate crystal is employed and the phase matching condition is fulfilled. If so, $\omega_3$ can be the sum (sum frequency generation, SFG, Fig. 2.2a) or the difference (difference frequency generation, DFG, Fig. 2.2b) of the incident beams' frequencies, depending on the respective polarizations with regard to the crystal orientation. Commonly, that means only one mixing process can be optimally phase matched throughout a particular configuration between the incoming electromagnetic fields and the crystal. This aspect is also reflected by Eq. (2.31) as the phase matching condition can be fulfilled for one certain frequency by tuning the crystal angle $\theta$. In both cases, the field intensity $I(\omega_1 \pm \omega_2)$ is proportional to the causing field intensities (see Eq. (2.26)). For $\omega_1 = \omega_2$ a special form of SFG appears, the second harmonic generation (SHG).

Related to difference frequency mixing is the optical parametric amplification (OPA, Fig. 2.2c). Here, the notation changes from $\omega_3 = \omega_1 - \omega_2$ to $\omega_{idler} = \omega_{pump} - \omega_{signal}$. The signal pulse is assumed to be a weak seed wave that is amplified using the intense pump field. This is accompanied by the generation of an idler pulse at the difference frequency. In contrast to DFG, attention should be paid to the aspect that the creation of a signal and an idler photon can be initiated by solely one pump photon, which excites an atom in the crystal to a certain virtual state. From there a decay via two-photon emission takes place, also in the absence of signal photons (parametric fluorescence). But in the presence of an incident signal field the decay is stimulated, thus amplifying the signal

pulses, which is the actual objective of OPA.

The term parametric refers to the fact that the initial and final quantum-mechanical states within the described light–matter interaction are identical, so that population returns to the ground state after very short intervals in virtual states and is consequently not transferred to other real states. According to this, photon energy is conserved and parametric processes can be described via a real susceptibility or the real part of the refractive index, respectively, since absorption necessitates the imaginary part and includes a population transfer to excited states [12]. In this sense, the previously introduced mixing processes are of parametric nature as well.

Note that in general none of the mentioned methods proceeds with 100 % conversion efficiency so that incident beams always remain to a certain extent as residual pulses. In Fig. 2.2 this fact is only depicted for the OPA process since all three outgoing light fields are relevant and will be used subsequently (see Section 3.1.2).

### $\chi^{(3)}$-**processes: WLC, SPM**

The generation of spectrally broadened laser pulses is of significant importance for time-resolved spectroscopic experiments. For instance, in case of the above-mentioned OPA, a broad (though weak) seed spectrum can be diversely applicable by amplifying a desired spectral range out of it via adjusting the crystal angle in Eq. (2.31). It is thus possible to generate intense laser pulses tunable over a considerable spectral region, ranging from the UV to the near infrared. Such a desirable electromagnetic field is the so-called white light continuum (WLC, or supercontinuum, SC, Fig. 2.2d). The mechanism for its emergence is highly multifactorial, meaning that several nonlinear processes have to be comprised [20], inter alia, self phase modulation (SPM) [21], optical shock-wave formation due to self-steepening [22], and space–time focusing [23]. Some of these are related to an intensity-dependent refractive index

$$n = n_0 + n_2 I(t), \tag{2.33}$$

which is also associated to processes that will be mentioned later (see Sec. 2.5). Therefore, a more detailed description of the nonlinear refractive index, which is also referred to as the optical Kerr effect [12], shall be given in the following.

The generation of a WLC is based on the third-order susceptibility $\chi^{(3)}$ that is also included in the corresponding total nonlinear polarization

$$P(t) = \varepsilon_0 \Big[ \chi^{(1)} + \frac{3\chi^{(3)}}{2c\varepsilon_0 n} I(t) \Big] E^+(t) + \text{c.c.}. \tag{2.34}$$

This expression already incorporates an adaptation of the general form depicted in Eq. (2.24). The summation for the third-order term has been carried out for three electromagnetic fields oscillating at the same frequency [9], resulting in a form $P^{(3)} = 3\varepsilon_0 \chi^{(3)} |E|^2 E$. Additionally Eq. (2.14) has been taken into account for the field intensity.

The linear refractive index can be written as $n_0 = \sqrt{1 + \chi^{(1)}}$, so that in compliance with Eq. (2.34) the total index of refraction with respect to the total susceptibility

$n = \sqrt{1 + \chi^{\text{tot}}}$ becomes

$$n = \sqrt{1 + \chi^{(1)} + \frac{3\chi^{(3)}}{2c\varepsilon_0 n_0}I(t)} = n_0\sqrt{1 + \frac{3\chi^{(3)}}{2c\varepsilon_0 n_0^3}I(t)} \approx n_0 + \frac{3\chi^{(3)}}{4c\varepsilon_0 n_0^2}I(t). \qquad (2.35)$$

The last step implies that $n_2 I(t)$ with the nonlinear coefficient index $n_2 = \frac{3\chi^{(3)}}{4c\varepsilon_0 n_0^2}$ is small in comparison to $n_0$.

The intensity dependence causes both temporal and spatial changings of the pulse structure, for instance self-focusing and self phase modulation (SPM). By taking a closer look at the changes the phase of a pulse experiences due to the nonlinear coefficient index, the latter leads to an intuitive understanding of the spectral broadening in a SC. In a simple representation, the phase of a pulse, traveling a distance $z$ through a material with sufficient $\chi^{(3)}$, can be described by

$$\Phi = \omega t - kz = \omega t - \frac{n\omega}{c}z = \omega\left(t - \frac{n_0}{c}z\right) - A \cdot I(t), \qquad (2.36)$$

with $A = n_2\omega z/c$ depending linearly on $n_2$. The outcome of this is that the momentary frequency

$$\omega = \frac{\mathrm{d}\Phi}{\mathrm{d}t} = \omega_0 - A\frac{\mathrm{d}I}{\mathrm{d}t} \qquad (2.37)$$

obtains a term in addition to the carrier frequency $\omega_0$. During the rise of the pulse $(\mathrm{d}I(t)/\mathrm{d}t > 0)$ $\omega$ gets smaller, whereas $\omega$ rises while the pulse decays $(\mathrm{d}I(t)/\mathrm{d}t < 0)$, so that the onset of a WLC is red-shifted and the ending is blue-shifted. Hence, the nonlinear refractive index leads to the SPM and generates new spectral components that in fact broaden the pulse. This should not be confused with the likewise appearing phase modulation associated with GVD, which is due to the linear refractive index. If the light fields, incident on a material which permits $\chi^{(3)}$-processes, differ with respect to intensity or frequency, the SPM is expanded to the cross-phase modulation (XPM) (see Sec. 2.5).

### 2.2.3 Shaping and characterizing laser pulses in the UV

Nonlinear crystals are the material of choice to mix different optical fields and thereby generate new ones. Beyond that, new possibilities are opened up when an acoustic wave is superposed with an electromagnetic field in a crystal that is highly birefringent for both types of waves. In doing so, the amplitude and phase of laser pulses can be shaped [24, 25]. The most established way to manipulate the properties of a laser pulse is a non-acoustic method via a liquid crystal display (LCD) that is positioned in the Fourier plane inside a zero-dispersion compressor (also known as $4f$-setup) [26, 27]. Instead of a LCD it is also possible to place an acousto–optic modulator (AOM) mask inside this arrangement [28, 29]. However, in order to circumvent the complicated alignment and high adjustment effort of a spatial light modulator based on a $4f$-setup, one can take advantage of an acousto–optic programmable dispersive filter (AOPDF) [30–33]. An alternative that has especially evolved to shape laser pulses in the UV spectral region, since LCDs commonly are not transmittive in this spectral regime.
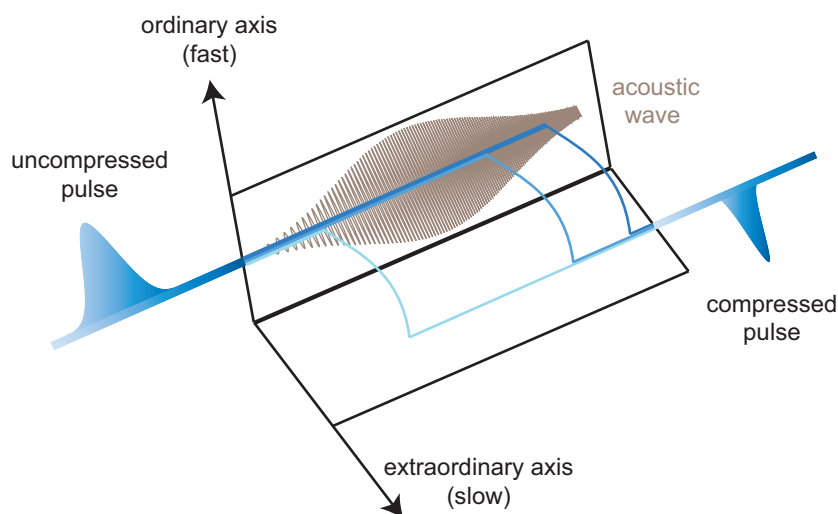
**Figure 2.3:** Principle of an AOPDF: The acoustic wave establishes a longitudinal grating in the birefringent crystal. At adjustable crystal positions the different spectral components of the incoming optical field can be diffracted to the extraordinary axis that provides a slower group velocity than the ordinary axis. Thus, each wavelength of the incoming laser pulse has a tunable propagation time through the crystal allowing for shaping of the phase. Figure based on [31].

### Shaping UV laser pulses with an AOPDF

Basically, an AOPDF consists of a birefringent crystal like potassium dihydrogen phosphate ($KH_2PO_4$, KDP) in case of an application in the UV and a piezoelectric transducer connected to a radio frequency (RF) generator, which injects the acoustic wave into the crystal and thereby establishes a longitudinal transient grating. Both the acoustic and the optical waves pass collinearly through the crystal, while the optical pulse is polarized at first along the ordinary axis (fast axis, see Fig. 2.3). Due to the sonic velocity being orders of magnitude slower than the speed of light, the laser pulse encounters the position-dependent differing indices of refraction as quasi-static properties of the crystal. Through an anisotropic interaction (in contrast to an isotropic interaction in case of an AOM) the spectral components of the incoming light field are diffracted to the slow extraordinary axis when the phase matching condition and conservation of energy are fulfilled:

$$\mathbf{k}_{\text{diffracted}}(\omega_{\text{diffracted}}) = \mathbf{k}_{\text{acoustic}}(\omega_{\text{acoustic}}) + \mathbf{k}_{\text{input}}(\omega_{\text{input}}), \tag{2.38}$$

$$\omega_{\text{diffracted}} = \omega_{\text{input}} + \omega_{\text{acoustic}} \simeq \omega_{\text{input}}. \tag{2.39}$$

Consequently, by varying the frequency $\omega_{\text{acoustic}}$, the spectral components of the laser pulse can be diffracted to the extraordinary axis at different crystal positions. Since the axes provide differing group velocities, the overall propagation time of each wavelength through the crystal can be adjusted. Furthermore, the amplitude of the diffracted spectral part can be tuned by the acoustic power at the respective position in the crystal. As a result, phase and amplitude of a laser pulse can be shaped. In the time domain

the diffracted optical output $E_{\text{diffracted}}(t)$ of an AOPDF depends on the convolution of the optical input $E_{\text{input}}(t)$ and the acoustic signal $S_{\text{acoustic}}(t/\alpha)$:

$$E_{\text{diffracted}}(t) \propto E_{\text{input}}(t) * S_{\text{acoustic}}(t/\alpha). \tag{2.40}$$

$S_{\text{acoustic}}(t/\alpha)$ depends on the RF signal applied to the transducer and on the scaling factor $\alpha = \Delta n(V/c)$, which in turn is related to the ratio between the acoustic wave velocity $V$ and the speed of light, and the difference of refractive indices between ordinary and extraordinary axes in the crystal $\Delta n$. Typical values of $\alpha$ are on the order of $10^{-7}$. This enables the manipulation of optical fields oscillating with hundreds of Terahertz (UV spectral regime) via signals in the Megahertz region [32].

In practice, phase and amplitude can be shaped independently from each other in two ways. First, via parameters of which the phase and amplitude functions are built up. Basically, these are the center position $\lambda$ and the width of the pulse envelope to perform amplitude shaping, and the first four Taylor coefficients in agreement with Eq. (2.6) to manipulate the phase. The second possibility is to define the desired phase and amplitude functions via sampling points. The maximum number of independently programmable sampling points $N$ depends on the spectral resolution of the device $\delta\lambda$ and the bandwidth of the incident laser pulse $\Delta\lambda$ [34]:

$$N = \frac{\Delta\lambda}{\delta\lambda} = 1.25 \cdot \Delta n \cdot L \cdot \frac{\Delta\lambda}{\lambda^2} \, , \text{ with} \tag{2.41}$$

$$\delta\lambda = 0.8 \cdot \frac{\lambda^2}{\Delta nL}. \tag{2.42}$$

For a KDP crystal of length $L = 50\,\text{mm}$ ($\Delta n = 0.045$) and a UV pulse centered around $300\,\text{nm}$ with a bandwidth of $5\,\text{nm}$, e.g., a requested phase function can be sampled with 156 points. The numerical prefactor in Eq. (2.41) can vary slightly when the orientation of the incoming beam with respect to the crystal geometry is altered. Similar treatments hold for AOPDFs applied in the visible [35] and in the MIR [36] spectral regions.

Like other pulse-shaping techniques, an AOPDF also exhibits unwanted effects due to space–time coupling, namely a group-delay-dependent displacement of the tailored output [37]. At least partially, this can be stemmed if additional effort is put into a mutable refractive telescope in front of the AOPDF [38, 39].

**Characterizing laser pulses in the UV**

Pulse characterization is mandatory for all kinds of measurements using tailored laser pulses, as the experimental outcome is postulated to be strongly dependent on the pulse shape. However, also in standard time-resolved experiments additional phase contributions will be accumulated due to numerous interactions with crystals, lenses, or polarization-affecting materials. As a consequence, the spectral and temporal composition of the applied laser pulses is clearly altered, until the interaction of interest with the molecular system under investigation takes place. Generally, this alteration leads to a temporal elongation of the pulse that should fully be taken into account once the result of a photoinduced chemical reaction is analyzed. Therefore, the actual pulse form is worth

## self-referencing pulse characterization
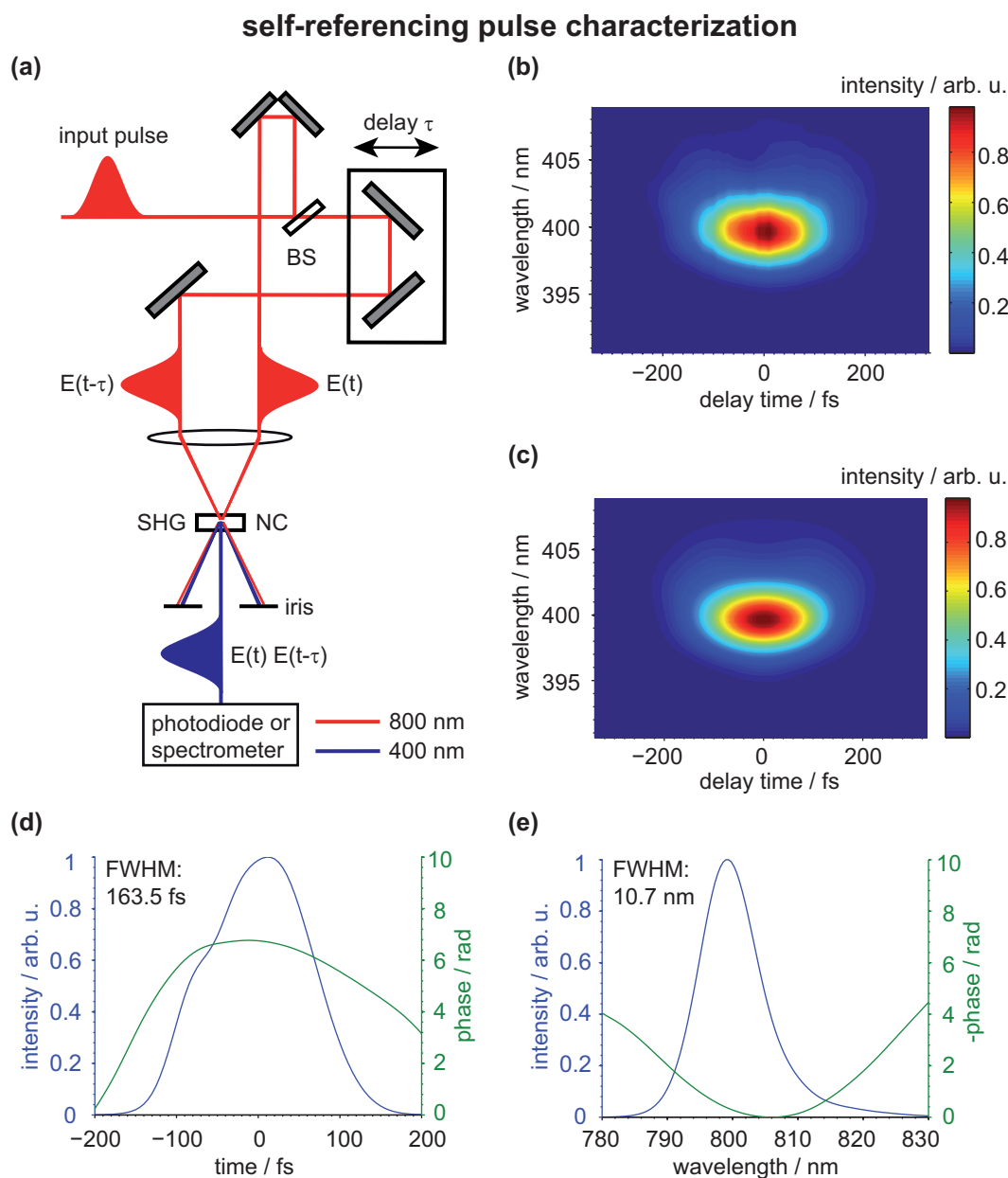


**Figure 2.4:** Schematic depiction of a self-referencing pulse characterization (a) with exemplary FROG traces (b)–(c) and retrieved spectral and temporal intensity- and phase functions (d)–(e). The input pulse is divided into two by a beamsplitter (BS), one part is delayed and subsequently overlapped with its replica in a nonlinear crystal (NC) to perform second harmonic generation (SHG). Exploiting phase-matching conditions, merely the cooperative signal of both pulses is detected, the fundamental beams and the according second harmonics are blocked by an iris. Detection of the $\tau$-dependent signal via a photodiode leads to an intensity autocorrelation; with a spectrometer FROG traces are recorded. The measured FROG trace of a 800 nm pulse, centered around 400 nm respectively, is shown in (b). The FROG algorithm provides the reconstructed complement (c), accompanied by the according temporal (d) and wavelength-dependent (e) intensity and phase functions, including the temporal and spectral FWHM. (b)–(e) illustrate the full set of information derived from a FROG measurement and analysis.

knowing in all types of measurements making use of ultrashort light fields, and usually an according pulse characterization setup completes the experimental instrumentation.

Pulse characterization is a wide field consisting of several different techniques implemented in various geometries. In the following the focus lies on the method that has been utilized within the scope of this thesis: the frequency-resolved optical gating (FROG) [40–42] and more precisely the cross-correlation FROG (XFROG) [43, 44], which is a specialization of the FROG technique with respect to the intersected light fields oscillating at different frequencies. In general, FROG is a further development of an intensity autocorrelation. In the latter, the laser beam to be characterized is divided into two and subsequently spatially and temporally overlapped in a nonlinear crystal (see Fig. 2.4a). Furthermore both beams are noncollinearly incident on the crystal, which is not necessary but in the following assumed. The temporal overlap can be attuned, as one of the two pulse replica travels along a motorized delay stage in front of the crystal. The motor-controlled delay therefore is equivalent to the temporal delay $\tau$ between the overlapping pulses. For both temporal and spatial overlap a cooperative signal is created, as explained in Sec. 2.2.2, and detected by a photodiode while scanning along the $\tau$-axis. As a result, only intensity related information on a laser pulse are revealed, which gives a feedback about the pulse duration, for instance. In a FROG measurement the detection is carried out spectrally resolved so that the measured signal additionally contains information on the optical spectrum including the frequency-dependent phase function.

Considering the difference and sum frequency generation as described in Section 2.2.2, the pulse that has to be examined determines which process is appropriate. For instance, the characterization of laser pulses in the visible spectral region can easily be done by means of the second harmonic generation, usually performed in a BBO crystal. In a self-referencing manner as delineated in the preceding paragraph, the pulse and its replica overlap and create a new cooperative signal at half the wavelength or twice the frequency, respectively (Fig. 2.4a). Due to the phase matching condition that has to be obeyed thereby, the noncollinear geometry ensures that the measured signal is spatially separated from the two original beams, and therefore interfering contributions are eliminated. For every delay step $\tau$ the signal is recorded spectrally resolved, thus leading to a two-dimensional representation as a function of the signal frequency $\omega$ and $\tau$. This is called a FROG trace (see Fig. 2.4b), which can be expressed in the discussed case of a SHG-FROG as

$$I_{\text{SHG–FROG}}(\omega, \tau) = \left| \int_{-\infty}^{\infty} E(t)E(t - \tau)e^{-i\omega t}\mathrm{d}t \right|^2 . \tag{2.43}$$

From this measurement, the complete electric field including the phase can be extracted (see Fig. 2.4c–e). This is done with a numerical algorithm that iteratively calculates a FROG signal and minimizes the deviation from the measured trace [42].

To characterize laser pulses in the UV spectral region a different technique has to be utilized, since a self-referencing approach is no longer applicable. This is because the phase matching condition can no longer be fulfilled. Furthermore, it is due to the physical properties of the available nonlinear crystals, that drastically diminish the efficiency of

**cross-referencing pulse characterization**

**(a)**

UV input pulse

reference
input pulse

delay $\tau$

$E_{ref}(t-\tau)$                    $E_{UV}(t)$

DFG ☐☐ NC

blocker

$E_{UV}(t)\,E_{ref}(t-\tau)$

| | |
|---|---|
| photodiode or spectrometer | 800 nm |
| | 590 nm |
| | 400 nm |
| | 338 nm |

**(b)**

intensity / arb. u.

**(c)**

intensity / arb. u.

**(d)**

FWHM:
62.5 fs

**(e)**

FWHM:
2.9 nm
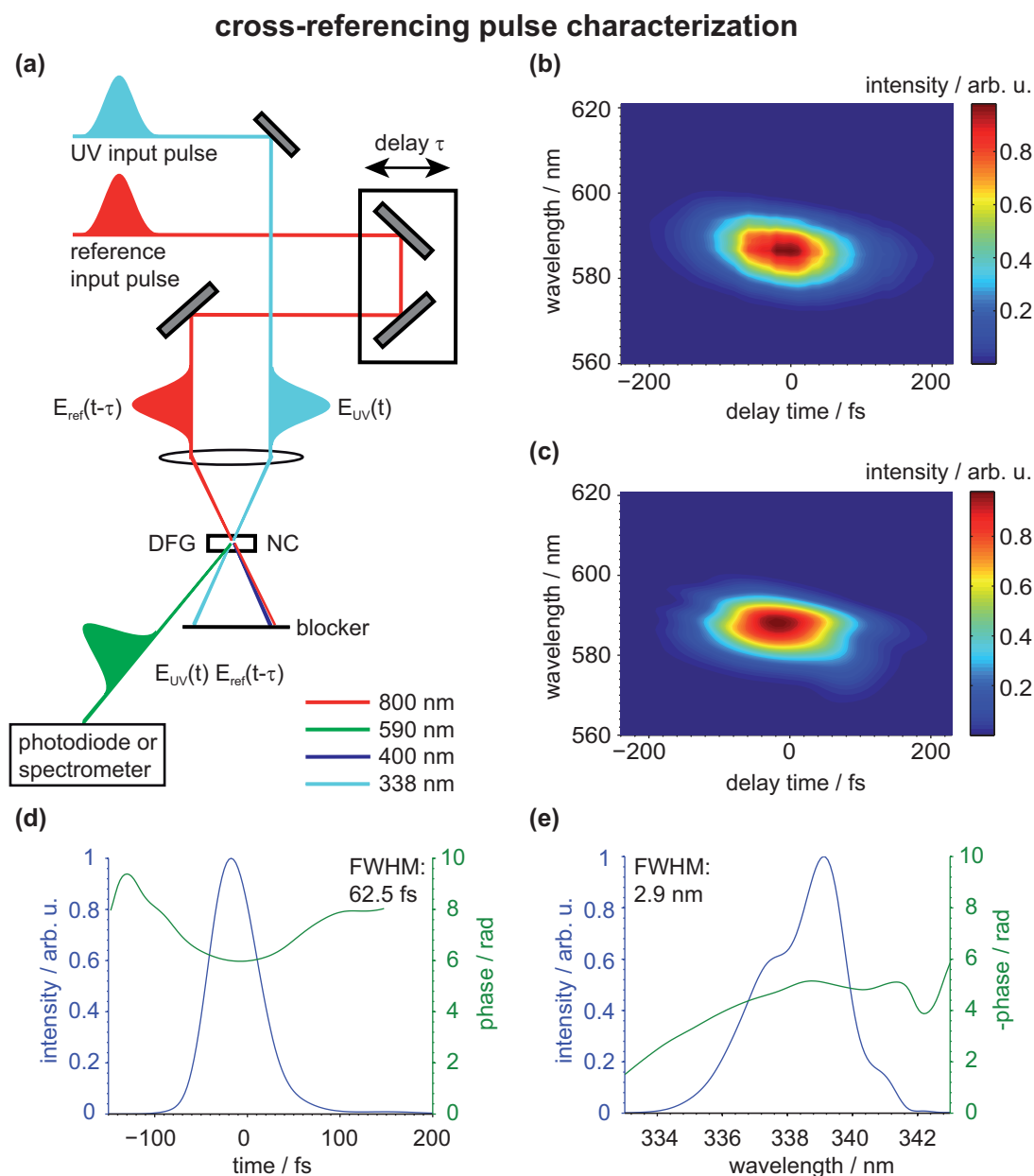
**Figure 2.5:** Schematic depiction (a) and results (b)–(e) of a cross-referencing pulse characterization. In contrast to the self-referencing technique, explained in Fig. 2.4, the UV input pulse to be characterized is mixed with an already known reference pulse in a nonlinear crystal (NC) to perform difference frequency generation (DFG). Likewise, phase-matching is exploited and the detection of the $\tau$-dependent cooperative signal via a photodiode leads to an intensity autocorrelation; with a spectrometer cross-correlation FROG (XFROG) traces are recorded. The measured DFG-XFROG trace illustrated in (b) shows a pulse centered around 590 nm that arises from a UV pulse centered around 338 nm mixed with a 800 nm reference pulse (the one shown in Fig. 2.4). The FROG algorithm provides the reconstructed complement (c), accompanied by the according temporal (d) and wavelength-dependent (e) intensity and phase functions, including the temporal and spectral FWHM.

second harmonic generation the smaller the involved wavelengths become (BBO, e.g., shows nearly 100% absorption below 190 nm). Therefore, one can take advantage of a cross-referencing technique by mixing the unidentified UV pulse with a well known visible or NIR reference pulse in a DFG process, as depicted in Fig. 2.5a. The latter can be the fundamental light at 800 nm that has been characterized in turn before via a SHG-FROG measurement. This transfers the desired information on the electric field from the UV to the visible region. An according cross-correlation FROG trace is shown in Fig. 2.5b and can be mathematically formulated as

$$I_{\text{XFROG}}(\omega, \tau) = \left| \int\limits_{-\infty}^{\infty} E_{\text{UV}}(t) E_{\text{ref}}^*(t - \tau) e^{-i\omega t} \mathrm{d}t \right|^2. \tag{2.44}$$

Again, an algorithm has to be used for the reconstruction and retrieval of the complete electric field (see Fig. 2.5c–e) [42, 45]. In Figure 2.5b–e an example of a characterized UV pulse is given, that has not been specially shaped or actively manipulated. All higher order phase contributions derive from unavoidable light-matter interactions the pulse experiences till the actual experiment takes place. The same is also true for the reference pulse presented in Figure 2.4b–e.

The precise experimental implementation of the AOPDF as well as of the pulse characterization devices will be presented in Section 3.3.1; in Section 6.1 preliminary results for prospective experiments are illustrated.

## 2.3 Electronic and vibrational structure of molecules

To investigate photoinduced chemical reactions, on the one hand certain implements are necessary, like ultrashort laser pulses with differing wavelengths, of which the theoretical understanding, generation and characterization have been introduced in the previous sections. On the other hand, it is essential to comprehend the processes on a molecular level, induced by such light fields. Thus, this section discusses briefly the basic concepts behind the different molecular transitions upon varying optical excitations.

Central to the according quantum-mechanical formulation is the solution of the time-independent, non-relativistic Schrödinger equation that describes a molecular system consisting of N nuclei and M electrons located at $\mathbf{r}_{\text{M}}$ and $\mathbf{R}_{\text{N}}$ [46–49]:

$$\hat{H}(\mathbf{r}_{\text{M}}, \mathbf{R}_{\text{N}}) |\Psi_{mol}(\mathbf{r}_{\text{M}}, \mathbf{R}_{\text{N}})\rangle = E |\Psi_{mol}(\mathbf{r}_{\text{M}}, \mathbf{R}_{\text{N}})\rangle. \tag{2.45}$$

The Schrödinger equation includes the molecular wave function $|\Psi_{mol}(\mathbf{r}_{\text{M}}, \mathbf{R}_{\text{N}})\rangle$, the energy eigenvalue $E$ and the Hamiltonian $\hat{H}(\mathbf{r}_{\text{M}}, \mathbf{R}_{\text{N}})$ that comprises the kinetic energy of the electrons and the nuclei, the electron–electron potential energy, the nuclear–nuclear potential energy and the electron–nuclear potential energy:

$$\hat{H}(\mathbf{r}_{\text{M}}, \mathbf{R}_{\text{N}}) = \mathcal{T}_{\text{e}} + \mathcal{T}_{\text{n}} + \mathcal{V}_{\text{ee}} + \mathcal{V}_{\text{nn}} + \mathcal{V}_{\text{en}}. \tag{2.46}$$

An analytic solution of the Schrödinger equation, even for small molecules, is nonexistent. Hence, approximations have to be adopted, for instance the well-known Born–

Oppenheimer approximation. It utilizes the mass difference between electrons and protons, which is on the order of $10^3$, and assumes that the electrons' positions instantaneously adapt to the comparatively slowly moving nuclei. This allows for a separation of the total molecular wave function into an electronic part and a nuclear wave function:

$$|\Psi_{mol}(\mathbf{r}_\mathrm{M}, \mathbf{R}_\mathrm{N})\rangle = |\Psi_e(\mathbf{r}_\mathrm{M}, \mathbf{R}_\mathrm{N})\rangle |\Psi_n(\mathbf{R}_\mathrm{N})\rangle. \tag{2.47}$$

The spin wave function has been neglected in this notation and the electronic wave function $|\Psi_e(\mathbf{r}_\mathrm{M}, \mathbf{R}_\mathrm{N})\rangle$ incorporates $\mathbf{R}_\mathrm{N}$ as a parameter. Insertion of Eq. (2.47) into the Schrödinger equation (confer Eq. (2.45)), under consideration of the according contributions to the Hamiltonian, therefore yields an electronic Schrödinger equation at fixed coordinates $\mathbf{R}_\mathrm{N}$ and a nuclear Schrödinger equation [48]:

$$(\mathcal{V}_\mathrm{en} + \mathcal{V}_\mathrm{e} + \mathcal{T}_\mathrm{e}) |\Psi_e(\mathbf{r}_\mathrm{M}, \mathbf{R}_\mathrm{N})\rangle = E_\mathrm{S}(\mathbf{R}_\mathrm{N}) |\Psi_e(\mathbf{r}_\mathrm{M}, \mathbf{R}_\mathrm{N})\rangle, \text{ and} \tag{2.48}$$

$$[\mathcal{T}_\mathrm{n} + E_\mathrm{S}(\mathbf{R}_\mathrm{N}) + \mathcal{V}_\mathrm{n}(\mathbf{R}_\mathrm{N})] |\Psi_\mathrm{n}(\mathbf{R}_\mathrm{N})\rangle = E |\Psi_\mathrm{n}(\mathbf{R}_\mathrm{N})\rangle. \tag{2.49}$$

For every value of the parameter $\mathbf{R}_\mathrm{N}$ the electronic part is solved to receive the particular energy eigenvalues $E_\mathrm{S}(\mathbf{R}_\mathrm{N})$ first. Thereafter, based on the results obtained, the nuclear Schrödinger equation is computed. The energy eigenvalues define the shape of the potential energy, pursuant to which the motions of all nuclei take place.

The dimension of the full potential energy landscape depends on the number of atoms the molecule consists of. Figure 2.6 depicts the potential energy surface (PES) of one electronic state of an exemplary triatomic molecule ABC, whose nuclear configuration is determined by two bond lengths and the bond angle; the latter is fixed in the graph shown. Consequently, since there are 3N degrees of freedom for all kinds of molecular motions, with an increasing number of atoms, PESs only represent a certain part of the full description of the potential energy in a single electronic state. Typically, the choosing of the coordinate axis falls on particular geometric quantities, which are of special interest during the photophysical reaction to be investigated; one thus also speaks of reaction coordinates on the axis of PESs. If such a reaction coordinate is defined, the analysis of a photoinduced reaction can be simplified by looking at a two-dimensional potential energy curve. In case of a diatomic molecule this is the full energetic description, provided that a translation of the whole system is omitted. For more complicated molecules it is a reduction to a two-dimensional representation in the sense that a potential energy curve is simply a cut through the PES or a projection of the PES on the reaction coordinate of interest. This is illustrated in Figure 2.7 that pictures two electronic singlet bound states $S_0$ and $S_1$, on top of which vibrational states $\nu = 0, 1, 2, ...$ can be seen. Rotational states that build a substructure on top of every vibrational state are omitted due to their limited relevance in liquid phase experiments. Both curves exhibit corresponding equilibrium bond distances $R_0$ and $R_1$ where the potentials' slopes are zero.

For completeness, it should be mentioned that the adiabatic PESs shown, derived with the Born–Oppenheimer approximation, can fail to describe the realistic behavior of molecules. It is not unusual that two electronic levels energetically approach each other at one nuclei configuration. If the energy gap is comparable to the energy distance between vibrational states or even smaller, the assumption that the electrons instantaneously adapt to positional changes of the nuclei is no longer valid. In this case
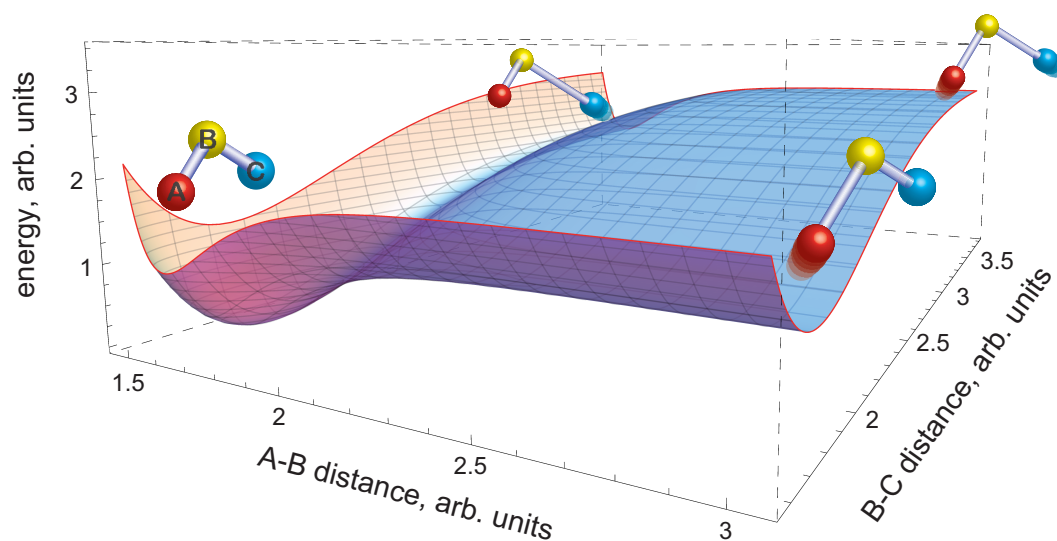
**Figure 2.6:** Potential energy surface of an exemplary triatomic molecule ABC modeled with two Morse potential functions along the bond distances A–B and B–C, respectively. For a diatomic molecule AB, a single Morse potential along the bond distance (red projections onto the boundary surfaces) would be the full energetic description of one electronic state. In case of a triatomic molecule, the bond angle has to be fixed so that an PES as shown represents all information. In case of larger molecules, providing 3N-6 degrees of freedom for vibrational motions (3N-5 for linear molecules), a PES only reflects a particular extract of the energy eigenvalues, which have been calculated by means of the Schrödinger equation.

vibrational and electronic interactions are strongly correlated, i.e., vibronic coupling has to be taken into account and the necessity of a nonadiabatic treatment of molecular transitions arises [50, 51].

There are many ways to model and calculate the shape of PESs (see Sec. 2.4), depending on the type and size of the molecule. A quite simple and neat approach is the use of Morse potentials

$$E_S(R) = D_e[1 - e^{-\alpha(R-R_0)}]^2, \tag{2.50}$$

as depicted in the Figures 2.6 and 2.7. The curvature is defined by $\alpha$, $D_e$ is the sum of zero point energy and dissociation energy. Morse potentials are analytic solutions of the Schrödinger equation [49]. Despite the simple form, they comprise some essential aspects concerning the general behavior of molecules, including the distance of energy between adjacent vibrational states, which decreases with increasing quantum number $\nu$. This is also reflected by the energy eigenvalues:

$$E_\nu = \hbar\omega_0 \left[ (\nu + \frac{1}{2}) - \beta(\nu + \frac{1}{2})^2 \right], \quad \nu = 0, 1, 2, .... \tag{2.51}$$

The anharmonicity constant $\beta$ is a measure of the deviation from the harmonic ansatz, that is only valid for small deflections $|R - R_0|$.

Interactions of a molecular system with an external electromagnetic field entail changes in the population of certain molecular states. Therefore, once the potential energy land-

scapes are specified, transitions between electronic and vibrational states have to be taken into account. In compliance with Fermi's golden rule, the rate of a transition from an initial state $|\Psi_i\rangle$ to a final state $|\Psi_f\rangle$ is proportional to the absolute square of the dipole matrix element $M_{if}$:

$$w_{i \to f} \propto |M_{if}|^2. \tag{2.52}$$

The general form of the transition dipole matrix element in bra-ket notation is given by

$$M_{if} = \langle \Psi_i | \boldsymbol{\mu} | \Psi_f \rangle. \tag{2.53}$$

The electric dipole operator $\boldsymbol{\mu}$ contained therein depends both on the location of all electrons and nuclei. With the according nuclear charges $Z_N e$ the dipole operator can be written as

$$\boldsymbol{\mu} = \sum_N Z_N e \mathbf{R}_{\mathrm{N}} - \sum_M e \mathbf{r}_{\mathrm{M}} = \boldsymbol{\mu}_{\mathrm{n}} + \boldsymbol{\mu}_{\mathrm{e}} \tag{2.54}$$

and split into an electronic and a nuclear part. Under consideration of the Born–Oppenheimer approximation determined in Equation (2.47), the dipole matrix element becomes

$$M_{if} = \langle \Psi_{\mathrm{n},i} \Psi_{\mathrm{e},i} | \boldsymbol{\mu}_{\mathrm{n}} + \boldsymbol{\mu}_{\mathrm{e}} | \Psi_{\mathrm{e},f} \Psi_{\mathrm{n},f} \rangle. \tag{2.55}$$

Since the electronic wave functions are orthogonal to each other, the dipole matrix element can be simplified to the following form [49]:

$$M_{if} = \langle \Psi_{\mathrm{e},i} | \boldsymbol{\mu}_{\mathrm{e}} | \Psi_{\mathrm{e},f} \rangle \times \langle \Psi_{\mathrm{n},i} | \Psi_{\mathrm{n},f} \rangle. \tag{2.56}$$

The first term is the electronic transition dipole element. The absolute square of the second term, $|\langle \Psi_{\mathrm{n},i} | \Psi_{\mathrm{n},f} \rangle|^2$, is called the Franck–Condon factor. Whether, and if so, to what extent a transition occurs, depends in the first instance on non-vanishing contributions of $|M_{if}|^2$. From this, the selection or transition rules emerge. The intensity of a transition depends on the overlap of the corresponding wave functions, i.e., the overlap integral included in the Franck–Condon-factor. Consequently, a transition between two states is more likely to take place from one maximum of the probability density to another. The maxima are located at the equilibrium bond distance $R_0$ for $\nu = 0$ but shift to the points of intersection between the potential curve and the vibrational states with increasing vibrational quantum numbers. As an electronic transition proceeds much faster than the nuclear motion does, vibronic transitions are depicted by vertical lines in potential energy schemes. This is known as the Franck–Condon principle and illustrated with the aforementioned aspects in Figure 2.7.

Another important aspect gained from this, is that a molecular system after excitation contains a certain amount of excess energy with respect to the vibrational ground state in the excited electronic level. The relaxation from a vibrationally hot state takes place via different mechanisms that are broadly categorized into inter- and intramolecular processes [52–54]. The latter is known as intramolecular vibrational redistribution (IVR), i.e., vibrational energy, initially localized in a certain mode, is redistributed among many of the vibrational modes of a molecule (3N-6 or 3N-5 in case of a linear molecule). In general, IVR proceeds on a faster timescale than the second mechanism, the vibrational relaxation via an intermolecular energy transfer, where the hot vibrational modes are
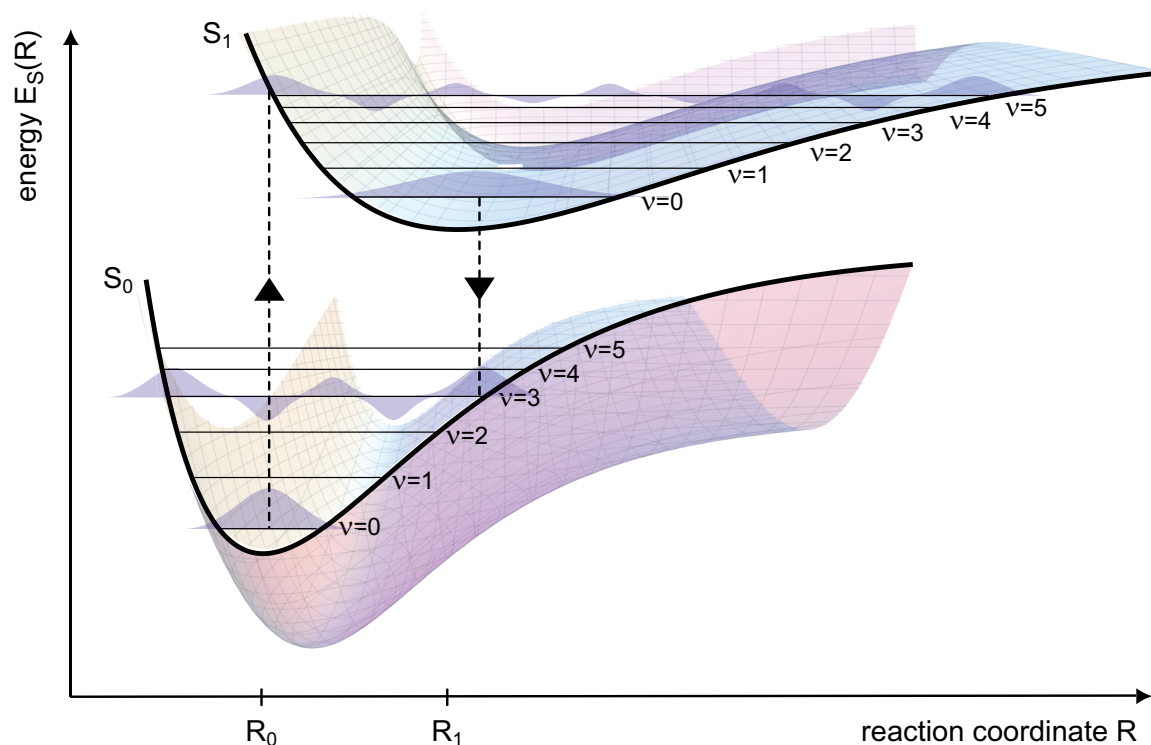
**Figure 2.7:** Potential energy curves of two bound singlet electronic states $S_0$ and $S_1$ in combination with the according vibrational levels $\nu = 0, 1, 2, \ldots$ and exemplary vibrational wave functions. Owing to the anharmonicity, the distance of energy between adjacent vibrational levels decreases with increasing quantum number $\nu$. Pursuant to the Franck–Condon principle, vibronic transitions are depicted by vertical arrows, since electronic transitions proceed instantaneously in comparison to nuclear movements. Furthermore, transitions are more likely to happen between the maxima of the probability densities or the participating wave functions, respectively. For a diatomic molecule the PESs indicated in the background would not exist, as there would be only one degree of freedom for molecular vibrations.

directly coupled to parts of the solvent molecules, which act as a thermal bath. Although the IVR is called an intramolecular process, both mechanisms have a strong solvent dependence in common. For instance, water can assist in vibrational relaxation. This is due to its large dipole in conjunction with fast, abrupt reorientation dynamics that provide a rapidly fluctuating local electric field, whereby the full influence of many internal modes is realized for vibrational relaxation [55, 56]. On the other hand, IVR can be hindered by the solvent. Even if no molecular transitions are resonant with Raman or IR fundamental frequencies of the solvent, the average amount and distance of the solvent–solute bonds is crucial for IVR time constants [57, 58]. In other words, the solvation shell structure that surrounds and couples to the vibrational system, decides whether hydrogen bonds spatially trap vibrational excitations, thus inhibiting IVR or not.

A theoretical description of solvent-dependent relaxation processes can be carried

out by dint of evaluating the frequency–frequency correlation function (FFCF) [59, 60], which is the likelihood that a molecular system remembers a preceding excitation frequency. It is defined as

$$C(t) = \langle \delta\omega(0)\,\delta\omega(t)\rangle. \qquad (2.57)$$

In this expression, $\delta\omega(t)$ denotes a momentary frequency fluctuation from the average value $\langle\omega\rangle$, i.e., $\delta\omega(t) = \omega(t) - \langle\omega\rangle$. The FFCF comprises a homogeneous and an inhomogeneous contribution to the line shape of a transition. In this sense it can be written in the form

$$C(t) = \frac{\delta(t)}{T_2} + \sum_i \Delta_i^2 \exp\left(\frac{-t}{\tau_i}\right). \qquad (2.58)$$

The first, homogeneous term, represented by a delta function $\delta(t)$ is caused by fast structural fluctuations that affect every subunit $i$ of the whole system likewise. Its time constant $T_2$ includes contributions to line broadening from the natural vibrational lifetime, from the pure dephasing, and from orientational relaxation. The second, inhomogeneous part is different for every subunit $i$, because of differing structural microenvironments, and therefore emerges as an averaged effect. It is modeled via a sum of exponentials with frequency fluctuation amplitudes $\Delta_i$ and correlation times $\tau_i$. Since the local environment of a molecular group in the condensed phase constantly fluctuates, the transition frequency fluctuates as well (a process called spectral diffusion). Therefore, the FFCF of a particular transition decays with time. By a comparison between rephasing and non-rephasing amplitudes in a two-dimensional infrared spectroscopy (2D-IR) experiment, the temporal evolution of the FFCF can be extracted, enabling conclusions concerning the temporal evolvement of the solvation shell structure [61, 62].

A further nonradiative relaxation process that might occur is the transition between different electronic states, subsequent to which energetically higher lying vibrational states might be addressed and energy redistribution processes as described can succeed. This sort of relaxation is commonly known as internal conversion (IC). If the participating electronic states are of differing spin multiplicity, the according transition is further specified as intersystem crossing (ISC) [63]. The latter proceeds in general on longer timescales than transitions where the spin multiplicity is preserved.

The phenomena described will be taken up again in the experimental Sections 4.3.3 and 5.3.

## 2.4 Calculating molecular ground states with DFT

In order to gain insight into a quantum-mechanical system such as a molecule and to elucidate its behavior during a photoinduced reaction, the Schrödinger Equation (2.45) has to be solved. As stated in the previous Section 2.3, in case of a many-body problem of interacting electrons this cannot be done analytically. Therefore, numerical approaches embedded in computational methods have to be applied. The Nobel Prizes 1998 to John Pople and Walter Kohn and 2013 to Martin Kaplus, Michael Levitt, and Ariel Warshel substantiate the importance and adaptability of this versatile and complex subject, that will most probably continue to gain in significance with steadily increasing computing

power. However, in the following it is expedient to restrict the discussion of this wide field to the methods actually applied .

Within the scope of this thesis, transition metal complexes and organic molecules together with their respective reaction products have been under investigation. For a more reliable analysis of the experimental data, it has proven to be beneficial to have a certain knowledge of the corresponding ground state structures and vibrational absorption frequencies. For this purpose, calculations based on the density functional theory (DFT) [64, 65] have been performed. This method combines reasonable computational costs with sufficient accuracy concerning the outcomes obtained. However, it is appropriate to discuss modern DFT in terms of the Hartree–Fock model, since the latter facilitates the understanding of DFT and furthermore a combination of both yields more accurate results without getting too expensive with respect to the computing effort.

### 2.4.1 The Hartree–Fock approximation

The Hartree–Fock method is an ab initio or first principle, wave function based procedure to approximately solve the Schrödinger equation that includes the exact M-electron wave function, provided that the Born–Oppenheimer approximation still applies. A simple, yet physically sensible substitute for $\Psi_e(\mathbf{r}_1, \mathbf{r}_2, ..., \mathbf{r}_M)$ is a product of M orthonormal one-electron wave functions $\psi_M(\mathbf{r}_M)$, called spin orbitals, that are in turn products of a spatial orbital $\Phi_M(\mathbf{r}_M)$ and a spin function $\sigma(s) = \alpha(s)$ or $\beta(s)$:

$$\Psi_e(\mathbf{r}_1, \mathbf{r}_2, ..., \mathbf{r}_M) \approx \psi_1(\mathbf{r}_1) \cdot \psi_2(\mathbf{r}_2) \cdots \psi_M(\mathbf{r}_M). \tag{2.59}$$

Since electrons are fermions, the wave function has to be antisymmetric under particle exchange. Consequently, it can also be approximated in the form of a normalized Slater determinant $\Psi_{SD}$:

$$\Psi_e(\mathbf{r}_1, \mathbf{r}_2, ..., \mathbf{r}_M) \approx \Psi_{SD} = \frac{1}{\sqrt{M!}} \begin{vmatrix} \psi_1(\mathbf{r}_1) & \psi_1(\mathbf{r}_2) & \dots & \psi_1(\mathbf{r}_M) \\ \psi_2(\mathbf{r}_1) & \psi_2(\mathbf{r}_2) & \dots & \psi_2(\mathbf{r}_M) \\ \vdots & \vdots & \ddots & \vdots \\ \psi_M(\mathbf{r}_1) & \psi_M(\mathbf{r}_2) & \vdots & \psi_M(\mathbf{r}_M) \end{vmatrix}$$

$$= \frac{1}{\sqrt{M!}} \det\{\psi_1(\mathbf{r}_1)\psi_2(\mathbf{r}_2) \cdots \psi_M(\mathbf{r}_M)\}. \tag{2.60}$$

It should be explicitly stressed at this point that the applied approximation lies in the fact that the exact wave function cannot be expressed as a single determinant; an expansion towards an exact term would be a linear combination of Slater determinants. The single-determinant approximation does not reflect the Coulomb correlation properly, meaning that the instantaneous repulsion of the electrons is not taken into consideration accurately. In other words, the M electrons do not interact directly with each other but experience an averaged, effective repulsive potential [65]. The finding of adequate expressions for electronic exchange and correlation functions is of major interest in the framework of DFT as well (see below).

By means of the variational principle one can now calculate the Slater determinant that yields the lowest energy $E_{HF}$ for the whole quantum-mechanical system. Within the

Hartree–Fock method this is done by varying the spin orbitals $\psi_i$ of the corresponding Slater determinant $\Psi_{\text{SD}}$. For that purpose it is convenient to rewrite the Hamiltonian into the form

$$\hat{H} = \sum_i^M \left( -\frac{1}{2} \nabla^2(\mathbf{r}_i) - \sum_k^N \frac{Z_k e}{|\mathbf{r}_i - \mathbf{R}_k|} \right) + \frac{1}{2} \sum_i^M \sum_j^M \frac{1}{|\mathbf{r}_i - \mathbf{r}_j|}$$
$$= \sum_i^M \hat{h}_i + \frac{1}{2} \sum_i^M \sum_j^M \hat{w}_{ij}, \tag{2.61}$$

with the single-particle operator $\hat{h}_i$ and the two-electron operator $\hat{w}_{ij}$ [66]. Exploiting the orthogonality of $\psi_i$ yields then for the energy

$$E_{\text{HF}} = \langle \Psi_{\text{SD}} | \hat{H} | \Psi_{\text{SD}} \rangle$$
$$= \sum_i^M \langle \psi_i | \hat{h}_i | \psi_i \rangle + \frac{1}{2} \sum_i^M \sum_j^M \left( \langle \psi_i \psi_i | \hat{w}_{ij} | \psi_j \psi_j \rangle - \langle \psi_i \psi_j | \hat{w}_{ij} | \psi_j \psi_i \rangle \right). \tag{2.62}$$

The first term represents the contributions of the kinetic energy and the nuclei–electron attraction of the i-th electron. The second and third term reflect the Coulomb interactions between the i-th and the j-th electron and therefore are called Coulomb integral and exchange integral, respectively. $E_{\text{HF}}$ is a functional of the spin orbitals $\psi_i$ ($E_{\text{HF}} = E[\psi_i]$), which means that it maps a function, the spin orbitals, onto a number, the energy, in contrast to a function, which maps a number onto another number. As already indicated by the name, functionals are the main mathematical concept of DFT, as will be discussed below. In order to find those $\psi_i$ for which $E_{\text{HF}}$ is minimized, a slightly modified functional including Lagrangian multipliers $\epsilon_i$ has to be introduced. By setting the first derivative of this functional to zero, one finally ends up with the Hartree–Fock equations (for a detailed derivation see [67]):

$$\hat{f}_i \psi_i = \epsilon_i \psi_i, \text{ with } i = 1, 2, ..., M. \tag{2.63}$$

In these M equations, which look like eigenvalue equations, the Lagrangian multipliers have the physical interpretation of orbital energies. The Fock operator $\hat{f}$ is defined as

$$\hat{f}_i = -\frac{1}{2} \nabla^2(\mathbf{r}_i) - \sum_k^N \frac{Z_k e}{|\mathbf{r}_i - \mathbf{R}_k|} + \mathcal{V}_{\text{HF}}(i) = \hat{h}_i + \mathcal{V}_{\text{HF}}(i). \tag{2.64}$$

The Hartree–Fock potential $\mathcal{V}_{\text{HF}}(i)$ is an average repulsive potential that the i-th electron experiences due to the M-1 remaining electrons. Furthermore it incorporates the non-local, non-classical exchange contribution. Both are also given in Eq. (2.62). According to that, as one-particle operator, $\hat{f}$ replaces the Hamiltonian from Eq. (2.61), neglects the two-electron repulsion operator $\hat{w}_{ij}$, and therefore instantaneous particle correlations are entirely omitted. This is why the HF method is a mean-field theoretical ansatz.

On the basis of these considerations, some aspects concerning the Hartree–Fock method in general shall be summarized:

1. The HF potential contains all spin orbitals $\psi_i$, thus every Fock operator $\hat{f}_i$ depends on the spin orbitals as well and Eqs. (2.63) are no regular eigenvalue problems that would be solvable in a closed form. Instead, they have to be solved iteratively with a technique called self-consistent field (SCF). This technique begins with a guessed set of orbitals, then creates the Slater determinant and calculates the HF equations, resulting in a new set of orbitals. During this procedure, the energy is minimized till a predefined convergence criterion is met. However, the first guess for the orbital set is not an arbitrary one, but a linear combination of basis functions, the basis set. Its complexity and the kind of basis functions that are chosen, e.g., Gaussian type orbitals [67], is specified with respect to the actual system that has to be calculated, in compliance with an acceptable computation effort.

2. In Eq. (2.62), the double summation for $i = j$ is not excluded so that a Coulomb self-interaction of one electron is calculated in the corresponding integral. This repulsion would also be included in the case of a system consisting only of one single electron, which is physically nonsensical. In the HF method, however, the exchange term compensates for this self-interaction issue: for $i = j$ the Coulomb and the exchange integrals become identical and cancel out. For a one-electron system only the electron–nucleon interaction would remain. Unfortunately, in the DFT the embedding of the exchange energy and the avoiding of the self-interaction issue are major challenges.

3. Owing to the variational principle, the absolute value of $E_{\text{HF}}$ derived with a single Slater determinant, which is an approximate wave function, is always smaller than the correct ground state energy $E_0$. The difference is called correlation energy $E_{\text{HF}}^{\text{C}} = E_0 - E_{\text{HF}}$, because it is mainly due to the missing electron correlation contribution that consists of a dynamical and a non-dynamical or static part [65]. There are so-called post Hartree–Fock methods like the Coupled-Cluster method (CC), the Møller–Plesset perturbation theory (MP), or the complete active space self consistent field method (CASSCF) that are able to capture both types of electron correlation [66].

4. Nevertheless, for calculations on a system with M electrons, every computational procedure based on the Hartree–Fock scheme has to deal with 3M coordinates or 4M if the spin is included. Consequently, they are computationally demanding and disadvantageous with respect to the scaling when the size of the system under investigation grows. This aspect is circumvented by DFT calculations, as will be discussed in the following paragraph.

## 2.4.2 The framework of density functional theory

The central element of density functional theory is the probability density $\rho(\mathbf{r})$, commonly named electron density, which is a multiple integral over all but one of the spatial coordinates and over the spin coordinates:

$$\rho(\mathbf{r}) = M \sum_s \int d\mathbf{r_2} \cdots \int d\mathbf{r_M} |\Psi_e(\mathbf{r}, s, \mathbf{r}_2, ..., \mathbf{r}_M)|^2, \qquad (2.65)$$

with $\rho(\mathbf{r})\mathrm{d}\mathbf{r}$ being the probability density to find any electron in a region $\mathrm{d}\mathbf{r}$ around $\mathbf{r}$. It is normalized to the number of electrons: $\int \mathrm{d}\mathbf{r}\rho(\mathbf{r}) = M$. Following the first Hohenberg–Kohn theorem [68], the ground state energy of a system with M electrons is a functional of the ground state electron density, and the latter uniquely defines the Hamiltonian of the system. Hence, the challenge to gain knowledge about a quantum-mechanical system has been reduced to calculations depending on three variables (four if the spin is considered), instead of 3M or 4M, respectively, as shown above.

The energy functional is composed of the kinetic energy, the interaction with the external potential, and the electron–electron interaction and can be written as

$$E[\rho] = \mathcal{T}[\rho] + \mathcal{V}_{\mathrm{ext}}[\rho] + \mathcal{V}_{\mathrm{ee}}[\rho]. \tag{2.66}$$

Thus, it picks up again the contributions of the Hamiltonian defined in Eq. (2.61). But in the following, the different parts are expressed in terms of the electron density. The functional representing the nucleus–electron interaction potential is

$$\mathcal{V}_{\mathrm{ext}}[\rho] = \int \rho(\mathbf{r}_i)\hat{\mathcal{V}}_{\mathrm{ext}}(\mathbf{r}_i)\mathrm{d}\mathbf{r}_i = -\sum_k^N \int \frac{\rho(\mathbf{r}_i)Z_k}{|\mathbf{r}_i - \mathbf{R}_k|}\mathrm{d}\mathbf{r}_i. \tag{2.67}$$

The electron–electron functional and the kinetic functional are summarized to the Hohenberg–Kohn functional $\mathcal{F}[\rho] = \mathcal{T}[\rho] + \mathcal{V}_{\mathrm{ee}}[\rho]$, of which the accurate form is unknown. A significant part of the electron–electron interaction is the classical Coulomb interaction (the second term in Eq. (2.62)), so that the whole electron–electron interaction can be separated into a classical part $\mathcal{C}[\rho]$ and a non-classical part $E_{\mathrm{ncl}}[\rho]$, which comprises the self-interaction correction and the Coulomb exchange and correlation:

$$\mathcal{V}_{\mathrm{ee}}[\rho] = \frac{1}{2}\int\int \frac{\rho(\mathbf{r}_i)\rho(\mathbf{r}_j)}{|\mathbf{r}_i - \mathbf{r}_j|}\mathrm{d}\mathbf{r}_i\mathrm{d}\mathbf{r}_j + E_{\mathrm{ncl}}[\rho] = \mathcal{C}[\rho] + E_{\mathrm{ncl}}[\rho]. \tag{2.68}$$

Concerning the kinetic functional, Kohn and Sham suggested an approach that effectively outsources the necessity of an approximation [69]. Instead of determining the kinetic energy by dint of the accurate functional $\mathcal{T}[\rho]$, a notional system of M non-interacting electrons is introduced, so that a certain amount of the kinetic energy can be calculated exactly and the remainder has to be handled in an approximate manner. A system of M non-interacting electrons can be described by a single Slater determinant wave function composed of M orthonormal orbitals $\Phi_i$, called Kohn–Sham orbitals. Within the Hartree–Fock method the Slater determinant itself is an approximation to an accurate wave function of a M-electron system. Though, for M electrons that do not interact among themselves but move in the field of an effective potential (like the Hartree–Fock potential $\mathcal{V}_{\mathrm{HF}}$ described in Eq. (2.64)) a single Slater determinant constitutes the exact wave function. In such a system, the exact kinetic energy is

$$\mathcal{T}_{\mathrm{KS}}[\rho] = -\frac{1}{2}\sum_i^M \langle\Phi_i|\nabla^2|\Phi_i\rangle = \mathcal{T}[\rho] - \mathcal{T}_{\mathrm{X}}[\rho] \tag{2.69}$$

and therefore the difference between the kinetic energy of the real, interacting system and a residual part $\mathcal{T}_{\mathrm{X}}[\rho]$. Analogously to the Hartree–Fock formalism, one can now

derive a Hamiltonian to this non-interacting reference system with an effective potential $\mathcal{V}_{\mathrm{KS}}$ and eigenvalue equations of the form

$$\hat{f}_i^{\mathrm{KS}} \Phi_i = \epsilon_i \Phi_i, \text{ with } i = 1, 2, ..., M$$

$$\hat{f}_i^{\mathrm{KS}} = -\frac{1}{2} \nabla^2 + \mathcal{V}_{\mathrm{KS}}(i), \tag{2.70}$$

including the Kohn–Sham operator $\hat{f}^{\mathrm{KS}}$. The potential can be chosen such that the electron density of this auxiliary system, $\rho_{\mathrm{S}}(\mathbf{r})$, is identical to the ground state electron density of the target system, $\rho_0(\mathbf{r})$, that includes all occurring particle interactions [65]. It is the sum of the absolute square of all occupied Kohn–Sham orbitals:

$$\rho_{\mathrm{S}}(\mathbf{r}) = \sum_i^M |\Phi_i(\mathbf{r})|^2 = \rho_0(\mathbf{r}). \tag{2.71}$$

In summary, the total energy functional can be rewritten in the form

$$E[\rho] = \mathcal{V}_{\mathrm{ext}}[\rho] + \mathcal{T}_{\mathrm{KS}}[\rho] + \mathcal{T}_{\mathrm{X}}[\rho] + \mathcal{C}[\rho] + E_{\mathrm{ncl}}[\rho], \tag{2.72}$$

where the unknown contributions are further combined to the exchange-correlation functional $E_{\mathrm{XC}}[\rho]$:

$$E_{\mathrm{XC}}[\rho] = \mathcal{T}_{\mathrm{X}}[\rho] + E_{\mathrm{ncl}}[\rho] = (\mathcal{T}[\rho] - \mathcal{T}_{\mathrm{KS}}[\rho]) + (\mathcal{V}_{\mathrm{ee}}[\rho] - \mathcal{C}[\rho]) . \tag{2.73}$$

It incorporates the not exactly known non-classical effects of the potential energy (self-interaction correction, exchange, and correlation) as well as a contribution that has been ignored due to a non-interacting kinetic energy.

In a final step, what has been introduced so far can be subsumed. The energy functional of a real system, described by Equation (2.72), which depends on the Kohn–Sham orbitals as indicated in the Equations (2.69) and (2.71), can be explicitly written in the form

$$E[\rho] = - \sum_i^M \int \sum_k^N \frac{Z_k}{|\mathbf{r}_1 - \mathbf{R}_k|} |\Phi_i(\mathbf{r}_1)|^2 \mathrm{d}\mathbf{r}_1 - \frac{1}{2} \sum_i^M \langle \Phi_i | \nabla^2 | \Phi_i \rangle$$

$$+ \frac{1}{2} \sum_i^M \sum_j^M \int \int |\Phi_i(\mathbf{r}_1)|^2 \frac{1}{|\mathbf{r}_1 - \mathbf{r}_2|} |\Phi_j(\mathbf{r}_2)|^2 \mathrm{d}\mathbf{r}_1 \mathrm{d}\mathbf{r}_2 + E_{\mathrm{XC}}[\rho]. \tag{2.74}$$

Only for the exchange-correlation functional no explicit expression can be given. Still a formal similarity to the results within the Hartree–Fock framework can be recognized (see Eqs. (2.61) and (2.62)) and in the same manner as above, the variational principle can be applied to find the Kohn–Sham orbitals that minimize the energy. They satisfy the set of equations

$$\left( -\frac{1}{2} \nabla^2 + \left[ \int \frac{\rho(\mathbf{r}_2)}{|\mathbf{r}_1 - \mathbf{r}_2|} \mathrm{d}\mathbf{r}_2 + \mathcal{V}_{\mathrm{XC}}(\mathbf{r}_1) - \sum_k^N \frac{Z_k}{|\mathbf{r}_1 - \mathbf{R}_k|} \right] \right) \Phi_i = \epsilon_i \Phi_i, \tag{2.75}$$

called Kohn–Sham equations. The term in squared brackets is exactly the effective potential $\mathcal{V}_{\mathrm{KS}}$ from Eq. (2.70). Hence, if one can calculate the different contributions of the potential $\mathcal{V}_{\mathrm{KS}}$, it can be inserted in the Kohn–Sham equations Eq. (2.75). This yields the orbitals and consequently the ground state electron density and the corresponding energy. Since the effective potential depends on the electron density and likewise on the Kohn–Sham orbitals, again this has to be done iteratively within a SCF-procedure, analogously to the Hartree–Fock method. Therefore, the Kohn–Sham orbitals are expanded in terms of basis sets, which are appropriate for the specific molecular system under investigation.

The potential $\mathcal{V}_{\mathrm{XC}}$ that arises from the exchange-correlation energy $E_{\mathrm{XC}}$ is defined as the functional derivative of the latter with respect to the electron density:

$$\mathcal{V}_{\mathrm{XC}}(\mathbf{r}) \equiv \frac{\partial E_{\mathrm{XC}}[\rho]}{\partial \rho(\mathbf{r})}. \tag{2.76}$$

It is worth emphasizing that within the DFT formalism described so far, accurate expressions for $\mathcal{V}_{\mathrm{XC}}$ or $E_{\mathrm{XC}}$ would yield the exact energy eigenvalue of the Schrödinger equation. Up to this point, there is no approximation incorporated in contrast to the Hartree–Fock method.

Nevertheless, to work with DFT one has to introduce approximations for the unknown exchange correlation potential and functional, respectively. The more accurate the chosen functional is, the higher the quality of a calculation using DFT becomes. Compared to quantum chemistry methods based on wave functions, a systematic procedure to improve functionals does not exist in DFT [65, 70] and the choice of an appropriate functional varies with the properties of the molecular system. However, there are approaches that have been established throughout the past decades. First, there is the rather simple concept of the local density approximation (LDA) [71]. The functional depends solely on the electron density, which is modeled by a uniform electron gas that is an exact solution for the exchange correlation functional. LDA, however, fails to calculate bond lengths correctly; its use in quantum chemistry therefore is strongly limited. An advancement of the LDA is the generalized gradient approximation (GGA) that additionally exploits the gradient of the electron density. Thereby, the inhomogeneous electron density in molecules is taken into consideration.

In practice, it is common to use functionals whose exchange and correlation contributions derive from different approaches. Becke, for instance, developed in 1988 the well-known pure GGA exchange functional, called B88 [72]. In the same year, Lee, Yang and Parr introduced a correlation functional, simply denoted by LYP [73], which contains empirical parameters and which is not derived from a uniform electron gas LDA. Both partial functionals combined, provide the widely used BLYP functional. Through yet another admixture of Hartree–Fock type exchange energy, hybrid functionals can be created. In doing so, one only has to rely on approximations concerning the electron correlation, which is the missing part in the Hartree–Fock formalism. A very prominent result is the three-parameter hybrid functional named B3LYP [74–76]

$$E_{\mathrm{XC}}^{\mathrm{B3LYP}} = a E_{\mathrm{X}}^{\mathrm{LDA}} + (1-a) E_{\mathrm{X}}^{\mathrm{HF}} + b E_{\mathrm{X}}^{\mathrm{B88}} + (1-c) E_{\mathrm{C}}^{\mathrm{LDA}} + c E_{\mathrm{C}}^{\mathrm{LYP}}, \tag{2.77}$$
$$\text{with } a = 0.8,\ b = 0.72,\ \text{and } c = 0.81.$$

The B3LYP functional predominantly has been in use within the scope of this thesis (see Secs. 4.3.1 and 5.3.1), as it provides good results for transition metal structures and a reliable scalability when it comes to the comparison between theoretical and experimental findings [77–80].

Besides the choice of an appropriate functional, the second prerequisite that is necessary for a DFT calculation is to determine the basis set, of which the spin orbitals shall consist of. A rough distinction is made between Gaussian-type orbitals (GTO) and Slater-type orbitals (STO). STOs are exponentials combined with spherical harmonics, thus imitating the exact eigenfunctions of the hydrogen atom, whereas GTOs only consist of Gaussian exponentials. From a physical point of view it seems understandable that usually a lot more GTOs than STOs are necessary to achieve an equal accuracy. However, the calculational complexity that arises from STO basis sets, which is generally associated with elaborate numerical techniques, in turn strengthens the applicability of GTOs. Since the use of GTOs allows for analytic calculations of the occurring integrals, again a further development is the attempt to resemble as much as possible a single STO function by a linear combination of GTOs. This produces a single contracted Gaussian function (CGF).

Regarding chemical bonds, the valence electrons merit specific attention. Therefore, valence orbitals are represented by more than one basis function or CGF, respectively, while the core electrons generally are represented by a minimal set. Those split-valence basis sets [81] bear the additional advantage that various orbitals enable the electron density to adjust to the molecular surrounding. This aspect is further intensified by adding polarization and diffuse functions. The former are functions of higher angular momentum, more precisely with one additional node compared to the highest valence orbital, meaning for example that f-type orbitals would be added to a basis set with d-type functions. Polarization functions are necessary to enable orbitals to leave their originally symmetric shape, thus mimicking the deformations that arise as a result of chemical bonding. The diffuse functions are long-ranging Gaussian basis functions that correct the atomic orbitals in the region of large distances from the nuclei.

This leads to an understanding what the expression 6-311+G** for the basis set that has been used for DFT calculations throughout this work comprises [82]. From left to right:

6    Every orbital of the non-valence shells is represented by one contracted Gaussian function that is built up by 6 GTOs.

311    The next block consists of three numbers, meaning that the valence orbitals are composed of three CGFs each; the actual numerical value defines the quantity of summands within the linear combination of Gaussian functions. Hence, each CGF representing a valence orbital is made up of three, one, and another one primitive Gaussian function with different shapes. Accordingly, three numbers behind the hyphen imply a split-valence triple basis set.

+    The plus sign tells that diffuse functions are added to valence atomic orbital of every atom except hydrogen atoms (two plus signs connote that diffuse functions are also added to the orbitals of hydrogen atoms).

G    This basis set works with GTOs, therefore the G.

** The two asterisks indicate the addition of polarization functions to every atom, hydrogen atoms included. Instead of asterisks one can further specify what kind of orbitals (d, f, etc.) and how many of them shall be taken into account for hydrogen atoms and the residual atoms separately.

To conclude this section, a short overview shall be given how the theoretical background is actually implemented and exploited, in order to elucidate the ground state of a molecular system. Using the software package Gaussian 09 [83], the procedure begins by defining the geometrical structure of the molecule as realistic as possible. This is done in an internal coordinate representation (Z-matrix), which describes each atom in terms of a number that defines its positioning within an arbitrary order, its bond length, bond angle, and dihedral angle with respect to neighboring atoms. The more correct this first starting geometry is, the less computational effort has to be put into the subsequent ge-
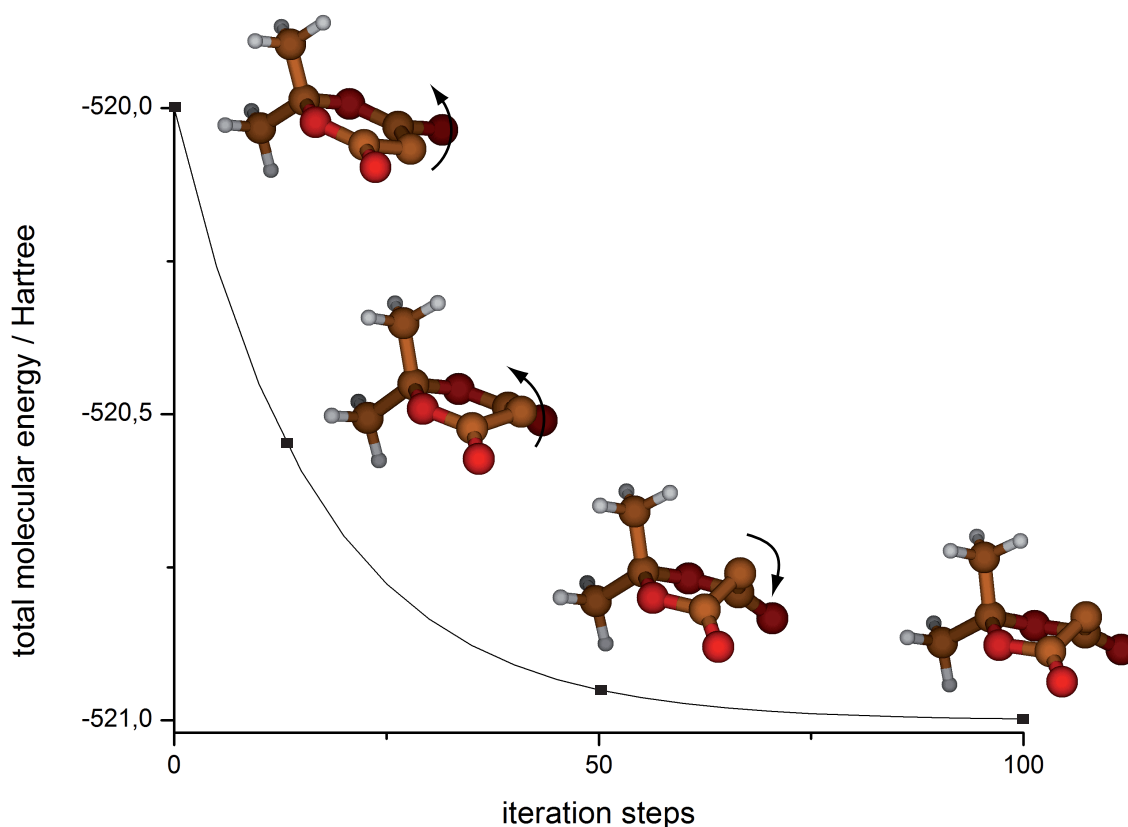


**Figure 2.8:** Exemplary geometry optimization for the equilibrium structure within a DFT calculation by means of the singlet carbene of 5-diazo Meldrum's acid. The procedure begins with a guessed, initial structure, that should not differ too much from the realistic molecular appearance. A computer cluster iteratively minimizes the total molecular energy of the system, expressed in Hartree (Ha or $E_h$, which is roughly the electric potential energy of the hydrogen atom in the ground state and twice its ionization energy $1\,Ha = 27.211\,eV$), till a preassigned convergence criterion is met. This yields the optimized molecular geometry, which in turn forms the substantial part for the subsequent calculation of the vibrational modes in the ground state (see Fig. 2.9). The arrows indicate the direction of the major geometrical changes.
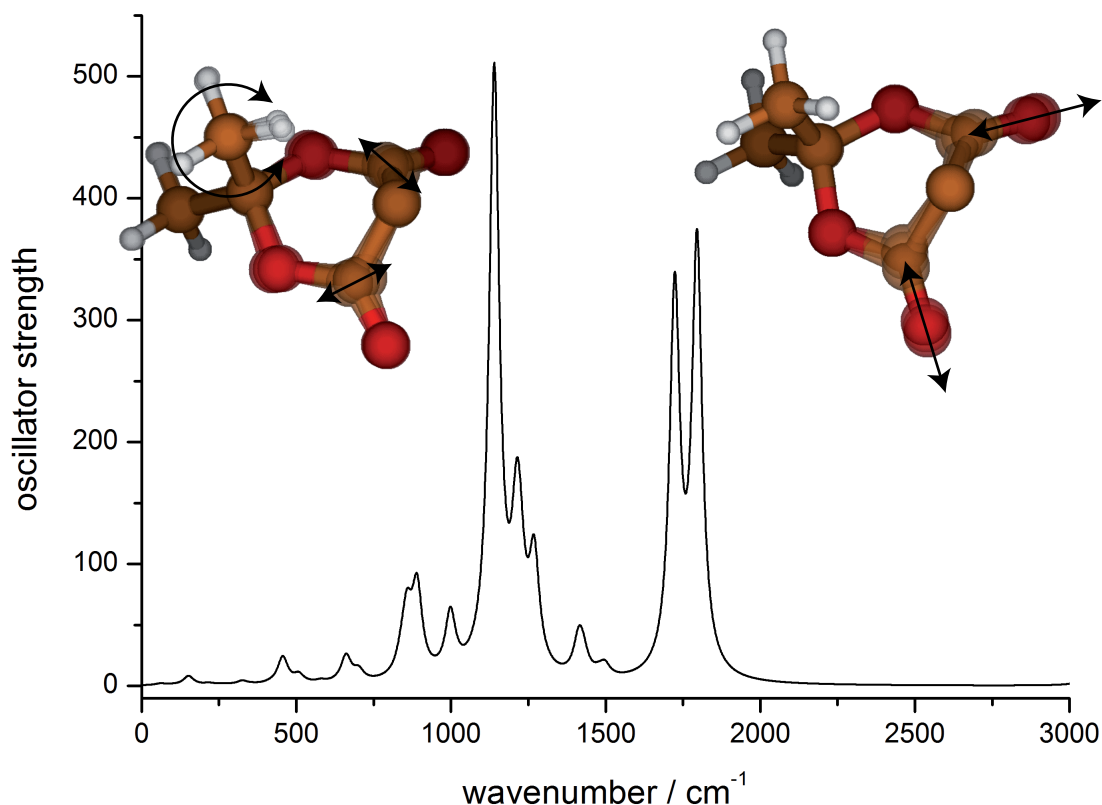
**Figure 2.9:** Vibrational spectrum and exemplary vibrational modes of the singlet carbene of 5-diazo Meldrum's acid, calculated via the Gaussian 09 software package that utilizes DFT. The vibration depicted on the left hand side refers to the mode with the highest oscillator strength. It is located in the fingerprint region and derives from a mixture of bending and stretching of many parts of the molecule, including the hydrogen atoms in the methyl groups. On the right hand side the typical symmetric and antisymmetric C=O stretching modes are shown, where the vibrational motion is mainly located at the functional groups. The arrows highlight the major vibrational deflections.

ometry optimization and the more likely the optimal, real structure will be revealed. For the geometry optimization of the equilibrium structure, one has to determine what functional and basis set shall be applied and whether a solvation model shall be included, for example in the form of a polarized continuum model (PCM). These information (initial Z-matrix, functional, basis set, and further options) form an input file that is processed by a computer cluster that minimizes the total energy of the system iteratively till a preassigned convergence criterion is met (see an exemplary molecule in Fig. 2.8). The output is a Z-matrix that represents the optimized molecular geometry.

Now that the optimal configuration is known, the potential energy surface of the ground state is defined. The curvature of the PES dictates the vibrational frequencies and normal modes in the molecular ground state that are calculated in the next step. The according results are shown in parts in Figure 2.9. Along with a spectrum that can be identically interpreted as a steady-state absorption spectrum in the MIR spectral region,

two exemplary vibrational modes are further illustrated. On the one hand, the vibration with the highest oscillator strength, which is proportional to the probability of absorbing a photon with an appropriate wavelength, is depicted. This mode of the fingerprint region is due to a mixture of bending and stretching of many parts of the molecule, including the hydrogen atoms in the methyl groups. On the other hand, at higher frequencies, a typical C=O stretching mode is shown, where the vibrational motion is mainly located at the functional groups. The major benefit of having access to those simulated data is obvious. If in any kind of spectroscopic measurement within the scope of this thesis a signature at a certain wavelength occurs that cannot be unambiguously assigned to a reaction product, spectra from DFT calculations can help in the process of interpreting experimental data.

A vibrational analysis within the framework of DFT, carried out with Gaussian 09, reveals further information, amongst others the heat capacity, the Gibbs free energy, bond strengths or the enthalpy of the simulated molecular species, subdivided by their different contributions. This is subsumed under the thermochemistry section in the output file of Gaussian.

The explanations given so far concentrated on the calculation of molecular ground states. A discussion on the possibility of calculating excited states, for example via time-dependent density functional theory (TDDFT) [84–86], is omitted. Although it is an exciting and promising way to gain further information about a molecular system upon photoexcitation, this wide and complex field of research has not been exploited by the author of this work himself.

## 2.5 Pump–probe spectroscopy in the MIR

The previous sections conduced to providing insight into the nature of femtosecond laser pulses as well as into the nature of molecular systems interacting with electromagnetic fields in general. Both aspects combined form the theoretical background against which the main experimental technique of this work is embedded: the ultrafast UV-pump–MIR-probe spectroscopy that offers the opportunity of tracing and investigating photoinduced chemical reactions [87]. The associated fundamentals and the possible outcomes appearing in the course of an according measurement will be discussed in the following sections.

### 2.5.1 General detection scheme

Depending on the absorption properties of the molecule under investigation, the generation of ultrashort laser pulses in the UV or visible spectral region allows for the stimulation of vibronic transitions. These pump pulses trigger a photoinduced chemical reaction that can subsequently be monitored via changes in the vibrational signature of the reactant or secondary photoproducts. To achieve this, probe pulses in the MIR have to be created and superposed with the afore excited sample volume. In this regard, the temporal shortness of femtosecond laser pulses is exploited to effectively execute the required frequency conversion processes. But beyond that, it features a time resolution
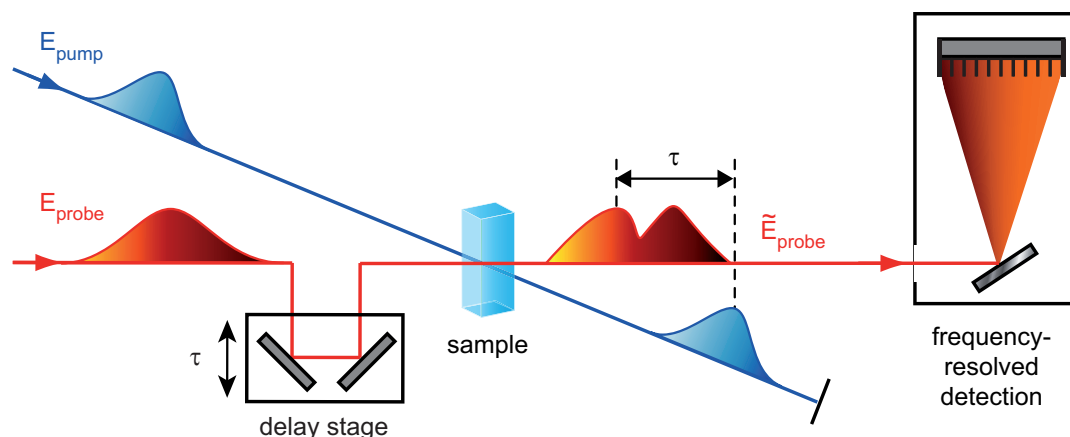
**Figure 2.10:** Schematic depiction of an UV-pump–MIR-probe experiment. Ultrashort pump pulses in the UV excite the molecular system, thus triggering a photoinduced reaction. Probe pulses in the MIR interact with the excited molecules and monitor the changes in the vibrational signature of the reactant or secondary photoproducts at continuously shifted delay times $\tau$. In combination with a spectrally-resolved detection, this results in a transient map of the photoinduced molecular reaction dynamics, as described in greater detail in Fig. 2.11.

that is indispensable to map photoinduced chemical reactions. By means of a motorized delay stage, the arrival time difference at the sample between pump and probe pulses can be scanned continuously (depicted schematically in Fig. 2.10). For each time step $\tau$, the momentary status of the photoinduced dynamics in the sample is recorded in a frequency-resolved manner. More precisely, due to the initial excitation and the subsequently proceeding photoreaction, the probe pulses are subject to absorption changes that vary with time and frequency. This leads to a series of stationary difference spectra, which, if stringed together in the correct temporal order, provide a map of the photoreaction dynamics, as shown in Figure 2.11. The limiting factors concerning the temporal resolution predominantly are the pulse durations of the pump and probe pulses. A similarly widespread experimental technique employs another interaction with UV/Vis pulses instead of MIR pulses to probe the molecular dynamics. This would trace the evolution of the electronic states [88, 89].

According to the Beer–Lambert law, the intensity of the probe beam at a certain wavelength $\lambda$ after intersecting the sample is

$$I(\lambda, \tau) = I_0(\lambda)\, e^{-\sigma(\lambda)N(\tau)d}, \tag{2.78}$$

with $I_0(\lambda)$ being the unaffected probe intensity before the sample is passed, $\sigma(\lambda)$ is the absorption cross section that is specific to the molecular system in the sample, $N(\tau)$ indicates the number of molecules that absorb photons with a wavelength $\lambda$ after the delay time $\tau$, and $d$ is the sample thickness. From this, a common measure in optical spectroscopy can be derived, the optical density

$$OD(\lambda, \tau) = -\log_{10}\left[\frac{I(\lambda, \tau)}{I_0(\lambda)}\right] = \frac{\sigma(\lambda)N(\tau)d}{\ln(10)}, \tag{2.79}$$

which is simply the Beer–Lambert law in terms of absorbance. In transient absorption spectroscopy as described above, the central quantity of interest is the change of absorbance the probe pulses experience at varying delay times due to the stimulation of the sample molecules by the pump pulses. This is the difference between the optical densities of the sample with and without a preceding excitation:

$$\Delta OD(\lambda, \tau) = -\log_{10}\left[\frac{I(\lambda, \tau)}{I_{\text{ref}}(\lambda)}\right] = \frac{1}{\ln(10)}\sigma(\lambda)\big[N(\tau) - N_0\big]d, \qquad (2.80)$$

where the reference intensity $I_{\text{ref}} = I_0(\lambda)\, e^{-\sigma(\lambda)N_0 d}$ represents the case without any excitation. Summarizing the results from Eq. (2.80) for numerous time steps and the wavelengths that are covered by the probe spectrum, yields an image of the photoinduced population dynamics (see Fig. 2.11).

There are different factors that determine the change of absorbance the probe pulses experience when passing the subensemble of excited molecules. Provided that the pump pulses spectrally overlap with an absorption band of the reactant, the inevitable depletion of the ground state population follows (ground state bleaching, GSB). As the pump pulses excite a portion of the sample molecules from the formerly populated electronic ground state $S_0$ to higher lying states $S_1,...,S_n$, the absorption of the ground state decreases. The according difference spetrum exhibits a negative $\Delta OD$ value at the spectral positions where the vibrations of the ground state PES were located prior to the excitation. With increasing time, the ground state population might partially or entirely refill since relaxation processes take place. Consequently, the ground state bleach signal recovers fully to zero $\Delta OD$ or, in case that an intermediate or stable photoproduct is irreversibly formed, remains at a constant level. From such an incomplete bleach recovery the quantum yield can be deduced, with which the photoreaction branches towards continuative reaction channels.

Emerging photoproducts on the other hand provide characteristic vibrational signatures that are nonexistent in the absence of pump pulses. Therefore, they appear as positive changes in absorbance, mostly at wavelengths different from the position of the GSB. Their persistence is temporary in case of reaction intermediates or permanent in case of stable products. Shortly after the pump event, the product molecules possess excess energy and higher lying vibrational states are occupied, as explained in Sec. 2.3. Due to the anharmonicity of PESs the distance of energy between adjacent vibrational levels decreases with increasing quantum number (see Fig. 2.7). Hence, the maxima of the product absorption bands shift from smaller to higher frequencies until the vibrational cooling to lower states is completed. However, it might occur that the functional groups of photoproducts vibrate at outlying and unknown spectral regions or provide minor oscillator strengths, so that a detection becomes hardly feasible.

### 2.5.2 Coherent effects

Beside the time-dependent formation of photoproducts on the basis of which the temporal evolution of reaction channels can be disclosed, transient data also exhibit unwanted features. Even though they partially derive from characteristics of the molecular sample
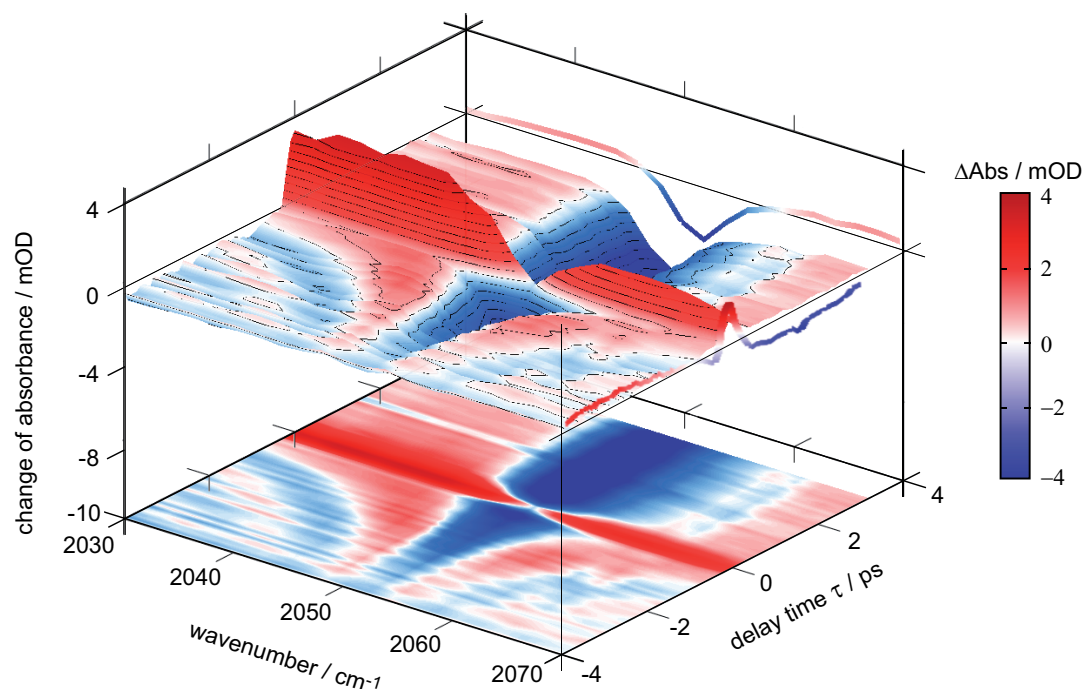
**Figure 2.11:** Representative outcome of a time-resolved UV-pump–MIR-probe measurement (recorded on a manganese-tricarbonyl complex that is further described in Chapter 5). The three-dimensional contour-map illustrates the change of absorbance, depending on the wavenumbers provided by the MIR probe spectrum and the varying delay times between the excitation and probe events. It is assembled by traces along the $\tau$-axis at fixed frequencies, which reflect the transient absorption behavior of the system under investigation. Slices along the wavenumber-axis at fixed delay times yield difference spectra. Both reduced depictions are exemplified at the according boundary surfaces. In general, transient maps are discussed in the form of projections onto the time-frequency coordinate system, as shown at the bottom. For an unambiguous identification of the changes of absorbance, the results typically are encoded with colors. At positive delay times, the ground state bleach of the reactant molecules is observable. Around zero delay time, the coherent artifact is the predominant contribution, while the oscillating signature at negative delay times is due to the perturbed free induction decay. The latter two effects are specified in Section 2.5.2.

and therefore contain information that are specific to the system under investigation, they rather hinder the interpretation and analysis of the data, especially for very short delay times. These effects include the perturbed free induction decay (PFID) [90] and the coherent artifact [91, 92].

### Perturbed free induction decay (PFID)

In the context of a coherent excitation of multiple vibrational states, coherent implies that the involved wave functions exhibit a particular phase relation, so that they can effectively add up and show interference effects that evolve in time. This is why the terms *coherent* and *phase-sensitive* are sometimes used equivalently. In addition, the
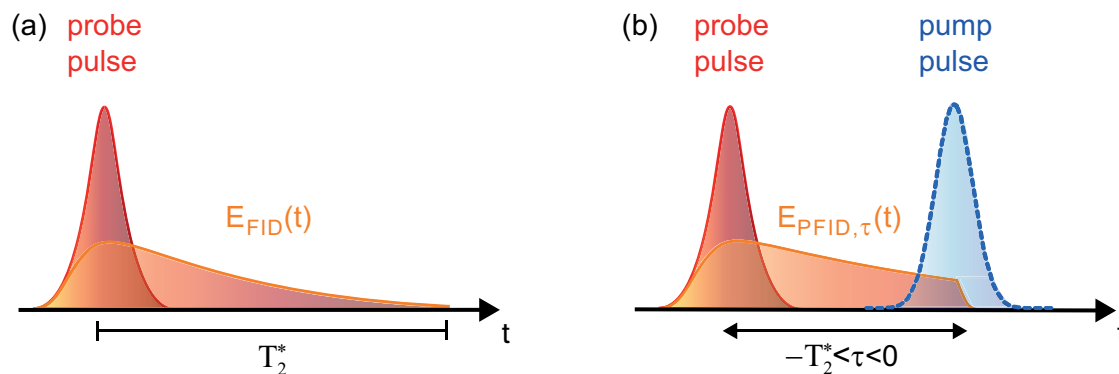
**Figure 2.12:** With the onset of a MIR probe pulse resonant to a vibrational transition, a coherent polarization is generated that decays within its dephasing time $T_2^*$, thus irradiating the light field $E_{\mathrm{FID}}(t)$. This is the free induction decay (FID), shown in (a). (b) illustrates that an electronic excitation initiated by a pump pulse perturbs the temporal and spectral properties of the FID, so that the PFID light field extinguishes, provided that the interaction takes place within the time window $-T_2^* < \tau < 0$. Correspondingly, in a pump–probe experiment the PFID signal is recorded due to the difference of absorbance that is caused by the light field $E_{\mathrm{PFID},\tau}(t) - E_{\mathrm{FID}}(t)$. At negative delay times, Figure 2.11 illustrates the shape of a PFID signal by means of measured data, whereas Figure 2.13 depicts the PFID signal simulated according to Eq. (2.82). Figure based on [93].

use of a coherent light source is presumed, so that, to express it differently, an excitation with coherent light induces molecular coherences (off-diagonal elements in terms of the density matrix formalism), which decay in the absence of an appropriate light field. More precisely, it is the phase relation between the participating wave functions that is no longer maintained but dissipated due to spontaneous emission events and the influence of the microscopic environment (with respect to the latter, in the following no distinction is made between homogeneous or inhomogeneous broadening effects that influence the relaxation (see Sec. 2.3) and dephasing process).

This leads to measurable irradiation like the photon echo [94] or the free induction decay (FID) [93]. The latter is the radiative decay within the dephasing time $T_2^*$ of a coherent polarization, which is induced by MIR probe pulses resonant to a vibrational transition. In a time-resolved experiment where the pump pulse is blocked, the detector records the probe pulses as well as the FID signal $E_{\mathrm{FID}}(t)$ (see Fig 2.12a). The onset of an excitation pulse may now disturb the spectral and temporal properties of the free induction decay, provided that it affects the coherent polarization within the time window $-T_2^* < \tau < 0$, as otherwise the coherence has already completely dephased or it is not yet established in the sample. This yields the PFID light field $E_{\mathrm{PFID},\tau}(t)$ and consequently—in a pump–probe experiment—the difference of absorbance due to the field $E_{\mathrm{PFID},\tau}(t) - E_{\mathrm{FID}}(t)$ is recorded (see Fig 2.12b).

Since the PFID induces absorbance changes at negative delay times (illustrated in Fig. 2.11), it does not contain any additional information about the photoinduced molec-

**Figure 2.13:** Simulated signal of the PFID according to Eq. (2.82) for a vibrational transition centered at $2050\,\mathrm{cm}^{-1}$ with a phase relaxation time $T_2^* = 800\,\mathrm{fs}$. It decreases exponentially towards negative delay times and its spectral extent clearly outreaches the bandwidth of the corresponding absorption line, so that the simulation resembles the experimental data, depicted in Fig. 2.11, quite well.
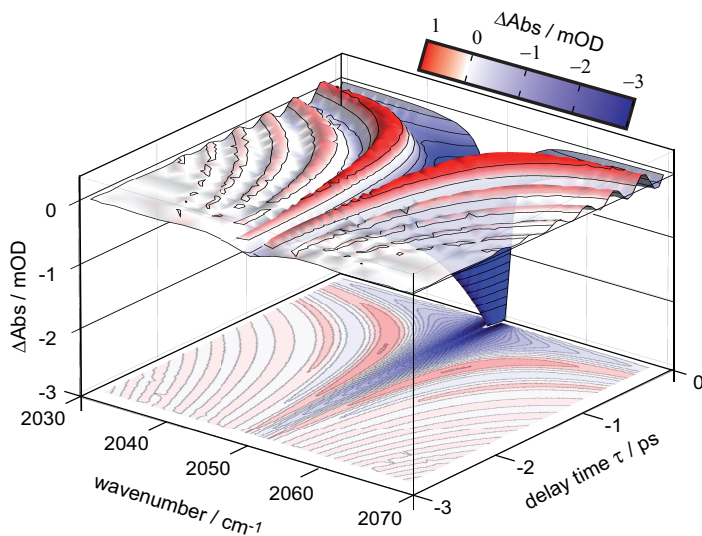


ular dynamics, although its shape arises from molecular properties, namely from the bandwidth $\Delta\tilde{\nu}$ of the involved vibrational transition. The dephasing time is not further specified in terms of homogeneous and inhomogeneous contributions, it is simply related to the bandwidth of a transition by:

$$T_2^* = \frac{1}{\pi c \Delta\tilde{\nu}}. \tag{2.81}$$

In comparison to electronic transitions, vibrational transitions may have rather small bandwidths on the order of $10\,\mathrm{cm}^{-1}$ so that the decaying PFID signal is observable up to a few picoseconds before zero delay time. However, it should be noted that a PFID signal spectrally covers more than the involved transition bandwidth. Under the assumption that the incident probe and pump pulses are sufficiently short to be approximated by Dirac delta functions [93, 95], the detected difference signal for $\tau < 0$ is

$$\Delta\mathrm{Abs}(\omega, \tau; \omega_a) \propto -e^{\tau/T_2^*} \frac{\cos[(\omega - \omega_a)\tau]/T_2^* - (\omega - \omega_a)\sin[(\omega - \omega_a)\tau]}{(\omega - \omega_a)^2 + (1/T_2^*)^2}, \tag{2.82}$$

with $\omega_a$ being the center frequency of the vibrational absorption band and $\omega$ being the detected frequency. This theoretical model is illustrated in Figure 2.13 for a vibrational transition centered at $2050\,\mathrm{cm}^{-1}$ with a phase relaxation time $T_2^* = 800\,\mathrm{fs}$. It resembles quite well the measured PFID signal depicted in Figure 2.11. Central to the absorption line (where the GSB sets in after zero delay time) and for $\tau < 0$, the change of absorbance decreases exponentially with the time constant $T_2^*$. Alongside the resonance, the signal oscillates with a frequency that is the detuning $(\omega - \omega_a)$ between the absorption center and the detected frequency. So it is apparent why the PFID's spectral extent clearly outreaches the bandwidth of the GSB. The derivation to Eq. (2.82) together with more realistic model calculations, including Gaussian shaped probe pulses, are presented in [93].

**Coherent artifact**

In general, pump–probe spectroscopy is described in a sequential manner, meaning that two interactions with the pump field are followed by one interaction with the probe field [96]. If pump and probe pulse overlap temporally and spatially, coherent terms arise since the order of impact is mixed and becomes non-sequential [97]. This motivates the designation of the second effect that can impede the analysis of transient data, the coherent artifact. It is also called coherent spike due to its appearance in pump–probe spectroscopy, where it forms a dominant, short-living signal around zero delay time that extends across a wide spectral range, as can be seen in Fig. 2.11. Besides other contributions like stimulated Raman scattering, its cause is mainly discussed in terms of the cross-phase modulation (XPM) [98, 99]. Whereas self-phase modulation (see Sec. 2.2.2) is the effect, where the intensity of a laser pulse has an impact on its own phase due to the Kerr effect in nonlinear media, cross-phase modulation (XPM) occurs when the intensity of one pulse affects the phase of another one. According to Eqs. (2.33) and (2.35), the intense pump pulse modulates in a time-dependent manner the refractive index of a medium that provides higher order nonlinear susceptibility. This applies to transient spectroscopy in the liquid phase, since the pump pulse passes the dissolved sample surrounded by two windows of a flow-through cuvette. Thereby, XPM is both related to $\chi^{(3)}$ and to $\chi^{(5)}$ contributions [100]. Assumed that both pump and probe pulses overlap spatially in the cuvette, the modulated refractive index alters the spectral composition of the probe pulses for the period of temporal overlap, i.e., around zero time delay, thus generating absorption changes during this short interaction. Those can substantially conceal weak transient features arising from the photoinduced molecular dynamics. The lifetime of the coherent artifact is mainly determined by the pump pulse duration.

There are possibilities to circumvent or at least reduce the disturbing implications caused by the coherent artifact or the PFID. As regards to the first, it is beneficial to use solvents with low nonlinear susceptibility and thin cuvette windows of low dispersion (e.g. $CaF_2$). If this is not possible owing to particular experimental demands, accompanying measurements in pure solvent and a subsequently performed correction procedure can render the data analysis unambiguously [101]. As regards to the second, Fourier filtering schemes can suppress the PFID and facilitate the analysis of molecular dynamics recorded via UV-pump–MIR-probe measurements [102].

With this, the basic theoretical principles are set to understand the processes involved in the experiments carried out within this thesis. The following chapter deals with the concrete experimental configuration, its components and functionality, whose interplay gains insight into chemical reactions on a microscopic scale.

# 3 Experimental configurations

The previous chapter introduced the theoretical framework around femtosecond laser pulses, which is in outline their mathematical representation and their characteristics in the course of nonlinear interactions with matter. In this sense, matter could be a nonlinear crystal to induce frequency conversion processes as well as a quantum-mechanical system that shall be examined. Especially the latter motivated further considerations on the applicability of ultrashort laser pulses to investigate light-induced chemical reactions in a time-resolved fashion, particularly in the context of pump–probe spectroscopy.

The present chapter treats the physical implementation of those theoretical concepts. Accordingly, in the following sections the applied experimental devices will be introduced and their functionality will be explained. To provide a first overview, it is convenient to adopt the order of appearance from the preceding chapter. Hence, as illustrated in Figure 3.1, a schematic experimental configuration begins with an apparatus that allows for the generation of femtosecond laser pulses, which is the key building block for most experiments presented in this work. These fundamental femtosecond pulses subsequently are split into two fractions and transferred to frequency conversion devices to generate MIR probe and UV/VIS pump pulses. As described above, with respect to the upcoming pump–probe experiment where both types of laser pulses are superposed in the sample, it is furthermore required to insert a tunable delay stage with a retroreflector into one of the beam paths. In a final step, an appropriate signal detection sensitive to the probe pulses is needed. These are the basic components in order to perform pump–probe spectroscopy. Supplementary devices aim amongst others for the shaping and characterization of the pump and probe pulses to make this basic spectroscopic scheme more versatile.

However, as the experimental settings have evolved several times throughout this thesis, the measurements presented below have been realized under different experimental circumstances with diverse implements. This is taken into account by the structure of this chapter. Each of the following sections describes the respective equipment that has been in use to perform the measurements discussed in one of the Chapters 4–6. This aspect is also illustrated in Figure 3.1 that gives an overview which experimental techniques have been applied (OPA, SHG, THG, etc.), and additionally, which layout has been used within the following chapters. The latter is illustrated in terms of colors. The yellow highlighted instruments are parts of the measurements described in Chapter 4; a precise explanation of their functionality is given in Section 3.1. The green highlighted devices constitute the instrumentation for Chapter 5, the corresponding specifications are presented in Section 3.2. The blue highlighted devices mainly are part of the experiments in Chapter 6, accordingly this chapter ends with their introduction in Section 3.3.
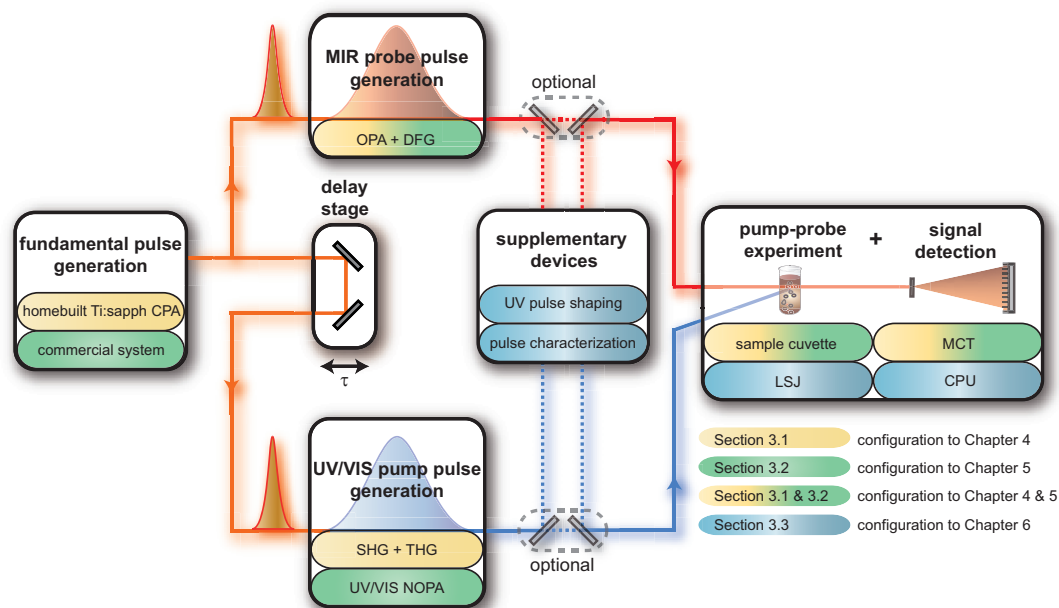
**Figure 3.1:** Schematic depiction of the experimental implementation. Primarily, the basic components to perform pump–probe spectroscopy are introduced: After the generation of the fundamental femtosecond pulses, the beam is split into two fractions to generate the MIR probe and the UV pump pulses. One optical path is directed over a motorized stage in order to introduce the temporal delay $\tau$, which is necessary for the subsequent pump–probe experiment that ends in the probe signal's detection. Optionally, to make this basic spectroscopic scheme more versatile, supplementary devices can be included. This elementary configuration describes the instrumentation related to the measurements presented in the Chapters 4–6. Which device in detail has been used in the corresponding chapter is illustrated in terms of colors. The yellow highlighted instruments are parts of the measurements described in Chapter 4; a precise explanation of their functionality is given in Section 3.1. The green highlighted devices constitute the instrumentation for Chapter 5, the corresponding specifications are presented in Section 3.2. The blue highlighted devices mainly are part of the experiments in Chapter 6, so that this chapter ends with the belonging introduction in Section 3.3.

## 3.1 Setup to investigate the photochemistry of DMA

In the following, the major implements will be presented that have been used to study the multisequential photochemistry of 5-diazo Meldrum's acid (DMA), as described in Chapter 4. These include the corresponding chirped pulse amplification (CPA) laser system delivering the fundamental femtosecond laser pulses (Sec. 3.1.1). Its output is split into two energetically equal fractions that supply the subsequent devices to generate the UV pump pulses via SHG and THG arranged in series on the one hand. On the other hand, the MIR probe pulses are generated in a tunable two-stage OPA followed by a DFG unit (Sec. 3.1.2). Afterwards, both partial beams are overlapped inside the sample which is positioned in the pump–probe setup to perform transient absorption measurements in the liquid phase (Sec. 3.1.3).
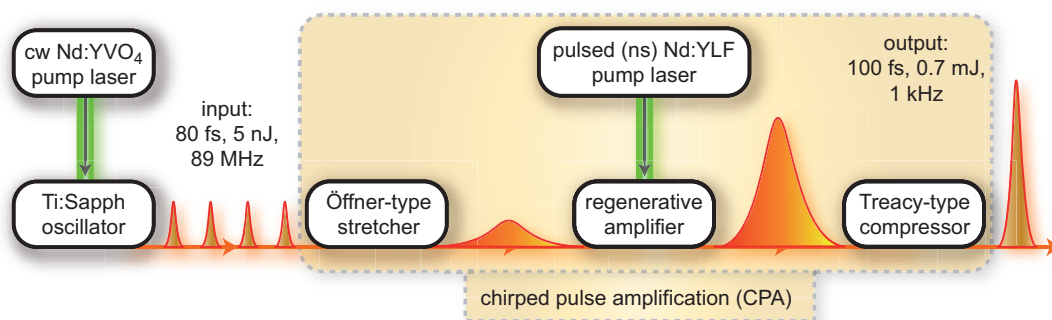
**Figure 3.2:** Working principle of a chirped pulse amplification (CPA) femtosecond laser system. A Ti:sapphire oscillator, pumped by a continuous-wave Nd:YVO$_4$ laser, produces pulses with a duration around 70 fs and a pulse energy of 5 nJ at a high repetition rate of 89 MHz. Serving as the input to the CPA system, they are therein temporally stretched in order to prevent damage to the subsequent amplification in a regenerative amplifier, which is pumped by a pulsed Nd:YLF laser, and finally recompressed. This yields pulses at 1 kHz repetition rate with an energy increased by five orders of magnitude and a comparable pulse duration.

### 3.1.1 Homebuilt femtosecond laser system

Throughout this work, ultrashort laser pulses have been generated by means of the chirped pulse amplification [103], whose working principle is illustrated in Fig. 3.2. Basically, it consists of four components, which are—with regard to this section—partially homebuilt. The first component is the Kerr-lens mode-locked Titanium:Sapphire oscillator, whose active medium is pumped by a commercial continuous-wave Nd:YVO$_4$ laser (Coherent Verdi V6) with an output power of 6 W at 532 nm. It contains an intracavity prism compressor to compensate for the GVD, mainly introduced by the active medium. Its design is extensively presented in [104] and holds for the homebuilt version as well as for the commercial version (Coherent Mira 900) that both have been employed to deliver laser pulses at a repetition rate of 89 MHz, centered around 800 nm, with an energy of 5 nJ, and a pulse duration of 80 fs. These pulses subsequently enter the CPA system in order to increase their energy drastically, so that the required nonlinear processes can be exploited afterwards. The CPA begins with an Öffner-type stretcher [105, 106] that temporally elongates the pulses by three orders of magnitude. This prevents damage or unwanted nonlinear effects in the active medium (Ti:sapphire) of the regenerative amplifier, which is pumped by a commercial Nd:YLF laser (Coherent Evolution 15), delivering nanosecond pulses with 9 W at 527 nm and a repetition rate of 1 kHz. The oscillator pulses seed the amplifier's active medium, whereat the pulse train enters the regenerative amplifier cavity through an intracavity Pockels cell combined with a dielectric thin film polarizer. After approximately ten round trips in the cavity—each one increasing the degree of amplification—the Pockels cell switches polarization and releases the amplified pulse. Thereby, the repetition rate of the Nd:YLF pump laser is adopted, i.e., the pulse energy is increased by five orders of magnitude at the expense of the repetition rate. After that, the pulses are recompressed in a Treacy-type compressor [107]. This is accompanied by a loss of circa 30% of pulse power, so that the

CPA yields output pulses with 0.7 mJ pulse energy. Since the amplifier medium has a limited gain bandwidth, i.e., not every spectral part of the input pulses is amplified equally (the spectral wings experience a lower gain than the central spectral region), the output pulses provide a slightly higher pulse duration of 100 fs in comparison to the input pulses from the oscillator. This phenomenon is known as spectral gain narrowing.

Pulse monitoring devices such as a spectrometer and an autocorrelator complete the setup for the fundamental laser pulse generation. As they provide continuous information about the spectrum and the pulse duration of both the oscillator pulses and the amplified pulses, it is possible to constantly optimize the operating mode of the system in terms of stability for the upcoming frequency conversion processes.

### 3.1.2 UV and MIR pulse generation

The fundamental light from the CPA system is subsequently used to create the pump and probe pulses in the UV and MIR spectral region, respectively. In the following, the according devices are explained in detail.

#### SHG + THG: UV pump pulse generation

Two frequency conversion units arranged in series transfer the p-polarized fundamental 800 nm laser pulses to the UV spectral region. More specifically, SHG followed by THG create pulses at 266 nm; the corresponding setup is highlighted in Figure 3.6, Section 3.1.3. Initially, the s-polarized second harmonic at 400 nm is generated in a BBO crystal (300 $\mu$m thickness, type I phase matching, $\Theta = 29°$ cutting angle). Since the conversion efficiency is as usual far below 100 %, there is residual fundamental light that can be recycled in the subsequent THG process, carried out in a second BBO crystal (200 $\mu$m, type I, $\Theta = 44°$). Therein, the sum frequency of 400 nm and 800 nm is generated, yielding pulses around 266 nm with an energy of 10 $\mu$J. For optimal adjustment conditions, in front of the SFG both incident beams are spatially separated by a beamsplitter, the 400 nm pulses are rotated with a half-wave plate to be p-polarized to fulfill the phase matching condition, and the 800 nm pulses are guided over a delay line. The latter in combination with the mirror M1 allows for fine-tuning of the spatial and temporal overlap of both incident beams in the crystal. Additionally, the noncollinear setup facilitates the separation of the 266 nm pulses from the remaining light fields that are no longer needed after the THG. Before intersecting the sample, the pump pulses are focused by the lens F1 ($f = 50$ cm), whose position is adjustable to optimize the diameter of the pump beam relating to the probe beam in the sample. With a half-wave plate the polarization of the pump pulses can be rotated to fit the magic angle of 54.7° with respect to the p-polarized probe pulses.

#### OPA + DFG: MIR probe pulse generation

The setup for the generation of stable ultrashort MIR probe pulses is based on a white light continuum combined with two optical parametric amplification processes. Its particular design, as depicted in Fig. 3.3, is derived from Hamm *et al.* [108, 109], however,
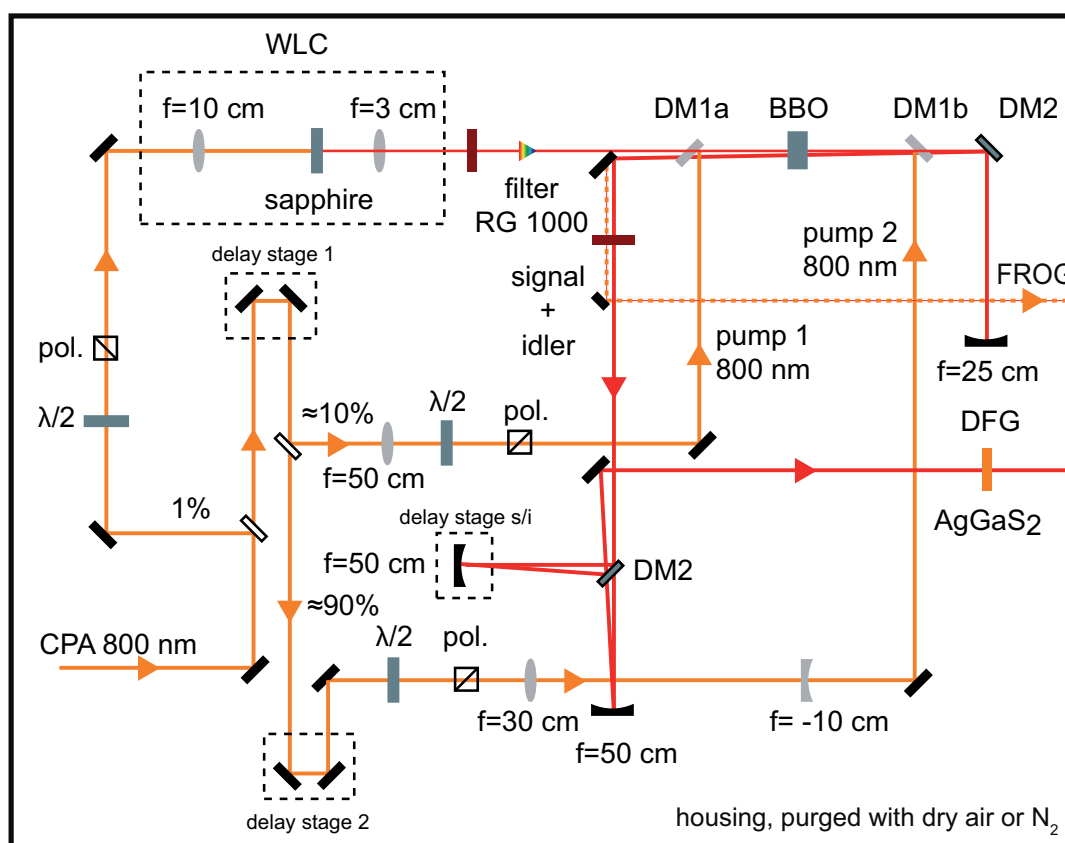
**Figure 3.3:** Setup for the generation of ultrashort MIR probe pulses. The infrared part of a white light continuum seeds two OPA processes in a BBO crystal. The resulting signal and idler pulses are mixed in a $AgGaS_2$ crystal for DFG to produce MIR pulses tunable between $(4 - 10)\,\mu m$. The residual light from the second pump stage is guided to the FROG setup where it serves as the reference pulse (see Sec. 3.3.1). Figure reprinted from [112].

the general idea of intensifying a certain bandwidth out of a weak supercontinuum, which acts as the seed pulse, by means of two successive amplification or pump stages, has prevailed in many applications [110, 111] (see also Sec. 3.2.2). The setup described in this section is comprehensively outlined in [112, 113], therefore, in the following only a short description of the working principle shall be given.

At the outset, the fundamental laser pulses are split into three fractions. The first fraction with $1\,\%$ of the whole power creates a WLC in a sapphire disk. Its intensity is adjustable via a combination of a half-wave plate and a polarizer that also regulates the correct polarization for the following first OPA process. Thereby, the second fraction with approximately $10\,\%$ of the incident power is collinearly superposed with the near-infrared part of the supercontinuum in a BBO crystal ($4\,mm$, type II, $\Theta = 27°$, $\Phi = 30°$). Again, a combination of half-wave plate and polarizer provides the required polarization and prevents the pump pulses to generate white light themselves in the BBO. Temporal and spatial overlap between the WLC and the first pump beam are adjusted by the delay stage 1 and the dichroic mirror DM1a (confer Fig. 3.3). This first OPA stage yields a signal and idler pair, whereby only the signal is used as the seed in the subsequent second
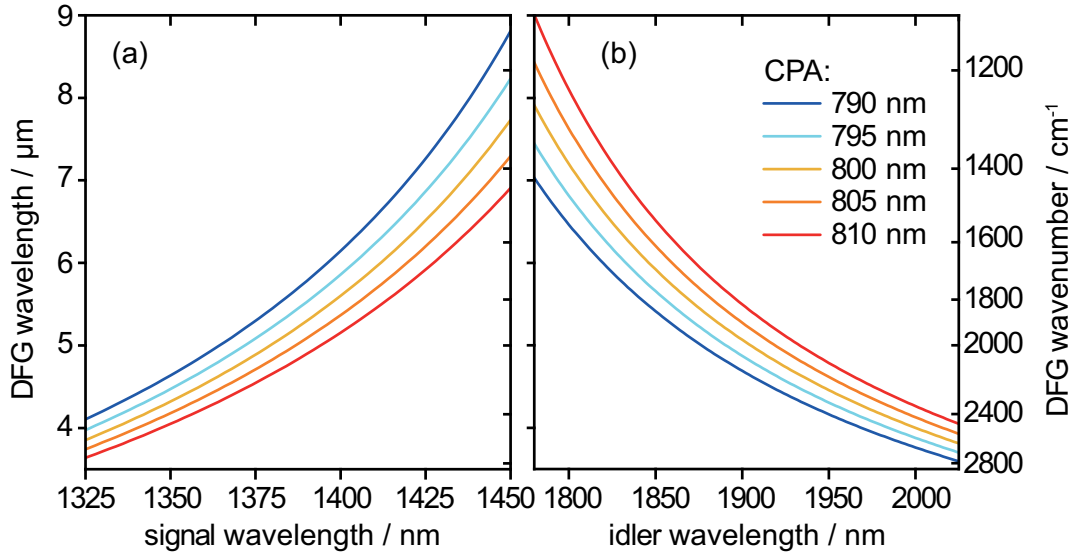
**Figure 3.4:** Spectral adjustability of the DFG probe pulses in wavelengths (left scale) and wavenumbers (right scale) as a function of the signal wavelengths (a) and the idler wavelengths (b) for given central wavelengths of the CPA that powers the OPA processes. Plots calculated according to Eqs. (3.3) and (3.4).

OPA process; the idler is filtered out by the dichroic mirror DM2. Within the same BBO crystal, but vertically shifted, the second pump beam with the remaining incoming pump power is collinearly overlapped with the signal pulses to generate a more intensive signal and idler pulse pair. Just as in the first pump stage, this process is likewise controlled with a combination of half-wave plate and polarizer and optimized with the delay stage 2 for temporal overlap and with the mirror DM1b for spatial match. Signal and idler are polarized perpendicular to each other (signal s-polarized, idler p-polarized) which fits the type II phase matching condition of the subsequent silverthiogalate ($AgGaS_2$) crystal (1mm, $\Theta = 39°$, $\Phi = 45°$). For an efficient difference frequency mixing, signal and idler are separated by the splitter DM2 and independently focused into the crystal, so that via the delay stage s/i the temporal overlap can be fine-tuned while one of the focusing gold mirrors optimizes the spatial overlap.

This procedure results in mid-infrared laser pulses with an energy of up to $600\,\mathrm{nJ}$, tunable in a spectral range of $(4-10)\,\mu\mathrm{m}$. The spectral adjustability is given by rotating the BBO crystal, thus changing the angle $\Theta$ which in turn defines the part of the WLC spectrum that serves as the seed and is effectively phase matched to become the signal pulse. The spectral position of the signal directly affects the idler wavelengths and consequently the MIR probe pulses are also spectrally fixed. Both in terms of the OPA processes and the DFG process, this can be expressed via the conservation of energy that determines the wavenumbers $\tilde{\nu}$ of signal, idler, and DFG output for a given central wavenumber of the CPA $\tilde{\nu}_{\mathrm{CPA}}$ that powers the whole device:

$$\tilde{\nu}_{\mathrm{CPA}} = \tilde{\nu}_{\mathrm{signal}} + \tilde{\nu}_{\mathrm{idler}}, \tag{3.1}$$

$$\tilde{\nu}_{\mathrm{DFG}} = \tilde{\nu}_{\mathrm{signal}} - \tilde{\nu}_{\mathrm{idler}}. \tag{3.2}$$

From the Eqs. (3.1) and (3.2), two useful relations can be derived that explain, which signal wavelength has to be adjusted, in order to achieve the desired MIR probe pulse wavelength or wavenumber, respectively:

$$\tilde{\nu}_{\mathrm{DFG}} = 2\tilde{\nu}_{\mathrm{signal}} - \tilde{\nu}_{\mathrm{CPA}}, \tag{3.3}$$

$$\tilde{\nu}_{\mathrm{DFG}} = \tilde{\nu}_{\mathrm{CPA}} - 2\tilde{\nu}_{\mathrm{idler}}. \tag{3.4}$$

Calculations following the relations (3.3) and (3.4) for varying CPA central wavelengths are illustrated in Fig. 3.4. Corresponding signal, idler, and DFG output spectra reflecting the adjustability of this device, henceforth briefly denoted as MIR-OPA, are shown in [112].

Aside from the pump–probe setup and the signal detection, what has been introduced up to now constitutes the preconditions to excite and probe a molecular system in a transient measurement. However, success or failure of such an experiment does not only depend on whether the appropriate instrumentation is available and operable. In fact it could even be argued that the essence of an efficient experiment is not to arrange every optical component in the right manner to build up the required devices. What is truly needed is to operate each configuration involved in the most optimal way at the same time and thus achieve the best possible data quality. This is also discussed in terms of improving the signal-to-noise ratio, which can be attained by a proper alignment and adjustments that provide stable signals with fluctuations as low as possible. Especially the latter is mainly governed by a robust, low fluctuating WLC. For these reasons, in the following the essential alignment steps for a steadily working MIR-OPA shall be given. Figure 3.5 is meant to support the comprehensibility by highlighting the significant parts:

1. As is customary in optical setups, also the components of the MIR-OPA are positioned within a plane parallel to the optical table, since every tipping of the beam paths with reference to the table plane complicates the alignment procedure. The 800 nm fundamental light's coupling into the MIR-OPA is managed with two mirrors in front of the device. They ensure that the incident beam lies within this particular plane, which—in case of the MIR-OPA—is conveniently defined by an iris aperture placed ahead of the sapphire disk in conjunction with the three combinations of a half-wave plate and a polarizer. In this regard, the three partial beams for the WLC generation and the two pump stages should not be drastically clipped by these components and the iris aperture should be encountered in the center, respectively. Especially if the diameter of the incoming beam is rather large, one has to take care of this aspect. Once this is done, two iris apertures in front of the implement can help to guide the fundamental beam into the MIR-OPA correctly and reproducible.

2. Next, the supercontinuum should be surveyed. Under proper conditions, the white light has a circular appearance without multiple filaments. Sapphire has a high
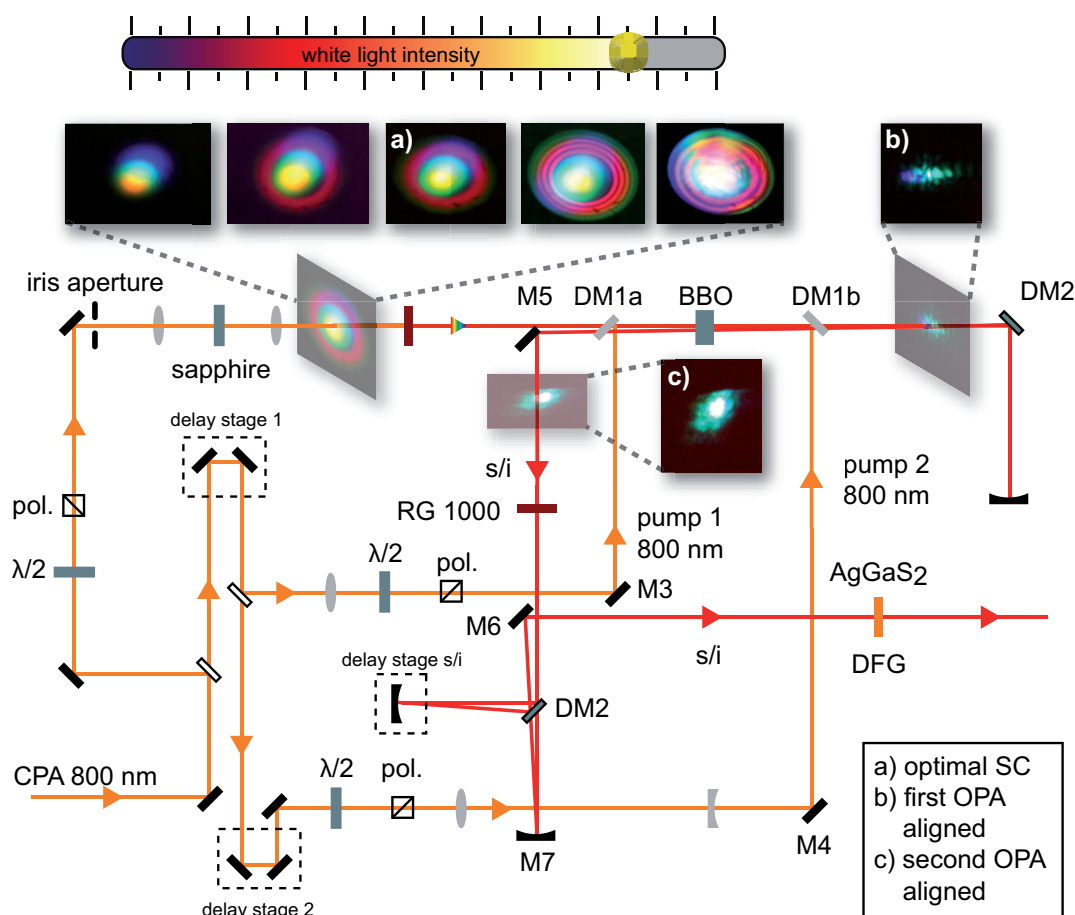
**Figure 3.5:** Depiction of the essential components that are involved in the alignment procedure of the MIR-OPA. The first five pictures in the upper row illustrate supercontinua for an increasing pump intensity that is adjusted by an iris aperture or the half-wave plate in front of the sapphire disk. The third picture—indicated with (a)—reflects the optimal SC to achieve stable MIR pulses. If the WLC and the first pump beam overlap temporally and spatially within the first OPA stage, the sum frequency can be observed behind DM1b, as illustrated in the picture indicated with (b). Similarly one can verify the spatial and temporal overlap in the second OPA stage behind the mirror M5 if a constructive signal arises like the one illustrated in the picture indicated with (c). The detailed alignment procedure is given in the text.

thermal conductivity. Given that the intensity of the white light pump beam is adjusted correctly with either the iris aperture or the half-wave plate, almost no long-term degradation effects are observed and a high pulse-to-pulse stability with a persistent spatial quality can be achieved. The optimal SC is the middle one in Fig. 3.5. The second and the fourth white light constitute the very limits inside of which the device can be operated, however, when multiple filaments become evident (confer fourth SC) or rather weak pump intensities are applied, the onset of fluctuations in the output signal will be entailed. The first and the fifth SC derive from significantly too weak or too high pump intensities, respectively. The latter certainly is above the long-term damage threshold of the sapphire disk, and

both are inapplicable for a stable MIR-OPA output.

3. With an appropriate supercontinuum, one removes the RG 1000 glass filter behind the SC generation stage and establishes the temporal and spatial overlap with the first pump beam in the BBO crystal. But before, it should strictly be checked that the first pump stage itself does not generate a WLC in the crystal. This is done by adjustments on the according half-wave plate and easily tested behind the mirror DM1b, where no colorful sparkle but only a blue light due to the SHG in the crystal should be visible. The SC passes the BBO crystal central in the upper region. By adjusting the mirrors DM1a and M3 iteratively, the pump beam has to be collinearly combined with the white light at a position in front of the crystal (shortly after DM1a) and behind the crystal (between DM1b and DM2). This also ensures the spatial overlap inside the crystal. The temporal overlap is achieved via the delay stage 1. With the RG 1000 glas filter inserted, one can observe a turquoise light beside the blue second harmonic behind DM1b, resulting from the SFG if the temporal overlap is met (see Fig. 3.5b). It is much more convenient if the overlap can be ascertained directly by eye, instead of using a powermeter, e.g., since both methods cannot reveal any information on the stability of the generated signal.

4. The amplified signal is redirected to the crystal in the same vertical plane but about 4 mm below in comparison to the first OPA stage. The overlap with the second pump beam is arranged similarly to the steps described before; but now, the first pump stage is blocked. Again, the intensity of the pump pulses should be adjusted to be well below the white light generation threshold in the BBO crystal. By iteratively tuning the mirrors M4 and DM1b one assures collinearity and spatial overlap between the signal and the pump beam. Adequate positions for reviewing are to the left of the crystal between DM1a and M5 and to the right of the crystal close to DM1b. With the delay stage 2, the temporal overlap is regulated. If the RG 1000 filter is inserted and the first stage unblocked, the delay stage 2 is slowly varied till a constructive signal is visible after M5 (see Fig. 3.5). This sum frequency signal derives from a correct spatial and temporal overlap in the second OPA stage. It is subsequently blocked by the second RG 1000 filter.

5. Now that the signal and idler pair is created, one should cross-check whether they propagate collinearly and overlapping. With an IR viewer, their projection onto a piece of paper can be observed ahead of DM2 and exactly in front of the $AgGaS_2$ crystal. There should be no spatial separation noticeable. In front of DM2 a certain separation is not unusual though, since the spatial overlap has been adjusted by looking at the visible part of the WLC together with the pump beams. However, with the IR viewer the crucial infrared beams are observed and those are spatially shifted with regard to the visible portion. A readjustment can mainly be carried out with M4 and DM1b. In case of the second position, the overlap can further be verified by blocking the signal or the idler alternately in the separated beam paths after DM2. In doing so, the spatial overlap of both beams in the crystal for difference frequency mixing is ensured as well.

6. When this is done successfully, a movable BBO crystal can be positioned behind

the second RG 1000 filter to generate the second harmonic of the signal pulses. This yields a bright red light that allows for a convenient coupling into the pump–probe setup. Thereby, the gold mirror M6 can be utilized so that this auxiliary light passes the pump–probe setup till it reaches the spectrometer without getting clipped at some point. It is also helpful for a first coupling into the spectrometer. Virtually independent of the central wavelength to which the spectrometer is set, a signal can be detected provided that the incident light passes the entrance slit. However, in order to detect the MIR probe pulses after the signal and the idler are successfully mixed in the $AgGaS_2$ crystal, the spectrometer has to be set to the correct central wavelength.

7. At this point, the decisive conditions are fulfilled to accomplish the adjustment procedure: signal and idler propagate collinearly, they overlap in the $AgGaS_2$ crystal, and afterwards enter the IR spectrometer that is set to the correct central wavelength. Consequently, only the s/i delay has to be tuned to achieve the temporal overlap and generate MIR pulses at the difference frequency, which becomes apparent by means of the IR spectrometer signal. Thereby, it is beneficial to monitor a series of about 100 pulses to see on the one hand the overall pulse intensity and on the other hand the pulse-to-pulse stability.

8. The final step is to find the configuration that generates highly intense pulses that provide the highest degree of stability that can be reached. For this purpose, the coupling into the spectrometer, every temporal and spatial overlap, and the half-wave plates regulating the pump intensities should be slightly readjusted. But in doing so, one should incessantly regard the spectrometer signal.

9. If the angle of the BBO crystal has been changed in order to tune the wavelengths of the MIR-OPA output, this alignment procedure has to be executed in particular. In this case, the inclination angle of the $AgGaS_2$ crystal has to be adjusted additionally. This angle can also be varied to slightly shift the central spectral position of the MIR pulses without rotating the BBO crystal. Fortunately, this does not measurably displace the optical path through the crystal or misalign the overlap between pump and probe pulses in the sample, respectively.

### 3.1.3 Pump–probe setup

Once the UV pump and MIR probe pulses are generated, they are guided into the pump–probe setup to perform transient absorption spectroscopy. What is basically needed for that is a sample, appropriate focusing mirrors or lenses to adjust the beam diameters in the sample, a delay stage, an optical chopper, and finally the detection device. Figure 3.6 summarizes the corresponding components in conjunction with the elements to generate the UV pulses, as described in Section 3.1.2.

The guidance of the MIR beam is carried out with gold mirrors. Spherical concave mirrors are used to recollimate the beam and for the focusing both into the sample and into the spectrometer. A germanium longpass filter (LPF, $2\,mm$ thickness, $\approx 100\,\%$ transmission for $2.4\,\mu m < \lambda < 5.5\,\mu m$) removes the residual signal and idler pulses. The pump beam is focused into the sample via a suprasil lens.
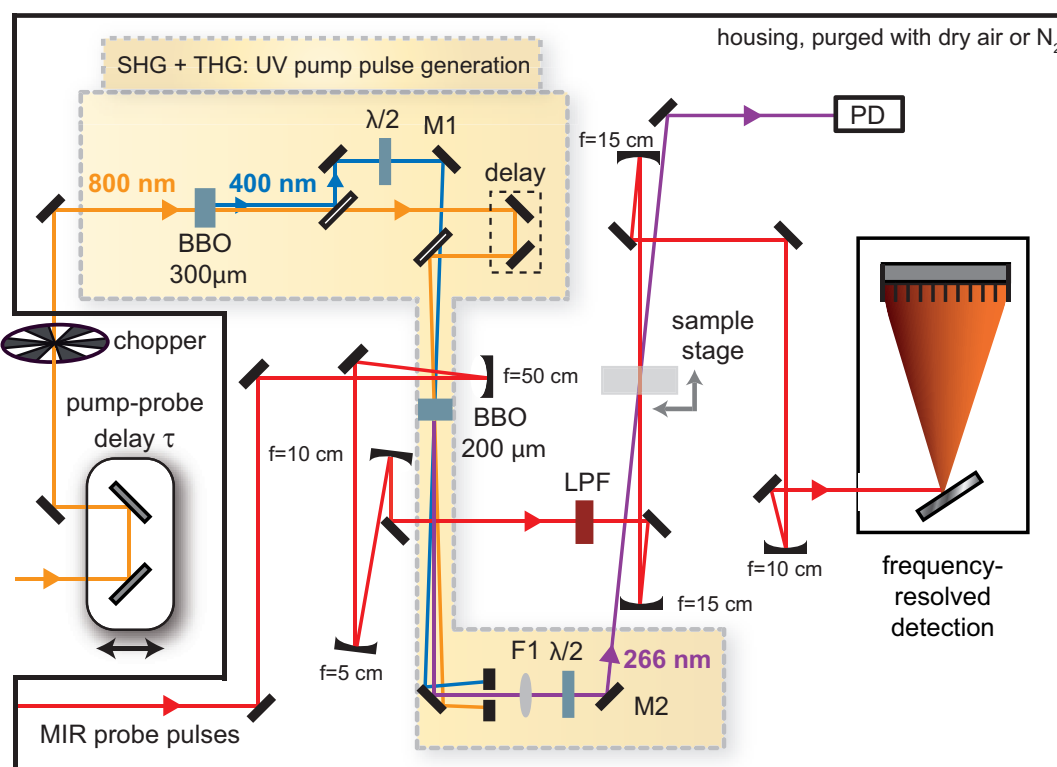
**Figure 3.6:** Experimental setup for transient UV-pump–MIR-probe spectroscopy in conjunction with the optical components to generate the UV laser pulses. The fundamental light is mixed with its second harmonic to initiate the THG that yields the pump pulses around 266 nm (see Sec. 3.1.2), which are superposed with the MIR probe pulses in the sample. A motorized stage varies the pump–probe delay $\tau$. Focusing elements determine the beam diameters at the sample position. After intersecting the sample, the probe pulses carry the information about the pump-induced changes of absorbance into the spectrometer.

At the sample position, a multifunctional table is installed that is based on a motorized linear actuator (Zaber technologies Inc.) combined with a stage that is driven by a micrometer screw along the beam propagation direction. On this sample stage different mounts can be placed; all of them exactly at the same position, namely the one where the molecular sample will be during a measurement. These include a knife edge, a pinhole, a germanium wafer and the sample cuvette. The knife edge is utilized to measure both the pump and probe beam diameters along the horizontal axis (by means of the linear actuator) as well as along the vertical axis (manually with a micrometer screw). During such a knife-edge scan, the beams are stepwise clipped while the remaining signal is recorded with the spectrometer in case of the probe beam and with a photodiode (PD) in case of the pump beam. In this setup, the beam diameters have been set to approximately $350\,\mu$m for the pump beam and $260\,\mu$m for the probe beam, respectively. That way it is guaranteed that only sample volumes are probed that have been excited prior to this, which improves the data quality considerably, but obviously only if both beams fully overlap at the sample position. This is assured via a pinhole.
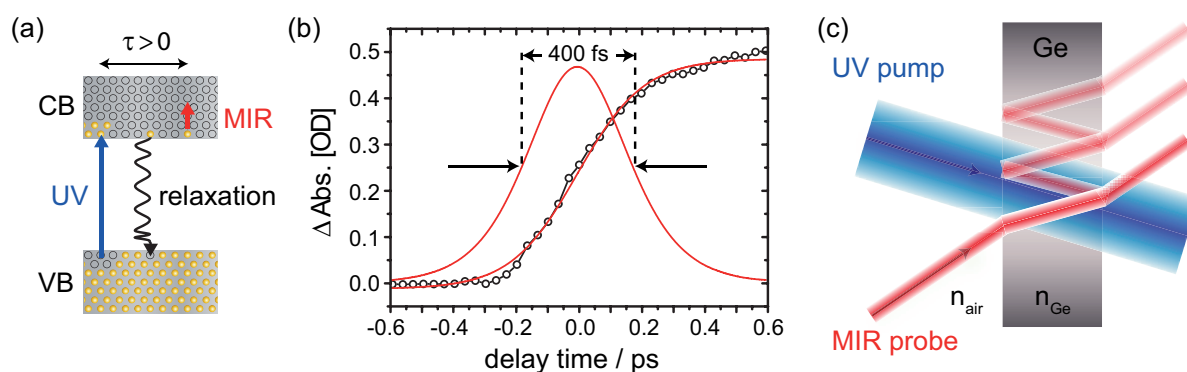
**Figure 3.7:** Cross-correlation measurement in a germanium wafer. (a) A UV pump photon has sufficient energy to exceed the bandgap and transfer electrons from the valence band (VB) to the conduction band (CB). These free charge carriers can absorb photons from the probe pulse at delay times $\tau > 0$, provided that prior to this relaxation processes have not transferred all particles back to the VB. (b) Pump–probe measurements in germanium offer information about the position of zero delay time. Additionally the shape of the absorbance change signal reflects the time resolution of the transient spectrometer. (c) Germanium can also be exploited to optimize the spatial overlap of the pump and probe beams, provided that the ratio of the involved refractive indices ($n_{Ge} \approx 4 \cdot n_{air}$ at $\lambda = 5.0 \, \mu m$) is taken into account (for further explanations, see text).

Beside the spatial overlap, one also has to be aware of the temporal offset between the pump and probe pulses. Both beams are delayed with respect to each other by a motorized stage (M-IMS600, Newport) with a length of 600 mm, which is equivalent to a maximum delay time $\tau$ of around 3.5 ns. To find out at which position on the stage the temporal delay is zero, i.e., at which position pump and probe beam enter the sample cell simultaneously, a cross-correlation measurement in a germanium wafer is carried out [114, 115]. Due to the energetic distance between the valence band (VB) and the conduction band (CB) in semiconductors, germanium is highly transmissive in the infrared spectral region. However, ultraviolet photons can overcome the bandgap and instantaneously excite electrons to the CB where they populate free states. From those, MIR photons can be absorbed as long as the free charge carriers have not completely relaxed back to the VB (see Fig. 3.7a). This change of absorbance is measured as a function of the delay time $\tau$, an according result is depicted in Fig. 3.7b. Since the employed laser pulses are not infinitely short, the transient is rather of sigmoidal shape than perfectly steplike. Nevertheless, the position on the delay stage for which $\tau$ equals zero can be identified. Additionally, the time-resolution of the transient spectrometer can be derived by fitting the measured transient with a step function. The derivative is a Gaussian of which the FWHM reflects the temporal resolution of the experiment that is around 400 fs. Figure 3.7b also illustrates that a pump–probe measurement on germanium offers huge signal strength on the order of several hundreds of mOD. Therefore, it is expedient to optimize the spatial overlap with it instead of using a pinhole. Provided that one aspect is taken into account: the refractive index of germanium in the infrared is

much greater than the one of air ($n_{Ge} \approx 4.0$ for $\lambda = 5.0\,\mu\text{m}$) so that, according to Snell's law, the probe beam is strongly refracted to the vertical of the plane of incidence. As a consequence, multiple reflections of the probe pulses inside the germanium wafer remain within the excited cross-section and cause further pump–probe signals (see Fig. 3.7c; for clarity, the beam diameters are not illustrated in the correct proportion). If one of these signals is confused with the main pump–probe overlap, the position of zero delay time would be set at a wrong negative value. However, due to their comparatively low signal intensity, they are easily distinguishable from the major signal that arises at $\tau = 0$.

When those preparatory steps are completed, the flow-through cuvette (Omni-cell, LOT Oriel) is mounted on the sample stage. The cuvette consists of two $BaF_2$ or $CaF_2$ windows ($2\,\text{mm}$ thickness each). Both materials are highly transmissive within a wide spectral range $200\,\text{nm} < \lambda < 9\,\mu\text{m}$ covering the pump as well as the probe wavelengths. A teflon spacer, usually of $100\,\mu\text{m}$ thickness, defines the distance of the cuvette windows and accordingly the optical path length of the flow cell. A peristaltic pump (Cole Parmer, Masterflex L/S) constantly pushes the dissolved sample fluid through the cuvette to ensure that two successive excitations do not interact with the same molecules.

The transient absorption signal detection completes the pump–probe setup. The IR spectrometer (Chromex 250 is/sm spectrograph/monochromator) comprises three different blazed gratings (grating 1: $300\,\text{groves/mm}$, blaze wavelength $2\,\mu\text{m}$, upper limit of reflectance $5.625\,\mu\text{m}$; grating 2: $150\,\text{groves/mm}$, blaze wavelength $4\,\mu\text{m}$, upper limit of reflectance $11.251\,\mu\text{m}$; grating 3: $75\,\text{groves/mm}$, blaze wavelength $8\,\mu\text{m}$, upper limit of reflectance $225.02\,\mu\text{m}$). From the grating, the signal is reflected frequency-resolved into an array of 32 mercury cadmium telluride (MCT) photodetectors, cooled with liquid nitrogen (Infrared Associates Inc.). Thereby, the spectral increment between two adjoining detectors depends on the utilized grating: with grating 1, two photodiodes are separated by $4.3\,\text{nm}$; in case of grating 2 by $10.2\,\text{nm}$. The output voltages from the photodetectors are sent to a preamplifier (MCT-3200, Infrared Systems Development Corp.) and from there into a sample and hold integrator device before they are forwarded to the analog-to-digital converter (PCI 6033-E, National Instruments) in the laboratory computer.

To measure pump-induced absorption changes and to minimize thereby the influence of long-term fluctuations from the CPA system on the data quality, every other pump pulse is blocked by a mechanical chopper operating at $500\,\text{Hz}$. By processing the signals of two consecutive probe pulses, i.e., $I_{\text{pump open}}$ and $I_{\text{pump blocked}}$, the changes of absorbance $\Delta OD(\lambda, \tau)$ can be calculated on a shot-to-shot basis:

$$\Delta OD(\lambda, \tau) = -\log_{10}\left[\frac{I_{\text{pump open}}(\lambda, \tau)}{I_{\text{pump blocked}}(\lambda)}\right]. \tag{3.5}$$

An exemplary result is already depicted above (confer Fig. 2.11, Sec. 2.5).

The whole pump–probe setup and the MIR-OPA are surrounded by a housing that can be purged with dry air or nitrogen to diminish the influence of water vapor absorption, which might conceal molecular absorption signatures, particularly around $1700\,\text{cm}^{-1}$.

## 3.2 Setup to investigate the photochemistry of a CORM

This section gives an overview of the instrumentation that has been utilized to investigate the photochemistry of a manganese-tricarbonyl complex (a CO releasing molecule, CORM); the corresponding results are presented in the Chapter 5. Some of the following devices already have been described in the previous section, whereas others are new additions or replacements, as it is outlined in the introductory Figure 3.1. Therefore, this section specifies the instrumentation in terms of changes or advances with respect to the previously depicted implements, while the overall structure is maintained: a commercial CPA laser system (Sec. 3.2.1) generates the fundamental pulses. These are not split into fractions, but entirely directed into a commercial noncollinear OPA that creates the excitation pulses, which are tunable across the ultraviolet and visible spectral region (Sec. 3.2.2). The residual fundamental beam subsequently seeds the MIR-OPA that remains unchanged in its configuration. Finally, both beams are overlapped inside the modified pump–probe setup (Sec. 3.2.3).

### 3.2.1 Commercial CPA laser system

The partially homebuilt laser system has been replaced by a commercial setup (Solstice, Spectra Physics), whose basic working principle—the chirped pulse amplification— remains the same. It delivers output pulses at a repetition rate of $1\,\mathrm{kHz}$, centered around $800\,\mathrm{nm}$, with a $100\,\mathrm{fs}$ pulse duration, and a pulse energy of $2.6\,\mathrm{mJ}$. The output is split
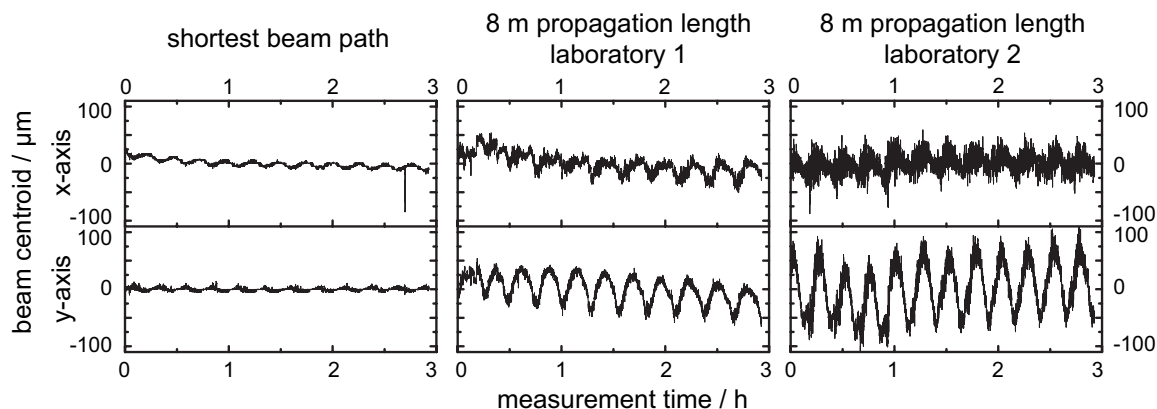


**Figure 3.8:** Monitoring of the CPA system's beam pointing along the x- and y-axis on a CCD sensor at three different positions: first, directly behind the CPA system that is located in the laboratory 2, which corresponds to the shortest possible beam path. Second, after eight meters of propagation to the optical table in laboratory 1. Third, after eight meters of propagation, but in this case the beam covered the distance on the same table and stayed in the laboratory 2. Whereas the beam centroids' fluctuations are as expected minimal at the first position, they are more pronounced but comparable in intensity at the second and third position. This substantiates that an active beam stabilization is not necessary. The oscillating contribution with a period of $15\,\mathrm{min}$, which is similarly visible in each measured trace, stems from periodic temperature fluctuations inside the laboratories, mainly caused by the climate control.

into three energetically equal beams, one of which provided the fundamental light for the subsequent instrumentation.

However, this CPA system is installed in a laser laboratory different from the one where the experiments for this thesis have been performed. For this reason, the beam is guided along two periscopes from one laboratory (lab 2) through the wall onto the optical table of the adjacent laboratory (lab 1). It thereby covers a total distance of eight meters, which raises the question to what extent the beam pointing stability is worsened. To address this issue, the beam pointing is monitored along the x- and y-axis on the CCD chip of a webcam (SPC900NC/00, Philips; pixel size $5.6\,\mu\mathrm{m}^2$) at three different positions: first, as a reference, directly behind the CPA system, which corresponds to the shortest possible beam path where the fluctuations should be minimal. Second, after a beam propagation length of eight meters towards the optical table in laboratory 1 at the position where the beam is subsequently directed into the first frequency conversion device. Third, for comparative purposes, again after eight meters of propagation but in this case the beam covered the distance in the laboratory 2 on the same optical table on which the CPA system is located. The measurement time is comparable to that of a transient absorption experiment. The two-dimensional intensity distribution on the CCD chip is fitted by a 2D Gaussian from which the centroids along the x- and y-axis are derived. Figure 3.8 presents the results obtained. As expected, the beam pointing at the first position only shows minor fluctuations; the centroids on the webcam along the x- and y-axis merely move a few microns. At the second position, the fluctuations are in contrast clearly discernible and appear even slightly intensified at the third position. However, experience has demonstrated that beam pointing fluctuations on this order of magnitude do not impair the data quality of the experiments carried out in laboratory 2 or even demand constant readjustments of the instrumentation. Nor does the oscillating contribution with a period of $15\,\mathrm{min}$, which is similarly visible in each measured trace. It stems from periodic temperature fluctuations inside the laboratories, mainly caused by the climate control. As a result, there is no need of an active beam stabilization device in laboratory 1 and one can take advantage of a modern, more robust turnkey system, which spares the laborious adjustment work that has been necessary in case of the previous setup.

## 3.2.2 NOPA: UV pulse generation

The SHG followed by THG to generate the excitation pulses has been replaced by a commercial noncollinear OPA (TOPAS-White, Light Conversion Ltd.). Its design is shown in Fig. 3.9. Apart from the fact that the beams intersect the active medium (BBO 2) noncollinearly, its basic working principle is comparable to that of the MIR-OPA (confer Sec. 3.1.2). One fraction of the incident fundamental pulses creates a WLC that is subsequently chirped. It seeds two pump stages arranged in series, where the pump beams are the second harmonic (BBO 1) of another fraction of the incoming light. The spatial and temporal overlaps are adjusted by two delay stages and the mirrors in front of the BBO 2 crystal, respectively. In comparison to a collinear OPA, the noncollinear geometry between the seed and pump beams thereby allows for a broader amplification bandwidth with a high parametric gain [117–120]. This yields laser pulses in the visible
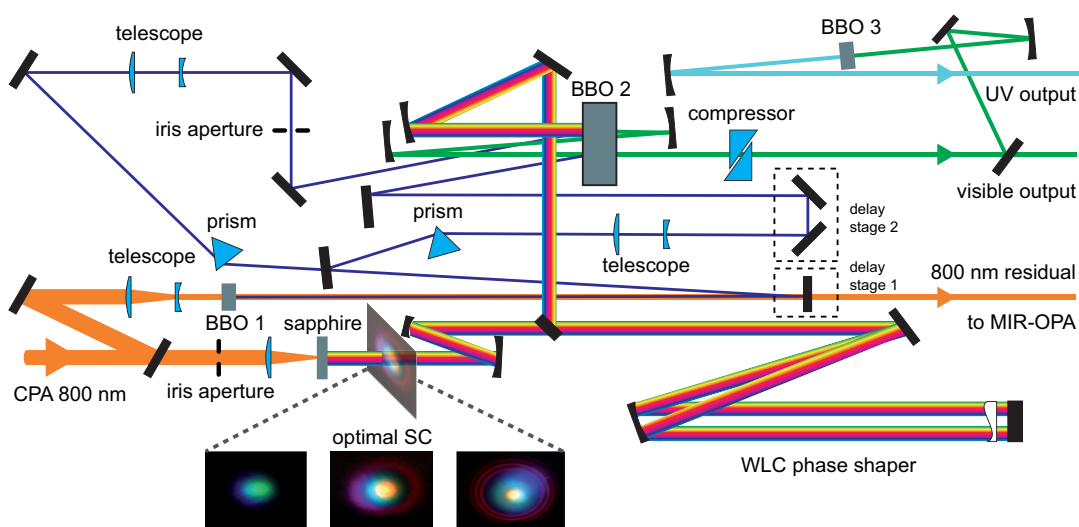
**Figure 3.9:** Optical beam path of the commercial noncollinear OPA (TOPAS-White, Light Conversion Ltd.). A small fraction of the incoming fundamental pulses creates a WLC in a sapphire disk. The optimal SC is free of multiple filaments but intensive enough to form a red superfluorescence ring. The remaining fundamental light is frequency doubled (BBO 1) and split into two fractions that subsequently serve as the pump beams to amplify the WLC seed pulses (which are chirped inside the phase shaper). In both pump stages, the participating beams overlap noncollinearly in the crystal BBO 2, which results in pulses tunable across the visible spectral range. After passing two adjustable glass wedges (compressor), these visible pulses can be frequency doubled to generate a spectrally tunable output in the UV (see Fig. 3.10). The residual beam from the first SHG leaves the device to power the MIR-OPA simultaneously. Figure partially adapted from [116].

range that pass a compressor, consisting of two vertically movable glass wedges. To create UV pulses, the second harmonic of those visible pulses can be generated subsequently via a third crystal (BBO 3). The residual beam from the first SHG leaves the device to power the MIR-OPA simultaneously.

The alignment of the NOPA is mainly ensured by a correct coupling into the device through two iris apertures. Moreover, the WLC has to be stable and without multiple filaments but intensive enough to form a red superfluorescence ring (see Fig. 3.9). Further notes on the alignment procedure can be found in the excellent user's manual to the TOPAS-White [116].

One major benefit of the commercial NOPA installation is that it circumvents the limited spectral flexibility of a SHG followed by a THG. The central wavelength of the visible output can be varied computer controlled. Hence, the UV output is tunable too. Figure 3.10 summarizes the normalized spectra obtained at various central wavelengths in the UV/VIS spectral region. In the visible range, the output power is on the order of a few ten milliwatts ($\approx 50$ mW @ 550 nm and $\approx 30$ mW @ 720 nm, e.g.) with average pulse durations around 20 fs; in the ultraviolet region, the output power is reduced by a factor of ten ($\approx 5$ mW @ 265 nm) while the pulse durations average 30 fs.

So the UV pulses are less intense than the former ones created via second and third
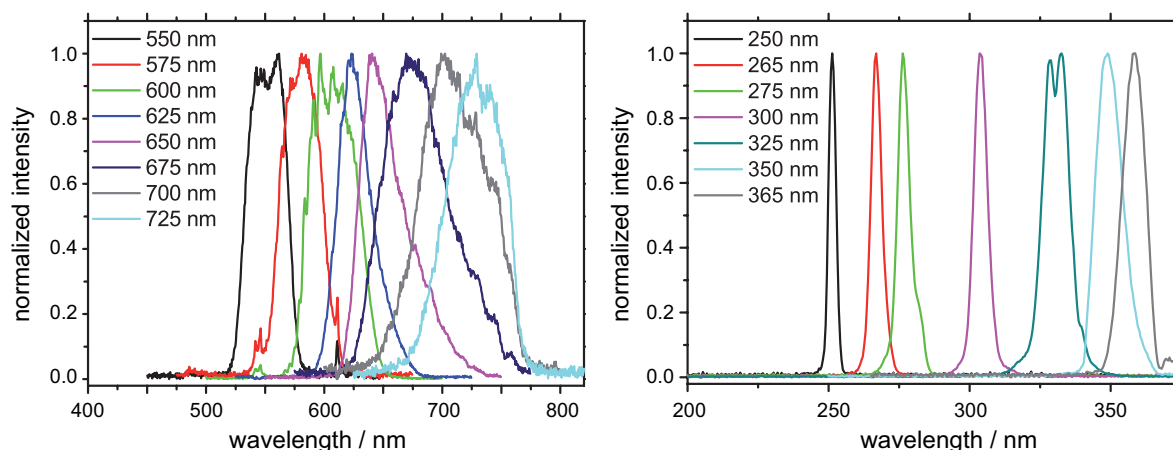
**Figure 3.10:** Spectral tunability of the TOPAS-White demonstrated by means of normalized spectra at various central wavelength in the visible and ultraviolet spectral region. Pulse durations and output power for 740 mW CPA input pulses: in the visible range $\approx$ 50 mW @ 550 nm and $\approx$ 30 mW @ 720 nm with average pulse durations around 20 fs; in the ultraviolet region, the output power is reduced to $\approx$ 5 mW @ 265 nm while the pulse durations average 30 fs.

harmonic generation. Whereas in the previous configuration the fundamental light was highly efficient directed to the pump–probe setup via specially coated dielectric mirrors ($R_{800\,nm} > 99\,\%$) and the frequency conversion was implemented shortly in front of the sample (confer Fig. 3.6), the NOPA is located at the beginning of the whole instrumentation scheme. Due to the tunability, its output is guided to the sample via several aluminum mirrors that provide high reflectance ($R_{average} > 90\,\%$) for broadband applications. However, they stay far below the reflectivity of the dielectric mirrors. Additionally, the optional UV pulse shaper further decreases the intensity of the pump pulses. As a result, in order to exploit the available pump intensity more efficiently, the properties of the focussing optical components in the pump–probe setup have to be modified.

### 3.2.3 Modified pump–probe setup

The first modification is related to the pump–probe delay stage, which is located in the beam path of the probe pulses in front of the MIR-OPA. The MIR-OPA thereby is unaffected by the slightly varying beam diameters of the incident light, which depend on the stage position (the longer the beam path, the more divergent the beam is), provided that the iris aperture that regulates the WLC intensity is adjusted correctly (confer Fig. 3.5 and Sec. 3.1.2).

The modifications on the pump–probe setup mainly refer to the methods how the pump and the probe pulses are focused into the sample (see Fig. 3.11 in comparison to Fig. 3.6 from Sec. 3.1.3). In case of the probe beam, the 1:2 telescope behind the recollimating spherical mirror has been widened to a 1:5 telescope so that the beam's spot size almost fills the whole clear aperture of the focusing mirror in front of the sample stage. According to Eq. (2.22), this enables to achieve a strongly focused probe beam
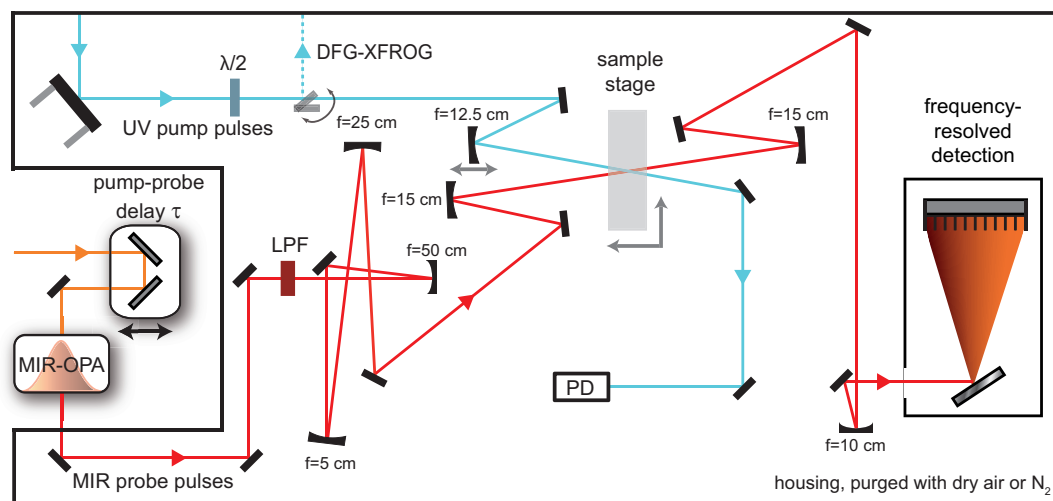
**Figure 3.11:** Experimental setup for transient absorption spectroscopy, which is in comparison to Fig. 3.6 primarily modified in terms of the methods and properties how the pump and the probe pulses are focused into the sample. With widened spot sizes in the range of the clear aperture of mirrors with one inch diameter, focal beam waists of $85\,\mu$m for the excitation pulses and $60\,\mu$m for the probe pulses are adjusted.

in the sample with a focal beam waist of approximately $60\,\mu$m.

With respect to the excitation beam path, first a gimbal mirror mount driven by micrometer screws that allows for a highly accurate coupling into the pump–probe setup has been installed. With a flip mount, the incident beam can be directed to the FROG setup for pulse characterization measurements (confer Sec. 3.3.1). Instead of the suprasil lens, the focusing into the sample is carried out by a spherical aluminum mirror (f=12.5 cm) so that the spectral tunability of the pump pulses is taken into account. Since the UV beam enters the setup with a spot size close to the clear aperture of a mirror with a one inch diameter, the excitation pulses can be focused into the sample with a focal beam waist of approximately $85\,\mu$m. To optimize the data quality, this value can be adjusted, as the focusing mirror is mounted on a stage that can be driven along the beam propagation direction with a micrometer screw.

## 3.3 Further instrumentation for prospective experiments

This section deals on the one hand with the instrumentation that complements the transient spectrometer described above. This includes the installation of a UV pulse shaper and the setup to record SHG- and DFG-XFROG traces for pulse characterization measurements (Sec. 3.3.1), as well as the detection of MIR pulses in the visible spectral range by means of the chirped pulse upconversion (Sec. 3.3.2). On the other hand, a configuration is introduced that allows for the detection of two-photon absorption (Sec. 3.3.3). Each of these implements is meant to provide a basis for prospective experiments. The experimental results obtained with these devices are presented in Chapter 6.
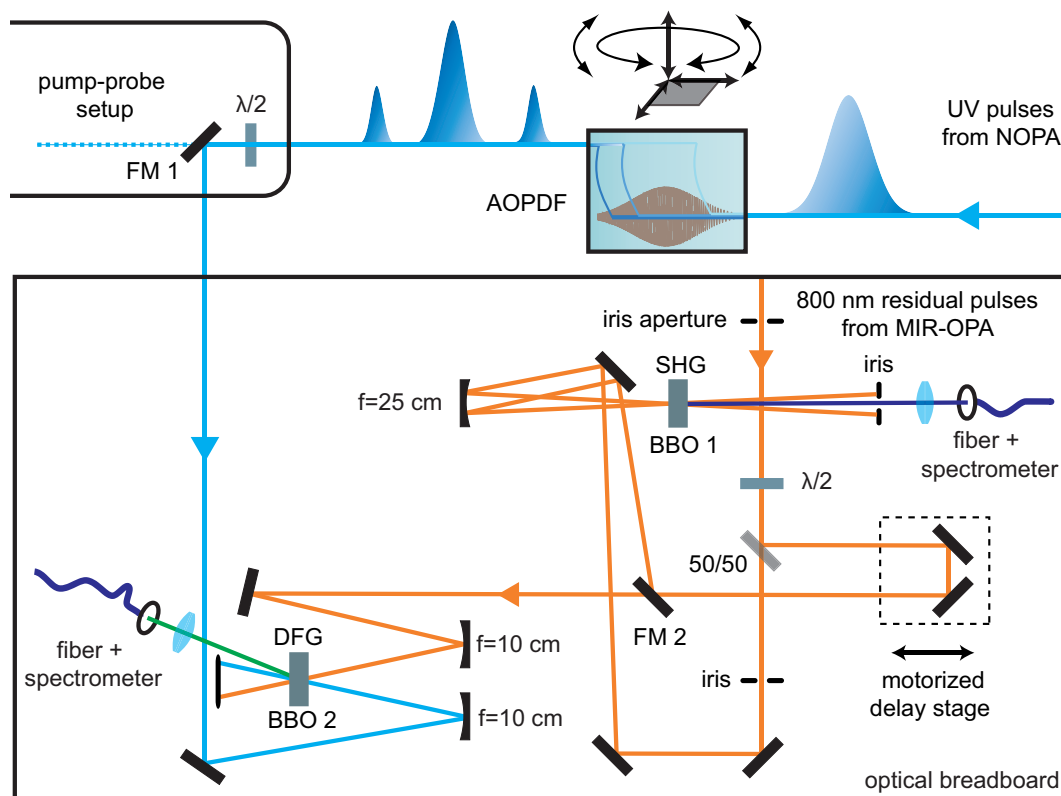
**Figure 3.12:** Combined SHG-FROG and DFG-XFROG setup for characterization of UV laser pulses. On the one hand, the setup can be used to characterize the 800 nm reference pulses by means of measuring a SHG-FROG trace. On the other hand, by tipping a flip mount (FM 2) the UV laser pulses are mixed with the reference beam and DFG-XFROG traces can be recorded. Optionally, the UV pulses are shaped before via an AOPDF (Dazzler, Fastlite) which is mounted on a table that is movable within six degrees of freedom in order to optimally adjust the diffraction inside the crystal.

## 3.3.1 UV Dazzler and DFG-XFROG setup

The device for shaping laser pulses in the UV spectral region is an AOPDF (Dazzler UV-250-400, Fastlite) consisting of a 50 mm long KDP crystal while the pulse characterization is carried out by means of FROG measurements. The corresponding theoretical backgrounds are given in Section 2.2.3. Figure 3.12 illustrates the beam paths to characterize the fundamental 800 nm pulses via SHG-FROG, which subsequently serve as reference pulses in the DFG-XFROG to characterize the shaped UV pulses. The AOPDF is mounted on a table that is movable within six degrees of freedom: a 3-axis linear translation stage, which covers adjustments along the x-, y-, and z-axis, is combined with a tip and rotation platform to optimally adjust the diffraction inside the crystal. As noted above, the reference pulses are the residual beam from the second pump stage of the MIR-OPA. The UV pulses are guided via a flip mount (FM 1) from the pump–probe setup to the FROG.

To measure a SHG-FROG trace, the 800 nm reference beam is split by a 50/50 beam-

splitter into two fractions. The reflected part is guided along a motorized linear actuator that varies the temporal delay in the upcoming frequency mixing processes. A flip mount (FM 2) directs the pulses towards a spherical mirror (f=25 cm), which focuses both partial beams noncollinearly into the crystal (BBO 1, 50 $\mu$m thickness, type I phase matching, $\Theta = 29.2°$) to generate 400 nm pulses. The constructive SHG signal is detected by a fiber spectrometer (HR2000+, Ocean Optics) while the delay stage scans the temporal offset between both participating beams. The residual light fields are blocked.

If the mount FM 2 is removed, a DFG-XFROG trace can be measured. One fraction of the well characterized reference pulses propagates to the second BBO crystal (BBO 2, 100 $\mu$m, type II phase matching, $\Theta = 55.5°$) where it is noncollinearly mixed with the unknown shaped UV pulses. Both beams are independently focused into the crystal by two spherical mirrors (each with f=10 cm). The resulting difference frequency signal is again detected by a fiber spectrometer for varying temporal offsets.

The whole FROG setup is mounted on an optical breadboard to facilitate the transportation and its application in different laboratories. An accurate and reproducible coupling into the device is ensured by two iris apertures. Half-wave plates both inside the reference and the UV beam paths allow for adjustments on the polarizations according to the types of phase matching.

## 3.3.2 CPU: Converting MIR pulses to the visible spectral range

In order to circumvent the technical constraints of a direct multichannel detection in the MIR via a MCT array (confer Sec 3.1.3), the technique of chirped-pulse upconversion (CPU) [121] can be applied. Within the CPU, the MIR probe pulses are transferred to the visible spectral region to benefit from the sophisticated silion CCD technology in conjunction with higher resolutions or lower bandwidths per pixel, respectively, provided by the optical gratings. Figure 3.13 depicts the corresponding experimental implementation: a fraction of the incident CPA fundamental beam is directed into a stretcher (which initially has been the compressor of the homebuilt laser system, see Sec. 3.1.1) where it is downchirped to a pulse duration of approximately 100 ps. After passing a delay stage (note that this stage does not scan the pump–probe delay time), it is focussed by a lens (f=25 cm) into a magnesium oxide doped lithium niobate (MgO(5%):LiNbO$_3$) crystal (450 $\mu$m, type I phase matching, $\Theta = 45.4°$). The MIR beam is equally split by a KBr window behind the sample. One fraction is guided unchanged into the IR spectrometer. The second part propagates towards a 90° off-axis parabolic gold mirror (f=152 mm), which focuses the beam into the crystal to generate the sum-frequency around 690 nm (in case of an MIR pulse centered at 2000 cm$^{-1}$). A 750 nm shortpass filter (SPF) blocks the residual MIR and NIR pulses, whereas the visible beam propagates through a recollimating lens (f=15 cm) before entering the visible spectrograph (Acton SpectraPro 2500i, Princeton Instruments, 690 nm central calibration wavelength). With this configuration, both detection techniques (MCT and CPU) can basically be operated simultaneously.

The spectrometer comprises a blazed grating (1200 grooves/mm, blaze wavelength 750 nm) and a thermoelectrically cooled, front-illuminated 2048 x 512 pixel CCD camera (PIXIS, Princeton Instruments), which features a spectral bandwidth of 0.019 nm per

**Figure 3.13:** Experimental setup to transfer the MIR probe pulses to the visible spectral domain via chirped- pulse upconversion (CPU). A fraction of the CPA fundamental light is downchirped in a stretcher and superposed with one half of the MIR probe pulses in a MgO(5%):LiNbO$_3$ crystal. The resulting sum frequency signal is spectrally dispersed and subsequently detected by a 2048 x 512 pixel CCD camera. The second half of the MIR beam is guided unchanged into the IR spectrometer for simultaneous detection.

pixel between 670 and 709 nm. Depending on the measurement speed, 20 pixels can be binned vertically and averaged over 300 ms or, in order to achieve a single-shot data acquisition, an extra binning of horizontal pixel pairs can be performed, which yields spectra consisting of 1024 pixels with a bandwidth of 0.038 nm per recorded data point. Due to cross-phase modulations between the chirped fundamental light and the MIR pulses, narrow spectral features in the MIR spectrum can appear strongly distorted in the upconverted spectra [122]. Therefore, each spectrum acquired is corrected by a removal of the cross-phase modulation contributions. Additionally, signal replicas caused by reflections in the CPU crystal occurring at 6.8 ps are Fourier-filtered in an area of 1 ps in the time domain. Following a frequency-resolved cross-correlation measurement, the dominant spectral phase contribution of the chirped NIR pulse is the second-order parameter $b_2 = -3.97 \, \text{ps}^2$.

The results derived from a comparative study on chirped-pulse upconversion and direct MCT detection that elucidates the pros and cons of both techniques related to differing experimental circumstances are presented in the Section 6.3.

### 3.3.3 Detecting two-photon absorption

Two-photon absorption (TPA) is a nonlinear process of light–matter interaction. For a molecular system that exhibits absorption bands in the UV spectral domain but none in the visible range, the nonresonant case of TPA is discussed: the system is excited due to the simultaneous absorption of two photons of which the total energy is sufficient to reach a higher electronic state. Thereby, the first photon leads to a short-lived virtual state from where the second photon excites the system to an energetically higher lying real state, assumed that the latter takes place within the lifetime of the virtual energy level, which is on the order of $10^{-15}$ fs [123]. Focused intensive ultrashort laser pulses can provide such high photon densities.

The nonlinear properties of TPA can be described by the following approach [9, 12]:

$$\frac{\mathrm{d}I(z)}{\mathrm{d}z} = -\alpha_0 I(z) - \beta I^2(z), \tag{3.6}$$

with $\alpha_0$ being the linear coefficient of absorption, $\beta$ the TPA coefficient, and $I(z)$ the intensity after passing a medium of length $z$. Within the scope of nonresonant TPA, the linear coefficient vanishes so that integration of Eq. (3.6) yields

$$I(z) - I_0 = -\beta z I_0 I(z), \tag{3.7}$$

with the incident light intensity $I_0$. If the absorption inside the sample volume is small, the change in pulse intensity is approximately

$$I(z) - I_0 = -\beta z I^2(z) = -\sigma N_0 z I^2(z), \tag{3.8}$$

where the TPA coefficient is exchanged by the molecular TPA cross-section $\sigma$, and the number density of molecules $N_0$. Taking into account the Gaussian beam profile of the visible pump pulses, the ratio between $I(z)$ and $I_0$ is [124]

$$\frac{I(z)}{I_0} = \frac{\ln(1 + I_0 \sigma N_0 z)}{I_0 \sigma N_0 z}. \tag{3.9}$$

A treatment in the formalism of perturbation theory using the second quantization basically leads to the same result [48]. The incident light field possesses $n$ photons. Two excitations—from the initial to the virtual state and from there to the final state—correspond to a resulting light field with $n - 2$ photons due to the annihilation operator that has to be applied two times. The transition probability $W$ is proportional to the absolute square of the transition matrix which in turn is proportional to $\sqrt{n}\sqrt{n-1}$:

$$W \propto n(n - 1) \propto I^2, \tag{3.10}$$

The last relation holds since the intensity of the incident light field is proportional to the photon number and it is assumed that $n \approx n - 1$, as it is the case for highly intense laser pulses.

So it is obvious that the duration of the utilized visible laser pulses as well as their energy is of great importance in the course of detecting TPA. The experimental implementation therefore comprises an autocorrelator (pulseCheck, A.P.E.) to determine the
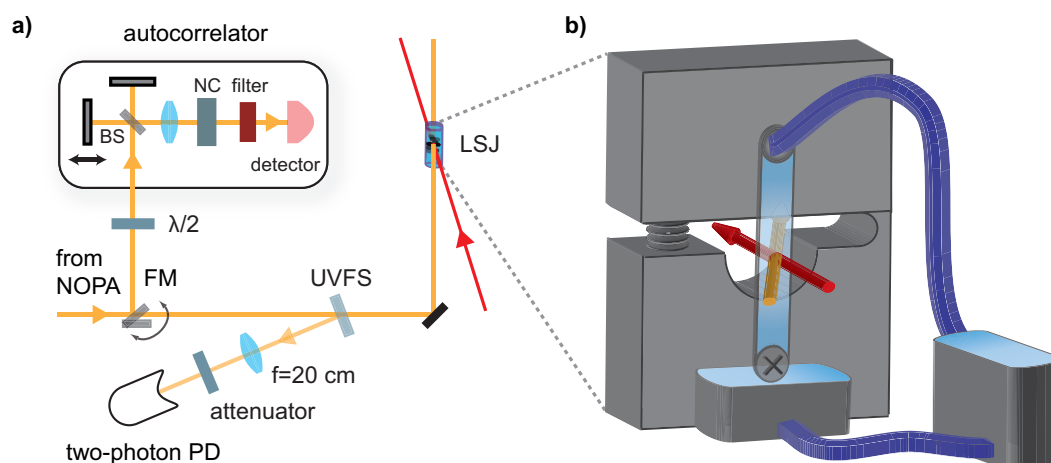
**Figure 3.14:** (a) Setup to detect two-photon absorption (TPA) signals. Since TPA is strongly dependent on the duration and the energy of the utilized visible pump pulses, the beam can be directed to an autocorrelator via a flip mount (FM) to record the pulse duration. Additionally, a UV fused silica (UVFS) window constantly guides 5% of the beam to a two-photon photodiode to monitor the pulse energy. To prevent the generation of a WLC in the sample windows due to the high pump intensities, a wire-guided flowing liquid sample jet (LSJ) driven by a micro annular gear pump replaces the sample cuvette (b). Two stainless steel wires, each of $100\,\mu m$ thickness, are parallelly clamped with a distance of $5\,mm$. A screw presses the upper and lower element of the LSJ mount apart so that the tension of the wires can be varied. This affects both the thickness of the liquid film (approximately $60\,\mu m$) and its homogeneity.

pulse duration and a two-photon photodiode (SG 01S, Scitec Instruments Ltd.) to monitor the pulse energy (see Fig. 3.14a). The photodiode features one-photon absorption only in the UV region between $200\,nm$ and $400\,nm$ so that a photocurrent in the visible range solely derives from two photons. Via a flip mount, the visible pump pulses can be guided into the autocorrelator, whereas a 5% fraction of the pump beam is directed to the photodiode by a UV fused silica window (UVFS) to constantly monitor the pulse energy.

To impede the generation of a WLC in the cuvette windows, which would easily occur due to the high pump pulse intensities, a wire-guided flowing liquid sample jet (LSJ) [125] driven by a micro annular gear pump replaces the sample cuvette and the peristaltic pump (see Fig. 3.14b). Basically, the LSJ consists of two stainless steel wires, each of $100\,\mu m$ thickness, that are parallelly clamped with a distance of $5\,mm$. A screw presses the upper and lower element of the LSJ mount apart so that the tension of the wires can be varied. This affects both the thickness of the liquid film (approximately $60\,\mu m$) and its homogeneity. Both quantities are customarily adjusted in such a way that the signal's noise in the IR spectrometer of the MIR probe pulses which pass through the LSJ is minimized. A pinhole can be inserted between the wires to facilitate the adjustment of the spatial overlap in the sample film.

# 4 Ultrafast multisequential photochemistry of 5-diazo Meldrum's acid

## 4.1 Introduction

One of the major goals of ultrafast transient absorption measurements is to unravel the dynamics and the participating reaction intermediates that constitute a photoinduced chemical reaction. Whereas conventional chemistry mainly focuses on the overall outcome of a reaction sequence, femtochemistry implies both the observation of macroscopic measures and microscopic quantum-mechanical processes that evolve in time. In this sense, it is a particular challenge if the system under investigation features a manifold of sequential and competing parallel reaction pathways, as it is offered by the photochemistry of 5-diazo Meldrum's acid (DMA) in alcohol solution. The following chapter presents the results obtained by a study to elucidate the first nanoseconds of the partially bimolecular light-induced reaction dynamics of DMA, revealing ultrafast structural dynamics, characteristic time scales and associated consecutively emerging chemical species.

DMA belongs to the class of $\alpha$-diazocarbonyls that play an essential role for electronic microchips and many other industrial chemistry procedures [126, 127]. The key properties making them so useful as photoactive compounds in positive photoresists are based upon the photoinduced loss of a diazo group accompanied by a reformation of the molecular structure to form ketene, also known as Wolff rearrangement [128, 129], whose mechanism has given rise to a long controversy. It can either take place in a concerted manner, where the ketene is formed directly by losing the diazo group synchronously with the rearrangement, or in a stepwise one, where the ketene is formed via a carbene intermediate and a subsequent rearrangement, or a concurrent combination of both [130–133]. By using ultrafast transient absorption spectroscopy, intermittent reaction dynamics become observable and evidence for different reaction schemes has been collected, as recently reviewed by Burdzinski and Platz [134]. It was even reckoned that all cyclic diazocarbonyl compounds exhibit a dominant concerted and a minor stepwise reaction pathway.

This assumption is in line with a recent ultrafast study of diazonaphtoquinone (DNQ), widely used for photoresist applications [127], in which a formation of the ketene within 300 fs or faster has been found, proving a concerted mechanism, but also indications for a concurrent carbene formation are discussed [135, 136]. Blancafort and coworkers confirmed computationally that such a stepwise mechanism should be possible as well for
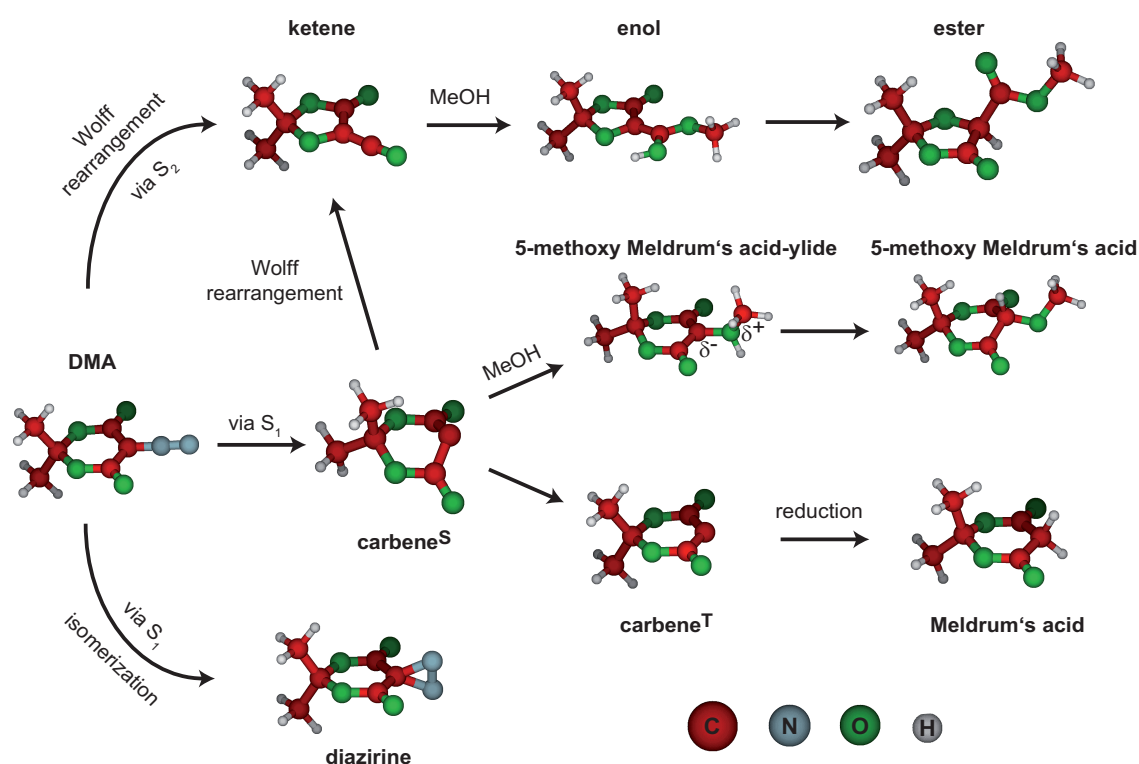
**Figure 4.1:** Scheme of the photoreaction of 5-diazo Meldrum's acid (DMA) dissolved in methanol. DMA in conjunction with a R-OH solvent provides three main reaction channels upon photoexcitation: (1) the Wolff rearrangement reaction that forms ketene and ends up in an ester formation, (2) a carbene formation that leads to methoxy Meldrum's acid or Meldrum's acid by reducing the triplet carbene molecule, (3) an isomerization of the DMA molecules to diazirine. Figure adapted with permission from [1]. © (2010) American Chemical Society.

this molecular system [137], however, the concerted way occurs likewise [138, 139]. In an experiment on DMA, Burdzinski *et al.* [140] observed a sub-picosecond ketene formation, i.e., a concerted mechanism, but also contributions assigned to a singlet carbene with a lifetime of only 2.3 ps.

But for all that, although DMA exhibits a rich photochemistry, ultrafast studies [140–142] have not addressed successive reaction dynamics of the ketene and carbene species and the information that can be derived with respect to intermediate products. This also is of interest concerning the applications of DMA, since it is employed for high-resolution purposes as photoactive compound in deep ultraviolet lithography [126, 127, 143, 144] and as dopant for laser ablation in polymer matrices [141, 142, 145–147]. Known reactions after excitation with UV light comprise the formation of a carboxylate ester via an intramolecular Wolff rearrangement; further reaction channels are an isomerization to diazirino Meldrum's acid and a reduction to Meldrum's acid [148–151], as illustrated in Figure 4.1.

This chapter deals with the light-induced bimolecular reaction of DMA in alcohol solution. A reaction with a solvent molecule can thereby occur both for the ketene

and the carbene intermediates, which are formed upon UV excitation. As subsequent reaction paths to specific photoproducts are present and identifiable by means of their absorption characteristics in the MIR, the research on such bimolecular reactions also addresses the question of whether and under which conditions both ketene and carbene are formed for a specific compound. Measurements with additional alcohol solvents prove the accurate differentiation between uni- and bimolecular reaction pathways. Density functional theory calculations on the normal modes (confer Sec. 2.4.2) and steady-state Fourier-transform infrared (FTIR) spectroscopy of both the reactant and the products in the chemical equilibrium accompany the analysis of the transient spectra in order to reliably identify the reaction products, thus permitting a coherent picture of the ultrafast photochemistry of DMA.

The results presented in the following have been published in [1]. In various ways, they are a significant extension to the preliminary work, described in [113]: first, due to further time-resolved measurements in additional alcohol solvents on the one hand and for longer pump–probe delay times on the other hand. Second, due to more elaborate DFT calculations that have been carried out both on possible reaction intermediates and stable reaction products, again in further molecular environments, in order to substantiate the data analysis. Third, especially owing to the extensive peer-reviewing process prior to the publication of this study, additional measurements have been performed to confirm the argumentation and several passages of the data analysis and presentation have been revised and expanded to be more instructive and convincing.

## 4.2 Materials and methods

The femtosecond pump–probe setup employed for the time-resolved experiments is described in Section 3.1. The MIR probe pulses were tuned between 1550 and $2250\,\mathrm{cm}^{-1}$ and subsequently detected via the grating 2 inside the IR spectrometer. To obtain detailed single kinetic traces around zero delay time, the step size of the $600\,\mathrm{mm}$ delay line was chosen smaller around the temporal overlap than at longer delay times (which is reflected in the density of data points in the transient data). The effect of varying pump-probe overlap for longer delay times due to misalignment or changes in the divergence of the pump beam could not be observed, which in general would cause a continuous loss of signal, regardless of its sign or spectral position. The data analysis was performed with a sum of exponential functions.

The DMA sample was purchased from TCI Europe (CAS: 7270-63-5) as 5-Diazo-2,2-dimethyl-1,3-dioxane-4,6-dione. In all experiments it was used without further purification or other treatment and dissolved in spectroscopic-grade methanol, ethanol, or isopropanol. Due to its small extinction coefficient in the infrared, high sample concentrations of $47\,\mathrm{mM}$ were employed leading to an optical density of 1.5 at $266\,\mathrm{nm}$. Steady-state infrared spectra were recorded by a Fourier transform infrared spectrometer (FT/IR-4100, JASCO) with a resolution of $1\,\mathrm{cm}^{-1}$. Contributions of the solvent were taken into account by measuring the solvent spectrum separately and by subtracting it from the sample spectrum. Steady-state UV/VIS spectra were recorded by a spectrophotometer (U-2000, Hitachi).

DFT calculations of DMA in vacuum and in respective molecular environments were performed as described in Section 2.4. The density functional Becke three-parameter hybrid method in combination with the Lee-Yang-Parr correlation functional (B3LYP) was used. Both the molecular geometry optimization and the calculations for the normal modes and their amplitudes were carried out using the 6-311+G** basis set.

## 4.3 Results

### 4.3.1 DFT calculations and FTIR spectroscopy

FTIR spectra were recorded for DMA dissolved in methanol and initially without any previous photochemical conversion (see Fig. 4.2a; blue). The absorption spectrum in the chemical equilibrium shows significant bands at 1719, 1735 and 1753 cm$^{-1}$ that can clearly be identified with combined stretching modes of C=O groups while the strong absorption band at 2172 cm$^{-1}$ should be assigned to the stretching vibration of the C=N=N group (compare for instance the value of 2169 cm$^{-1}$ reported for this vibration for DMA in chloroform [134]). Other sample preparation techniques in the solid phase [Attenuated Total Reflection (ATR) and DMA pressed in a KBr pellet] reproduced the absorption bands of the solution phase spectra exactly. Furthermore, the output of the DFT calculations for DMA in methanol confirm the assignment of the occurring absorption bands and will be discussed in greater detail above.

In addition, two different radiation sources were applied to get a first impression of the photoproducts whose appearance should also be expected in the transient absorption experiments. According to UV/VIS spectra (see inset of Fig. 4.2a), DMA exhibits a strong absorption signature in the UV regime around 245 nm and a minor one at 330 nm. Therefore, a medium pressure UV radiation source with a broad but distinct line spectrum in the UV and visible spectral regions that provides high emission at 255 nm is utilized, while the emission bands beyond 300 nm only excite few molecules due to the much weaker DMA absorption. The sample was positioned in a silica tube surrounded by the mentioned radiator. Figure 4.2a shows the FTIR spectra of DMA in methanol after 15 (black) and 60 minutes (red) of such irradiation. By looking at the decreasing absorption band of the diazo group at 2172 cm$^{-1}$ one can state that after 15 minutes of irradiation nearly one third of the DMA molecules have been converted and that after one hour of irradiation the reactant has been converted completely. In the regime around 1740 cm$^{-1}$ both of the primary maxima of absorption vanish while gradually new major absorption bands at 1766 and 1808 cm$^{-1}$ and minor ones at 1760 and 1805 cm$^{-1}$ rise. It has to be noted that this data does not show the pure excitation belonging to the 250 nm absorption band (because of the spectrally broad UV excitation), yet the aspired reaction channel with its intermediates will contribute significantly.

The second utilized radiation source was a frequency-tripled pulsed Nd:YAG laser (355 nm, ns pulse duration). Figure 4.2b depicts the FTIR spectrum of DMA in methanol after 10 minutes of such irradiation. Again, circa 30% of the educt has been converted which leads to emerging absorption signatures at 1710, 1768 and 1796 cm$^{-1}$.

In combination with the FTIR data, calculations were performed on the optimal
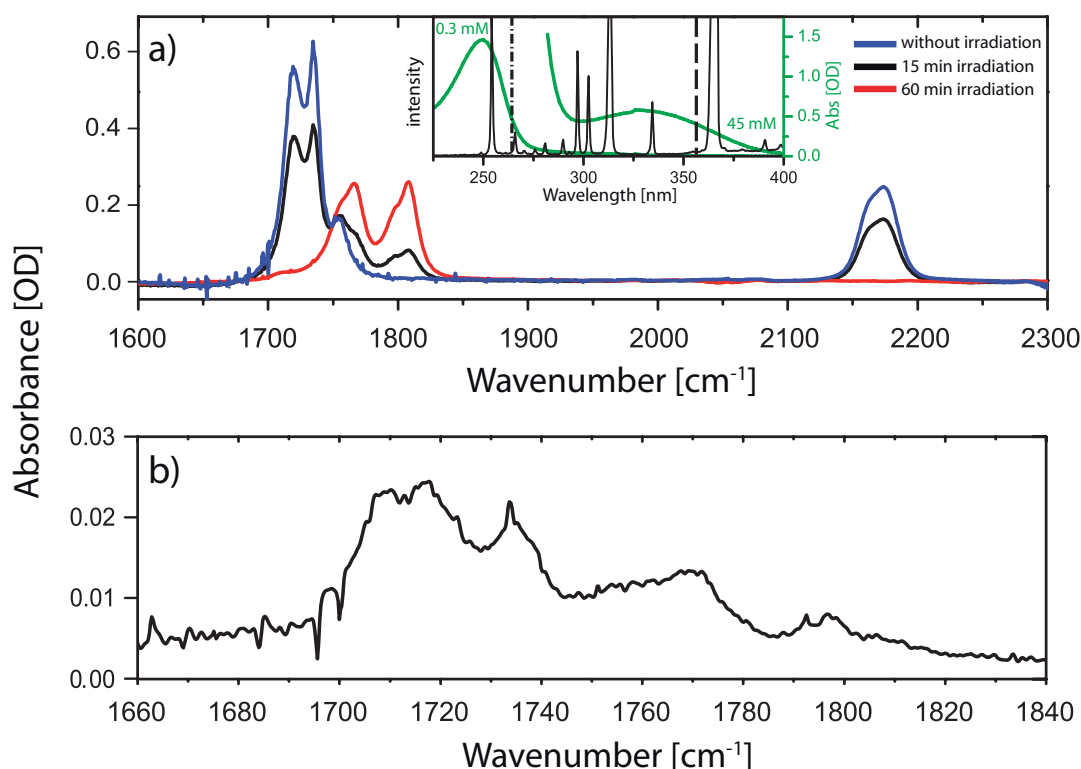
**Figure 4.2:** FTIR spectra of (a) a DMA/MeOH dissolution in the original state as well as after irradiation with a medium pressure UV lamp and (b) a frequency-tripled pulsed Nd:YAG laser. The inset shows in green the UV/VIS absorption spectrum of DMA (note the different concentrations to uncover the weaker absorption band at 330 nm) and the spectra of the medium pressure UV lamp (black curve), the Nd:YAG laser (dashed line) and the UV excitation pulses (dot-dashed line). (a) Blue curve: Under initial conditions midinfrared steady-state absorption spectroscopy reveals four significant bands at 1719, 1735, 1753 cm$^{-1}$ (combined stretching modes of C=O groups), and at 2172 cm$^{-1}$ (stretching vibration of the C=N=N group). After 15-minute (black curve) and 60-minute (red curve) irradiation with a UV emitter the DMA specific absorption at 2172 cm$^{-1}$ decreases toward zero while new maxima of absorption rise at 1766 and 1808 cm$^{-1}$. (b) After 10-minute irradiation with a frequency-tripled Nd:YAG laser the same kind of diminishing DMA absorption can be noticed while new absorption bands at 1710, 1768 and 1796 cm$^{-1}$ appear. Note the different x-axis scale. Figure reprinted with permission from [1]. © (2010) American Chemical Society.

molecular geometry and with it on the vibrational normal modes in different environments (isolated, chloroform, methanol) of any chemical species whose appearance could be expected in the transient data. In terms of the upcoming time resolved experiments, the analysis concentrates here on the methanol solvent and reveals—besides a slight shift due to the different solvent—very good agreement concerning the spectral positions with the calculations of Burdzinski *et al.* [140]. The chemical species of interest are in general the emerging products and intermediates of a thermal or photolytic conversion of $\alpha$-diazocarbonyl compounds [148].

The corresponding subsumption is sketched in Figure 4.3. Apart from the triple

**DMA**

| FTIR | DFT | assignment | rel. IR intens. |
|---|---|---|---|
| 1719 | 1739 | $v_{as}$(C=O) | 1 |
| 1735 | 1754 | $v_{sym}$(C=O) | 0.681 |
| 1753 | | | |
| 2172 | 2288 | $v$(C=N=N) | 0.513 |

**ester**

| FTIR | DFT | assignment | rel. IR intens. |
|---|---|---|---|
| 1766 | 1791 | $v_{Ester}$(C=O) | 0.483 |
| 1808 | 1824 | $v_{Ring}$(C=O) | 0.514 |

**diazirine**

| FTIR | DFT | assignment | rel. IR intens. |
|---|---|---|---|
| 1710 | 1775 | $v_{as}$(C=O) | 0.764 |
| 1768 | 1785 | $v_{sym}$(C=O) | 0.674 |
| 1796 | 1824 | $v$(N=N) | 0.217 |

**Meldrum's acid**

| DFT | assignment | rel. IR intens. |
|---|---|---|
| 1706 | $v_{as}$(C=O) | 0.547 |
| 1774 | $v_{sym}$(C=O) | 0.459 |

**ketene**

| DFT | assignment | rel. IR intens. |
|---|---|---|
| 1782 | $v$(C=O) | 0.589 |
| 2239 | $v$(C=C=O) | 0.911 |

**enol**

| DFT | assignment | rel. IR intens. |
|---|---|---|
| 1704 | $v$(C=C) | 0.971 |
| 1777 | $v$(C=O) | 0.429 |

**carbene$^{S/T}$**

| DFT S/T | assignment | rel. IR intens. |
|---|---|---|
| 1682/1662 | $v_{as}$(C=O) | 0.865/1.121 |
| 1762/1717 | $v_{sym}$(C=O) | 0.723/0.446 |

**5-methoxy Meldrum's acid**

| DFT | assignment | rel. IR intens. |
|---|---|---|
| 1779 | $v_{as}$(C=O) | 1.131 |
| 1820 | $v_{sym}$(C=O) | 0.699 |

**5-methoxy Meldrum's acid-ylide**

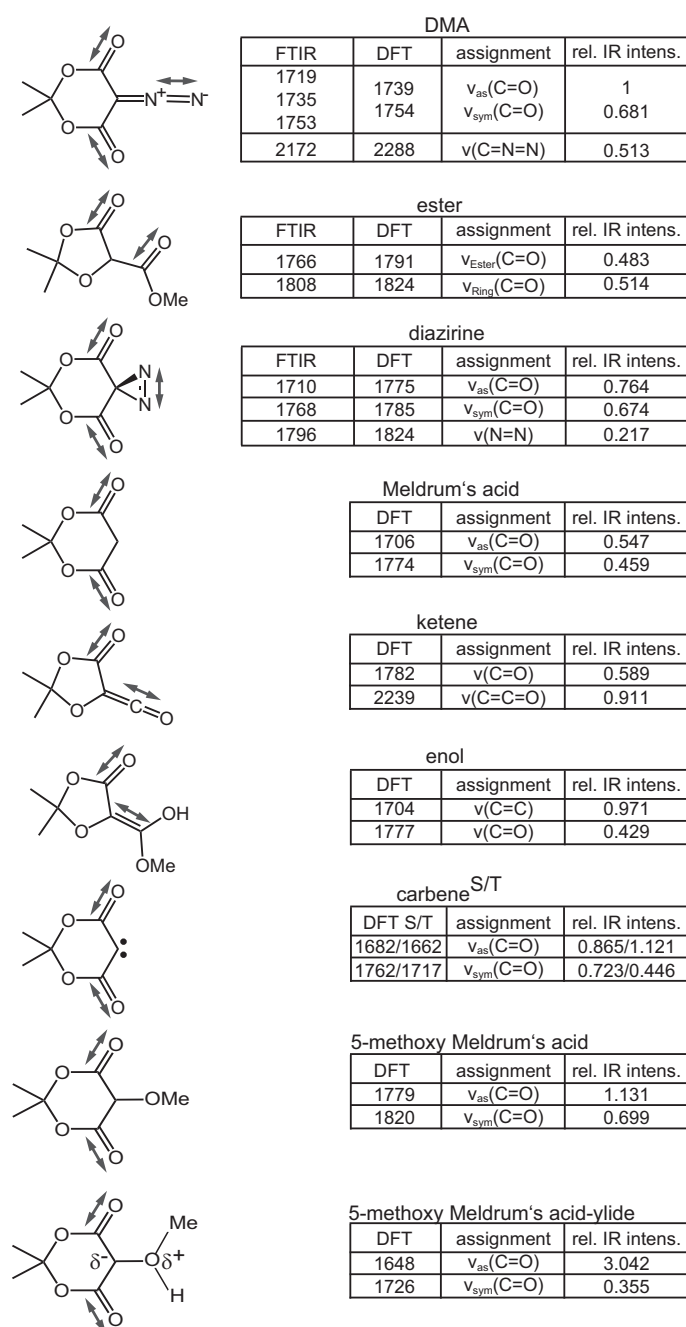| DFT | assignment | rel. IR intens. |
|---|---|---|
| 1648 | $v_{as}$(C=O) | 3.042 |
| 1726 | $v_{sym}$(C=O) | 0.355 |

**Figure 4.3:** Illustration of the spectral position in cm$^{-1}$ of vibrational modes of the relevant chemical species in methanol, defined by DFT calculations on the one hand and experimentally measured by FTIR spectroscopy on the other hand. As some species like enol and ketene occur as intermediates, there is no FTIR data available. The amplitudes of the modes from the DFT calculations are given in the right-hand column, normalized to the strongest mode of DMA. Figure reprinted with permission from [1]. © (2010) American Chemical Society.
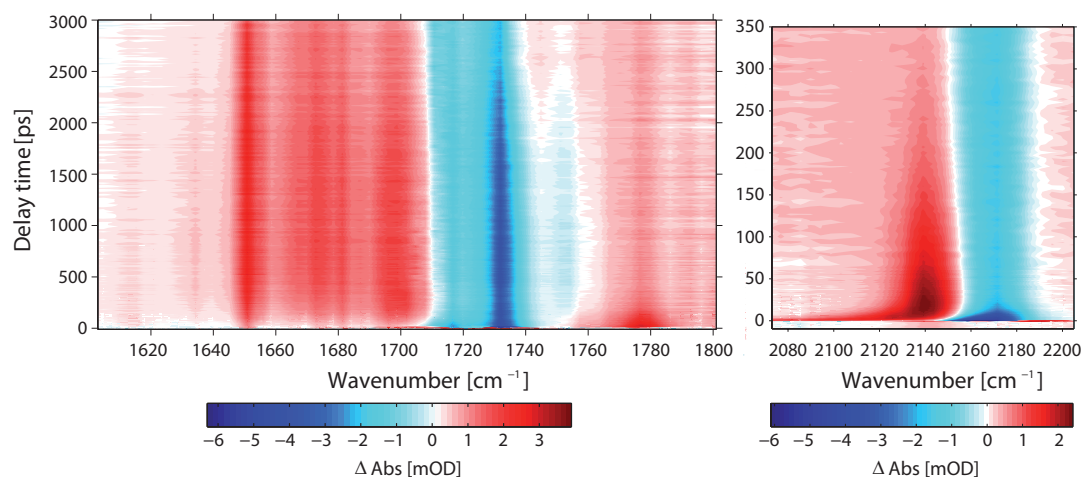
**Figure 4.4:** Coloured two-dimensional contour plot of the temporally and spectrally resolved midinfrared transient absorption experiments of DMA dissolved in methanol. Both in the region around 1740 cm$^{-1}$ (absorption due to C=O stretching vibrations) and around 2170 cm$^{-1}$ (absorption due to diazo and C=C=O keto stretching vibrations) one can see ground state bleach of DMA after photoexcitation with 267 nm femtosecond pump pulses. Furthermore a variety of significant positive contributions due to arising photoproducts illustrates the partly bimolecular photochemistry of DMA in methanol. Their origin and temporal progression is discussed by means of the particular transients (i.e., Figs. 4.5, 4.6, 4.7, and 4.8). Figure reprinted with permission from [1]. © (2010) American Chemical Society.

splitting of the reactant's C=O absorption which could not be reproduced by the DFT calculations, there is a good agreement between experiment and theory, although all theoretical results tend to slightly higher wavenumbers in comparison to the FTIR outcomes. These deviations might be adjusted by applying an appropriate scaling factor for the DFT results [77], however, this is not done due to a limited gain in information content for the upcoming analysis. Although the DFT prediction for the diazo absorption and for the ketene's C=C=O absorption should lie at lower wavenumbers [141], the bands nevertheless can be unambiguously identified and the exact wavenumber can be determined from the absorption spectra.

The strong modes at 2172 cm$^{-1}$ and in the region around 1740 cm$^{-1}$ belonging to the reactant absorption will be taken as marker modes for the transient absorption measurements (in the following identifiable as ground state bleach), since these comprise characteristic spectral signatures to observe diazo as well as C=C=O keto group vibrations, and C=O stretching vibrations, respectively.

## 4.3.2 Femtosecond midinfrared spectroscopy

The photochemistry of DMA in methanol upon excitation with frequency-tripled Ti:Sa pulses at a wavelength of 267 nm spans at least three distinguishable reaction channels, some of which are of the bimolecular kind (see Fig. 4.1). Femtosecond vibrational spectroscopy was applied in the spectral regions from 1550 to 1900 cm$^{-1}$ and from 2000 to

$2250\,\mathrm{cm}^{-1}$, whereas only data is shown that actually illustrates any kind of transient absorption signal.

Figure 4.4 gives an overview of the whole set of spectrally and time-resolved transient absorption signals of DMA dissolved in methanol. The coloured two-dimensional contour plot on the right-hand side summarizes the transient spectral evolution of DMA around $2140\,\mathrm{cm}^{-1}$, showing two important features. Firstly, a negative change in absorbance centered at $2172\,\mathrm{cm}^{-1}$ that relaxes partially up to a level where it remains constant during the residual delay time. Secondly, a positive change in absorbance that increases in strength and shifts continuously from lower ($2080\,\mathrm{cm}^{-1}$ right after zero delay time) to higher wavenumbers until it remains steady at $2135\,\mathrm{cm}^{-1}$. Within $500\,\mathrm{ps}$, this positive absorption vanishes completely (confer Fig. 4.11).

More in detail, Figure 4.5 depicts the related time evolution at chosen frequencies. In accordance with the steady-state spectra of DMA (see Fig. 4.2) the negative absorption is assigned to the ground state bleach (GSB) of DMA, more precisely to the bleaching of the C=N=N stretching vibration in the electronic ground state upon photoexcitation with a subsequent relaxation to the latter within $20\,\mathrm{ps}$. From this bleach recovery, a quantum yield of 30% can be derived. In other words, 30% of the initially excited molecules do not relax back to the ground state but form further photoproducts.

The positive absorption at $2135\,\mathrm{cm}^{-1}$ is assigned to the C=C=O stretching vibration of the ketene whose formation coincides with the DMA GSB. Its spectral position agrees very well with other studies [140, 141] and the behavior to shift towards higher frequencies within $15\,\mathrm{ps}$ can be explained by vibrational cooling of vibrationally excited ketene molecules [152, 153] (see Sec. 2.3). Changes of absorption at negative delay times and nearby zero delay time are due to the PFID and the coherent artifact. From the former, one can derive some information like the linewidth of a vibrational transition but in general it does not reveal new insights into molecular dynamics (see Sections 2.5.1 and 2.5.2). By contrast, absorption lines that only appear after the pump pulse do not exhibit a PFID, so that the rise times of the photoproducts reflect real dynamical information [93, 154]. Measuring transient absorption spectra of pure methanol along the whole mentioned frequency domain did not show any dynamics.

On the left-hand side of Fig. 4.4 one can see transient absorption signals between 1605 and $1805\,\mathrm{cm}^{-1}$. Figure 4.6 gives a clearer insight into the temporal evolution of the particular transient absorption behavior that will be presented in the following. Reasons and explanations for the respective chemical assignments are given in the Section 4.4 after the presentation of the experimental data.

It seems that these experimental results derive from various molecular dynamics. The most prominent and easily interpretable feature might be the broad negative contribution in the region around $1740\,\mathrm{cm}^{-1}$ that actually consists of three bands of absorption. It is assigned to the GSB of DMA molecules (detectable at this spectral position by characteristic C=O stretching vibrations) followed by the expected partial recovery (see Fig. 4.6). Again, the comparison of this spectral area with the steady-state spectra fits very well, as do the DFT calculations on the normal modes of DMA. An intrinsic physicochemical property of a transient describing a GSB is its constantly persisting level of absorption after the recovery. By contrast, the signal at $1732\,\mathrm{cm}^{-1}$ rises between
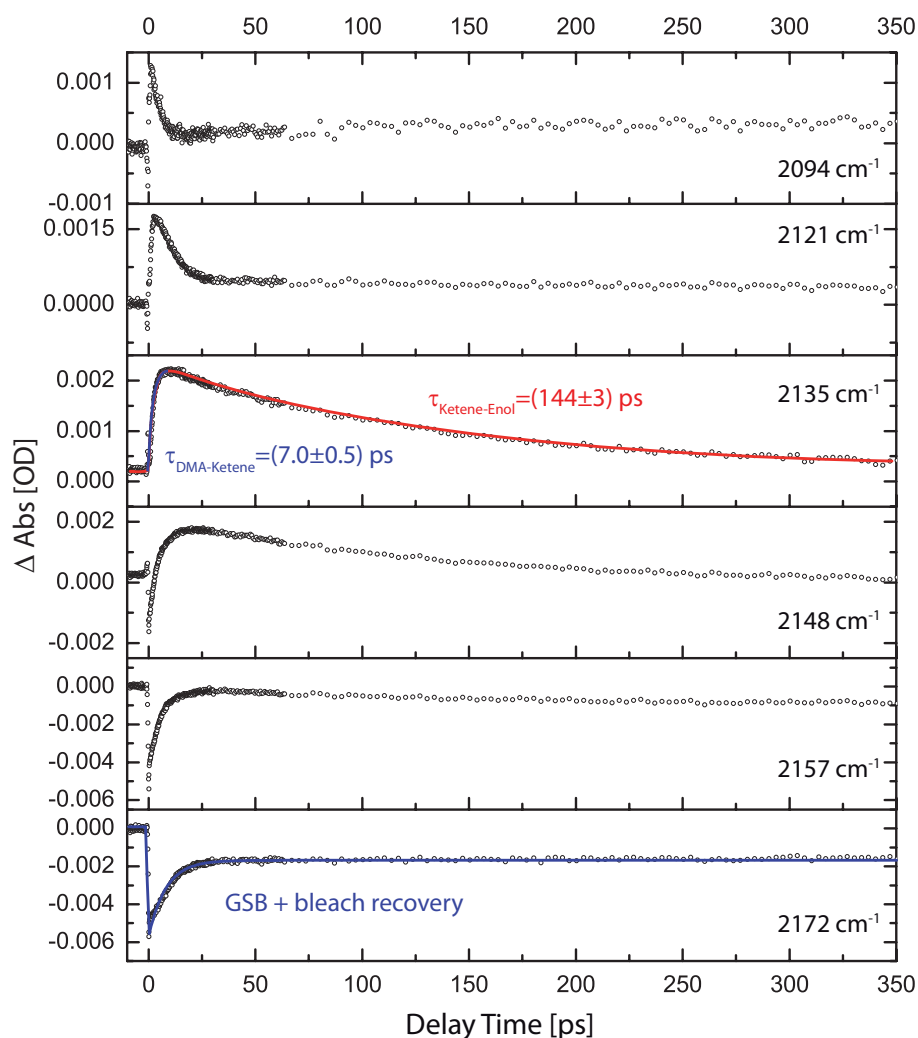
**Figure 4.5:** Exemplary transients from the spectral region between 2070 and 2200 cm$^{-1}$ presenting the temporal evolution of: (1) The ground state bleach (GSB) with a subsequent bleach recovery of DMA (2172 cm$^{-1}$), (2) the formation of the ketene intermediate that has an overall lifetime of 144 ps and is undetectable after roughly 500 ps (2135 cm$^{-1}$; confer Fig. 4.11), and (3) the vibrational relaxation of "hot" ketene molecules (2080-2135 cm$^{-1}$). The fits and the resulting time constants are discussed in the Discussion section. Figure reprinted with permission from [1]. © (2010) American Chemical Society.

1500 and 3500 ps delay from -4 to -1 mOD change in absorbance (see Fig. 4.6). Also in the 1717 cm$^{-1}$ transient this behavior is observed but less pronounced (from -1.5 to -1 mOD), indicating that a new absorption signal sets in which is blueshifted relative to the GSB maximum at 1732 cm$^{-1}$. At 1740 cm$^{-1}$ this new absorption leads to a change in sign of the transient absorption signal (from -1.1 to 0.3 mOD between 1500 and 3500 ps), while at 1757 cm$^{-1}$ it can be observed in a mostly isolated fashion (since the absorption changes sign, one can exclude that it stems from a detuning of the pump–probe constellation due to the movement of the delay stage, as already stated above in Sec. 4.2). At this spectral position there is only the weak tail of the ketene formation,
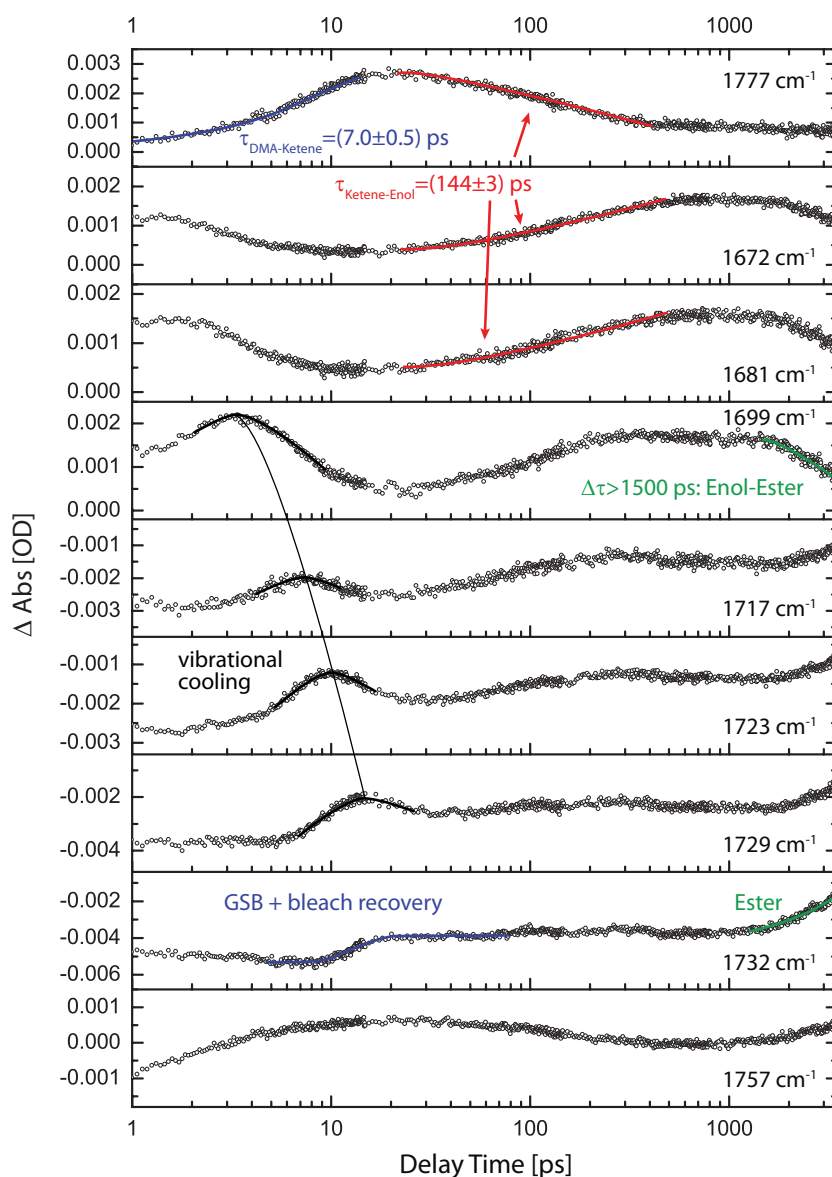
**Figure 4.6:** Characteristic transients from the spectral region between 1670 and 1780 cm$^{-1}$ presenting the temporal evolution of: (1) The GSB of DMA with the following bleach recovery, (2) the vibrational relaxation of excited DMA molecules in the electronic ground state, (3) the formation of the ketene intermediate arising from the absorption of C=O stretching vibrations, (4) its subsequent decrease due to the formation of a consecutive intermediate and (5) again the decrease of the latter because of the emergence of a last measurable and consecutive photoproduct. The coloured curves highlight the exponentially fitted regions of the transient data that provide the characteristic time constants. Note the logarithmic time scale. Figure reprinted with permission from [1]. © (2010) American Chemical Society.

together with a faint contribution of the DMA GSB during the first 3 ps, until from 1500 ps on a constant rise in absorbance occurs (from zero to 0.5 mOD). This transient provides the same temporal development like the one at 1732 cm$^{-1}$ but without the overlapping GSB. These characteristics cannot be found at any other position of the
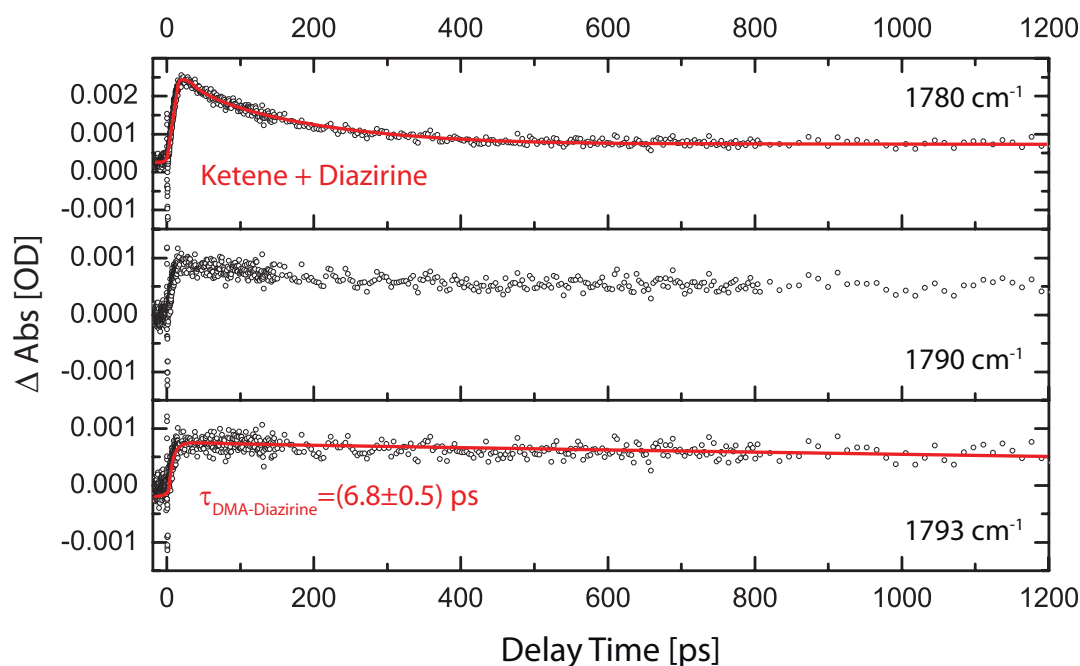
**Figure 4.7:** At the top: Transient of two superposed positive contributions of absorption (at $1786\,\mathrm{cm}^{-1}$) deriving from the ketene formation and another photoproduct. The isolated temporal evolution of the latter is observable at the spectral position around $1793\,\mathrm{cm}^{-1}$. Figure reprinted with permission from [1]. © (2010) American Chemical Society.

recorded time-resolved data.

For short delay times up to 20 ps in the spectral region beginning at $1655\,\mathrm{cm}^{-1}$ and fading into the GSB, one can observe once more a positive absorption that shifts with time towards higher intensities and frequencies, attributed to cooling of vibrationally "hot" DMA molecules in the $S_0$ ground state [135, 155]. To specify, one can precisely observe it in Fig. 4.6 during the first 20 ps in the transients at 1699, 1717, 1723 and $1729\,\mathrm{cm}^{-1}$. Once the vibrational cooling process is completed, the ground state bleach recovery reaches its highest level and remains constant.

Another transient absorption signal can be seen at $1777\,\mathrm{cm}^{-1}$. Since it shows exactly the same temporal behavior after zero delay time like the positive absorption at $2135\,\mathrm{cm}^{-1}$ (concerning both its formation and its decrease), this positive and short-living signal is assigned to the C=O stretching vibration of the arising ketene molecules. This attribution is perfectly confirmed by the DFT data (see Fig. 4.3).

In the spectral domain between 1635 and $1702\,\mathrm{cm}^{-1}$ a broad contribution of positive absorbance occurs. It is composed of five specifiable kinetic traces whose intensity varies between $\Delta\mathrm{OD}$ values of 0.5 and 2.3 mOD. All five traces exhibit an equal temporal behavior: They rise from zero delay time on until they reach a maximum in absorbance after roughly 500 ps. The following plateau declines again for delays beyond 1500 ps and probably tends to zero change of absorption after approximately 4 ns, although the latter cannot be detected due to the limited range of the employed delay stage. Figure 4.6 shows three transients (1672, 1681 and $1699\,\mathrm{cm}^{-1}$) as an example of this
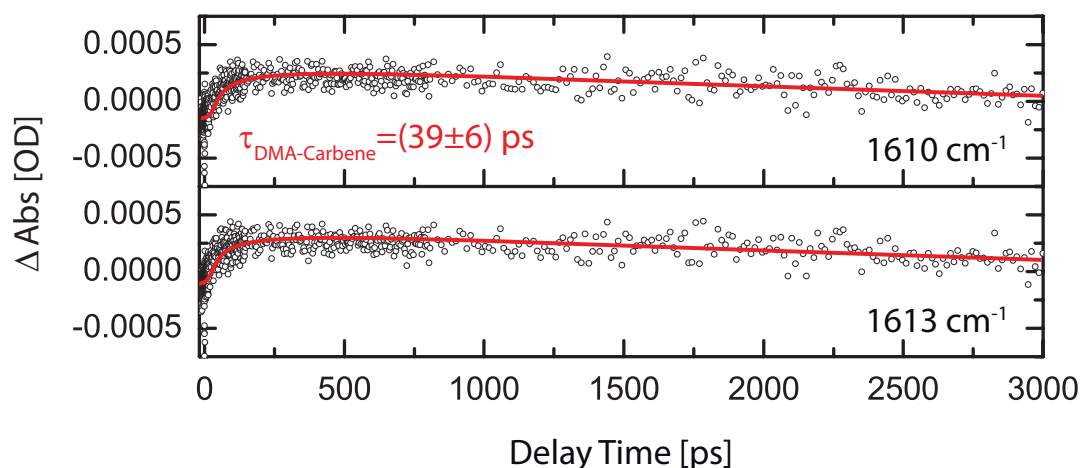
**Figure 4.8:** Transients describing a very weak absorption signal at $1613\,\mathrm{cm}^{-1}$, whose temporal properties do not match any other recorded transient feature. It is therefore likely to constitute an independent signal associated with a molecular species not represented in the other signals. Figure reprinted with permission from [1]. © (2010) American Chemical Society.

temporal progression.

There is an interesting attribute about the transient signal at $1777\,\mathrm{cm}^{-1}$: While the pure ketene absorption observable at $2135\,\mathrm{cm}^{-1}$ fully decreases towards zero mOD within 500 ps (confer Figs. 4.5 and 4.11), this absorption does not. There is another underlying absorption signature which also shows up in an isolated fashion at $1793\,\mathrm{cm}^{-1}$ (see Fig. 4.7). In comparison, their temporal evolution properties differ significantly both for short and long delay time scales.

Finally, at $1613\,\mathrm{cm}^{-1}$ a transient absorption signal was detected whose properties relating to its temporal development differ substantially from any other mentioned transient feature. Concerning the maximal change of absorption values it is the weakest signal of all recorded data with roughly 0.3 mOD. Figure 4.8 gives an overview of the according temporal evolution.

### 4.3.3 Influence of the molecular environment

Based on the fact that DMA dissolved in methanol provides different reaction channels upon photoexcitation (see [148]), some of which include solvent molecules in the reaction dynamics while others do not, the question arises which of the described transient features belongs to what kind of reaction pathway. Therefore, additional time-resolved measurements were carried out with two solvents that exhibit a hydroxyl group as well, ethanol and 2-propanol, providing information on the steric hindrance of the photoreaction due to the molecular environment.

Figure 4.9 summarizes the main implications of the steric hindrance to the temporal evolution of the photoreaction. The results of these experiments are as follows: While the time constant of the ketene decomposition (detectable around $1777\,\mathrm{cm}^{-1}$ and $2135\,\mathrm{cm}^{-1}$) shifts significantly towards longer values with the used solvent, the absorption band at
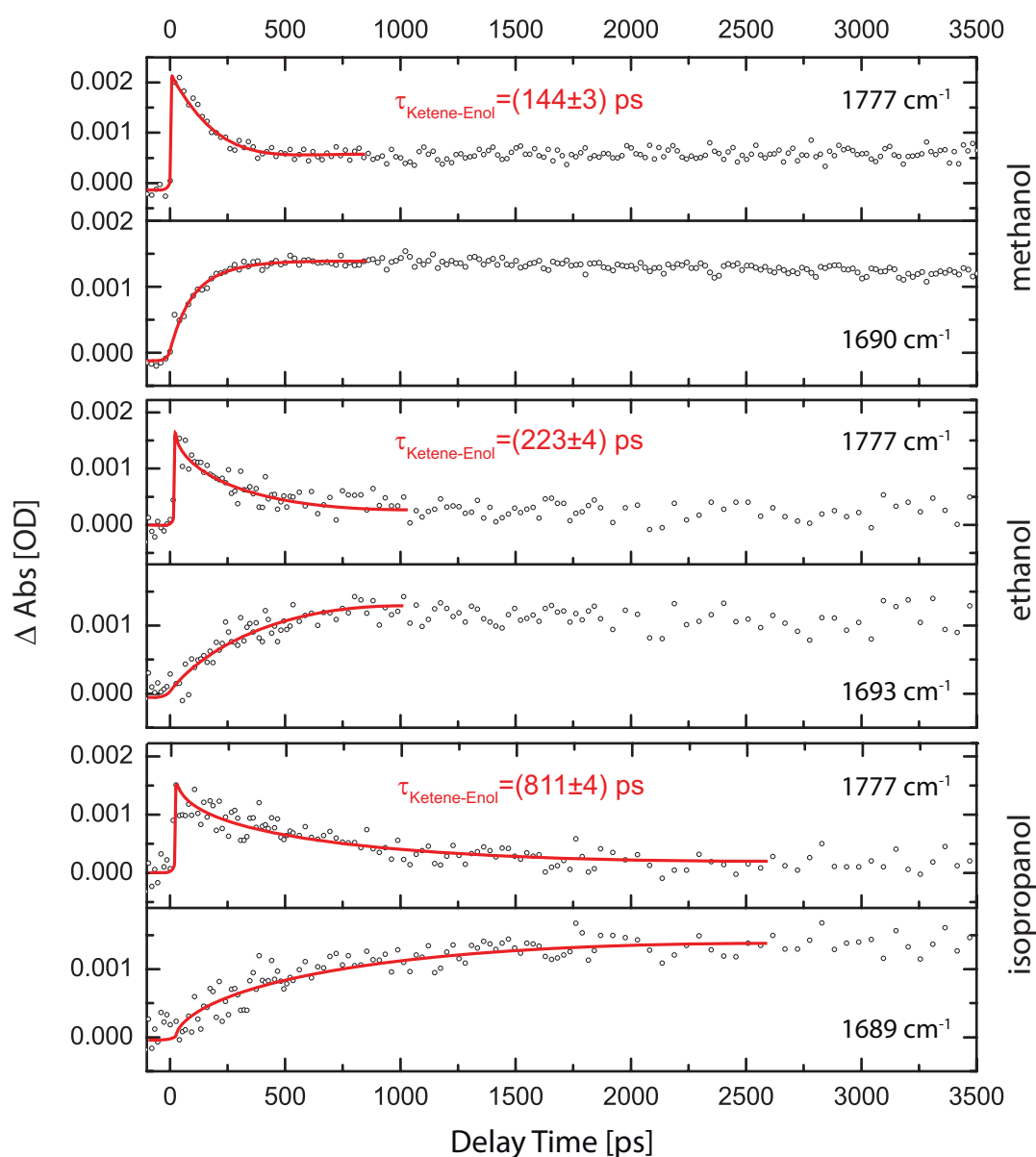
**Figure 4.9:** Representative transients regarding the steric hindrance of the photoreaction due to the molecular environment. Illustrated are transients of the ketene formation with its subsequent decomposition (around $1777\,\mathrm{cm}^{-1}$) in conjunction with transients showing a simultaneous and temporally matching formation of a secondary product (depicted from the spectral region around $1690\,\mathrm{cm}^{-1}$). In each case for methanol, ethanol and isopropanol as solvent one can state a consistent elongation of the time constants describing the photoreaction. Figure reprinted with permission from [1]. © (2010) American Chemical Society.

$1793\,\mathrm{cm}^{-1}$ turns out to be nearly unaffected. Equally, the time constants describing the ketene formation, the GSB and the bleach recovery do not change significantly by means of the molecular environment. In contrast to this, all the positive absorption signals between 1635 and $1702\,\mathrm{cm}^{-1}$ show a temporal elongation, in a simultaneous fashion for each solvent and temporally consistent with the decreasing ketene signatures. The steric

hindrance also has an effect on the rise in absorbance at 1732 and 1757 cm$^{-1}$ observed for delay times longer than 1500 ps in methanol. In the case of 2-propanol, it is retarded in such a way that it putatively sets in after the maximum delay time (i.e. 3.5 ns) and is therefore no longer detectable.

## 4.4 Discussion

Many different chemical species taking part in the investigated partly bimolecular reaction dynamics of DMA dissolved in methanol, ethanol, and 2-propanol, respectively, have to be considered. The DFT calculations already indicate overlapping or at least adjoining bands of absorption. The transient absorption spectra which were measured in two different spectral areas (from 1550 to 1900 cm$^{-1}$ and between 2000 and 2250 cm$^{-1}$, confer Fig. 4.4) depict this circumstance. Figure 4.10 illustrates the discussed results in the spectral region between 1605 and 1805 cm$^{-1}$ by means of plotted cuts along the frequency axis of Fig. 4.4 at certain delay times. Via a sum of exponential fits, which provide time constants for the according molecular dynamics, and which are complemented by additional analysis, steady-state spectra and simulations, the entire set of transient absorption spectra are interpreted with the microscopic picture of the reaction in mind in the following way:

After excitation of the DMA molecule to the $S_5$ and $S_7$ states [140] and internal conversion to the $S_2$ state, nitrogen elimination occurs on a time scale too fast for the setup described in Section 3.1 ($\tau \leq 350$ fs). This step is followed by a reaction involving a singlet carbene intermediate to the ketene. The [1,2]-shift of the alkoxide group seems to be the rate determining step of this unimolecular reaction since no carbene intermediate can be detected. Between 2080 and 2140 cm$^{-1}$, one observes the vibrational cooling of vibrationally excited ketene molecules that reaches its final spectral position within 15 ps. At 2135 cm$^{-1}$, as well as at 1777 cm$^{-1}$, the formation of the ketene intermediate is observable with a time constant $\tau_{\text{DMA}-\text{ketene}} = 7.0 \pm 0.5$ ps (comparable to the transient absorption experiments on other diazocarbonyl compounds carried out by Vleggaar *et al.* [156]), whereas the nascent, vibrationally "hot" ketene molecules are formed within the time resolution of the transient spectrometer, in agreement with the recent studies of DMA in chloroform [140]. Due to this result one can conclude that a concerted reaction clearly occurs, without excluding the appearance of a concurrent carbene formation, which yet supposedly manifests itself in a different spectral region (see below).

The ketene possesses a very electrophilic carbonyl atom in the ketene group, since it is part of a carbonyl group and part of a vinylogous carbonyl group (Michael system). The quasi-unimolecular kinetic of the nucleophilic addition of a methanol molecule to this carbon atom is therefore very fast with a time constant of $\tau_{\text{ketene}-\text{enol}} = 144 \pm 3$ ps. Since it is supposed that the hard oxygen interacts preferably with the harder antibonding $\pi^{\star}$-orbital of the carbonyl group instead of the softer $\pi^{\star}$-orbital of the Michael system, the product of this addition reaction is the enol in Figure 4.12. The bleaching of the reactant (ketene) can be observed at the ketene mode at 2135 cm$^{-1}$ and at its carbonyl mode at 1777 cm$^{-1}$, whereas the product formation (enol) can be followed at 1650-1700 cm$^{-1}$. The transients in Figure 4.6 underline the temporal consistency of this assignment.
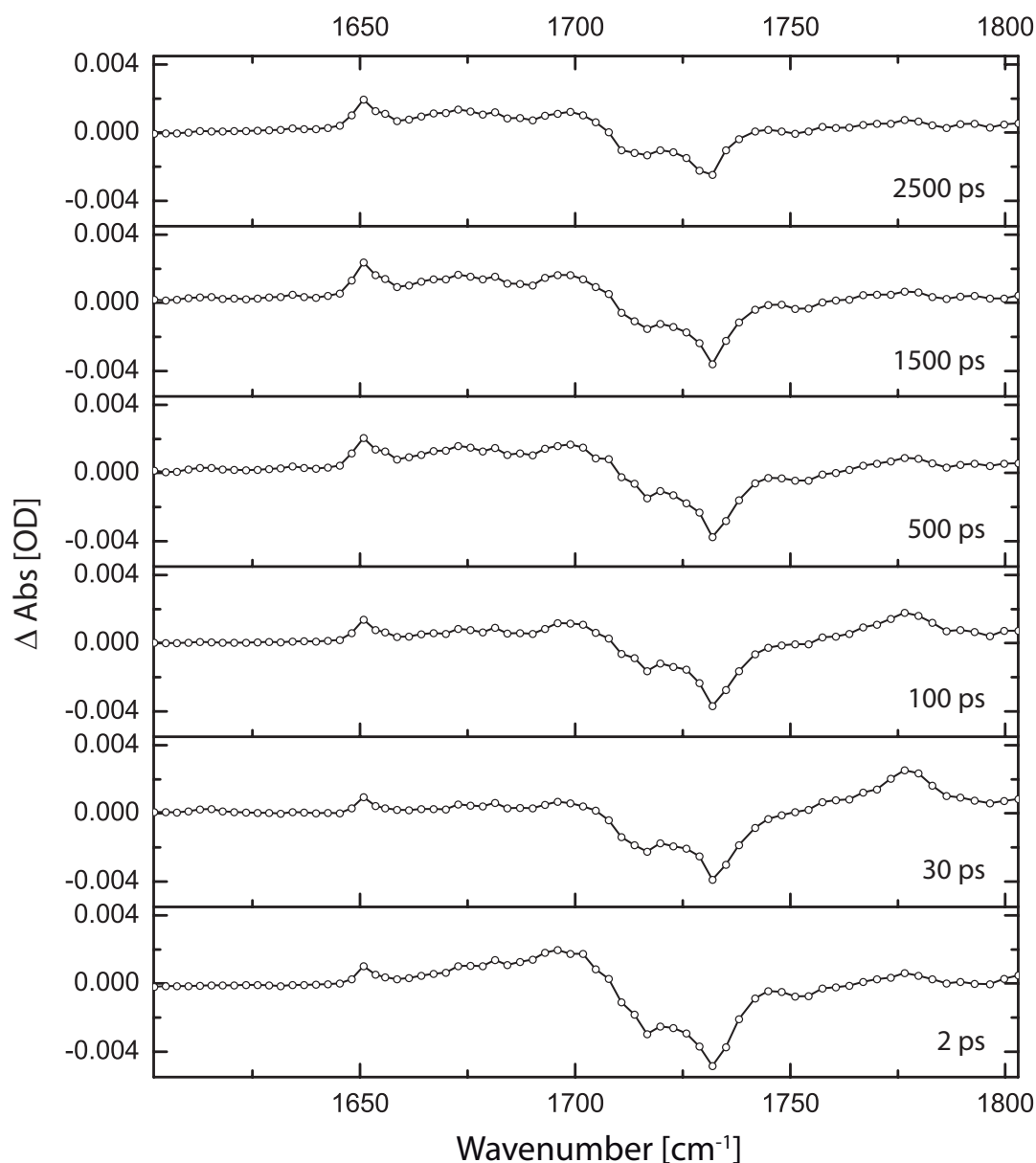
**Figure 4.10:** Transient midinfrared spectra of DMA dissolved in methanol at different delay times between 2 and 2500 ps in the spectral region from 1605 to 1805 cm$^{-1}$ illustrating on the one hand the ground state bleach of DMA. The positive changes of absorption on the other hand are discussed more in detail on the basis of the transients shown in Figs. 4.6, 4.7, and 4.8. Figure reprinted with permission from [1]. © (2010) American Chemical Society.

The Wolff rearrangement finishes with the keto–enol tautomerization, an intramolecular protonation–deprotonation step converting the enol into the ester; which can be seen in the transient absorption data as well. In what follows for larger delays, it appears that the enol contributions decrease significantly after 1500 ps delay time while at the same time a new absorption appears in the region around 1740 cm$^{-1}$. This superposition of the GSB and the rather late emergence of a photoproduct cannot be observed in

**Figure 4.11:** Transient at $2142\,\mathrm{cm}^{-1}$ demonstrating the complete decomposition of the ketene intermediate within 500 ps. Figure reprinted with permission from [1]. © (2010) American Chemical Society.
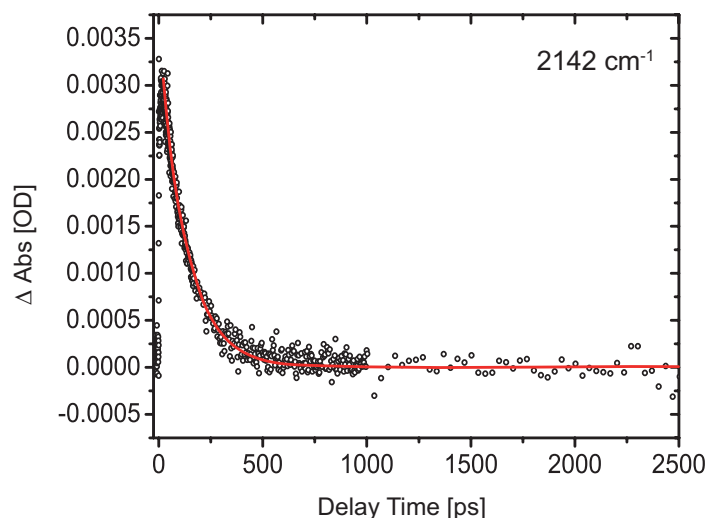
other spectral regions, e.g., around $2170\,\mathrm{cm}^{-1}$ where the isolated DMA GSB is recorded. This transient behavior therefore is assigned to the tautomerization of the enol to the ester, the last link of the reaction channel that is initialized by the Wolff rearrangement. Figure 4.6 summarizes and illustrates this interpretation on the basis of characteristic transients.

The pure ketene absorption around $2135\,\mathrm{cm}^{-1}$ demonstrates that all contributions of the ketene vanish within the first 500 ps (confer Fig. 4.11) and consequently the change of absorption drops back to zero mOD. The transient at $1777\,\mathrm{cm}^{-1}$ does not reproduce this result. From zero delay time on the ketene absorption is superposed by a positive absorption that nearly remains constant along the whole time axis. This contribution is assigned to the formation of diazirine, which is practically stable on the time scale monitored here [150]. It emerges isolated at $1793\,\mathrm{cm}^{-1}$ with a time constant $\tau_{\mathrm{diazirine}} = 6.8 \pm 0.5$ ps (see Fig. 4.7). The DFT calculations predict an overlapping absorption of the ketene and the diazirine in good spectral agreement with the transient data.

Bogdanova *et al.* [148] state that the outcome of the photolysis of DMA is wavelength dependent in such a way that 355 nm irradiation should emphasize the formation of diazirine, as well as of Meldrum's acid, although the corresponding quantum efficiency stays quite low. Accordingly, Wolff rearrangement and isomerization derive from two different electronically excited states (Zhang *et al.* [157] mention a minor photoinduced process leading para-methoxy-3-phenyl-3-methyl diazirine directly from the $S_2$ state to the corresponding diazo compound. Even if a similar process is assumed to take place inversely, there is no evidence in the data supporting this molecular behavior). The FTIR experiments (confer Fig. 4.2) agree with this statement: The medium pressure UV radiator produced mainly ester molecules and minor contributions of diazirine (due to the continuous radiation spectra). The referring FTIR data show new strong absorption bands at $1766\,\mathrm{cm}^{-1}$ and $1808\,\mathrm{cm}^{-1}$ (ester assignment) and a weak one at $1796\,\mathrm{cm}^{-1}$. The Nd:YAG laser should preferentially produce diazirine and suppress the ester formation. Consistently, the FTIR data does not show new absorption bands around 1740 and

$1760\,\mathrm{cm}^{-1}$ but again at $1796\,\mathrm{cm}^{-1}$. Meldrum's acid could also be produced in at most minor quantities, which is confirmed by Figure 4.2, where no pronounced peaks at its two absorption maxima (at $1753\,\mathrm{cm}^{-1}$ and $1785\,\mathrm{cm}^{-1}$) [158, 159]) are observable. Additionally, the FTIR measurements denote an absorption band around $1710\,\mathrm{cm}^{-1}$ that consequently derives from the lower electronically excited state too. However, since the quantum efficiency for this pathway is obviously quite low, it seems hardly feasible to separate this contribution from the strong positive enol absorption and the nearby lying similarly strong negative DMA GSB in the time-resolved data. Not only is Meldrum's acid formation expected to be marginal, diazirine also better fits into the assignment of the steady-state and transient data when taking the overall upshift in frequency of the DFT calculations into account. Moreover, the similar rise time of the transients at $1777\,\mathrm{cm}^{-1}$ and $1793\,\mathrm{cm}^{-1}$ underlines this identification since diazirine formation should occur on a similar timescale to that of ketene formation. The formation of Meldrum's acid would take longer, regardless of whether Meldrum's acid is a reaction product of a triplet carbene or of a singlet carbene species that interacts with solvent molecules by inserting an OH-group and subsequently undergoing the Norrish type II phototransformation [150]. Hence, the identification of photoproducts in the transient and the FTIR data is in good agreement.

The experiments investigating the influence of the solvent on the photoreaction support the described connections between transient absorption data and designated reaction channels: the upshift of time constants due to the growing molecular size of the solvent significantly affects reaction pathways where the solvent is involved, namely, the proceeding of the ketene to the enol, whereby the ester formation consequently gets retarded as well (confer Fig. 4.9). Molecular processes that do not interact directly with the solvent molecules such as the DMA GSB around 1740 and $2170\,\mathrm{cm}^{-1}$, the ketene composition, the vibrational cooling of the ketene (around $2110\,\mathrm{cm}^{-1}$) and the DMA (around $1700\,\mathrm{cm}^{-1}$), or the absorption that is assigned to the diazirine formation remain virtually unaffected by the steric hindrance. These are first-step processes directly after the DMA excitation.

At $1613\,\mathrm{cm}^{-1}$ the weakest positive change of absorption occurs within $\tau = 39 \pm 6\,\mathrm{ps}$ and decays almost completely within $3\,\mathrm{ns}$ (see Fig. 4.8). Possible intermediate precursors have a decay time of $39\,\mathrm{ps}$ or maybe even much shorter, with vibrational cooling and conformational changes possibly being responsible for the $39\,\mathrm{ps}$ rise of the observed species. These characteristics do not fit in with any other recorded and analyzed reaction channel (i.e., the Wolff rearrangement reaction with its subsequent photoproducts and the diazirine isomerization). Hence, it is possibly a signature of a triplet carbene to form Meldrum's acid. Although the specific molecular absorption cross-sections are not taken into accunt, the very low signal intensity points at a low quantum efficiency for this reaction channel which might indicate this cautious assignment, for which the excited system has to undergo an internal conversion and a subsequent intersystem crossing to enter this reaction pathway. Another assignment might be the 5-methoxy Meldrum's acid-ylide [160]. The results from the DFT calculations, depicted in Fig. 4.3, are in line with both assignments. On the one hand, the calculated vibrational modes (1648 and $1662\,\mathrm{cm}^{-1}$) are closer to $1613\,\mathrm{cm}^{-1}$ than any other mode of all the possible reaction intermediates and products, with the deviation actually being not too far if

one takes into account the general trend that the vibrational frequencies are numerically overestimated. On the other hand, only small quantities of both species (triplet carbene and 5-methoxy Meldrum's acid-ylide) can be expected, but since the corresponding modes are in addition the strongest ones of all modes in Figure 4.3, an observation is not unlikely.

Following this hypothesis, the composition and decomposition of the singlet carbene should be completely carried out within 39 ps, although there is no direct evidence for it in our transient data. Other groups describing the temporal evolution of various carbene species under the very crucial impact of different solvents state lifetimes of similar magnitude [160–162]. More precisely, the singlet carbene of methyl styryldiazoacetate dissolved in methanol decays within 38 ps, while the triplet state persists on a timescale of some nanoseconds [162]. Other investigations with further chemical compounds such as p-biphenyl diazo species discovered upper lifetimes of the singlet carbene in the range of 700 ps [133]. However, Burdzinski *et al.* measured the lifetime of singlet carbene to be 2.3 ps (with DMA dissolved in chloroform). That the observed signal originates from contaminations in the solvent (e.g., of water dissolved in methanol which has an absorption band in this spectral region [163]) can be ruled out, because there is no signal observable if only methanol is used. Considering these facts, an assignment of this transient to the triplet carbene or 5-methoxy Meldrum's acid-ylide is likely but without having detected the previous singlet species or an evidence for the subsequently formed Meldrum's acid/5-methoxy Meldrum's acid. An assignment to the singlet carbene does not seem reasonable due to the slow 39 ps rise time.

The low quantum yield of the discussed transient in combination with the fact that there is neither a hint for a subsequent reaction channel in the transient data nor some indirect evidence in the transients describing the ketene dynamics makes a definite assignment of a molecular process corresponding to this spectral signature impossible. Hence, there is no evidence for a contribution of a stepwise Wolff rearrangement via a carbene intermediate in the transient data.

In the long term, the absorption at $1613 \, \mathrm{cm}^{-1}$ decreases monotonously with a time constant well beyond the maximum observation window. Likewise, the transients describing the diazirine development do. This can be explained by a reisomerization of the diazirine to DMA. Unfortunately, due to the weakness of the according signals and the long decay time, this reisomerization of DMA could not be inferred from the GSB.

While the bimolecular reaction of the ketene intermediate has been disclosed on an ultrafast time scale, the fate of the carbene intermediate has to be further explored in future experiments to allow for an unequivocal assignment.

## 4.5 Conclusions

Upon photoexcitation with 266 nm pump pulses, DMA is excited to a set of highly excited states (preferentially to the $S_7$ and $S_5$ states) [140]. Within less than 100 fs the relaxation to the dissociative $S_2$ state takes place, from which the ketene formation following the Wolff rearrangement is initiated. Figure 4.12 gives an overview of the dis-
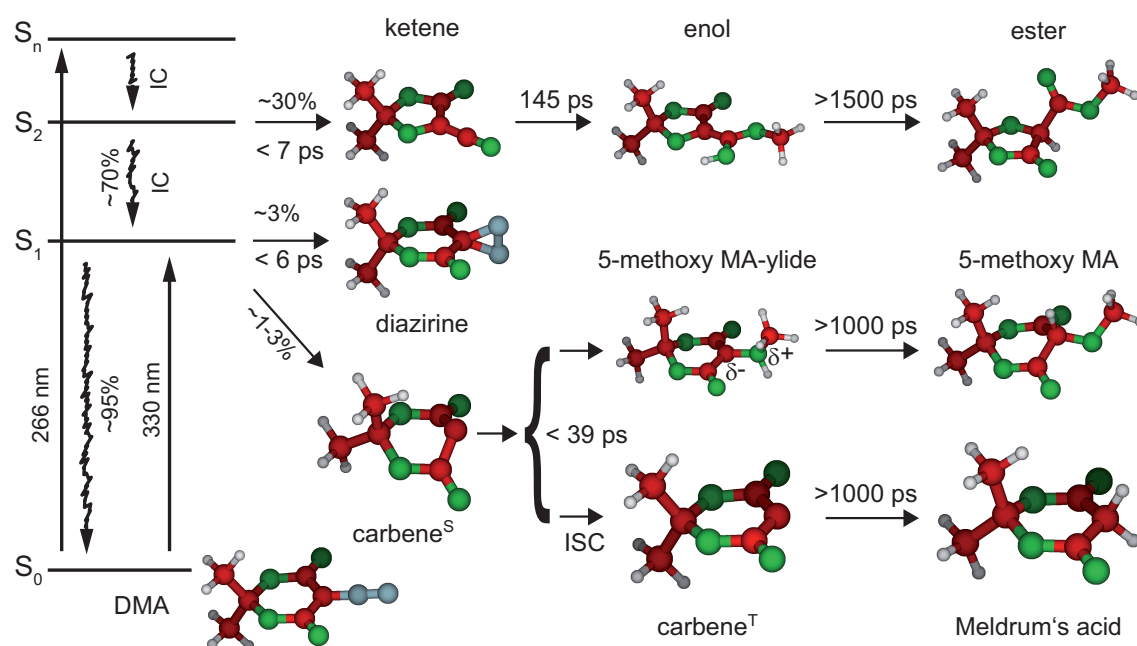
**Figure 4.12:** Schematic illustration of the detected reaction processes of DMA in methanol upon UV photoexcitation combined with the according experimentally investigated time constants. IC stands for internal conversion and ISC for intersystem crossing. The brace indicates two possible reaction pathways, both of which, according to the theoretical results, might explain the observed dynamics. Figure adapted with permission from [1]. © (2010) American Chemical Society.

cussed experimental observations. Whereas the formation of diazirine and ketene occurs almost instantaneously after DMA excitation and also ultrafast geminate recombination after $N_2$ cleavage cannot be excluded, the time constants given in Figure 4.12 represent how long it takes until these species are observable in the experiment. Vibrationally excited ketene molecules are formed via a very fast concerted mechanism. The according quantum efficiency amounts to 30 % and therefore represents the highest developed reaction channel in these experiments. Subsequently, enol is formed by nucleophilic addition of the solvent (methanol, ethanol or 2-propanol) to the ketene. Due to steric hindrance the temporal evolution of this process is strongly coupled to the involved solvent. After 1500 ps, the corresponding absorption bands begin to decrease while in the region of the DMA ground state bleach ($1740 \, \text{cm}^{-1}$) a positive change of absorption begins to evolve (in comparison, the isolated DMA GSB that can be seen at $2172 \, \text{cm}^{-1}$ remains constant along the complete time axis). Under considerations of the temporal consistency and supporting analytical methods (i.e., DFT calculations and FTIR spectroscopy), this positive change of absorption is assigned to the ester. The ester represents the final step of the reaction channel that is initialized by the Wolff rearrangement.

In the course of the second possible reaction pathway, DMA relaxes to the first electronically excited state and isomerizes to form diazirine. This process appears in the transient spectra at 1777 and $1793 \, \text{cm}^{-1}$. It is not affected by the solvent, which seems plausible since there is no solvent molecule involved in the isomerization process. Com-

pared to the ketene formation, it exhibits a different temporal behavior concerning both the formation itself and the persistence on nanosecond time scales. A small absorption decrease can be explained by the reisomerization of the diazirine back to the DMA.

The transient data also reveal the existence of a weak spectrotemporal signature at $1613\,cm^{-1}$ whose temporal properties differ from those of all other reaction channels and their absorption characteristics. Therefore, it is likely that it is associated with a further intermediate molecular species from the accessible reaction sequence, supposedly a triplet carbene involved in the reaction pathway towards the formation of Meldrum's acid or a 5-methoxy Meldrum's acid-ylide, deriving from the singlet carbene as well, which might evolve to form 5-methoxy Meldrum's acid.

# 5 Ultrafast photochemistry of a manganese-tricarbonyl CORM

## 5.1 Introduction

The current chapter presents the results from ultrafast UV-pump–MIR-probe transient absorption measurements on the manganese-tricarbonyl complex $[Mn(CO)_3(tpm)]Cl$ (tpm = tris(2-pyrazolyl)methane) dissolved in heavy water, which releases on average two [164] or even all three [165] carbon monoxide (CO) ligands upon UV irradiation and accordingly belongs to the class of the so-called PhotoCORMs. It has been shown to be tissue-selective and cytotoxic against cancer cells [164].

In general, additionally to nitric oxide (NO) and hydrogen sulfide ($H_2S$), CO has been identified as the third gasotransmitter in higher organisms, including humans, which is endogenously generated from heme by the activity of heme oxygenase enzymes and is widely studied for its signaling function and cytoprotective activity. For the exploitation of the latter for therapeutic applications in medicine, CO-releasing molecules are investigated as a safe-to-handle in situ source of carbon monoxide [166–171]. To serve as a CO prodrug, CORMs have to be stable in air and water, be soluble in physiological buffer, and specifically accumulate in the targeted tissue. Various trigger mechanisms are studied to initiate the CO release in a controlled fashion, including ligand exchange reactions in solution [172, 173], enzyme activation (ET-CORMs) [174], and photoactivation in the PhotoCORMs [175–177]. Especially the latter would allow for a dark-stable CORM prodrug to distribute in the body only to be activated in a spatially and temporally precisely controlled way by application of a focused light pulse. While the general CO release and biological activity profiles of a significant number of PhotoCORMs have been explored in detail, virtually nothing is known to date about the primary photophysical and photochemical steps involved in the carbon monoxide release from the metal coordination sphere. In particular, although many CORMs can release almost all of the carbonyl ligands bound to the metal, in most cases it remains unknown whether this actually occurs in a stepwise or concerted fashion. It is also unknown, whether each CO release is triggered by photons or whether oxidization of the central atom plays a role as well.

In the last decades, the ultrafast dynamics of CO release in metal carbonyls has been investigated for many compounds and under various conditions. Probably the substance studied in most detail is iron pentacarbonyl $Fe(CO)_5$, whose photodissociation has been observed in the gas phase via transient ionization with different laser wavelengths [178–180] or by transient electron diffraction [181], and in solution with infrared [182–185] or X-ray [186, 187] transient absorption. These studies corroborate the great interest in

the initial steps of CO photolysis from metal carbonyls and underline the multifaceted reaction pathways that may occur: in the gas phase, depending on the excitation wavelength used, several to all CO ligands can be liberated, and even quantum control of the photochemistry of $Fe(CO)_5$ was demonstrated [188, 189]; in the liquid phase usually one but in some solvents also two of the CO ligands are released on an ultrafast timescale after absorption of one UV photon [183–185]. Among other substances studied in solution are, for instance, metal carbonyls with only CO ligands [190–193] (even with two [194–196] or three [197] bonded metal atoms), but also complexes with, for example, cyclopentadienyl [198–200] and more complex organic ligands [201] which may even perform photochelation upon CO dissociation [202, 203].

Although the variety of ultrafast studies on metal carbonyls in solution is vast, aqueous environments have been omitted so far for metal carbonyls (in contrast to CO release from heme proteins pioneered by Anfinrud and coworkers [204, 205] in water). Very recently, the Kubarych group [56, 206, 207] has investigated the CO vibrations of metal carbonyl complexes in water with femtosecond MIR pulses. Yet, the ultrafast dynamics of CO photolysis from a metal carbonyl in the biologically most relevant solvent water have not been reported in the literature, despite the high significance with regard to the CO release from PhotoCORMs in envisaged biological applications.

The work presented in the following comprises time-resolved absorption measurements with excitation pulses at two different central wavelengths on the one hand, and the utilization of a further UV pump pulse that might repump the photoproducts after the initial pump event on the other hand. The experiment is complemented by linear absorption spectroscopy both in the UV and in the MIR in combination with DFT and time-dependent DFT (TDDFT) calculations. It is the result of a cooperation with the group of Ulrich Schatzschneider from the chemistry department at the university of Würzburg. The synthesis of the molecule under investigation as well as the TDDFT calculations have been performed in his group. In parts, the following sections have been published in [2, 3].

## 5.2 Materials and methods

The employed femtosecond transient absorption setup is described in Section 3.2. Pump pulses were generated at either 264 nm or 347 nm with pulse durations of approximately 50 fs and pulse energies of 1–2 μJ in front of the sample. The MIR probe pulses were tuned between 1800 and 2100 cm$^{-1}$ and subsequently detected via the grating 2 inside the IR spectrometer. The time resolution of the transient spectrometer is 300 fs.

Steady-state UV absorption spectra were recorded with a spectrometer (V-670, JASCO) in a cuvette with two 4 mm $CaF_2$ windows and a sample thickness of 100 μm. The same cuvette was also used for the time-resolved studies with sample concentrations of 3–5 mM. The steady-state FTIR spectra were recorded in a JASCO FT/IR-4100 spectrometer.

The CORM was synthesized according to the procedure as described in [208]. The experiments have been performed with the CORM dissolved in heavy water, since the

absorption of MIR probe light in the 1800–2100 cm$^{-1}$ spectral region is much lower for D$_2$O than for H$_2$O [209]. The UV absorption in the solvent is negligible for wavelengths above 200 nm [210].

DFT calculations for determination of the wavenumbers of the vibrational modes in aqueous environment were carried out as described in Section 2.4.2, using the density functional Becke three-parameter hybrid method in combination with the Lee-Yang-Parr correlation functional (B3LYP) and the 6-311+G** basis set. The aqueous surrounding was included by a polarizable continuum model (PCM) in the self-consistent reaction field (SCRF).

TDDFT calculations for exploring the electronic levels involved in the excitations were performed with ORCA 2.6 on a Linux cluster using TZV(P) or better basis sets on Mn, N, and O, and a VDZ basis set on all other atoms with the `Grid4` and `TightSCF` options [211, 212]. The first 30 singlet excited states were calculated in the gas phase.

## 5.3 Results

### 5.3.1 Steady-state spectra and DFT calculations

The CO-releasing molecule under investigation is depicted in Figure 5.1a together with its spatial structure resulting from the DFT geometry optimization. The steady-state ultraviolet absorption spectrum of the compound is shown in Figure 5.1b. Two distinct absorption bands are found at 265 nm and 348 nm, together with a strong absorption extending into the far UV. Both underlying transitions will be identified in the TDDFT calculations and the influence on the photochemical CO release for excitation into the two bands will be explored. Hence, experiments either with pump pulses at a central wavelength of 264 nm or 347 nm, respectively (see pump pulse spectra in Figure 5.1b), are carried out.

The infrared absorption of the CO vibrations of the CORM in D$_2$O is displayed in Figure 5.1c. The bands at 2051 and 1958 cm$^{-1}$ correspond to the symmetric and the antisymmetric C≡O stretching vibration, respectively. The later is degenerate due to the C$_{3v}$ symmetry of the molecule.

TDDFT calculations have been performed for the [Mn(CO)$_3$(tpm)]$^+$ cation in the gas phase, the results are displayed in Figure 5.2. The three highest occupied molecular orbitals (HOMOs), which are almost degenerate, show a high electron density at the manganese atom and exhibit mostly Mn 3d character, with small contributions from metal–carbon bonding. Additionally, TDDFT calculations of the first 30 singlet excited states are computed, which identifies the major transitions that can be induced with the pump pulse spectra of Figure 5.1b.

The three HOMOs are mostly centered on the manganese atom and are constituted by the three doubly occupied Mn d orbitals, as expected for a low-spin 3d$^6$ system. The electron density of the accessible lowest unoccupied molecular orbitals (LUMOs) is either located on the tpm ligand (LUMO and LUMO+1) or delocalized over all three CO ligands (LUMO+2 to LUMO+5). Whereas the former might indicate that excitation
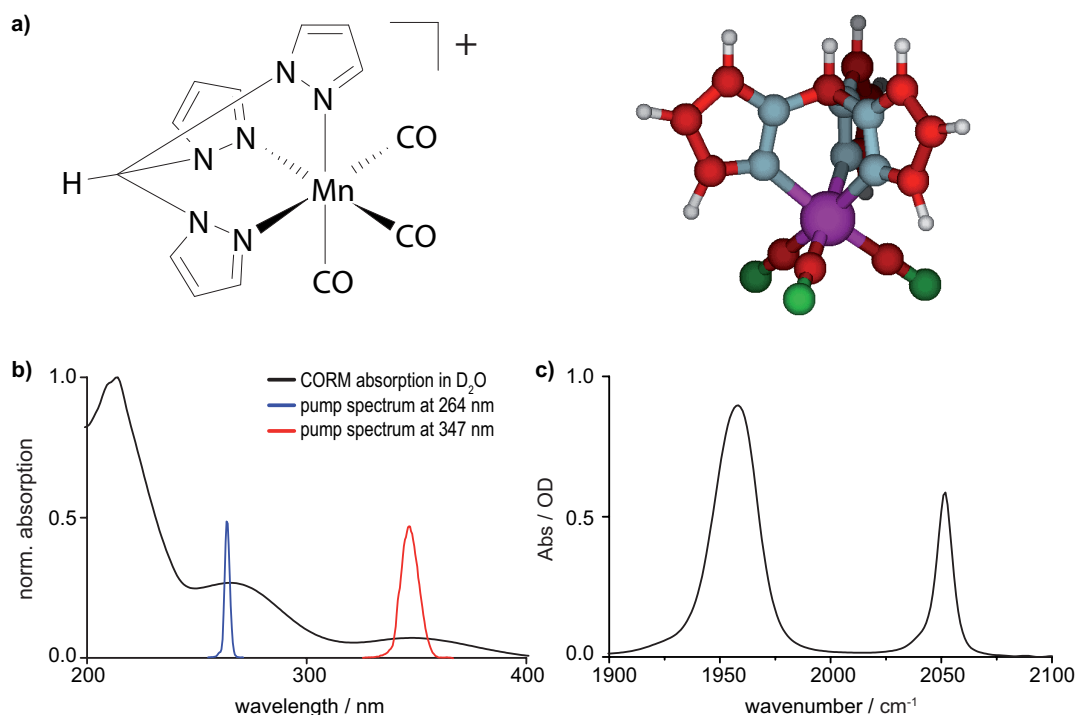
**Figure 5.1:** (a) The studied CO-releasing molecule (manganese-tricarbonyl complex $[Mn(CO)_3(tpm)]Cl$ (tpm = tris(2-pyrazolyl)methane)) together with the structure resulting from the DFT geometry optimization. (b) Its absorption spectrum (black) in $D_2O$ solution, together with the spectrum of the pump pulse, which is either centered at 264 nm (blue) or 347 nm (red), respectively. (c) Infrared absorption spectrum of the CORM dissolved in $D_2O$ in the spectral region of the CO vibrations. Figure adapted with permission from [2]. © (2013) American Chemical Society.

will not lead to CO photolysis, the latter might imply the contrary, namely, that several CO ligands could be released as the excess energy introduced by a 264 nm photon could be sufficient for such a process [199]. For the two LUMOs (LUMO+2 and LUMO+3) reached upon 347 nm excitation, a high electron density is located around the metal atom and one or two of the CO ligands. The associated antibonding character indicates that CO will be photochemically dissociated by 347 nm excitation.

The TDDFT results for the CORM can be compared to the band assignments of well-studied manganese tricarbonyls for which the photochemical behavior is known. For $CpMn(CO)_3$ compounds (Cp=cyclopentadienyl derivatives of the form $C_5H_4Y$, the simplest being $C_5H_5$) in alkane solution, a UV absorption band in the region around 325–350 nm is observed which was assigned to a Mn $\rightarrow$ Cp charge-transfer (CT) transition, also comprising some Mn $\rightarrow$ CO CT character. A further UV band around 250 nm is assigned to an intraligand $\pi \rightarrow \pi^*$ transition in the arene ring [213]. A quantum yield of 1, with no dependence on the UV wavelength, has been found for the release of one CO ligand from $CpMn(CO)_3$ in various organic solvents [214], in the nonpolar solvent isooctane it is 0.65 [215]. As a remarkable aspect, it is reported for several solvents
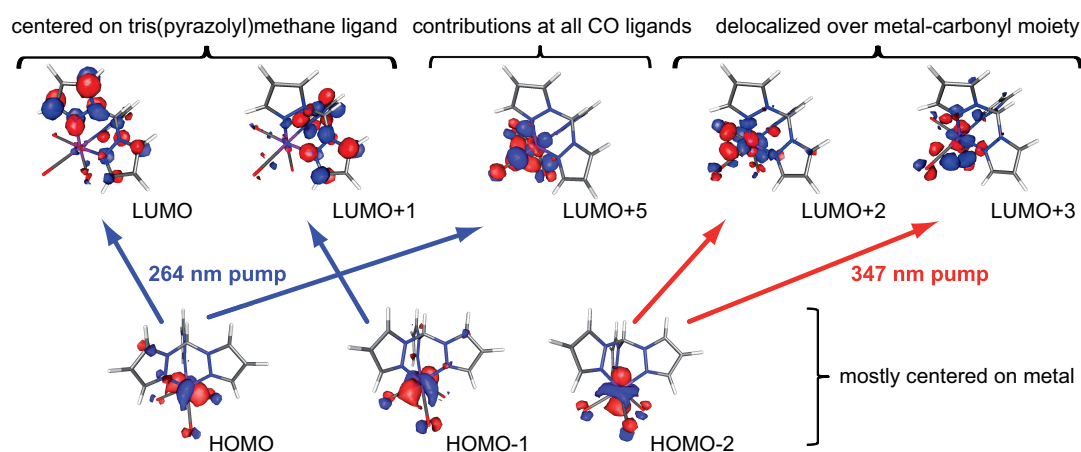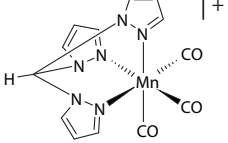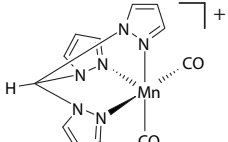
**Figure 5.2:** TDDFT calculations for the dominating electronic transitions induced with the employed pump pulses at 264 nm or 347 nm, respectively. Whereas the three involved HOMOs exhibit an electron density mostly located at the manganese atom, the character of the accessible LUMOs varies strongly. Calculations performed by Ulrich Schatzschneider from the chemistry department at the university of Würzburg. Figure reprinted with permission from [2]. © (2013) American Chemical Society.
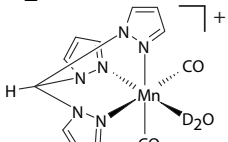
that irradiation of the dicarbonyl leads to further photochemical CO release [216]. This motivates the experiments with two successive pulses, pump and repump, to check if this is also possible for the CORM in aqueous solution investigated in this study.
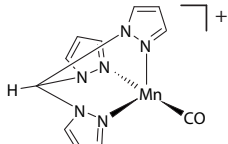
Upon UV excitation, several product molecules could be formed, ranging from an unaltered CORM through mono- and dicarbonyl species with additional solvent molecules as ligands to a carbene isomer of the CORM. DFT calculations provide the wavenumbers of the CO vibrations in a variety of putative photoproducts in aqueous solution. The results are rescaled with the optimal factor according to the employed functional and basis set from [217] and summarized in Figure 5.3. For the intact CORM, where a FTIR spectrum is available for comparative purposes, one can state that simulation and experiment are in good agreement. It is apparent that photoproducts with one or two released CO ligands should be observable by an absorption band on the low-energy side of the CORM's CO stretch spectrum displayed in Figure 5.1c. Higher spin multiplicity states are omitted in the following discussion, since they are clearly higher in energy (up to 1.8 eV between the singlet and the quintet state of the intact CORM, e.g.).
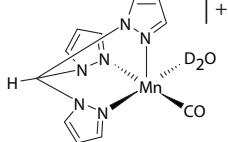
Another possibility that might occur after UV excitation is the cleavage of a Mn-N bond. In case it does not directly reform, a carbene isomer with a Mn–C bond could be formed. Compared to the N-coordinated pyrazole, a carbene isomer photoproduct is calculated (bottom row of Fig. 5.3) to show both the symmetrical and antisymmetrical C≡O stretching vibrations at much lower wavenumbers (1978 vs. 2036 cm$^{-1}$ and 1915/1920 vs. 1943 cm$^{-1}$). But probably more importantly, the significantly reduced difference between the positions of the two sets of C≡O bands (only 63 cm$^{-1}$ in the carbene isomer vs. 93 cm$^{-1}$ for the pyrazole binding mode) in conjunction with the rather low IR intensities, argue against the formation of such a species.
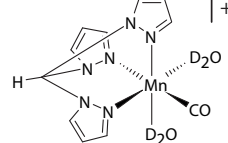
**intact CORM**

| FTIR / cm$^{-1}$ | DFT / cm$^{-1}$ | | assignment | rel. IR intens. |
| | singlet | quintet | | |
|---|---|---|---|---|
| 1958 | 1943 | 1871 | $\tilde{\nu}_{asym}$ (CO) | 1/1.07 |
| 1958 | 1943 | 1980 | | 1/0.44 |
| 2051 | 2036 | 2094 | $\tilde{\nu}_{sym}$ (CO) | 0.37/0.24 |

**dicarbonyl**

| DFT / cm$^{-1}$ | | | assignment | rel. IR intens. |
| singlet | triplet | quintet | | |
|---|---|---|---|---|
| 1885 | 1840 | 1861 | $\tilde{\nu}_{asym}$ (CO) | 0.64/0.66/1.03 |
| 1975 | 1987 | 2022 | $\tilde{\nu}_{sym}$ (CO) | 0.49/0.50/0.31 |

**dicarbonyl with D$_2$O ligand**

| DFT / cm$^{-1}$ | | | assignment | rel. IR intens. |
| singlet | triplet | quintet | | |
|---|---|---|---|---|
| 1864 | 1779 | 1842 | $\tilde{\nu}_{asym}$ (CO) | 0.64/0.84/1.18 |
| 1955 | 1970 | 2016 | $\tilde{\nu}_{sym}$ (CO) | 0.49/0.46/0.27 |

**monocarbonyl**

| DFT / cm$^{-1}$ singlet | assignment | rel. IR intens. |
|---|---|---|
| 1875 | $\tilde{\nu}$ (CO) | 0.54 |

**monocarbonyl with one D$_2$O ligand**

| DFT / cm$^{-1}$ singlet | assignment | rel. IR intens. |
|---|---|---|
| 1833 | $\tilde{\nu}$ (CO) | 0.73 |

**monocarbonyl with two D$_2$O ligands**

| DFT / cm$^{-1}$ singlet | assignment | rel. IR intens. |
|---|---|---|
| 1821 | $\tilde{\nu}$ (CO) | 0.76 |

**carbene isomer of the CORM**

| DFT / cm$^{-1}$ singlet | assignment | rel. IR intens. |
|---|---|---|
| 1915 | $\tilde{\nu}_{asym}$ (CO) | 0.44 |
| 1920 | | 0.44 |
| 1978 | $\tilde{\nu}_{sym}$ (CO) | 0.22 |

**Figure 5.3:** Spectral position of CO vibrations as obtained from DFT calculations for various possible photoproducts in aqueous environment, rescaled with the optimal factor from [217]. The amplitudes of the modes are given in the right-hand column, normalized to the strongest mode of the intact CORM. Figure adapted with permission from [2]. © (2013) American Chemical Society.
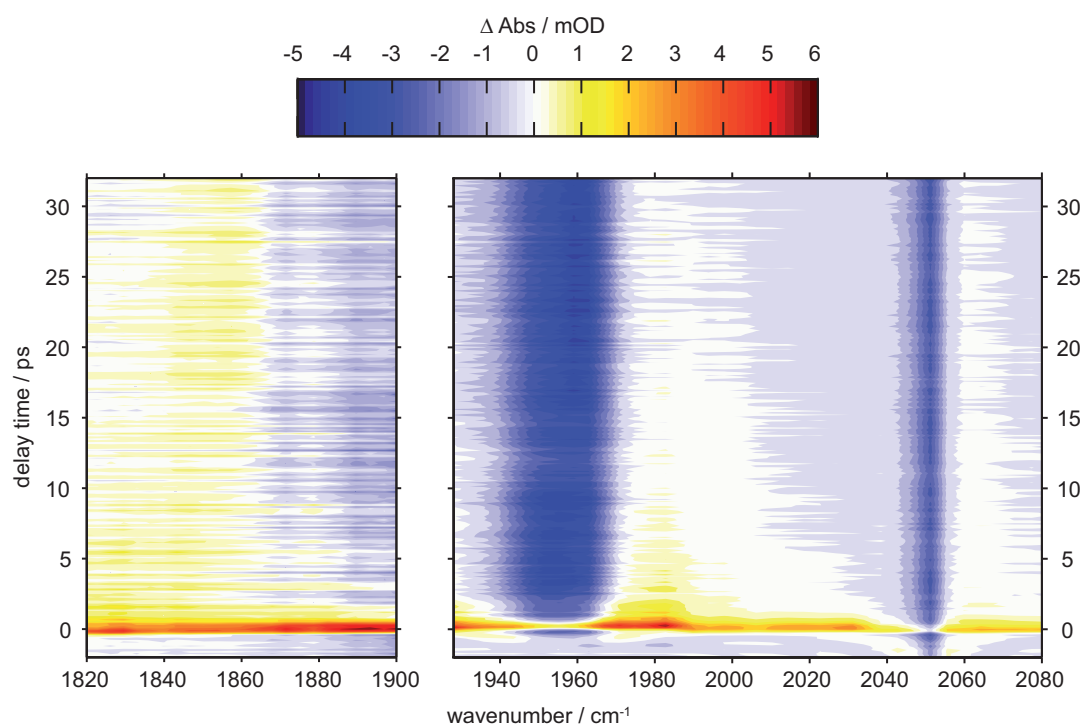
**Figure 5.4:** Transient absorption of the CORM, recorded with 264 nm pump and MIR probe pulses. Figure reprinted with permission from [2]. © (2013) American Chemical Society.

## 5.3.2  Transient MIR spectroscopy with two pump wavelengths

The dynamics following photolysis are monitored by femtosecond transient absorption. Figure 5.4 shows the MIR transient absorption signal recorded with 264 nm pump pulses; Figure 5.5 the one deriving from an excitation with 347 nm pulses. Note the differing temporal axes. The signal at negative pump-probe delay times is due to the PFID and will not be discussed any further. For short positive delay times, a strong absorption is observed at all probe wavenumbers that vanishes within the first few picoseconds. This contribution is not due to the CORM but instead obscures the very early dynamics of the compound. It matches the absorption of solvated electrons in $D_2O$ solution which can be generated at this pump wavelength [218] and was observed in transient measurements on the pure solvent as well. Furthermore, a pump-induced transmission change in the $CaF_2$ windows might add to this strong absorption at early delay times [198]. Within these first few picoseconds, solvation of a photoproduct will occur and hence free coordination sites due to released CO ligands are filled by $D_2O$ molecules on this timescale.

As can be seen from a comparison between Figure 5.4 and 5.5, the dynamics of the CO release after 347 nm excitation is very similar to the behavior with 264 nm pulses. The important features of these dynamics will be discussed by means of absorption changes at exemplary wavenumbers. For positive delay times, the MIR transient absorption exhibits two distinct ground-state bleach signals at 1958 and 2051 cm$^{-1}$ (blue in Figures 5.4 and 5.5), which agree with the band positions of the FTIR measurements (confer Fig. 5.1c). These bleach signals persist for delay times up to several nanoseconds
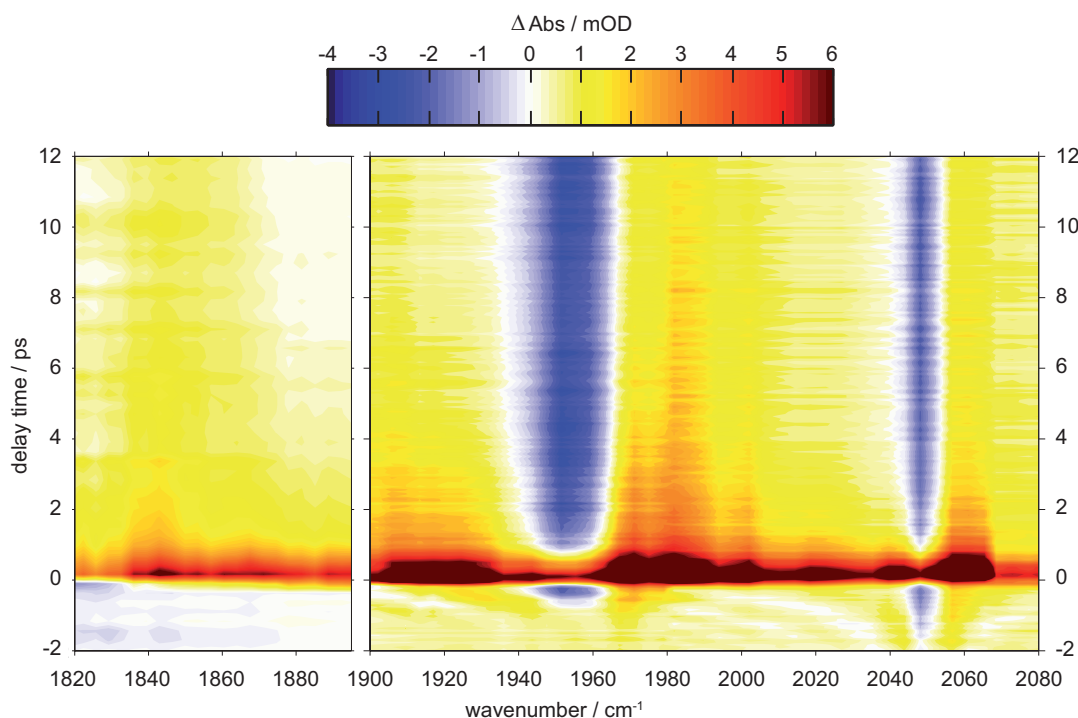
**Figure 5.5:** Transient absorption of the CORM, recorded with 347 nm pump and MIR probe pulses. Transients for selected wavenumbers after 347 nm excitation are analyzed in Figure 5.6 to explore the involved dynamic processes. The positive spikes for small positive delay times are due to solvated electron dynamics originating from a two-photon process [218].

(see Figs. 5.6a and 5.6b, where the bands are probed at 1951 and 2052 cm$^{-1}$). Thus, they evidence ultrafast CO liberation.

Two positive transient absorption signals appear in the spectral regions at around 1980 and 1857 cm$^{-1}$ and are observable over at least several nanoseconds (see Figs. 5.6c and 5.6d, where the bands are probed at 1982 and 1853 cm$^{-1}$, respectively). By comparison to the DFT calculations in Figure 5.3 and to FTIR measurements of long-lived intermediates [165, 219], it can be deduced that a stable dicarbonyl species is formed (most likely as a singlet), i.e., only one CO ligand has been photochemically dissociated on an ultrafast timescale and has been replaced by a D$_2$O molecule.

The energy needed to cleave the Mn–CO bond in Mn-containing CORMs [220] is less than half of the energy provided by absorption of a UV photon. There are no indications for the formation of a monocarbonyl, i.e., that two CO ligands are released simultaneously. Thus, the excess energy will be distributed among the vibrational modes of the dicarbonyl product, and it would be sufficient for several quanta of the CO stretch mode. In the literature, it was shown that UV excitation of hexacarbonyls leads to a significant amount of molecules with vibrational hot bands in the CO stretch [192]; however, such hot CO bands are absent in the photolysis of dicarbonyls [198].

From the data recorded, it can be inferred that the excess energy has to go to low-frequency modes of the dicarbonyl photoproduct. Before vibrational relaxation is over, these modes couple to the CO stretch [192] of the newly formed dicarbonyl. This gives
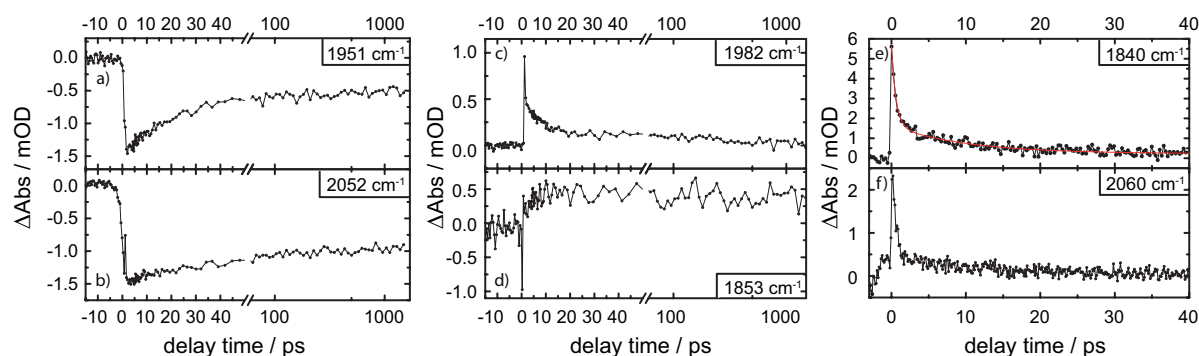
**Figure 5.6:** Transient absorption for exemplary wavenumbers. (a–d) Recorded for delays of up to 1.5 ns and with 347 nm pump pulses; note the change from a linear (-15 to 50 ps) to a logarithmic abscissa (>50 ps). Negative (a and b) and positive (c and d) signals persist for the full delay. (e, f) A shorter time scale to visualize cooling contributions that decay within the first 20 ps (red curve: biexponential fit to determine characteristic time constants); only the transient (f) was recorded with 264 nm excitation. Figure reprinted with permission from [2]. © (2013) American Chemical Society.

rise to a broadened absorption which narrows upon cooling, as is evident both in the spectral region at roughly 1980–2000 cm$^{-1}$ and also for the isolated product band at 1857 cm$^{-1}$ (yellow regions in Figures 5.4 and 5.5; by dint of the somewhat shorter temporal axes in Fig. 5.5, the narrowing is clearly illustrated). To clarify this, the latter is analyzed by probing red-shifted from the absorption band center at 1840 cm$^{-1}$ (see Fig. 5.6e). In a biexponential fit, two time constants (0.6±0.1) ps and (10±1) ps are found. While the former would fit solvation timescales in water [221] but its assignment is aggravated due to processes for very short pump–probe delays as described above, the latter evidences cooling of the hot photoproduct molecules. For hexacarbonyls in alkane, the low-frequency modes lose their energy a little slower within a few tens of picoseconds [192, 193]. The faster vibrational relaxation of our CORM dicarbonyl photoproduct can be attributed to effective water-assisted cooling. In this regard, water is a unique solvent as it has manifold possibilities for reorientational dynamics and a highly dynamical solvation shell resulting in a higher acceptance for vibrational energy (see also Sec. 2.3. This leads to the faster relaxation of hot CO ligands in aqueous [56, 206] compared to alkaneous solutions [192, 193].

As discussed, UV excitation of a CORM does not lead to the ultrafast release of two CO ligands. Moreover, for some of the molecules it does not even lead by all means to the release of one CO ligand. Although CO may dissociate, geminate recombination can restore the initial CORM by rebinding the photolyzed CO. Measurements for $Cr(CO)_6$ in alkanes have shown that this becomes less likely the smaller the solvent molecules are [193]. Such a behavior is recognized by looking at dynamics associated with wavenumbers of the intact CORMs; as a first aspect, a bleach recovery can be detected, as evident for early times in the signal of the antisymmetric CO stretch (confer Fig. 5.6a). Note that geminate recombination occurs within 1 ps accompanied by a broadening of the absorption due to the coupling of the CO band to the low-frequency

modes, and therefore, the recovery reflects again the cooling dynamics rather than re-combination dynamics [193]. Whereas the bleach recovery may also partially derive from the cooling of the overlapping dicarbonyl product absorption around $1980\,cm^{-1}$, the second aspect is more obvious for the symmetric CO stretch centered at $2051\,cm^{-1}$; the DFT calculations reveal that none of the possible products after photolysis absorbs at wavenumbers above $2000\,cm^{-1}$, except for the photoproducts in higher spin states. But as already mentioned above, the fact that they are clearly higher in energy (for instance, there is a difference in energy of $0.8\,eV$ between the singlet and the quintet of the dicarbonyl with $D_2O$ ligand) suggests that they are not worth considering. There-fore, a line broadening due to recombined CORMs is the origin of the positive signal at $2060\,cm^{-1}$ (see Fig. 5.6f). It is observed around the negative ground-state bleach, caused by CORMs that lost a CO ligand, and persists as long as the CORM is vibrationally hot.

Beyond that, the possibility of an excitation without any bond cleavage might exist for CORMs, as suggested by the TDDFT calculations depicted in Figure 5.2. There is no direct way to distinguish this scenario from geminate recombination on the grounds of a single transient absorption map. Nevertheless, two experimental findings indicate that this might occur by comparing data with different pump wavelengths. The signature of excited yet intact CORM on the blue-energy side of the symmetric CO stretch ground-state bleach (see Fig. 5.6f) seems more pronounced in the data with pump pulses at 264 nm than for those at 347 nm. If the recombination dynamics can be considered to be independent of the pump wavelength, 264 nm excitation might indeed involve LUMOs located mostly at the tpm ligand and hence lead less often to CO release. The second finding is that the yield of photolysis is not three times higher at 264 nm than at 347 nm, although the absorption is (confer Fig. 5.1b), which further supports that not every UV excitation will lead to CO release. Recording of a photolysis excitation spectrum, i.e., measuring the amount of released CO as a function of pump wavelength, could further substantiate this, but has not been performed so far.

### 5.3.3 Transient MIR spectroscopy with two consecutive pump pulses

In order to find out whether the dicarbonyl photoproduct can release a further CO ligand upon UV excitation, a consecutive UV pulse is employed which may repump the products 200 ps after the initial pump event. By splitting either the 264 nm or the 347 nm pump pulse with an interferometer setup, pump pulse pairs temporally separated by 200 ps are obtained (for a similar three-pulse experiment, see Ref. [88]) and probed 200 ps after the repump pulse. The ratio of the energies were chosen so that more than a quarter of the molecules in the probed volume were excited by pump or repump pulse and hence also a few of them would interact with both if possible. With one shutter in the pump beam path and another shutter in the repump beam path, difference spectra were recorded for the three cases that either only one of the excitation pulses is blocked or both beam paths are unblocked. Subtracting the first two cases from the latter provides difference spectra that reflect the repump-induced change of absorbance, i.e., the vibrational signature of

**Figure 5.7:** Difference spectrum derived from a pump–repump–probe measurement (red curve) together with an applied flat-top Fourier filter (black curve). The spectrum was obtained by subtracting the cases that either only one of the excitation pulses is blocked from the case in which both successive pump pulses are unblocked. Both the excitation pulses and the probe pulse are temporally separated by 200 ps, respectively.
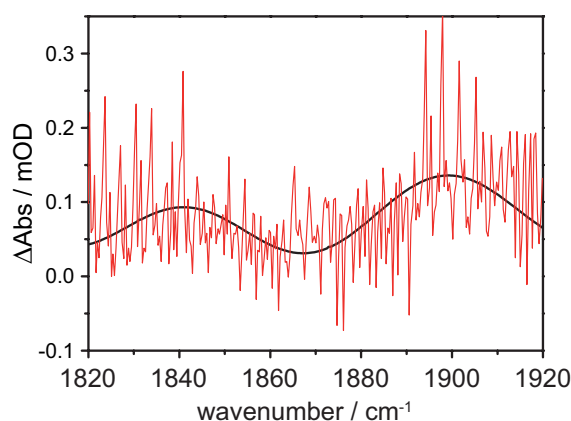
molecules that were sequentially excited twice within 200 ps. Figure 5.7 depicts a data set obtained from an averaging of 100 of such measurements (red curve) together with an applied flat-top Fourier filter (black curve).

Considering the DFT calculations, these very small signals around 1840 and 1900 cm$^{-1}$ could be caused by the formation of a monocarbonyl with one D$_2$O ligand or without an attached solvent molecule. At a first glance, this assignment seems appealing and plausible since a second photon might cleave another CO group. However, beside the weakness of the signals on the order of 50 $\mu$OD which is less than the noise in this measurement, there are further arguments for a lack of sequential UV-induced CO release. From the data discussed in the previous sections, it is obvious that it is a dicarbonyl that would be repumped after 200 ps delay time. According to that, the first counterargument is that the dicarbonyl can be repumped but no bond is broken at all (see explanations given above). Second, the dicarbonyl can be repumped and leads to the release of a ligand, but it is the new D$_2$O ligand which is photochemically dissociated (as discussed for CpMn(CO)$_3$ in [214], e.g.). In that case, the rebinding dynamics of the aqua ligand is not observable within the time resolution, identical to the replacement of CO by D$_2$O after the first pump pulse. Then, the probed signal would behave like if no repumping had occured. Third, the dicarbonyl intermediate does not absorb UV light and hence cannot be repumped. This is partially supported by strong red-shifts observed for the electronic absorption spectrum of CpMn(CO)$_3$ after photolysis of one CO [215]. Although in general it is likely that further UV absorption is possible, this would have to be conclusively clarified by future UV-pump–UV-probe transient absorption measurements.

The sinusoidal curve depicted in Figure 5.7 have been reproduced and did not show up in any other spectral region where the measurement has been performed likewise. Where they originate from remains uncertain.

## 5.4 Conclusions

Subsuming, as summarized in Fig. 5.8, UV excitation of an exemplary CO-releasing molecule in aqueous solution leads to ultrafast photolysis of one CO ligand, which may geminately recombine for some of the molecules. The liberated CO merges into the
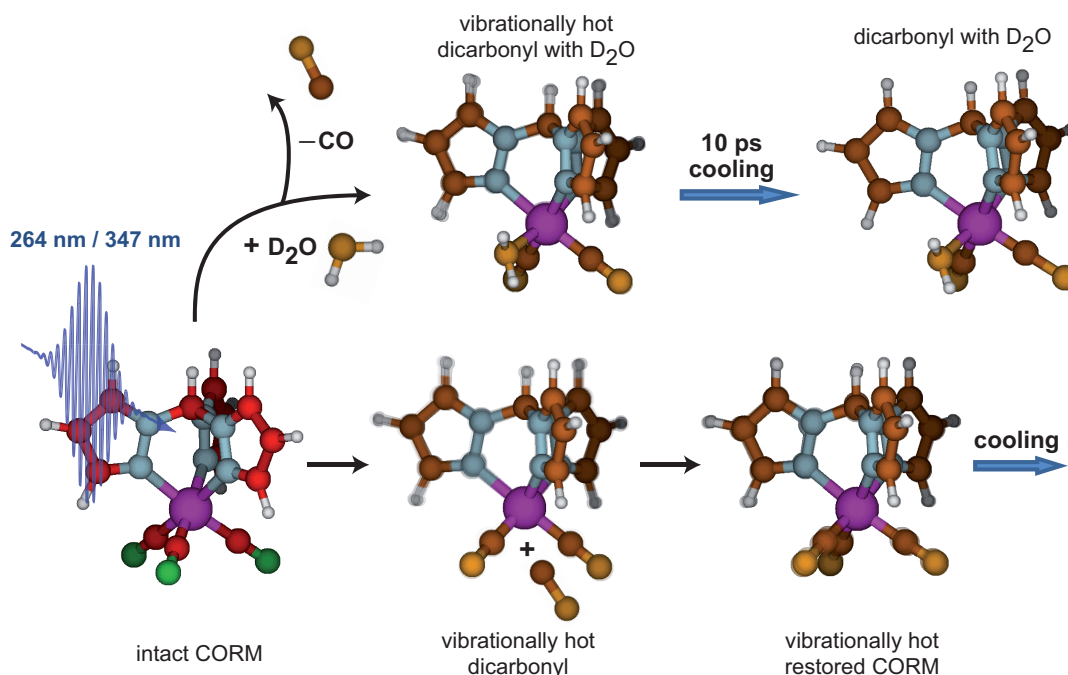
**Figure 5.8:** Predominantly, UV excitation of the CORM in aqueous solution leads to an ultrafast photolysis of one CO. The CO is liberated and a solvent molecule fills the unoccupied coordination site. Geminate recombination occurs but in comparison is a minor process. The excess energy, both in the dicarbonyl photoproduct and in the restored CORM, is transferred to low-frequency vibrational modes. Subsequent cooling occurs on a 10 ps time scale.

solvent environment and a water molecule occupies the vacant coordination site. If the CORM is excited in the higher-energy UV band, some molecules will not dissociate but the excitation might be located mostly at the trispyrazolyl ligand, as is suggested by TDDFT calculations and also in agreement with the experimental observations. Excess energy, both in the dicarbonyl photoproduct and in the CORM if still comprising three CO ligands after excitation, is transferred to low-frequency vibrational modes, which becomes observable due to line-broadening both in the dicarbonyl and recombined CO stretch modes. No CO hot bands are observed, i.e., the remaining CO ligands are not vibrationally excited through the UV excitation of the CORM.

Direct re-excitation with a second UV pulse did not lead to observable monocarbonyl species, hence a further interaction with UV light seems insufficient to release more CO ligands. Assumed that this is not due to non existent UV absorption characteristics of the dicarbonyl, further loss of CO most likely necessitates manganese oxidation as suggested by Berends and Kurz [165]. The elucidation of the primary processes presented here contributes to a comprehensive understanding of the biological activity of CORMs, which furthermore motivates its application in a two-photon absorption experiment (see Sec. 6.2).

# 6 Techniques for prospective transient absorption experiments

This chapter presents the outcome of preparative experiments that are meant to provide a basis for prospective studies. It comprises the shaping of ultrashort laser pulses in the UV (Sec. 6.1), the detection of two-photon absorption of a dimanganese decacarbonyl complex (Sec. 6.2), and a comparison between chirped-pulse upconversion and direct multichannel MCT detection to monitor transient absorption signals in the MIR (Sec. 6.3).

## 6.1 Pulse shaping and characterization in the UV

There exists a huge variety of organic compounds whose electronic transitions are predominantly triggered by photons in the UV spectral region. To investigate the associated photoinduced chemical reactions already is an important and promising task in itself. Being capable of shaping ultrashort laser pulses in the UV combines this aspect with the desired goal not only to monitor but to actively control the reaction on a microscopic scale, i.e., to guide the outcome to a favored product [222, 223] and perform even more seminal experiments in the future. This shall briefly motivate the subsequent presentation of some exemplary shaped and characterized UV pulses that are intended to supply a preliminary perspective for continuative investigations. The theoretical background to the utilized devices is given in Section 2.2.3, whereas the corresponding experimental implementations are described in Section 3.3.1. The unshaped input pulses used in the following are centered around 338 nm.

Figure 6.1a (upper row) depicts the measured and reconstructed DFG-XFROG traces accompanied by the retrieved temporal- and wavelength-dependent spectra of the input pulses that propagated through the Dazzler without being actively shaped. Obvious are the second and higher order phase terms that elongate the pulse duration to 873 fs FWHM. They derive from the 50 mm long KDP crystal and can be compensated by the device. With this preset ex works self-compensation the Dazzler adds -6582 fs$^2$, -2108 fs$^3$, and -560 fs$^4$ of phase to the input pulses. This leads to the temporally shortened pulses depicted in Figure 6.1b (lower row) with a pulse duration of 101 fs FWHM. However, apparently the pulses are still far away from being transform-limited, since the minimal duration of Gaussian pulses centered around 338 nm with a spectral FWHM of 6.5 nm would be 25.8 fs. The remaining phase terms are composed of contributions caused by unavoidable optical elements in front of the Dazzler, or they stem from an imperfect compression inside the TOPAS. Both causes are usual sources of disturbance with regard to the requirement of laser pulses that are temporally as short as possible.
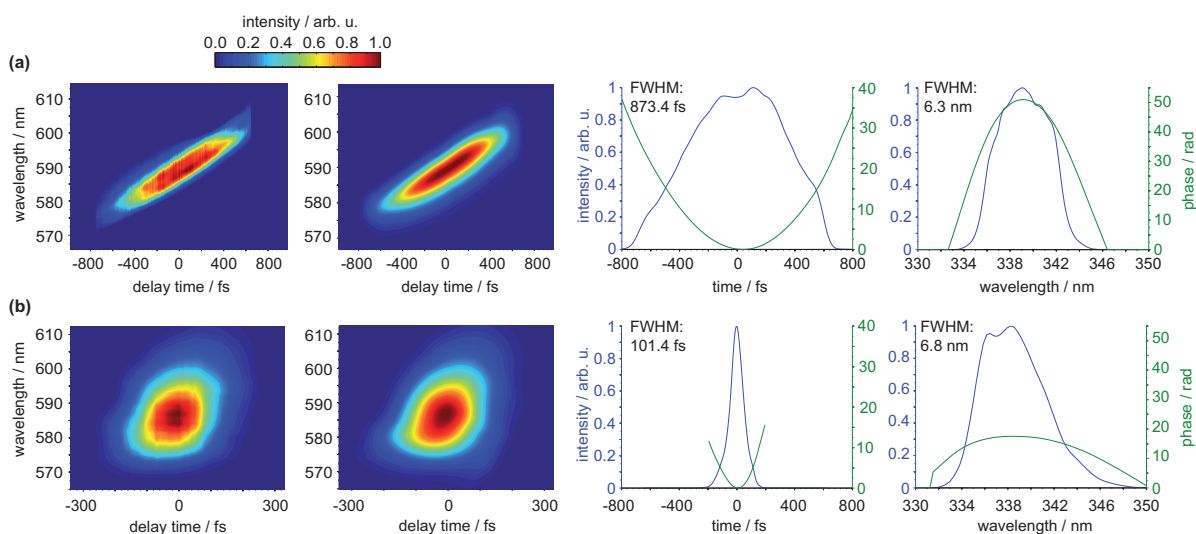
**Figure 6.1:** (a) The upper row illustrates the measured and reconstructed DFG-XFROG traces from UV pulses that propagate through the Dazzler without being actively shaped. The obvious phase contributions predominantly derive from the 50 mm long KDP crystal and lead to a pulse duration of 873 fs FWHM. The pulse shaper provides a self-compensation that leads to the pulses depicted in the lower row (b). These are significantly shortened in time but still show phase contributions of differing orders, which mainly derive from optical elements in front of the Dazzler or an imperfect postcompression inside the TOPAS. This suggests an appropriate precompression of the input pulses outside the pulse shaper in order not to decrease the shaping capacities due to the self-compensation.

Consequently, two aspects can be concluded. First, the compensation of the dispersion caused by the crystal should not be carried out by the shaping capabilities of the Dazzler itself. As the self-compensation already requires a certain amount of the shaping capacity—the Dazzler provides a maximum programmable delay of 4.5 ps at 250 nm and 3.5 ps at 400 nm—the flexibility is accordingly constricted for the actual experiment. Therefore, it is beneficial to compensate for the influence of the crystal outside the Dazzler with appropriate pulse compression techniques. Second, with an
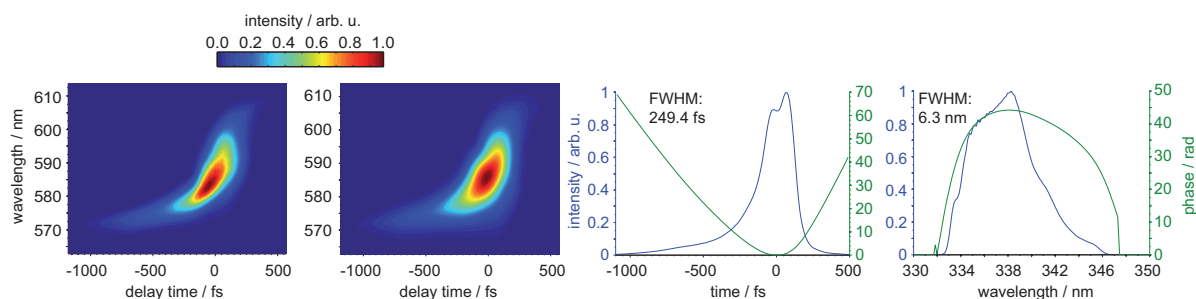


**Figure 6.2:** Measured and reconstructed DFG-XFROG traces of an exemplary UV pulse where the self-compensation by the Dazzler and additionally arbitrary higher order phase contributions (-32258 $fs^3$ and 318471 $fs^4$) have been applied.
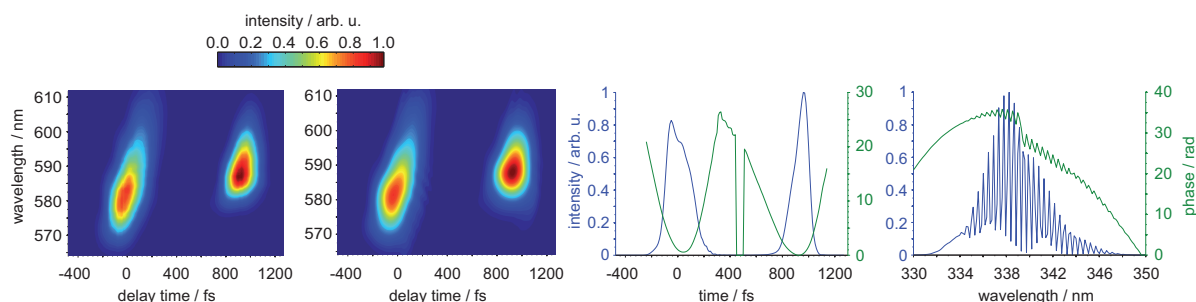
**Figure 6.3:** Measured and reconstructed DFG-XFROG traces of a double pulse separated by 1000 fs. The phase functions and amplitudes can be adjusted individually for each subpulse. With regard to multidimensional spectroscopy applications, high phase stability between the pulses is provided since both exactly pass through the same optical setup.

installed precompression one could additionally apply the inverse phase extracted from the data illustrated in Figure 6.1b. In doing so, the input pulses are optimally prepared for shaping and the potential of the Dazzler could fully be focused on the efforts of a control experiment. In such measurements, more complicated pulse shapes might arise that distinctly differ from a compressed transform-limited pulse. As an example, Figure 6.2 presents the measured and reconstructed DFG-XFROG traces of an UV pulse where the self-compensation by the Dazzler and additionally arbitrary cubic and quartic phase contributions (-32258 fs$^3$ and 318471 fs$^4$) have been applied.

With the generation of pulse sequences or simply double pulses, another field of application for the Dazzler can be envisioned. It is conveniently feasible to generate subpulses with identical spectral content, whose phase and amplitude can be shaped individually [224]. Furthermore, individually shaped subpulses centered around different spectral positions can be generated. The latter is depicted in Figure 6.3. For multidimensional spectroscopic experiments high phase stability between subpulses is indispensable and can be provided for laser pulses that exactly pass through the same optical setup. According applications have been reported using an AOM [225] or an LCD-based pulse shaper [226, 227] to generate phase-locked double-pulse sequences with adjustable coherence time. For those purposes, the practicability of an AOPDF for multidimensional spectroscopy experiments [228, 229] is further emphasized by ongoing enhancements of the producer of the Dazzler device (Fastlite). With the so-called *streaming*, over 100000 predefined pulse shapes at a repetition rate of 1 kHz can be loaded and successively applied, so that the temporal delay between two pulses can be scanned. Since AOPDFs are available with various active crystals, multidimensional spectroscopy both in the UV/VIS spectral regime but as well in the IR can be managed this way.

Based on these aspects one can summarize that the utilization of a pulse shaper is in many respects an efficient complement to the conventional pump–probe spectroscopy. In a first step, it can simply be employed to improve the temporal shape of the excitation pulses, in order to optimize the time resolution of a measurement, or in order to eliminate the potential influence of chirp on the outcome of a photoinduced reaction. In a second step, it is possible to perform more sophisticated spectroscopic experiments that are based on multiple excitation events, like ultrafast pump–repump–probe or two-

dimensional spectroscopic measurements, for instance. Especially with regard to the latter, the inherent phase-stability of pulse sequences generated by a Dazzler device is of great benefit. Furthermore, within the scope of a UV-pump–MIR-probe experiment the vibrational signature of a certain molecular species can serve as a feedback signal, whose strength can be actively manipulated via tailored excitation pulses. The specific pulse shape that steers the quantum mechanical system upon photoexcitation into a desired direction can be determined theoretically or adaptively using a learning loop [223, 230]. Since this great range of applications can be implemented in conjunction with laser pulses in the UV spectral region a multitude of promising prospects for further experiments in the future is opened up.

## 6.2 Obtaining two-photon excitation spectra

The phenomenon of two-photon absorption (TPA) offers a broad spectrum of applications, ranging from 3D lithographic microfabrication [231], through techniques for 3D optical data storage [232], to implementations in the medical and life sciences [233, 234]. Especially the latter motivates the preliminary experiment presented in the following. Due to the nature of biological tissues, light from 650 to 950 nm can penetrate skin and blood efficiently with depths up to 2 cm [235]. Compared to light in the visible and UV spectral regions, the damage to the organism thereby is rather low. Hence, it is possible to activate UV-absorbing compounds via TPA with NIR laser pulses. Moreover, TPA typically only takes place at the focal spot of a light beam due to the required high photon densities, so that it features a high spatial sensitivity.

Since one can imagine to deposit a certain amount of CORMs inside cancerous tissue and subsequently activate its capability of being cytotoxic against cancer cells via



**Figure 6.4:** (a) Absorption spectrum (black) of the studied dimanganese decarbonyl complex in isopropanol solution, together with the spectrum of one exemplary pump pulse, centered at 680 nm (red). The inset depicts the chemical structure of $Mn_2CO_{10}$. (b) Infrared absorption spectrum of the $Mn_2CO_{10}$ complex dissolved in isopropanol in the spectral region of the CO vibrations.
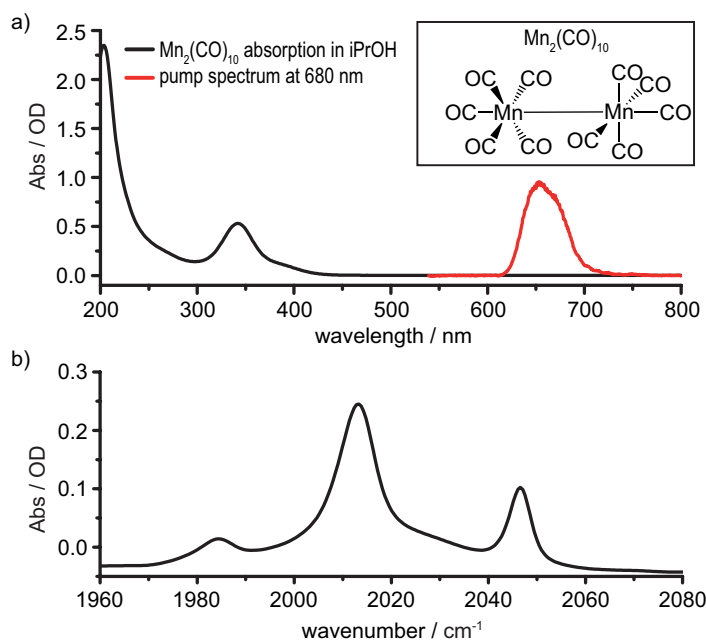
**Figure 6.5:** Photodissociation dynamics of $Mn_2CO_{10}$ upon single-photon excitation, recorded with 350 nm pump pulses and the LSJ. Besides the bleaching of the ground state at 1983, 2013, and 2047 cm$^{-1}$, two photoproducts arise: at 2015 and 2052 cm$^{-1}$ the formation of $Mn_2CO_9$ is indicated, whereas at 1983 cm$^{-1}$ a strong signal of $MnCO_5$ shows up. The latter overlaps with the GSB at the same position. Both the product bands and the bleaching show narrowing upon cooling.
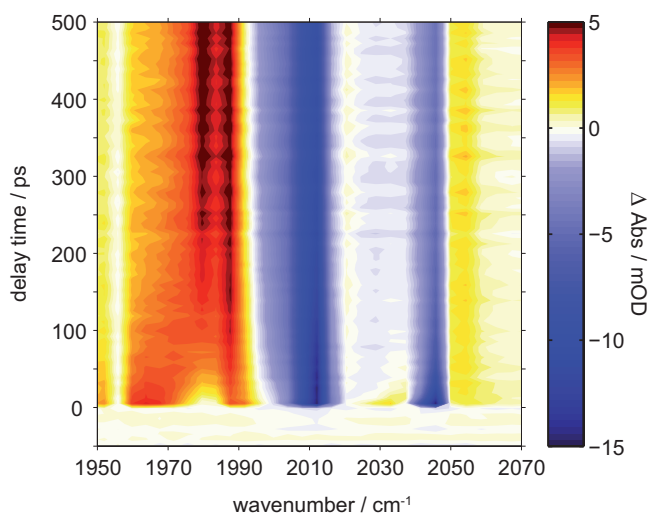


two-photon excitation, the biological applications of CORMs as described by the introductory words to Chapter 5 further motivate the usefulness of a sound TPA detection scheme. As described above (confer Sec. 3.3.3), such a scheme must thoroughly pay attention to the qualities of the utilized laser pulses, i.e., the pulse duration, the energy and spectral position. First attempts to excite the manganese-tricarbonyl complex presented in Chapter 5 with two photons centered around 700 nm failed; there was no TPA signal detectable. As a consequence, for further testings of the setup an easy-to-handle and commercially available reference molecule has been employed: the dimanganese decacarbonyl $Mn_2CO_{10}$ (for the chemical structure confer inset of Fig. 6.4a). The sample was purchased from ABCR (CAS: 10170-69-1). It was used without further purification or other treatment and dissolved in spectroscopic-grade isopropanol.

Similar to the manganese-tricarbonyl complex, the $Mn_2CO_{10}$ complex features an absorption around 340 nm but none in the visible spectral regime (see Fig. 6.4a). In addition, three strong stretching modes of C=O groups appear between 1970 and 2070 cm$^{-1}$ (see Fig. 6.4b), so that the detection via MIR probe pulses remains unaltered related to the previously described pump–probe experiments. The objective is now to obtain a two-photon excitation spectrum, which does not necessarily take the shape of the single-photon UV absorption spectrum. For this purpose, it is initially conducive to take a look at the photodissociation dynamics of $Mn_2CO_{10}$ upon UV-excitation, which are also known from the literature [195]. Figure 6.5 displays the corresponding transient map, recorded with 350 nm pump pulses and the LSJ as described in the Section 3.3.3. Besides the bleaching of the ground state at 1983, 2013, and 2047 cm$^{-1}$, two photoproducts arise in accordance with [195]. At 2015 and 2052 cm$^{-1}$ the formation of $Mn_2CO_9$ is indicated, whereas at 1983 cm$^{-1}$ a strong signal of $MnCO_5$ shows up. The latter overlaps with the GSB at the same position. Both product bands and the GSB narrow upon cooling, which is not of great relevance at this point. For the following it is of interest to state that the strongest change in absorbance with -8 mOD appears at 2013 cm$^{-1}$ and remains constant after roughly 200 ps along the residual measurement time. By means of such a distinct GSB value recorded for varying visible pump wavelengths at the same spectral

**Figure 6.6:** Difference spectra of $Mn_2CO_{10}$ excited with two 680 nm pump photons (red) and with one 340 nm pump photon (black). Both difference spectra are recorded after a delay time of 240 ps. The spectral positions of the bleach signals after two-photon excitation are comparable to those following a single-photon excitation, but with lower signal strengths.
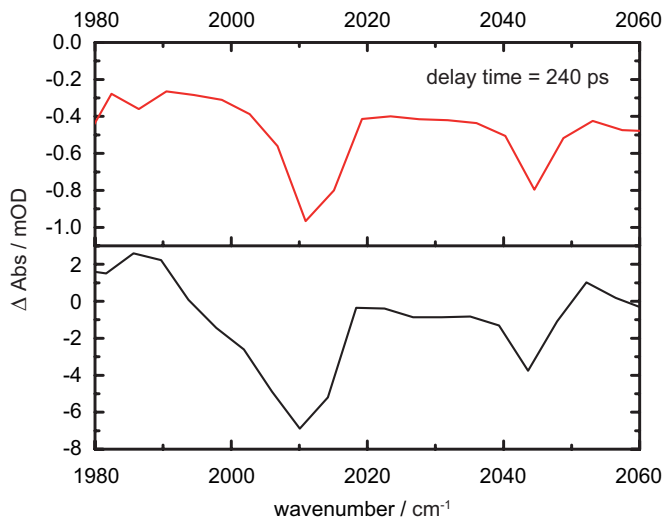


and temporal position, one can assemble a two-photon excitation spectrum.

Accordingly, the next step is to obtain GSB values after TPA for varying excitation wavelengths at the same probe wavelength and delay time. Obviously, it is thereby sufficient to omit transient measurements for each pump wavelength, since difference spectra already contain the relevant information. Like the upper one depicted in Figure 6.6, which was recorded with 680 nm pump pulses and a measured pump pulse energy of 8 μJ in front of the LSJ. Both the energy $E$ and duration $\tau_{FWHM}$ of the pump pulses have to be monitored while scanning the excitation wavelength, since both quantities might change in this process. Therefore, and due to the nonlinearity of the TPA (confer Sec. 3.3.3), each GSB value has to be normalized to $E$ and $\tau_{FWHM}$. In doing so, the influence of $E$ and $\tau_{FWHM}$ to the TPA signal is canceled out and exclusively the wavelength-dependent impact of the excitation to the molecule is revealed. Both quantities are measured with the two-photon photodiode and with the autocorrelator, respectively. The photodiode signal $S_{PD}$ caused by the TPA is [236]

$$S_{PD} = k(\lambda)\frac{E^2}{\tau_{FWHM}}, \tag{6.1}$$

with $k(\lambda)$ being the unknown and wavelength-dependent relative sensitivity of the diode, which can be derived from this equation, as all the three other quantities are measured. The recorded signal from the molecule following TPA can be expressed in a similar form:

$$S_{molecule} = a(\lambda)\frac{E^2}{\tau_{FWHM}}, \tag{6.2}$$

where the unknown $a(\lambda)$ contains molecular-specific quantities, i.e., the TPA coefficient, or the molecular TPA cross-section and the number density of molecules (see also Sec. 3.3.3, Eqs. (3.7) and (3.8)), respectively. As a consequence, the ratio between the detected signal $S_{molecule}/S_{PD}$ equals $a(\lambda)/k(\lambda)$.

This yields a corrected two-photon excitation spectrum, like the one illustrated in Figure 6.7 [237], which only shows three data points for pump wavelengths at 652, 679,

**Figure 6.7:** Comparison between the linear single-photon absorption spectrum and the two-photon excitation spectrum of $Mn_2CO_{10}$ dissolved in isopropanol [237]. As it is a preliminary result, only three data points for pump wavelengths at 652, 679, and 691 nm constitute the outcome of the measurement procedure as described in the text.
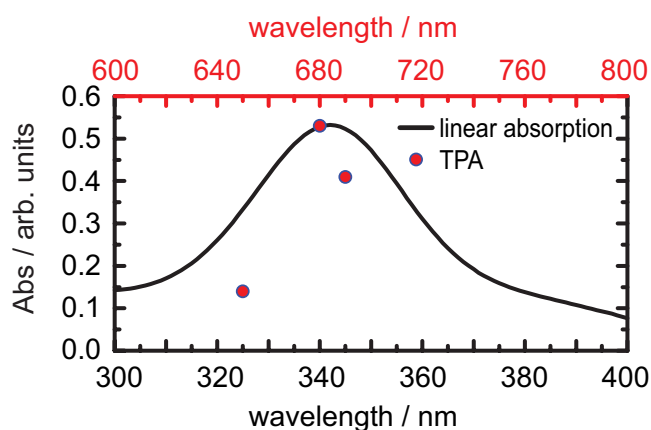
and 691 nm. It is a preliminary result whose completion was not further pursued within the scope of this work. Nonetheless, the whole procedure as described is realizable within a reasonable experimental effort and thereby elucidates both the transient single-photon induced molecular dynamics and the nonlinear TPA behavior of a molecular system in the liquid phase. In this sense, it uncovers a lot more and complementary information than the Z-scan method [238, 239], which is widely used to gain insight into the TPA cross-section of various compounds [240–242].

## 6.3 Recording transient MIR absorption data with the CPU technique

This section summarizes the pros and cons of two methods that are utilized to record weak ultrafast absorption changes on the order of a few mOD in the MIR spectral regime: the chirped-pulse upconversion (CPU) technique [121, 243, 244] on the one hand and the standard direct multichannel detection via MCT photodiode arrays on the other hand. The corresponding experimental configuration is explained in Section 3.3.2; the femtosecond pump–probe setup employed for the time-resolved experiments is described in Section 3.2. Please note that the pump–probe data presented in the following have been obtained in the single-shot data acquisition mode, which already includes a binning of two adjacent pixels. An additional binning is mentioned with respect to this aspect. Parts of the study presented in the following have been published in [4].

The number of pixels that are available to measure probe spectra directly in the MIR is the most evident difference related to the CPU detection technique. MCT detector arrays provide more than one order of magnitude less pixels (between 32 and 128 for HgCdTe) than CCD arrays (2048), giving the latter a significantly higher spectral resolution. A combination of several MCT arrays indeed increases the detection width [245], however, in doing so the already high costs for a single array would further grow. Another difference between both detection schemes concerns the handling. MCT detection needs a constant cooling by liquid nitrogen, which means in practice, in order to keep the noise at the lowest possible level, approximately every three hours liquid nitrogen has to
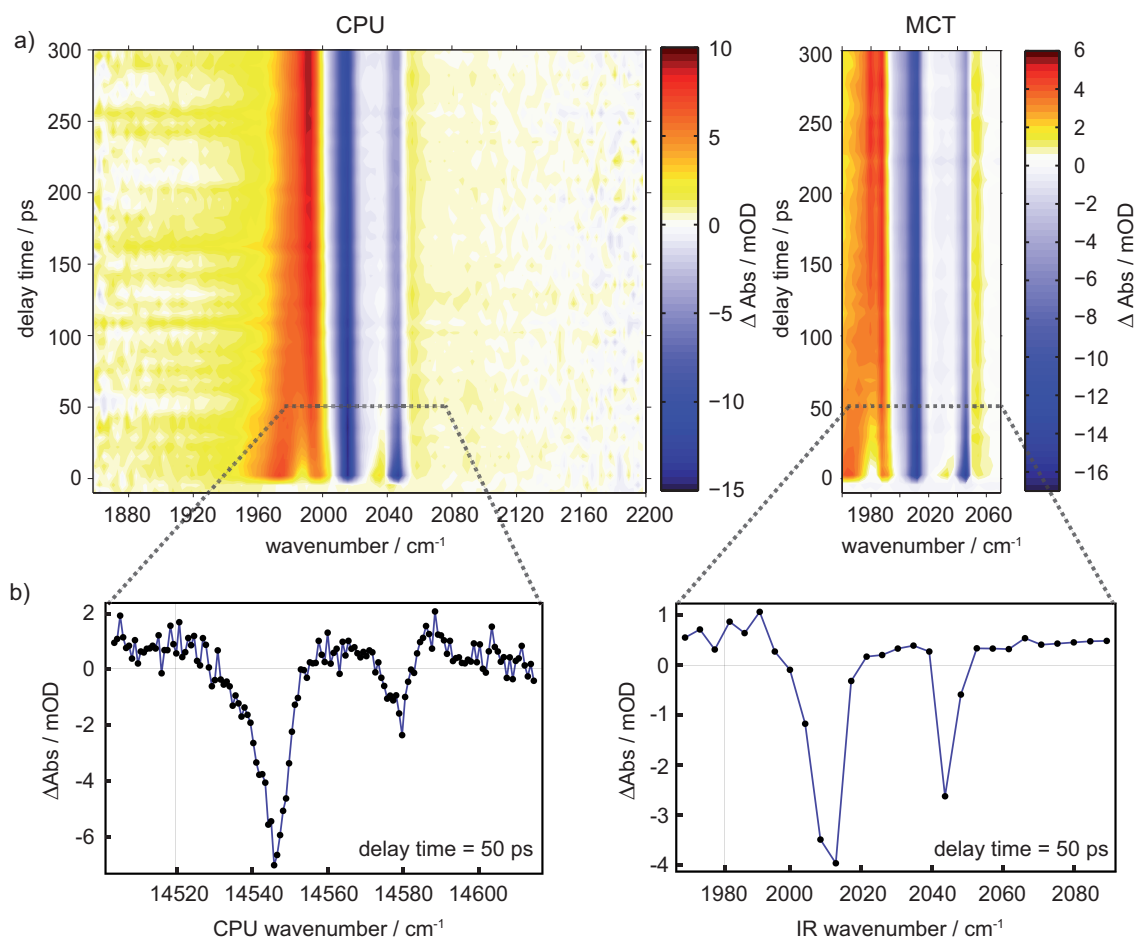
**Figure 6.8:** (a) The upper row displays transient maps of $Mn_2CO_{10}$ excited with 350 nm pump pulses, on the left hand side detected with the CPU, on the right hand side with the MCT array and grating 2. Both data sets show high data quality due to averaging of both 2000 consecutive laser shots and four consecutively recorded maps. For the CPU detection an additional binning of four adjacent pixels was applied. For comparative purposes, both wavenumber axes show equal spacing. If no binning is applied, spectrally narrow features can be examined. The lower row (b) illustrates difference spectra at delay times of 50 ps, recorded with the CPU technique without any additional pixel binning (left) and with the MCT array (right). The CPU retraces absorption signatures with five times more data points than the MCT detection.

be refilled. Moreover, the voltage readout of the single detector elements needs a more elaborate postprocessing prior to the analog-to-digital conversion. In comparison, the CPU consists of another nonlinear interaction inside a crystal that has to be aligned, but the CCD chip, which is constantly thermoelectrically cooled, is easier to handle and more cost-effective, which is certainly another reason why CPU evolved during the last years to become an established method for the detection of probe pulses in the MIR spectral range [154, 246–249].

To get a first impression of both techniques' performance within the scope of pump–probe spectroscopy, Figure 6.8a depicts transient maps of $Mn_2CO_{10}$ excited with 350 nm

**Figure 6.9:** MIR spectrum recorded by scanning the central IR spectrometer wavelength in 1 nm steps along one single HgCdTe pixel (red) and MIR spectrum obtained with the CCD camera after upconversion and chirp correction (blue). The gridlines indicate the 16 most intense water vapor lines taken from the GEISA database [250]. Figure adapted with permission from [4]. © (2013) Optical Society of America.
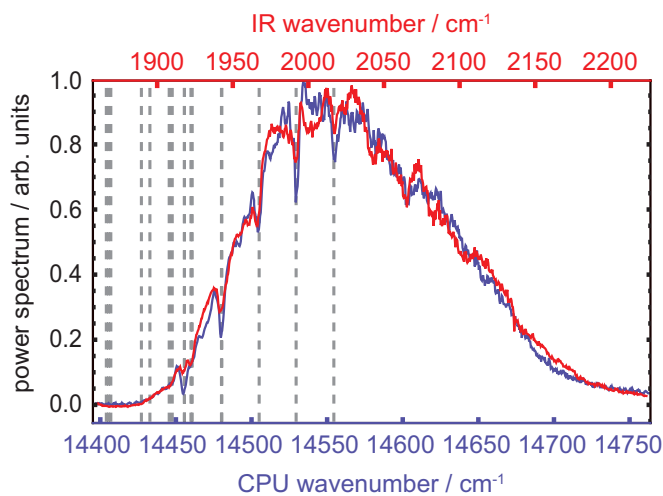
pump pulses, using the LSJ (confer Sec. 6.2). For comparative purposes, the wavenumber axes of both data sets show equal spacing. The data on the left hand side was recorded with the CPU technique, on the right hand side with the MCT array. To achieve a high data quality, both data sets result from an averaging of 2000 consecutive laser shots at fixed delay times as well as of four consecutively recorded complete maps. Furthermore, eight adjacent pixels were binned in case of the CPU detection which further decreases the noise in comparison to data recorded with less pixels binned (see below). The CPU transient map is clipped at the spectral positions where the CPU spectrum fades and accordingly the noise begins to dominate. In contrast, the MCT transient map is not clipped but shows the full spectral range that can be detected with one setting of the utilized grating 2, which features the best compromise between spectral resolution and coverage of the probe spectrum. By changing the grating, either the spectral resolution or the spectral sampling can be improved but not both within the same measurement. To elucidate spectrally narrow absorption signatures, one can take advantage of the maximal spectral resolution of the CPU technique by applying less pixel binning. This is illustrated in Figure 6.8b (left: CPU; right: MCT) by means of difference spectra at 50 ps delay time. Please note that these difference spectra are not extracted from the data sets displayed in Figure 6.8a, as they derive from a separate measurement with a binning of two adjacent pixels and less averaging. Whereas the MCT detection retraces the shape of the GSB signals only with five (at $2013\,cm^{-1}$) or three (at $2047cm^{-1}$) data points, the CPU offers five times more data points, thus providing much more detailed information about line shapes, for instance. From these considerations, the versatility of the CPU technique is evident. But so far no comparative information have been obtained concerning the signal-to-noise of both detection methods.

Hence, for a more detailed comparison, in the following the noise level of both methods during the detection of transient changes in absorbance shall be investigated. This is done by means of measurements on a 5 mM solution of $Co_4CO_{12}$ (purchased from Strem Chemicals, Inc., and used without any further treatment) dissolved in $CH_2Cl_2$. This molecule serves as a model system, since it is stable in dilute solution and its pho-
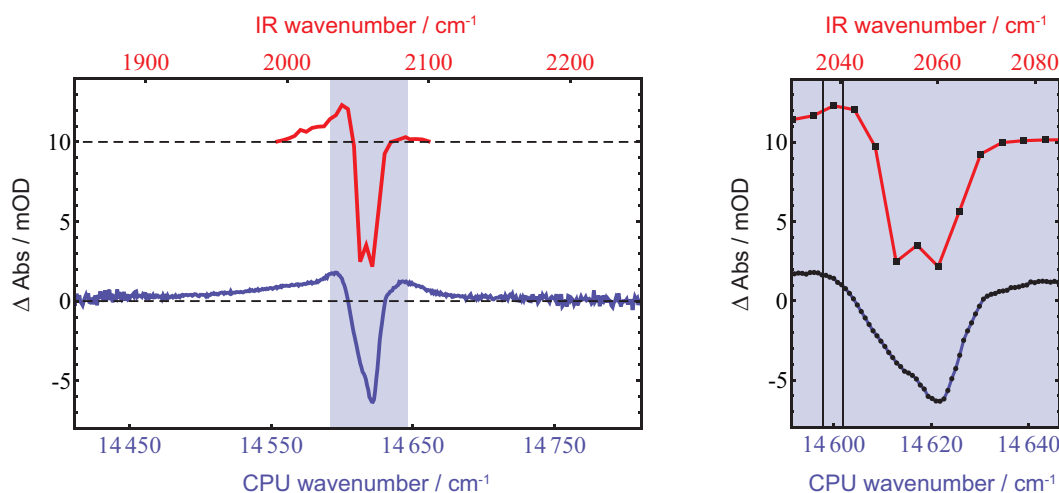
**Figure 6.10:** Difference spectra of $Co_4CO_{12}$, excited with 270 nm pump pulses at delay times of 6 ps, detected with the CPU technique (blue curves) and the MCT array (red curves, 10 mOD vertical offset), respectively. The data results from an averaging of 50000 consecutive laser shots (25000 pump–probe pairs). The light blue-shaded area highlights the spectral increment of both methods. The vertical lines inside the graphic on the right hand side delimit the data points by means of which the individual noise analysis is carried out (confer Figs. 6.11 and 6.12).

tochemistry, which is sufficiently understood [251] but will not be further discussed in the following, offers well detectable vibrational signatures from 1800 to 2100 cm$^{-1}$ (see Fig. 6.13b). The MIR probe spectrum used thereby is shown in Figure 6.9. The spectrum in red was directly recorded in the MIR by rotating the grating and thus scanning the central IR spectrometer wavelength in 1 nm steps along one single HgCdTe diode. Although it takes approximately five minutes of acquisition time, this measurement accurately reflects the spectrum of the MIR probe pulses unlike the simultaneous detection of 32 pixels. The spectrum is centered around 2028 cm$^{-1}$ and provides a FWHM of 154 cm$^{-1}$. The upconverted and chirp corrected spectrum (shown in blue) is recorded after 300 ms of exposure time. It is centered around 14554 cm$^{-1}$. With a FWHM of 151 cm$^{-1}$ it has only narrowed by 3 cm$^{-1}$ of spectral bandwidth owing to the upconversion process. The gridlines indicate the 16 most intense water vapor lines taken from the GEISA database [250]. With tight spectrometer entrance slits the water vapor absorption lines can be resolved and additionally conduce to calibrate the upconversion frequency. Due to a longer optical beam path of the MIR light through water vapor in the atmosphere of the laser laboratory the CPU spectrum exhibits stronger water vapor absorption lines.

With the MIR probe pulses shown in Figure 6.9 difference spectra of the $Co_4CO_{12}$ complex in a flow cell (100 $\mu$m optical path length), excited by 270 nm pump pulses at delay times of 6 ps have been recorded in the single-shot acquisition mode (see Fig. 6.10). The data results from an averaging of 50000 consecutive laser shots (25000 pump–probe pairs), both in case of the CPU and the MCT detection. Thereby, a measurement procedure was employed that successively acquires 2000 spectra with each detection method
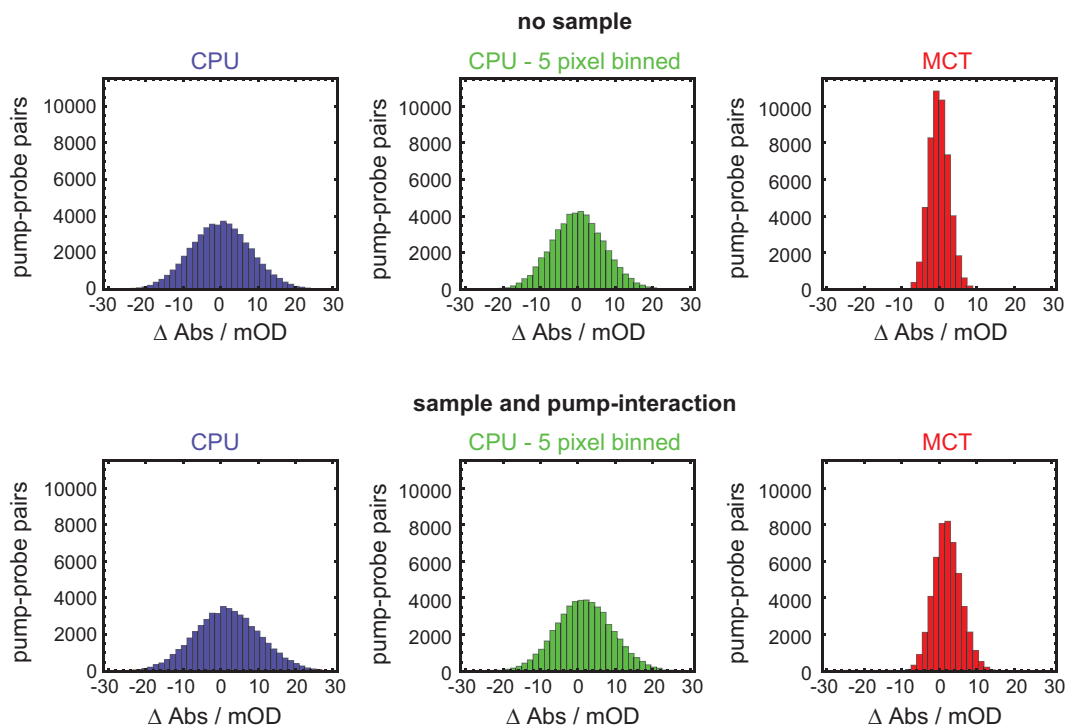
**Figure 6.11:** The histograms depict the Gaussian distributions of 50000 successively detected pump–probe pairs at $2039\,\mathrm{cm}^{-1}$ (confer Fig. 6.10) for the recording of the signal baseline (upper row, no sample) and for the molecular signal of $\approx 2\,\mathrm{mOD}$ (lower row, sample and pump-interaction), measured via CPU (blue), via the MCT array (red) and again via CPU but with a binning of five adjacent pixels (green). The latter equalizes the discrepancy regarding the spectral coverage of both methods. Figure adapted with permission from [4]. © (2013) Optical Society of America.

and repeats this recording 50 times. Although the simultaneous read out of both spectrometers for every single laser shot would be the optimal setting for such a comparative study, the chosen routine also diminishes the impact of mid- to long-term laser fluctuations on the data collection. The measurement procedure as described was carried out under constant experimental conditions for two scenarios: first, without a molecular signal and with no excitation pulses, which is equivalent to the recording of a baseline during the evaluation of pump–probe data. Second, with UV pulses that excite the liquid sample film inside the flow through cuvette. The changes of absorbance depicted in Figure 6.10 are the result of an averaging of successive background-corrected spectra. Again it is evident that a detection via CPU features superior attributes with respect to spectral sampling and coverage. To elucidate the noise level of both techniques, 50000 successive pump–probe pairs at a probe wavelength of $2039\,\mathrm{cm}^{-1}$ (data points delimited by vertical lines on the right hand side of Fig. 6.10, which correspond to a positive $\Delta\mathrm{OD}$ value of $\approx 2\,\mathrm{mOD}$) both for the detection of the signal baseline and the detection of a molecular signal have been recorded. The histograms in the upper row of Figure 6.11 reflect the corresponding Gaussian distributions in case that no sample and no pump

**Table 6.1:** Standard deviation of 50000 successively recorded pump–probe pairs at $2039\,\mathrm{cm}^{-1}$ according to the histograms illustrated in Fig. 6.11.

| measurement conditions | MCT | CPU | CPU - 5 pixel binned |
|:---:|:---:|:---:|:---:|
| no sample | 2.7 mOD | 8.1 mOD | 7.1 mOD |
| sample and pump-interaction | 3.7 mOD | 8.9 mOD | 7.7 mOD |

pulse have been utilized for CPU detection (blue), MCT detection (red), and again for CPU detection but with a binning of five adjacent pixels (green). The latter compensates for the discrepancy regarding the spectral coverage of both methods. The bottom row presents the results for the case that the flow through cuvette together with the sample were inserted and excited by a pump pulse. Table 6.1 subsumes the according standard deviations.

The distribution related to the CPU detection with no sample is three times broader than the one for MCT detection. In case of an inserted sample and pump-interaction, the distribution still is 2.4 times broader. The binning of five adjacent data points reduces the standard deviation of CPU detection with no sample by roughly 12%; in the measurement with sample and pump-interaction the deviation is reduced by 13%. Hence, in comparison to MCT detection, the distribution in the experiment for binned CPU detection with sample and pump-interaction is broadened by a factor of 2.1, the corresponding standard deviation is approximately twice the one for MCT detection. Provided that the alignment of the MIR OPA is executed properly, these values reflect the aspect that the fundamental $800\,\mathrm{nm}$ laser pulses can exhibit higher fluctuations than the output of the MIR OPA itself [109] and these instabilities are transferred to the CPU spectrum in the upconversion process. As a consequence, the signal-to-noise of the CPU detection method can be significantly improved if a scaling procedure is employed that normalizes individual CPU spectra with the spectrally integrated signal for every laser shot. In doing so, the standard deviation of the CPU detection with the binning of five adjacent data points is lower than the one of direct MCT detection, both for measurements with no sample and with sample and pump-interaction. For further explanations and results obtained by this normalization procedure see [4].

Assessing the absorption-change standard errors depending on the number of successively recorded pump–probe pairs both for the detection of the baseline and the changes in absorbance in a molecule, one can derive a value for the measurement time that is required to reach a desired noise level. Figure 6.12 illustrates double-logarithmic representations of the corresponding measurements. The left panel depicts the baseline-recording (no sample), the right panel the recording of absorption changes (sample and pump-interaction); the absorption-change standard errors in both panels have been evaluated for the single data point at $2039\,\mathrm{cm}^{-1}$ using the MCT detection (red), the CPU detection (blue), and the CPU detection with a binning of five adjacent pixels (green).

As the previous considerations already suggested, detection via the MCT array provides lower noise levels than the CPU detection, regardless of an applied binning. However, now one can estimate that it needs approximately six times the measurement time
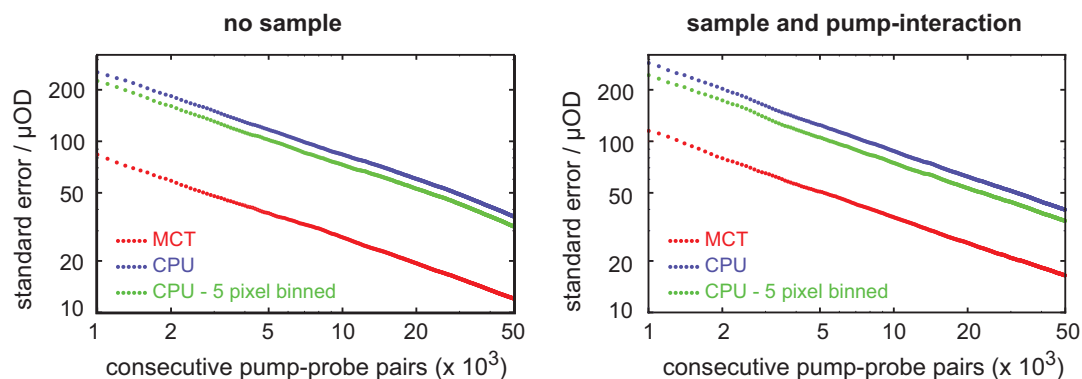
**Figure 6.12:** Standard errors of the absorption-change at $2039\,\mathrm{cm}^{-1}$ as a function of the number of successively recorded background-corrected pump–probe pairs for $\Delta\mathrm{Abs}{=}0$ (left graphic, no sample) and $\Delta\mathrm{Abs}{\approx}2\,\mathrm{mOD}$ (right graphic, sample and pump-interaction). Values for the MCT-detection are presented in red, for the CPU detection in blue, and for the CPU detection with a binning of five adjacent pixels in green. Note the double-logarithmic scale. Figure adapted with permission from [4]. © (2013) Optical Society of America.

with the CPU detection in order to achieve a data quality that is comparable to the detection via the MCT array. In case of a binning of five adjacent data points, the required measurement time still is elongated by a factor of approximately five. To find out how many pump–probe pairs have to be averaged to gain a specific noise level, one simply has to draw horizontal lines in the data of Figure 6.12 and look at the intersections for the corresponding detection technique. Again, normalization of the CPU spectra yields significant improvements so that the performance of MCT detection and CPU detection with an applied pixel binning become comparable with regard to signal-to-noise [4].

The tunability of the phase-matching condition inside the MgO(5%):LiNbO$_3$ crystal that transfers the MIR pulses into the visible spectral regime gives rise to another application of the CPU detection scheme. By adjustments on the crystal cut angle $\Theta$, the overall shape of the CPU probe spectrum can be modified. This might be beneficial for the purpose of investigating transient vibrational signatures that are spectrally separated in such a manner that they are precisely covered by the margins of the MIR spectrum. In such a scenario, the detector could saturate in the center part of the spectrum, whereas the spectral edges are barely detectable due to the comparatively low number of counts, which in turn deteriorates the signal-to-noise ratio. As a consequence, it seems desirable to be capable of pronouncing the wings of the spectrum with respect to the central part. To address this aspect, the Co$_4$CO$_{12}$ complex is well suited as it provides absorption bands separated by more than $200\,\mathrm{cm}^{-1}$ around 1860 and $2060\,\mathrm{cm}^{-1}$ but none in between (see Fig. 6.13a). With an MIR probe spectrum centered at $1940\,\mathrm{cm}^{-1}$ and providing a FWHM of $185\,\mathrm{cm}^{-1}$ (see Fig. 6.13b) it is possible to simultaneously detect absorption-change signals connected to both absorption bands. This is done with an averaging of 100000 pump–probe pairs in two different transient measurements: first, with a CPU spectrum for $\Theta = 45, 5°$ (see Fig. 6.13c; red spectrum), which corresponds to the optimal setting that transfers MIR pulses into the visible regime with the highest possible efficiency. However, in this configuration the intensity of the spectral margins is
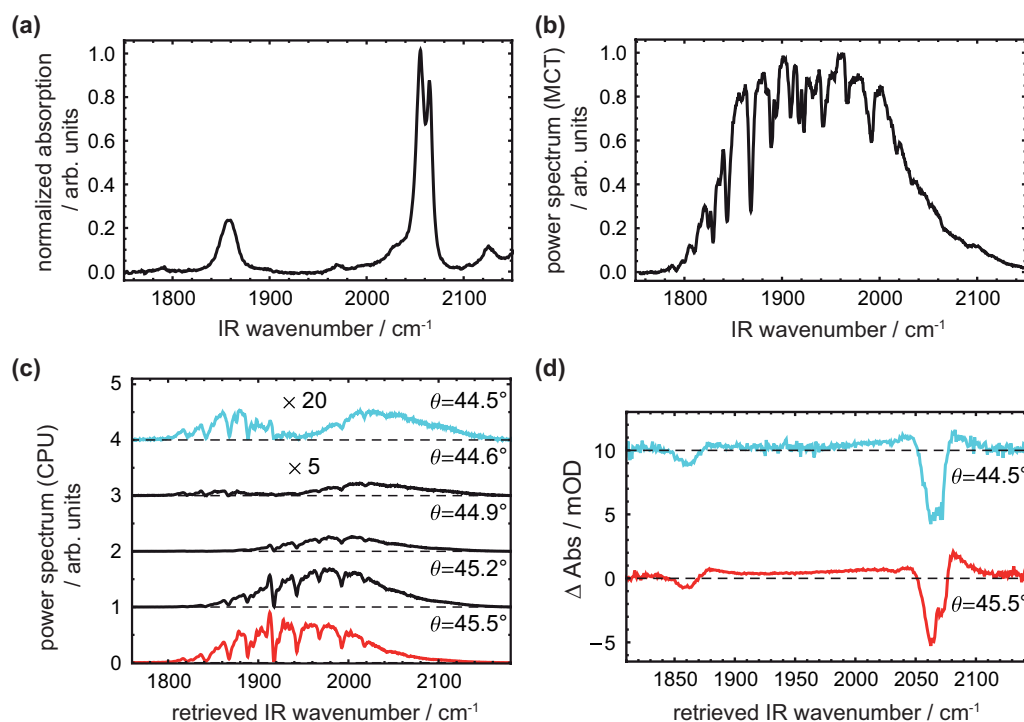
**Figure 6.13:** (a) MIR probe spectrum recorded by rotating the grating inside the IR spectrometer and thus scanning the central wavelength in 1 nm steps along a single HgCdTe diode. (b) FTIR absorption spectrum of $Co_4CO_{12}$ dissolved in dichloromethane. (c) CPU probe spectra generated by different phase-matching conditions due to varying crystal cut angles $\Theta$. (d) Transient absorption difference spectra of $Co_4CO_{12}$ at delay times of 6 ps, following an averaging of 100000 successive pump–probe pairs with two different CPU probe spectra, one generated by a phase-matching angle $\Theta = 44,5°$ (cyan, 10 mOD vertical offset), one by $\Theta = 45,5°$ (red). Figure reprinted with permission from [4]. © (2013) Optical Society of America.

clearly outreached by the central part. Therefore, for the second utilized CPU spectrum the crystal angle is slightly rotated to be $\Theta = 44,5°$ (see Fig. 6.13c; cyan spectrum). This modified CPU spectrum is in general less intensive but the spectral edges are more pronounced in comparison to the center part. Figure 6.13d presents the according transient absorption difference spectra at delay times of 6 ps recorded with the highly intensive CPU spectrum (red) and with the modified CPU spectrum (cyan). Both measurements reveal the same vibrational signatures, namely the GSB signals of the parent complex at 1860 and 2060 $cm^{-1}$. It is worth highlighting, that the noise level at the spectral margins is comparable in both measurements, although the modified CPU spectrum is 20 times less intensive than the spectrum derived from the optimal crystal setting. However, the noise in the central part of the difference spectra differs significantly, being worse under detection at $\Theta = 44,5°$. Figure 6.13c illustrates CPU spectra for further angle positions between the optimal and the modified case. Following the derivations from [12] in conjunction with the Sellmeier coefficients from [252], these measured spectra are very well confirmed by calculations of the SFG efficiency of a MgO(5%):LiNbO$_3$ with 450 $\mu$m

thichness for varying phase-matching angles. For further information in this regard, see [4].

To sum up, for the measuring of ultrafast changes of absorbance on the order of a few mOD in the MIR spectral regime two detection schemes have been juxtaposed. With a measurement routine that aimed at a high comparability between both techniques it has been revealed that the CPU detection via a CCD camera is a versatile and efficient alternative to the standard multichannel detection using a MCT photodiode array. Thereby, the upconversion process itself only causes negligible changes with regard to the spectral shape and bandwidth of the MIR laser pulses. Within the scope of exemplary UV-pump–MIR-probe measurements on different molecules in the liquid phase it became obvious that intensity fluctuations of the chirped beam are transferred to the MIR spectra in the course of the additional nonlinear upconversion process. This results in a significantly lower noise level in case of the direct MCT detection. However, the application of an appropriate normalization procedure for the CPU spectra can compensate for this issue, so that the detection of MIR signals via cost-effective and easy-to-handle CCD cameras yields a comparable signal-to-noise ratio, while the CPU technique still scores with its enhanced spectral resolution. Prospective studies might take advantage of the tunability of the phase-matching configuration of the CPU crystal. Corresponding to the experimental needs, the shape of the upconverted probe spectrum can be adjusted to fit the spectral distribution of the vibrational signatures under investigation.

# 7 Summary and outlook

The experimental technique predominantly employed within the scope of this thesis constitutes one subarea of femtochemistry: the time-resolved spectroscopy of photoinduced chemical reactions in the liquid phase by means of molecular signatures in the mid-infrared (MIR) spectral range. Probing transient vibrational states, i.e., dynamic changes in the vibrational motion of specific molecular subunits or functional groups allows for a distinct separation and assignment of measured signals to emerging molecular species. For this purpose, one key building block is indispensable, which most of the investigations carried out within the field of femtochemistry have in common: a coherent light source delivering ultrashort laser pulses with a temporal duration that matches the femtosecond time scale on which molecular motions typically occur. This instrumentation enables the observation of photoinduced chemical reactions from the starting point—the excitation event—to the appearance of intermediates to the final formation of stable photoproducts after several pico- or nanoseconds.

This work comprises the acquisition and presentation of time-resolved spectroscopic data related to promising molecular systems upon photoexcitation as well as the implementation and testing of experimental optical techniques both for the presented experiments but as well for experiments conceivable in the future. In addition, linear spectroscopy measurements and quantum-chemical simulations on the emerging chemical species have been carried out. In so doing, the primary processes and subsequently emerging reaction products of two compounds on a timescale of several nanoseconds after photoexcitation have been elucidated in great detail. Both compounds, the $[\text{Mn(CO)}_3(\text{tpm})]^+$ (tpm = tris(2-pyrazolyl)methane) CO-releasing molecule (CORM) and the 5-diazo Meldrum's acid (DMA), are of academic interest but in addition belong to molecular classes that might be utilized in the near future as dark-stable prodrugs under physiological conditions or that are already utilized in industrial chemistry procedures, respectively. The findings of both studies gave rise to implement and examine two techniques for prospective transient absorption experiments, namely the shaping and characterization of ultraviolet (UV) laser pulses and the recording of two-photon excitation spectra. Beyond that, since each of the depicted experiments is based on the detection of weak transient absorption signals in the MIR spectral region, two different detection schemes, via chirped-pulse upconversion (CPU) on the one hand and via direct multichannel MCT detection on the other hand, have been juxtaposed at the conclusion of this work. Since both techniques are suitable in femtosecond pump–probe measurements but thereby exhibit individual strengths and weaknesses, a comparative study provides clarification of the respective pros and cons.

The first study introduced within this work investigates the complex photochemistry of DMA [1], a photoactive compound used in lithography and industrial chemistry. By

femtosecond MIR transient absorption spectroscopy covering several nanoseconds, the light-induced dynamics and ultrafast formation of several photoproducts from the manifold of reaction pathways have been disclosed to form a coherent picture of the overall reaction scheme. After UV excitation of DMA dissolved in methanol to the second excited state $S_2$, 70% of excited molecules relax back to the $S_0$ ground state. In competing processes, they can either undergo an intramolecular Wolff rearrangement to form ketene, which reacts with a solvent molecule to an enol intermediate and further to carboxylate ester, or they first relax to the DMA $S_1$ state, from where they can isomerize to a diazirine. The third competing reaction channel, having the lowest quantum efficiency with respect to the first two channels, is the formation of a singlet carbene out of the $S_1$ state. From there an ylide can arise or, via an intersystem crossing, the triplet form of the carbene follows. Whereas the primary reaction steps occur on a picosecond timescale, the subsequently arising intermediates and stable photoproducts are formed within a few hundreds to thousands of picoseconds. For a reliable identification of the involved compounds, density functional theory calculations on the normal modes and Fourier-transform infrared spectroscopy of the reactant and the photoproducts in the chemical equilibrium accompany the analysis of the transient spectra. Additional experiments in ethanol and isopropanol led to slight spectral shifts as well as elongated time constants due to steric hindrance in transient spectra connected with the ester formation channel, further substantiating the assignment of the occurring reaction pathways and photoproducts.

The study demonstrated that the combination of linear and time-resolved spectroscopic measurements in conjunction with quantum-chemical calculations constitutes a powerful tool to unravel even highly complex photoreactions exhibiting multiple consecutive intermediate states within parallel reaction pathways. Although some of the individual reaction steps, for example the ketene formation via Wolff rearrangement, have been observed on ultrashort time scales before, this work encompassed the observation of the whole set of appearing photoproducts of DMA in different alcohol solutions within several nanoseconds. In this sense, the ultrafast photochemistry of DMA represents a prototype example for a multisequential reaction scheme, elucidated by the capabilities of femtosecond MIR spectroscopy.

With a modified instrumentation concerning amongst others the system delivering the fundamental laser pulses or the generation of the UV pump pulses, the next objective within this work was to elucidate the primary processes upon UV irradiation of a manganese tricarbonyl CORM in aqueous environment [2, 3]. The time-resolved experiment was performed with two different pump wavelengths and furthermore supported by linear spectroscopy methods and time-dependent density functional theory (TDDFT) calculations on the excited states as well as DFT calculations on the ground states. The measurements revealed that irradiating the compound with UV excitation pulses primarily leads to ultrafast photolysis of one CO ligand. Geminate recombination may occur within one picosecond but it remains a minor process as the photolyzed CO group is liberated and the unoccupied coordination site is predominantly filled by an incoming solvent molecule. There was no evidence for hot CO bands, i.e., the remaining CO ligands—in the dicarbonyl photoproduct as well as in the intact CORM—are not vibrationally excited through the UV excitation of the CORM. According to this, the

excess energy merges into low-frequency vibrational modes associated with the molecule as a whole. Since studies on a macroscopic scale at irradiation times of several minutes prove that UV irradiation eventually leads to the release of two or even all three CO ligands, further loss of CO most likely necessitates manganese oxidation or another interaction with light. To clarify the latter, a consecutive UV pulse was employed in order to excite the photoproducts subsequent to the initial pump interaction. However, the data obtained was not instructive enough to definitely exclude the manganese oxidation being responsible for the loss of further CO groups. Besides the exchange of a CO group by a solvent molecule or the geminate recombination, the employment of two different excitation wavelengths in combination with findings derived from the TDDFT calculations suggested another reaction process, namely the possibility that the excitation does not lead to any bond cleavage at all. As the CORM under investigation is tissue-selective and cytotoxic against cancer cells, knowledge of these first photoinduced reaction steps is essential for a full understanding of its biological activity.

Inspired by these two studies, experimental techniques for prospective transient absorption measurements have been implemented and tested within preparative measurements. First, in the course of a UV-pump–MIR-probe experiment with specifically tailored excitation pulses, one could pursue the aim of coherently controlling the outcome of a photoreaction in the liquid phase. Out of the rich photochemistry of DMA the vibrational signature of a particular molecular species might thereby serve as a feedback signal, which is a central part of a learning loop that adaptively determines the pulse shape that steers the quantum mechanical system upon photoexcitation into a desired direction. This motivated the installation and testing of devices by means of which the shaping and characterization of ultrashort laser pulses in the UV could be performed. Second, motivated by the biological applications of CORMs, one can imagine a scenario where a certain amount of CORMs is deposited inside cancerous tissue. Since the activation of CO loss by means of UV pulses is not possible due to the absorption characteristics of biological tissue, the simultaneous excitation via two photons from the visible spectral regime seems appealing. However, success or failure of such an application depends on whether the deposited compound efficiently absorbs two photons simultaneously, i.e., whether the two-photon absorption cross section is large enough. Therefore, a setup to record two-photon excitation spectra under full consideration of the crucial laser pulse parameters like the pulse duration, energy and central wavelength was arranged and tested. The first results were obtained with a commercially available reference system ($Mn_2CO_{10}$) but the setup as well as the described measurement and data analysis procedure can easily be applied to record the two-photon absorption cross section of more promising molecular systems. Third, as the detection of probe pulses in the MIR spectral region is part of each time-resolved measurement throughout this thesis, a comparison between the newly established technique of CPU and direct multi-channel MCT detection is presented by means of pump–probe experiments on $Mn_2CO_{10}$ and $Co_4CO_{12}$ with a 1 kHz shot-to-shot data acquisition [4]. It was shown that the CPU detection technique scores with its high spectral resolution and coverage of the easy-to-handle and more cost-effective CCD detectors. On the other hand, in the course of the additional nonlinear upconversion process intensity fluctuations of the chirped fundamental pulses are transferred to the probe spectrum in the visible regime. This

entails a lower signal-to-noise ratio than the direct MCT detection, which can be compensated by an additional normalization procedure applied to the CPU probe pulses. As a consequence, the CPU detection scheme offers more flexibility for future investigations employing MIR probe pulses. This is of great importance for many applications within the presented field of femtochemistry as a huge variety of time-resolved investigations on a multitude of systems in the liquid phase is based on the detection of weak transient absorption signals in the MIR spectral region.

# 8 Zusammenfassung und Ausblick

Die vorrangig im Rahmen dieser Arbeit eingesetzte experimentelle Technik stellt ein Teilgebiet der Femtochemie dar: die zeitaufgelöste Spektroskopie photoinduzierter chemischer Reaktionen in flüssiger Phase durch molekulare Charakteristika im mittleren infraroten (MIR) Spektralbereich. Die Detektion transienter Vibrationszustände, das heißt sich zeitlich verändernder Kernbewegungen von bestimmten molekularen Untereinheiten oder funktionellen Gruppen, ermöglicht es, Messsignale zu differenzieren und auftretenden Molekülspezies genau zuzuordnen. Zu diesem Zweck ist ein zentrales Element unabdingbar, das die meisten Experimente im Forschungsgebiet der Femtochemie gemein haben: eine kohärente Lichtquelle, die ultrakurze Laserpulse generiert, welche eine zeitliche Dauer auf der Femtosekunden-Zeitskala besitzen auf welcher sich Kernbewegungen typischerweise abspielen. Dieses Instrument ermöglicht die Beobachtung von photoinduzierten chemischen Reaktionen von dem Startpunkt an – der eigentlichen Anregung – über das Auftreten von Zwischenprodukten bis hin zu der abschließenden Herausbildung von stabilen Photoprodukten nach mehreren Piko- oder Nanosekunden.

Die vorliegende Arbeit umfasst die Beschreibung der Aufnahme und die Darstellung von zeitaufgelösten spektroskopischen Daten an molekularen Systemen, die vielversprechende Eigenschaften nach einer optischen Anregung zeigen. Darüber hinaus beschreibt sie den Aufbau und die Prüfung von experimentellen optischen Messmethoden, die sowohl für die hier präsentierten als auch für zukünftige, erweiterte Experimente der Anrege-Abfrage-Spektroskopie dienen. Zusätzlich wurden lineare Absorptionsmessungen und quantenchemische Simulationen mittels der Dichtefunktionaltheorie (DFT) durchgeführt, um auftretende chemische Spezies eindeutig identifizieren zu können. Auf diese Weise wurden sowohl die anfänglichen Reaktionsschritte als auch die darauffolgenden Reaktionsprodukte zweier Stoffe auf einer Zeitskala von mehreren Nanosekunden nach einer Photoanregung sehr detailliert dargestellt. Die untersuchten Substanzen sind zum einen $[Mn(CO)_3(tpm)]^+$ (tpm = tris(2-pyrazolyl)methan), das zur Gruppe der sogenannten CO-releasing molecules (CORM) gehört, und zum anderen 5-Diazo-Meldrumsäure (DMA). Beide sind von akademischem Interesse, gehören darüber hinaus aber zu anwendungsbezogenen Stoffgruppen, die im Falle der CORMs in naher Zukunft als Prodrug unter physiologischen Bedingungen eingesetzt werden könnten. Im Falle des DMA gibt es bereits Anwendungen in der chemischen Industrie. Die Erkenntnisse dieser beiden Untersuchungen führten hinsichtlich zukünftiger Anrege-Abfrage-Studien zu dem Aufbau und der Inbetriebnahme zweier weiterer experimenteller Techniken, die einerseits der Formung und Charakterisierung von Femtosekundenlaserpulsen im ultravioletten (UV) Spektralbereich und andererseits zur Aufnahme von Zwei-Photonen-Anregespektren dienen. Da jedes der dargestellten Experimente auf der Detektion von schwachen transienten Absorptionssignalen im MIR Spektralbereich beruht, wurden des Weiteren am

Ende dieser Arbeit zwei verschiedene Aufnahmemethoden gegenübergestellt: die Detektion mittels der Aufkonversion durch gechirpte Laserpulse (chirped-pulse upconversion, CPU) und die direkte Detektion von MIR-Laserpulsen mittels eines Arrays von Quecksilber-Cadmium-Tellurid-Detektoren (mercury cadmium telluride, MCT). Da beide Detektionstechniken für die Anrege-Abfrage-Spektroskopie geeignet sind, dabei jedoch unterschiedliche Stärken und Schwächen zeigen, schaffte die vergleichende Untersuchung diesbezüglich Klarheit.

In der ersten Studie wurde die komplexe Photochemie von DMA untersucht [1], das als photoaktive Substanz in lithographischen Prozessen verwendet wird. Mit transienter MIR-Absorptionsspektroskopie wurden die lichtinduzierte Bildung und ultraschnellen Dynamiken von zahlreichen Photoprodukten innerhalb eines Zeitfensters von einigen Nanosekunden enthüllt. Dies lieferte ein stimmiges Bild des gesamten Reaktionsschemas, welches aus mehreren Reaktionspfaden besteht. Durch einen UV-Laserpuls wird in Methanol gelöstes DMA in den zweiten elektronischen Zustand $S_2$ angeregt. 70% dieser Moleküle relaxieren wieder in den Grundzustand $S_0$, die restlichen 30% verteilen sich auf drei konkurrierende Reaktionspfade. Zum einen können die angeregten Moleküle über eine intramolekulare Wolff-Umlagerung zu Keten umgeformt werden. Dieses wiederum lagert ein Lösungsmittelmolekül an und bildet damit ein Enol als vorübergehenden Zwischenzustand. Schließlich tautomerisiert daraus Carbonsäureester. Zum anderen relaxiert ein Teil der angeregten Moleküle zunächst in den $S_1$-Zustand des DMA, von wo aus eine Isomerisierung zu Diazirin stattfindet. Der dritte parallele Reaktionspfad weist im Vergleich zu den ersten beiden die geringste Quanteneffizienz auf und führt über den $S_1$-Zustand zu einem Singulett-Carben. Dieses kann sich einerseits zu einem Ylid umwandeln, oder mittels eines Intersystem Crossing in ein Triplett-Carben übergehen. Während die primären Reaktionsschritte innerhalb einiger Pikosekunden ablaufen, werden die daraufhin erscheinenden Zwischenzustände und Endprodukte innerhalb einiger hundert bis tausend Pikosekunden gebildet. Für eine zuverlässige Identifizierung der involvierten Molekülspezies wurde die Analyse der zeitaufgelösten Daten sowohl durch DFT-Simulationen als auch durch lineare Absorptionsmessungen ergänzt. Beide Methoden lieferten wichtige Informationen über die Absorptionscharakteristika des Edukts sowie der auftretenden Zwischen- und Endprodukte. Wegen der sterischen Hinderung zeigten weitere zeitaufgelöste Absorptionsmessungen an in Ethanol oder Isopropanol gelöstem DMA geringe spektrale Verschiebungen und auch verlängerte Zeitkonstanten im Falle der Reaktionsprodukte, die mit der Bildung des Ester verbunden waren. Dies untermauerte um ein Weiteres die Zuordnung der jeweiligen Reaktionspfade und Photoprodukte.

Die Studie an DMA zeigte, dass die Kombination aus linearer und zeitaufgelöster Spektroskopie in Verbindung mit quantenchemischen Berechnungen ein mächtiges Werkzeug darstellt, um sogar äußerst komplexe Photoreaktionen zu entschlüsseln, die mehrere aufeinanderfolgende Zwischenzustände innerhalb parallel verlaufender Reaktionspfade aufweisen. Obwohl einige der einzelnen Reaktionsschritte wie zum Beispiel die Bildung des Ketens nach der Wolff-Umlagerung bereits auf ultrakurzen Zeitskalen untersucht wurden, umfasst diese Arbeit die Beobachtung aller auftretenden Photoprodukte des DMA gelöst in verschiedenen Alkoholen innerhalb einiger Nanosekunden nach der Photoanregung. In diesem Sinne stellt die ultraschnelle Photochemie von DMA ein Mu-

sterbeispiel für ein multisequentielles Reaktionsschema dar, das dank der Stärken der zeitaufgelösten MIR-Absorptionsspektroskopie entschlüsselt werden konnte.

Mit einer modifizierten experimentellen Ausstattung, unter anderem die Systeme betreffend, welche die Fundamentalstrahlung oder die UV-Anregungspulse generierten, war das nächste Ziel dieser Arbeit die primären photoinduzierten Prozesse eines Tricarbonyl-mangan-CORM in wässriger Lösung zu erforschen [2, 3]. Die zeitaufgelösten Experimente wurden mit zwei verschiedenen UV-Anregungswellenlängen durchgeführt und zusätzlich unterstützt durch lineare Absorptionsmessungen und zeitaufgelöste DFT-Berechnungen (TDDFT) der angeregten elektronischen Zustände sowie DFT-Berechnungen der Grundzustände. Die Messungen zeigten, dass die UV-Anregung der Substanz in erster Linie die ultraschnelle Photolyse einer einzelnen Carbonylgruppe zur Folge hat. Eine geminale Rekombination zum ursprünglichen Komplex kann innerhalb einer Pikosekunde auftreten. Jedoch ist dies ein untergeordneter Prozess, da die abgetrennte Carbonylgruppe freigesetzt wird und die unbesetzte Koordinationsstelle vorrangig von einem Lösungsmittelmolekül belegt wird. Sogenannte heiße Carbonyl-Absorptionsbanden wurden nicht detektiert. Das bedeutet, dass die verbleibenden CO-Liganden – sowohl im Falle des Dicarbonyl-Photoprodukts als auch im Falle des intakten CORM – durch die Anregungspulse nicht vibrationsangeregt werden. Demnach wird die Überschussenergie in Vibrationsmoden mit geringer Frequenz transferiert, was einer Schwingung des gesamten Moleküls entspricht. Da Untersuchungen auf makroskopischer Ebene mit Bestrahlungszeiten von mehreren Minuten zeigen, dass UV-Anregung letztlich zur Freisetzung von zwei oder sogar allen drei CO-Liganden führt, bedarf es zur weiteren Photolyse von CO höchstwahrscheinlich einer Oxidation des Mangan oder einer weiteren Wechselwirkung mit Licht. Um letzteres aufzuklären, wurde ein zweiter UV-Anregungspuls in Folge des ersten Anregungspulses eingesetzt. Dieser zweite Puls sollte die Photoprodukte des ersten Pulses noch einmal anregen. Jedoch waren die daraus erhaltenen Messdaten nicht aufschlussreich genug, um die Manganoxidation als Ursache für den Verlust von weiteren CO-Liganden ausschließen zu können. Neben dem Austauch einer CO-Gruppe mit einem Lösungsmittelmolekül sowie der geminalen Rekombination, wurde durch den Einsatz zwei verschiedener Anregungswellenlängen in Verbindung mit den Ergebnissen der TDDFT-Berechnungen die Möglichkeit eines weiteren Reaktionspfades entdeckt: es ist auch möglich, dass die Anregung des CORM zu überhaupt keinem Bindungsbruch führt und insofern ein Teil der angeregten Moleküle völlig intakt bleibt. Da bereits bekannt war, dass das untersuchte CORM gewebsselektiv ist und zytotoxisch gegenüber Krebszellen wirkt, sind die gesammelten Erkenntnisse bezüglich der primären photoinduzierten Reaktionsschritte essentiell, um die biologische Aktivität der Substanz vollständig zu verstehen.

Angeregt durch diese beiden Studien wurden experimentelle Techniken für weiterführende transiente Absorptionsmessungen implementiert und in vorbereitenden Messungen getestet. Erstens, im Rahmen eines UV-Anrege-MIR-Abfrage-Experiments mit speziell geformten Anregungspulsen könnte man das Ziel verfolgen, mittels kohärenter Kontrolle den Ausgang einer Photoreaktion in flüssiger Phase zu steuern. Dazu benötigt man ein Rückkopplungssignal, das als ein zentrales Element einer Lernschleife darüber Aufschluss gibt, ob die iterativ angepassten Pulsformen den Reaktionsverlauf in die gewünschte Richtung lenken. Eines der zahlreichen Absorptionssignale der reichhalti-

gen Photochemie von DMA kann dabei als Rückkopplungssignal dienen. Dieser Ansatz motivierte den Aufbau und erste Tests von Instrumenten, mit denen die Formung und Charakterisierung von ultrakurzen UV-Laserpulsen durchführbar ist. Als zweites, wegen der biologischen Anwendungsmöglichkeiten von CORMs, kann man sich eine Situation vorstellen, in der eine gewisse Menge an CORMs in krebsartigem Gewebe deponiert wird. Da die Aktivierung der zytotoxischen CO-Abgabe durch UV-Laserpulse wegen des Absorptionsverhaltens von biologischem Gewebe nicht möglich ist, wäre es naheliegend die Anregung durch zwei gleichzeitig aufgenommene Photonen im sichtbaren Spektralbereich durchzuführen. Jedoch hängen Erfolg oder Misserfolg einer solchen Anwendung davon ab, ob die eingelagerten CORMs auch auf effiziente Weise zwei Photonen gleichzeitig absorbieren, das heißt ob der Zwei-Photonen-Absorptionsquerschnitt groß genug ist. Deshalb wurde ein Messaufbau konstruiert und getestet, mit welchem man unter vollständiger Berücksichtigung der entscheidenden Laserpulsparameter (Pulsdauer, Pulsenergie und zentrale Wellenlänge) Zwei-Photonen-Anregespektren aufzeichnen kann. Die ersten Resultate wurden anhand eines kommerziell erhältlichen Referenzmoleküls ($Mn_2CO_{10}$) aufgenommen. Der Messaufbau sowie die beschriebene Messroutine und Datenauswertung lassen sich aber ebenso bei anderen Molekülen anwenden, so dass der Zwei-Photonen-Absorptionsquerschnitt von aussichtsreicheren Substanzen bestimmt werden kann. An dritter Stelle, da die Detektion von Abfragelaserpulsen im MIR Spektralbereich teil eines jeden zeitaufgelösten Experiments im Rahmen dieser Arbeit ist, wurde eine Vergleichsstudie durchgeführt, welche die neu entwickelte Technik der CPU einer direkten Aufnahme mittels eines MCT-Arrays gegenüberstellt. Anhand von Anrege-Abfrage-Messungen an $Mn_2CO_{10}$ und $Co_4CO_{12}$ mit einer 1 kHz Schuss-zu-Schuss Datenaufnahme [4] wurde gezeigt, dass die CPU-Detektionsmethode mit einer hohen spektralen Auflösung sowie Abdeckung punkten kann und die dabei eingesetzten CCD-Detektoren zudem einfach in der Handhabung und vergleichsweise kostengünstig sind. Auf der anderen Seite übertragen sich in dem zusätzlichen nichtlinearen Aufkonversionsprozess Intensitätsschwankungen von den gechirpten Fundamentallaserpulsen auf die Abfragelaserpulse im sichtbaren Spektralbereich. Dies bringt zwar ein geringeres Signal-Rausch-Verhältnis mit sich als bei der direkten MCT-Detektion, jedoch lässt sich dieser Nachteil kompensieren indem man ein geeignetes Normierungsverfahren auf die CPU-Abfragepulse anwendet. Demnach bietet die CPU-Detektionsmethode mehr Flexibilität hinsichtlich zukünftiger Anwendungen, in denen MIR-Abfragepulse Verwendung finden. Das ist von großer Bedeutung für viele Anwendungen innerhalb des präsentierten Teilgebietes der Femtochemie, da nicht nur ein Großteil der Experimente die in dieser Arbeit vorgestellt wurden auf der Detektion von schwachen transienten Absorptionssignalen im MIR-Spektralbereich basieren, sondern darüber hinaus eine große Vielfalt an zeitaufgelösten Untersuchungen von vielen verschiedenen System in flüssiger Phase existiert.

# Bibliography

[1] P. Rudolf, J. Buback, J. Aulbach, P. Nuernberger, and T. Brixner.
*Ultrafast Multisequential Photochemistry of 5-Diazo Meldrum's Acid.*
Journal of the American Chemical Society **132**, 15213–15222 (2010).

[2] P. Rudolf, F. Kanal, J. Knorr, C. Nagel, J. Niesel, T. Brixner, U. Schatzschneider, and P. Nuernberger.
*Ultrafast Photochemistry of a Manganese-Tricarbonyl CO-Releasing Molecule (CORM) in Aqueous Solution.*
The Journal of Physical Chemistry Letters **4**, 596–602 (2013).

[3] P. Rudolf, F. Kanal, D. Gehrig, J. Niesel, T. Brixner, U. Schatzschneider, and P. Nuernberger.
*Femtosecond Mid-Infrared Study of the Aqueous Solution Photochemistry of a CO-Releasing Molecule (CORM).*
EPJ Web of Conferences **41**, 05004 (2013).

[4] J. Knorr, P. Rudolf, and P. Nuernberger.
*A comparative study on chirped-pulse upconversion and direct multichannel MCT detection.*
Optics Express **21**, 30693–30706 (2013).

[5] C. Vogel.
*Die letzte Krankheit Goethe's, beschrieben und nebst einigen andern Bemerkungen über denselben, mitgetheilt von Dr. Carl Vogel, Grossherzogl. Sächsischem Hofrathe und Leibarzte zu Weimar.*
Journal der practischen Heilkunde (1833) 3-32, Darmstadt: E. Merck AG (1961).

[6] J. Eichler and H. J. Eichler.
*Laser, Bauformen, Strahlführung, Anwendungen* (2010).

[7] C. Rullière.
*Femtosecond Laser Pulses: Principles and Experiments.*
Springer-Verlag GmbH (2004).

[8] M. Wollenhaupt, A. Assion, and T. Baumert.
*Femtosecond Laser Pulses: Linear Properties, Manipulation, Generation and Measurement.*
In *Springer Handbook of Lasers and Optics*, pp. 937–983. Springer Science+Business Media, New York (2007).

[9] J.-C. Diels and W. Rudolph.
*Ultrashort Laser Pulse Phenomena.*
Academic Press, Burlington, 2 edn. (2006).

[10] A. E. Siegman.
*Lasers.*
University Science Books, Sausalito (1986).

[11] E. Hecht.
*Optik.*
Oldenbourg Wissenschaftsverlag, München, 4 edn. (2005).

[12] R. W. Boyd.
     *Nonlinear Optics.*
     Academic Press, Burlington, 3 edn. (2008).

[13] G. Sansone, E. Benedetti, F. Calegari, C. Vozzi, L. Avaldi, R. Flammini, L. Poletto, P. Villoresi,
     C. Altucci, R. Velotta, S. Stagira, S. De Silvestri, and M. Nisoli.
     *Isolated Single-Cycle Attosecond Pulses.*
     Science **314**, 443–446 (2006).

[14] T. Brixner.
     *Adaptive Femtosecond Quantum Control.*
     Dissertation, Julius-Maximilians-Universität Würzburg (2001).

[15] F. Träger.
     *Springer Handbook of Lasers and Optics.*
     Springer-Verlag GmbH (2007).

[16] W. Demtröder.
     *Laserspektroskopie: Grundlagen und Techniken.*
     Springer, 5., erw. u. neubearb. aufl. edn. (2007).

[17] Y. R. Shen.
     *Principles of Nonlinear Optics.*
     Wiley & Sons, wiley classics edn. (2002).

[18] J. E. Midwinter and J. Warner.
     *The effects of phase matching method and of uniaxial crystal symmetry on the polar distribution
     of second-order non-linear optical polarization.*
     British Journal of Applied Physics **16**, 1135 (1965).

[19] D. Meschede.
     *Optics, light and lasers.*
     Physics textbook. Wiley-VCH, Weinheim, 2., rev. and enlarged edn. (2007).

[20] I. Buchvarov, A. Trifonov, and T. Fiebig.
     *Toward an understanding of white-light generation in cubic media - polarization properties across
     the entire spectral range.*
     Optics Letters **32**, 1539–1541 (2007).

[21] R. R. Alfano.
     *The Supercontinuum Laser Source.*
     Springer, New York, 2nd edn. (2006).

[22] A. L. Gaeta.
     *Catastrophic Collapse of Ultrashort Pulses.*
     Physical Review Letters **84**, 3582–3585 (2000).

[23] J. E. Rothenberg.
     *Space-time focusing: breakdown of the slowly varying envelope approximation in the self-focusing
     of femtosecond pulses.*
     Optics Letters **17**, 1340–1342 (1992).

[24] A. Monmayrant, S. Weber, and B. Chatel.
     *A newcomer's guide to ultrashort pulse shaping and characterization.*
     Journal of Physics B: Atomic, Molecular and Optical Physics **43**, 103001 (2010).

[25] A. M. Weiner.
*Ultrafast optical pulse shaping: A tutorial review.*
Optics Communications **284**, 3669–3692 (2011).

[26] A. M. Weiner, D. E. Leaird, J. S. Patel, and J. R. Wullert.
*Programmable femtosecond pulse shaping by use of a multielement liquid-crystal phase modulator.*
Optics Letters **15**, 326–328 (1990).

[27] A. M. Weiner.
*Femtosecond pulse shaping using spatial light modulators.*
Review of Scientific Instruments **71**, 1929 (2000).

[28] C. W. Hillegas, J. X. Tull, D. Goswami, D. Strickland, and W. S. Warren.
*Femtosecond laser pulse shaping by use of microsecond radio-frequency pulses.*
Optics Letters **19**, 737–739 (1994).

[29] M. A. Dugan, J. X. Tull, and W. S. Warren.
*High-resolution acousto-optic shaping of unamplified and amplified femtosecond laser pulses.*
Journal of the Optical Society of America B **14**, 2348–2358 (1997).

[30] F. Verluise, V. Laude, J.-P. Huignard, P. Tournois, and A. Migus.
*Arbitrary dispersion control of ultrashort optical pulses with acoustic waves.*
Journal of the Optical Society of America B **17**, 138–145 (2000).

[31] F. Verluise, V. Laude, Z. Cheng, C. Spielmann, and P. Tournois.
*Amplitude and phase control of ultrashort pulses by use of an acousto-optic programmable dispersive filter: pulse compression and shaping.*
Optics Letters **25**, 575–577 (2000).

[32] D. Kaplan and P. Tournois.
*Theory and performance of the acousto optic programmable dispersive filter used for femtosecond laser pulse shaping.*
Journal de Physique IV **12**, Pr5–69/75 (2002).

[33] S. Coudreau, D. Kaplan, and P. Tournois.
*Ultraviolet acousto-optic programmable dispersive filter laser pulse shaping in KDP.*
Optics Letters **31**, 1899–1901 (2006).

[34] Fastlite.
*Theoretical Overview of the Dazzler™Device: User's Manual* (2006).

[35] A. Monmayrant, A. Arbouet, B. Girard, B. Chatel, A. Barman, B. J. Whitaker, and D. Kaplan.
*AOPDF-shaped optical parametric amplifier output in the visible.*
Applied Physics B **81**, 177–180 (2005).

[36] P. Tournois.
*Design of acousto-optic programmable filters in mercury halides for mid-infrared laser pulse shaping.*
Optics Communications **281**, 4054–4056 (2008).

[37] D. J. McCabe, D. R. Austin, A. Tajalli, S. Weber, I. A. Walmsley, and B. Chatel.
*Space-time coupling of shaped ultrafast ultraviolet pulses from an acousto-optic programmable dispersive filter.*
Journal of the Optical Society of America B **28**, 58–64 (2011).

[38]  N. Krebs, R. Probst, and E. Riedle.
      *Sub-20 fs pulses shaped directly in the UV by an acousto-ptic programmable dispersive filter.*
      Optics Express **18**, 6164–6171 (2010).

[39]  A. Reuß.
      *Aufbau einer Versuchsanordnung zur Kontrolle bimolekularer chemischer Reaktion mit geformten UV-Pulsen.*
      Diplomarbeit, Julius-Maximilians-Universität Würzburg (2011).

[40]  D. Kane and R. Trebino.
      *Characterization of arbitrary femtosecond pulses using frequency-resolved optical gating.*
      Quantum Electronics, IEEE Journal of **29**, 571–579 (1993).

[41]  R. Trebino, K. W. DeLong, D. N. Fittinghoff, J. N. Sweetser, M. A. Krumbügel, B. A. Richman, and D. J. Kane.
      *Measuring ultrashort laser pulses in the time-frequency domain using frequency-resolved optical gating.*
      Review of Scientific Instruments **68**, 3277–3295 (1997).

[42]  R. Trebino.
      *Frequency-Resolved Optical Gating: The Measurement of Ultrashort Laser Pulses.*
      Springer Netherlands, Har/Cdr edn. (2002).

[43]  S. Linden, H. Giessen, and J. Kuhl.
      *XFROG - A new method for amplitude and phase characterization of weak ultrashort pulses.*
      PHYSICA STATUS SOLIDI B-BASIC RESEARCH **206**, 119—124 (1998).

[44]  S. Linden, J. Kuhl, and H. Giessen.
      *Amplitude and phase characterization of weak blue ultrashort pulses by downconversion.*
      Optics Letters **24**, 569–571 (1999).

[45]  K. W. DeLong, D. N. Fittinghoff, R. Trebino, B. Kohler, and K. Wilson.
      *Pulse retrieval in frequency-resolved optical gating based on the method of generalized projections.*
      Optics Letters **19**, 2152–2154 (1994).

[46]  F. Schwabl.
      *Quantenmechanik.*
      Springer, Berlin, 6. a., korr. nachdr. 2004 edn. (2007).

[47]  D. Tannor.
      *Introduction to Quantum Mechanics: A Time-Dependent Perspective.*
      University Science Books, Sausalito (2007).

[48]  H. Haken.
      *Molekülphysik und Quantenchemie.*
      Springer-Lehrbuch. Springer, Berlin [u.a.] (2006).

[49]  W. Demtröder.
      *Experimentalphysik, Bd. 3. Atome, Moleküle und Festkörper.*
      Springer, Berlin, 3., überarb. a. edn. (2005).

[50]  F. Bernardi, M. Olivucci, and M. A. Robb.
      *Potential energy surface crossings in organic photochemistry.*
      Chemical Society Reviews **25**, 321–328 (1996).

[51] D. R. Yarkony.
     *Nonadiabatic Quantum Chemistry-Past, Present, and Future.*
     Chemical Reviews **112**, 481–498 (2012).

[52] G. A. Voth and R. M. Hochstrasser.
     *Transition State Dynamics and Relaxation Processes in Solutions: A Frontier of Physical Chemistry.*
     The Journal of Physical Chemistry **100**, 13034–13049 (1996).

[53] T. Schrader, A. Sieg, F. Koller, W. Schreier, Q. An, W. Zinth, and P. Gilch.
     *Vibrational relaxation following ultrafast internal conversion: comparing IR and Raman probing.*
     Chemical Physics Letters **392**, 358–364 (2004).

[54] E. T. Nibbering, H. Fidder, and E. Pines.
     *Ultrafast Chemistry: Using Time-Resolved Vibrational Spectroscopy for Interrogation of Structural Dynamics.*
     Annual Review of Physical Chemistry **56**, 337–367 (2005).

[55] D. Laage and J. T. Hynes.
     *A Molecular Jump Mechanism of Water Reorientation.*
     Science **311**, 832–835 (2006).

[56] J. T. King, M. R. Ross, and K. J. Kubarych.
     *Water-Assisted Vibrational Relaxation of a Metal Carbonyl Complex Studied with Ultrafast 2D-IR.*
     The Journal of Physical Chemistry B **116**, 3754–3759 (2012).

[57] J. T. King, C. R. Baiz, and K. J. Kubarych.
     *Solvent-Dependent Spectral Diffusion in a Hydrogen Bonded "Vibrational Aggregate".*
     The Journal of Physical Chemistry A **114**, 10590–10604 (2010).

[58] J. T. King, J. M. Anna, and K. J. Kubarych.
     *Solvent-hindered intramolecular vibrational redistribution.*
     Phys. Chem. Chem. Phys. **13**, 5579–5583 (2011).

[59] M. Khalil, N. Demirdöven, and A. Tokmakoff.
     *Coherent 2D IR spectroscopy: Molecular structure and dynamics in solution.*
     The Journal of Physical Chemistry A **107**, 5258–5279 (2003).

[60] N. T. Hunt.
     *2D-IR spectroscopy: ultrafast insights into biomolecule structure and function.*
     Chemical Society Reviews **38**, 1837–1848 (2009).

[61] K. Kwak, S. Park, I. J. Finkelstein, and M. D. Fayer.
     *Frequency-frequency correlation functions and apodization in two-dimensional infrared vibrational echo spectroscopy: A new approach.*
     The Journal of Chemical Physics **127**, 124503 (2007).

[62] D. G. Osborne and K. J. Kubarych.
     *Rapid and Accurate Measurement of the Frequency–Frequency Correlation Function.*
     The Journal of Physical Chemistry A **117**, 5891–5898 (2013).

[63] M. Bixon and J. Jortner.
     *Intramolecular Radiationless Transitions.*
     The Journal of Chemical Physics **48**, 715–726 (1968).

[64] R. G. Parr and W. Yang.
     *Density-Functional Theory of Atoms and Molecules.*
     Oxford University Press (1989).

[65] W. Koch and M. C. Holthausen.
     *A chemist's guide to density functional theory.*
     Wiley-VCH, Weinheim; New York (2001).

[66] S. Schinzel.
     *Quantum Chemical Investigations of Structure, Bonding and EPR Parameters of Manganese
         Complexes relevant to Photosystem II.*
     Dissertation, Julius-Maximilians-Universität Würzburg (2009).

[67] A. Szabo.
     *Modern Quantum Chemistry: Introduction to Advanced Electronic Structure Theory.*
     Courier Dover Publications (1996).

[68] P. Hohenberg and W. Kohn.
     *Inhomogeneous Electron Gas.*
     Phys. Rev. **136**, B864–B871 (1964).

[69] W. Kohn and L. J. Sham.
     *Self-Consistent Equations Including Exchange and Correlation Effects.*
     Phys. Rev. **140**, A1133–A1138 (1965).

[70] R. G. Parr and W. Yang.
     *Density-Functional Theory of the Electronic Structure of Molecules.*
     Annual Review of Physical Chemistry **46**, 701–728 (1995).

[71] T. Ziegler.
     *Approximate density functional theory as a practical tool in molecular energetics and dynamics.*
     Chemical Reviews **91**, 651–667 (1991).

[72] A. D. Becke.
     *Density-functional exchange-energy approximation with correct asymptotic behavior.*
     Physical Review A **38**, 3098 (1988).

[73] C. Lee, W. Yang, and R. G. Parr.
     *Development of the Colle-Salvetti correlation-energy formula into a functional of the electron
         density.*
     Physical Review B **37**, 785 (1988).

[74] A. D. Becke.
     *Density-functional thermochemistry. III. The role of exact exchange.*
     Journal of Chemical Physics **98**, 5648–5652 (1993).

[75] K. Kim and K. D. Jordan.
     *Comparison of Density Functional and MP2 Calculations on the Water Monomer and Dimer.*
     The Journal of Physical Chemistry **98**, 10089–10094 (1994).

[76] P. J. Stephens, F. J. Devlin, C. F. Chabalowski, and M. J. Frisch.
     *Ab Initio Calculation of Vibrational Absorption and Circular Dichroism Spectra Using Density
         Functional Force Fields.*
     The Journal of Physical Chemistry **98**, 11623–11627 (1994).

[77] A. P. Scott and L. Radom.
*Harmonic Vibrational Frequencies: An Evaluation of Hartree-Fock, Moller-Plesset, Quadratic Configuration Interaction, Density Functional Theory, and Semiempirical Scale Factors.*
The Journal of Physical Chemistry **100**, 16502–16513 (1996).

[78] D. Moigno.
*Study of the ligand effects on the metal-ligand bond in some new organometallic complexes using FT-Raman and -IR spectroscopy, isotopic substitution and density functional theory techniques.*
Ph.D. thesis, Julius-Maximilians-Universität Würzburg (2001).

[79] M. Bühl and H. Kabrede.
*Geometries of Transition-Metal Complexes from Density-Functional Theory.*
Journal of Chemical Theory and Computation **2**, 1282–1290 (2006).

[80] N. Panina, V. Demidov, and S. Simanova.
*A DFT study of transition metal complexes with 1,10-phenanthroline, C-C-dimeric 2,2′-bi-1,10-phenanthroline, and its tetraaza chromophore anion.*
Russian Journal of General Chemistry **78**, 919–924 (2008).

[81] R. Ditchfield, W. J. Hehre, and J. A. Pople.
*Self-Consistent Molecular-Orbital Methods. IX. An Extended Gaussian-Type Basis for Molecular-Orbital Studies of Organic Molecules.*
The Journal of Chemical Physics **54**, 724–728 (1971).

[82] W. J. Hehre, R. Ditchfield, and J. A. Pople.
*Self—Consistent Molecular Orbital Methods. XII. Further Extensions of Gaussian—Type Basis Sets for Use in Molecular Orbital Studies of Organic Molecules.*
The Journal of Chemical Physics **56**, 2257–2261 (1972).

[83] M. J. Frisch, G. W. Trucks, H. B. Schlegel, G. E. Scuseria, M. A. Robb, J. R. Cheeseman, G. Scalmani, V. Barone, B. Mennucci, G. A. Petersson, H. Nakatsuji, M. Caricato, X. Li, H. P. Hratchian, A. F. Izmaylov, J. Bloino, G. Zheng, J. L. Sonnenberg, M. Hada, M. Ehara, K. Toyota, R. Fukuda, J. Hasegawa, M. Ishida, T. Nakajima, Y. Honda, O. Kitao, H. Nakai, T. Vreven, J. A. Montgomery, Jr., J. E. Peralta, F. Ogliaro, M. Bearpark, J. J. Heyd, E. Brothers, K. N. Kudin, V. N. Staroverov, R. Kobayashi, J. Normand, K. Raghavachari, A. Rendell, J. C. Burant, S. S. Iyengar, J. Tomasi, M. Cossi, N. Rega, J. M. Millam, M. Klene, J. E. Knox, J. B. Cross, V. Bakken, C. Adamo, J. Jaramillo, R. Gomperts, R. E. Stratmann, O. Yazyev, A. J. Austin, R. Cammi, C. Pomelli, J. W. Ochterski, R. L. Martin, K. Morokuma, V. G. Zakrzewski, G. A. Voth, P. Salvador, J. J. Dannenberg, S. Dapprich, A. D. Daniels, Ö. Farkas, J. B. Foresman, J. V. Ortiz, J. Cioslowski, and D. J. Fox.
*Gaussian 09 Revision A.1* (2009).
Gaussian Inc. Wallingford CT 2009.

[84] L. Serrano-Andrés and M. Merchán.
*Quantum chemistry of the excited state: 2005 overview.*
Journal of Molecular Structure: {THEOCHEM} **729**, 99 – 108 (2005).

[85] C. A. Guido, D. Jacquemin, C. Adamo, and B. Mennucci.
*On the TD-DFT Accuracy in Determining Single and Double Bonds in Excited-State Structures of Organic Molecules.*
The Journal of Physical Chemistry A **114**, 13402–13410 (2010).

[86] A. D. Laurent and D. Jacquemin.
*TD-DFT benchmarks: A review.*
International Journal of Quantum Chemistry **113**, 2019–2039 (2013).

[87] P. Stoutland, R. Dyer, and W. Woodruff.
*Ultrafast infrared spectroscopy.*
Science **257**, 1913–1917 (1992).

[88] J. Buback, M. Kullmann, F. Langhojer, P. Nuernberger, R. Schmidt, F. Würthner, and T. Brixner.
*Ultrafast Bidirectional Photoswitching of a Spiropyran.*
Journal ot the American Chemical Society **132**, 16510–16519 (2010).

[89] J. Buback, P. Nuernberger, M. Kullmann, F. Langhojer, R. Schmidt, F. Würthner, and T. Brixner.
*Ring-Closure and Isomerization Capabilities of Spiropyran-Derived Merocyanine Isomers.*
The Journal of Physical Chemistry A **115**, 3924–3935 (2011).

[90] S. Yan, M. T. Seidel, and H.-S. Tan.
*Perturbed free induction decay in ultrafast mid-IR pump–probe spectroscopy.*
Chemical Physics Letters **517**, 36 – 40 (2011).

[91] M. Lebedev, O. Misochko, T. Dekorsy, and N. Georgiev.
*On the nature of "coherent artifact".*
Journal of Experimental and Theoretical Physics **100**, 272–282 (2005).

[92] B. Dietzek, T. Pascher, V. Sundström, and A. Yartsev.
*Appearance of coherent artifact signals in femtosecond transient absorption spectroscopy in dependence on detector design.*
Laser Physics Letters **4**, 38–43 (2007).

[93] P. Hamm.
*Coherent effects in femtosecond infrared spectroscopy.*
Chemical Physics **200**, 415–429 (1995).

[94] W. P. de Boeij, M. S. Pshenichnikov, and D. A. Wiersma.
*Ultrafast Solvation Dynamics Explored by Femtosecond Photon Echo Spectroscopies.*
Annual Review of Physical Chemistry **49**, 99–123 (1998).

[95] M. Joffre, D. Hulin, A. Migus, A. Antonetti, C. Benoît à la Guillaume, N. Peyghambarian, M. Lindberg, and S. Koch.
*Coherent effects in pump probe spectroscopy of excitons.*
Opt. Lett. **13**, 276–278 (1988).

[96] K. Wynne and R. M. Hochstrasser.
*The theory of ultrafast vibrational spectroscopy.*
Chemical Physics **193**, 211–236 (1995).

[97] A. L. Dobryakov, S. A. Kovalenko, and N. P. Ernsting.
*Electronic and vibrational coherence effects in broadband transient absorption spectroscopy with chirped supercontinuum probing.*
The Journal of Chemical Physics **119** (2003).

[98] K. Ekvall, P. van der Meulen, C. Dhollande, L.-E. Berg, S. Pommeret, R. Naskrecki, and J.-C. Mialocq.
*Cross phase modulation artifact in liquid phase transient absorption spectroscopy.*
Journal of Applied Physics **87**, 2340 (2000).

[99] M. Rasmusson, A. N. Tarnovsky, E. Åkesson, and V. Sundström.
*On the use of two-photon absorption for determination of femtosecond pump-probe cross-correlation functions.*
Chemical Physics Letters **335**, 201–208 (2001).

[100] K. Ekvall, C. Lundevall, and P. van der Meulen.
      *Studies of the fifth-order nonlinear susceptibility of ultraviolet-grade fused silica.*
      Opt. Lett. **26**, 896–898 (2001).

[101] M. Lorenc, M. Ziolek, R. Naskrecki, J. Karolczak, J. Kubicki, and A. Maciejewski.
      *Artifacts in femtosecond transient absorption spectroscopy.*
      Applied Physics B: Lasers and Optics **74**, 19–27 (2002).

[102] P. Nuernberger, K. F. Lee, A. Bonvalet, T. Polack, M. H. Vos, A. Alexandrou, and M. Joffre.
      *Suppression of perturbed free-induction decay and noise in experimental ultrafast pump-probe data.*
      Optics Letters **34**, 3226–3228 (2009).

[103] P. Maine, D. Strickland, P. Bado, M. Pessot, and G. Mourou.
      *Generation of ultrahigh peak power pulses by chirped pulse amplification.*
      IEEE Journal of Quantum Electronics **24**, 398–403 (1988).

[104] A. Assion.
      *Femtosekunden-zeitaufgelöste Untersuchungen molekularer Dynamik in schwachen und starken Laserfeldern.*
      Dissertation, Julius-Maximilians-Universität Würzburg (1998).

[105] A. Öffner.
      *Unit power imaging catoptric anastigmat* (1971).
      U.S. Patent 3748015.

[106] G. Cheriaux, P. Rousseau, F. Salin, J. P. Chambaret, B. Walker, and L. F. Dimauro.
      *Aberration-free stretcher design for ultrashort-pulse amplification.*
      Optics Letters **21**, 414–416 (1996).

[107] E. Treacy.
      *Optical Pulse Compression with Diffraction Gratings.*
      IEEE Journal of Quantum Electronics **5**, 454–458 (1969).

[108] P. Hamm, S. Wiemann, M. Zurek, and W. Zinth.
      *Highly sensitive multichannel spectrometer for subpicosecond spectroscopy in the midinfrared.*
      Opt. Lett. **19**, 1642–1644 (1994).

[109] P. Hamm, R. A. Kaindl, and J. Stenger.
      *Noise suppression in femtosecond mid-infrared light sources.*
      Optics Letters **25**, 1798–1800 (2000).

[110] R. A. Kaindl, M. Wurm, K. Reimann, P. Hamm, A. M. Weiner, and M. Woerner.
      *Generation, shaping, and characterization of intense femtosecond pulses tunable from 3 to 20 μm.*
      Journal of the Optical Society of America B **17**, 2086 (2000).

[111] G. Cerullo and S. De Silvestri.
      *Ultrafast optical parametric amplifiers.*
      Review of Scientific Instruments **74**, 1 (2003).

[112] D. Wolpert.
      *Quantum Control of Photoinduced Chemical Reactions.*
      Dissertation, Julius-Maximilians-Universität Würzburg (2008).

[113] P. Rudolf.
*Transiente Spektroskopie im mittleren Infraroten an 5-Diazo-Meldrumsäure.*
Diplomarbeit, Julius-Maximilians-Universität Würzburg (2009).

[114] T. M. Jedju and L. Rothberg.
*Tunable femtosecond radiation in the mid-infrared for time-resolved absorption in semiconductors.*
Applied Optics **27**, 615–618 (1988).

[115] M. T. P. Oberli, W. Frey, C. Ludwig, M. Woerner, T. Elsaesser, and W. Kaiser.
*Time Resolved Dynamics of Holes in p-type Germanium Photoexcited by Femtosecond Infrared Pulses.*
Brazilian Journal of Physics **26**, 520–524 (1996).

[116] *TOPAS Series Traveling-wave Optical Parametric Amplifiers User's Manual.*
Light Conversion Ltd. (2009).

[117] T. J. Driscoll, G. M. Gale, and F. Hache.
*Ti:sapphire second-harmonic-pumped visible range femtosecond optical parametric oscillator.*
Optics Communications **110**, 638–644 (1994).

[118] G. M. Gale, M. Cavallari, T. J. Driscoll, and F. Hache.
*Sub-20-fs tunable pulses in the visible from an 82-MHz optical parametric oscillator.*
Optics Letters **20**, 1562–1564 (1995).

[119] E. Riedle, M. Beutter, S. Lochbrunner, J. Piel, S. Schenkl, S. Sporlein, and W. Zinth.
*Generation of 10 to 50 fs pulses tunable through all of the visible and the NIR.*
Applied Physics B: Lasers and Optics **71**, 457–465 (2000).

[120] F. Langhojer.
*New techniques in liquid-phase ultrafast spectroscopy.*
Dissertation, Julius-Maximilians-Universität Würzburg (2009).

[121] K. J. Kubarych, M. Joffre, A. Moore, N. Belabas, and D. M. Jonas.
*Mid-infrared electric field characterization using a visible charge-coupled-device-based spectrometer.*
Optics Letters **30**, 1228–1230 (2005).

[122] K. F. Lee, P. Nuernberger, A. Bonvalet, and M. Joffre.
*Removing cross-phase modulation from midinfrared chirped-pulse upconversion spectra.*
Optics Express **17**, 18738–18744 (2009).

[123] W. G. Fisher, W. P. Partridge, C. Dees, and E. A. Wachter.
*Simultaneous Two-Photon Activation of Type-I Photodynamic Therapy Agents.*
Photochemistry and Photobiology **66**, 141–155 (1997).

[124] H. Lei, Z. Huang, H. Wang, X. Tang, L. Wu, G. Zhou, D. Wang, and Y. Tian.
*Two-photon absorption spectra of new organic compounds.*
Chemical Physics Letters **352**, 240 – 244 (2002).

[125] F. Koch.
*Einrichtung eines Flüssigkeitsjets für die zweidimensionale Spektroskopie.*
Bachelor thesis, Julius-Maximilians-Universität Würzburg (2010).

[126] J.-P. Fouassier and J. F. Rabek.
*Radiation Curing in Polymer Science and Technology: Fundamentals and Methods.*
Springer (1993).

[127] V. V. Krongauz and A. D. Trifunac.
*Processes in photoreactive polymers.*
Springer (1995).

[128] V. Nikolaev, N. Khimich, and I. Korobitsyna.
*Photolysis of 5-diazo-2,2-dimethyl-4,6-dioxo-1,3-dioxane (diazoisopropylidenemalonic acid).*
Chemistry of Heterocyclic Compounds **21**, 264–268 (1985).

[129] W. Kirmse.
*100 Years of the Wolff Rearrangement.*
European Journal of Organic Chemistry **2002**, 2193–2256 (2002).

[130] Y. Wang, T. Yuzawa, H.-o. Hamaguchi, and J. P. Toscano.
*Time-Resolved IR Studies of 2-Naphthyl(carbomethoxy)carbene: Reactivity and Direct Experimental Estimate of the Singlet/Triplet Energy Gap.*
Journal of the American Chemical Society **121**, 2875–2882 (1999).

[131] V. V. Popik.
*The role of molecular geometry in the Wolff rearrangement of alpha-diazocarbonyl compounds — Conformational control or structural constraints?*
Canadian Journal of Chemistry **83**, 1382–1390 (2005).

[132] A. Bogdanova and V. V. Popik.
*Experimental and Theoretical Analysis of the Photochemistry and Thermal Reactivity of Ethyl Diazomalonate and Its Diazirino Isomer. The Role of Molecular Geometry in the Decomposition of Diazocarbonyl Compounds.*
Journal of the American Chemical Society **126**, 11293–11302 (2004).

[133] G. T. Burdzinski, J. Wang, T. L. Gustafson, and M. S. Platz.
*Study of Concerted and Sequential Photochemical Wolff Rearrangement by Femtosecond UV-vis and IR Spectroscopy.*
Journal of the American Chemical Society **130**, 3746–3747 (2008).

[134] G. Burdzinski and M. S. Platz.
*Ultrafast time-resolved studies of the photochemistry of diazo carbonyl compounds.*
Journal of Physical Organic Chemistry **23**, 308–314 (2010).

[135] D. Wolpert, M. Schade, and T. Brixner.
*Femtosecond midinfrared study of the photoinduced Wolff rearrangement of diazonaphthoquinone.*
The Journal of Chemical Physics **129**, 094504–10 (2008).

[136] D. Wolpert, M. Schade, F. Langhojer, G. Gerber, and T. Brixner.
*Quantum control of the photoinduced Wolff rearrangement of diazonaphthoquinone in the condensed phase.*
Journal of Physics B: Atomic, Molecular and Optical Physics **41**, 074025 (2008).

[137] Q. Li, A. Migani, and L. Blancafort.
*MS-CASPT2 Assignment of the UV/Vis Absorption Spectrum of Diazoquinones Undergoing the Photoinduced Wolff Rearrangement.*
The Journal of Physical Chemistry A **113**, 9413–9417 (2009).

[138] Q. Li, A. Migani, and L. Blancafort.
*Wave Packet Dynamics at an Extended Seam of Conical Intersection: Mechanism of the Light-Induced Wolff Rearrangement.*
The Journal of Physical Chemistry Letters **3**, 1056–1061 (2012).

[139] G. Cui and W. Thiel.
*Photoinduced Ultrafast Wolff Rearrangement: A Non-Adiabatic Dynamics Perspective.*
Angewandte Chemie International Edition **52**, 433–436 (2013).

[140] G. Burdzinski, J. Rehault, J. Wang, and M. S. Platz.
*A Study of the Photochemistry of Diazo Meldrum's Acid by Ultrafast Time-Resolved Spectroscopies.*
The Journal of Physical Chemistry A **112**, 10108–10112 (2008).

[141] T. Lippert, A. Koskelo, and P. O. Stoutland.
*Direct Observation of a Photoinduced Wolff Rearrangement in PMMA Using Ultrafast Infrared Spectroscopy.*
Journal of the American Chemical Society **118**, 1551–1552 (1996).

[142] T. Lippert and P. O. Stoutland.
*Laser–material interactions probed with picosecond infrared spectroscopy.*
Applied Surface Science **109–110**, 43 – 47 (1997).

[143] B. Grant, N. Clecak, R. J. Twieg, and C. Grant Willson.
*Deep UV photoresists I. Meldrum's diazo sensitizer.*
Electron Devices, IEEE Transactions on **28**, 1300–1305 (1981).

[144] M. Endo, Y. Tani, M. Sasago, N. Nomura, and S. Das.
*Application of Photobleachable Positive Resist and Contrast Enhancement Material to KrF Excimer Laser Lithography.*
Japanese Journal of Applied Physics **28**, 2357–2361 (1989).

[145] M. A. Winnik, F. Wang, T. Nivaggioli, Z. Hruska, H. Fukumura, and H. Masuhara.
*Photoreaction of Meldrum's diazo in poly(methyl methacrylate) matrixes.*
Journal of the American Chemical Society **113**, 9702–9704 (1991).

[146] H. Fujiwara, Y. Nakajima, H. Fukumura, and H. Masuhara.
*Laser Ablation Dynamics of a Poly(methyl methacrylate) Film Doped with 5-Diazo Meldrum's Acid.*
The Journal of Physical Chemistry **99**, 11481–11488 (1995).

[147] C. Hahn, T. Lippert, and A. Wokaun.
*Comparison of the Ablation Behavior of Polymer Films in the IR and UV with Nanosecond and Picosecond Pulses.*
The Journal of Physical Chemistry B **103**, 1287–1294 (1999).

[148] A. Bogdanova and V. V. Popik.
*Experimental and Theoretical Investigation of Reversible Interconversion, Thermal Reactions, and Wavelength-Dependent Photochemistry of Diazo Meldrum's Acid and Its Diazirine Isomer, 6,6-Dimethyl-5,7-dioxa-1,2-diaza-spiro[2,5]oct-1-ene-4,8-dione1.*
Journal of the American Chemical Society **125**, 14153–14162 (2003).

[149] A. Bogdanova and V. Popik.
*Wavelength-Dependent Photochemistry of Diazo Meldrum's Acid and Its Spirocyclic Isomer, Diazirino Meldrum's Acid: Wolff Rearrangement versus Isomerization.*
Journal of the American Chemical Society **125**, 1456–1457 (2003).

[150] V. Nikolaev, V. Shevchenko, M. Platz, and N. Khimich.
*Chemistry of diazocarbonyl compounds: XXV. Comparative photochemistry of diazo compounds and sulfur ylides of the 1,3-dioxane-4,6-dione series.*
Russian Journal of Organic Chemistry **42**, 815–827 (2006).

[151] V. Shevchenko, N. Khimich, M. Platz, and V. Nikolaev.
*Chemistry of diazocarbonyl compounds: XXVII. Thermolysis and photolysis of diazirines, derivatives of 1,3-dioxane-4,6-dione.*
Russian Journal of Organic Chemistry **42**, 1213–1219 (2006).

[152] P. Hamm, S. M. Ohline, and W. Zinth.
*Vibrational cooling after ultrafast photoisomerization of azobenzene measured by femtosecond infrared spectroscopy.*
The Journal of Chemical Physics **106**, 519–529 (1997).

[153] S. Laimgruber, W. J. Schreier, T. Schrader, F. Koller, W. Zinth, and P. Gilch.
*The Photochemistry of o-Nitrobenzaldehyde as Seen by Femtosecond Vibrational Spectroscopy.*
Angewandte Chemie International Edition **44**, 7901–7904 (2005).

[154] P. Nuernberger, K. F. Lee, A. Bonvalet, M. H. Vos, and M. Joffre.
*Multiply excited vibration of carbon monoxide in the primary docking site of hemoglobin following photolysis from the heme.*
J. Phys. Chem. Lett. **1**, 2077–2081 (2010).

[155] M. Rini, A.-K. Holm, E. T. J. Nibbering, and H. Fidder.
*Ultrafast UV-mid-IR Investigation of the Ring Opening Reaction of a Photochromic Spiropyran.*
Journal of the American Chemical Society **125**, 3028–3034 (2003).

[156] J. J. M. Vleggaar, A. H. Huizer, P. A. Kraakman, W. P. M. Nijssen, R. J. Visser, and C. A. G. O. Varma.
*Photoinduced Wolff-Rearrangement of 2-Diazo-1-naphthoquinones: Evidence for the Participation of a Carbene Intermediate.*
Journal of the American Chemical Society **116**, 11754–11763 (1994).

[157] Y. Zhang, G. Burdzinski, J. Kubicki, S. Vyas, C. M. Hadad, M. Sliwa, O. Poizat, G. Buntinx, and M. S. Platz.
*Study of the S1 Excited State of para-Methoxy-3-phenyl-3-methyl Diazirine by Ultrafast Time Resolved UV-Vis and IR Spectroscopies and Theory.*
Journal of the American Chemical Society **131**, 13784–13790 (2009).

[158] R. A. Abramovitch.
*The Infrared Spectra of Some Cyclic Malonates.*
Canadian Journal of Chemistry **37**, 361–365 (1959).

[159] E. E. Ernstbrunner.
*The vibrational spectrum of the carbonyl group - a vindication of the orthodox approach.*
Journal of Molecular Structure **16**, 499 – 502 (1973).

[160] J. Wang, J. Kubicki, T. L. Gustafson, and M. S. Platz.
*The Dynamics of Carbene Solvation: An Ultrafast Study of p-Biphenylyltrifluoromethylcarbene.*
Journal of the American Chemical Society **130**, 2304–2313 (2008).

[161] J. Wang, J. Kubicki, H. Peng, and M. S. Platz.
*Influence of Solvent on Carbene Intersystem Crossing Rates.*
Journal of the American Chemical Society **130**, 6604–6609 (2008).

[162] Y. Zhang, J. Kubicki, and M. S. Platz.
*Ultrafast UV-Visible and Infrared Spectroscopic Observation of a Singlet Vinylcarbene and the Intramolecular Cyclopropenation Reaction.*
Journal of the American Chemical Society **131**, 13602–13603 (2009).

[163] D. Williams, T. Gatica, and W. Gordy.
      *The Infra-red Absorption of Mixtures of Water and Organic Liquids.*
      The Journal of Physical Chemistry **41**, 645–649 (1937).

[164] J. Niesel, A. Pinto, H. W. Peindy N'Dongo, K. Merz, I. Ott, R. Gust, and U. Schatzschneider.
      *Photoinduced CO release, cellular uptake and cytotoxicity of a tris(pyrazolyl)methane (tpm) manganese tricarbonyl complex.*
      Chemical Communications p. 1798 (2008).

[165] H.-M. Berends and P. Kurz.
      *Investigation of light-triggered carbon monoxide release from two manganese photoCORMs by IR, UV–Vis and EPR spectroscopy.*
      Inorganica Chimica Acta (2012).

[166] R. Alberto and R. Motterlini.
      *Chemistry and biological activities of CO-releasing molecules (CORMs) and transition metal complexes.*
      Dalton Trans. pp. 1651–1660 (2007).

[167] R. Motterlini and L. E. Otterbein.
      *The therapeutic potential of carbon monoxide.*
      Nat Rev Drug Discov **9**, 728–743 (2010).

[168] B. E. Mann.
      *Carbon Monoxide: An Essential Signalling Molecule.*
      In G. Jaouen and N. Metzler-Nolte (Editors), *Medicinal Organometallic Chemistry*, vol. 32 of *Topics in Organometallic Chemistry*, pp. 247–285. Springer Berlin Heidelberg (2010).

[169] U. Schatzschneider.
      *PhotoCORMs: Light-triggered release of carbon monoxide from the coordination sphere of transition metal complexes for biological applications.*
      Inorganica Chimica Acta **374**, 19–23 (2011).

[170] C. C. Romao, W. A. Blattler, J. D. Seixas, and G. J. L. Bernardes.
      *Developing drug molecules for therapy with carbon monoxide.*
      Chem. Soc. Rev. **41**, 3571–3583 (2012).

[171] R. D. Rimmer, A. E. Pierri, and P. C. Ford.
      *Photochemically activated carbon monoxide release for biological targets. Toward developing air-stable photoCORMs labilized by visible light.*
      Coordination Chemistry Reviews **256**, 1509–1519 (2012).

[172] W.-Q. Zhang, A. J. Atkin, I. J. S. Fairlamb, A. C. Whitwood, and J. M. Lynam.
      *Synthesis and Reactivity of Molybdenum Complexes Containing Functionalized Alkynyl Ligands: A Photochemically Activated CO-Releasing Molecule (PhotoCO-RM).*
      Organometallics **30**, 4643–4654 (2011).

[173] A. J. Atkin, I. J. S. Fairlamb, J. S. Ward, and J. M. Lynam.
      *CO Release from Norbornadiene Iron(0) Tricarbonyl Complexes: Importance of Ligand Dissociation.*
      Organometallics **31**, 5894–5902 (2012).

[174] S. Romanski, B. Kraus, U. Schatzschneider, J.-M. Neudörfl, S. Amslinger, and H.-G. Schmalz.
      *Corrigendum: Acyloxybutadiene Iron Tricarbonyl Complexes as Enzyme-Triggered CO-Releasing Molecules (ET-CORMs).*
      Angewandte Chemie International Edition **50**, 4038–4038 (2011).

[175] C. S. Jackson, S. Schmitt, Q. P. Dou, and J. J. Kodanko.
*Synthesis, Characterization, and Reactivity of the Stable Iron Carbonyl Complex [Fe(CO)(N4Py)](ClO$_4$)$_2$: Photoactivated Carbon Monoxide Release, Growth Inhibitory Activity, and Peptide Ligation.*
Inorganic Chemistry **50**, 5336–5338 (2011).

[176] J. S. Ward, J. M. Lynam, J. W. B. Moir, D. E. Sanin, A. P. Mountford, and I. J. S. Fairlamb.
*A therapeutically viable photo-activated manganese-based CO-releasing molecule (photo-CO-RM).*
Dalton Trans. **41**, 10514–10517 (2012).

[177] A. E. Pierri, A. Pallaoro, G. Wu, and P. C. Ford.
*A Luminescent and Biocompatible PhotoCORM.*
Journal of the American Chemical Society **134**, 18197–18200 (2012).

[178] L. B. nares, T. Baumert, M. Bergt, B. Kiefer, and G. Gerber.
*Femtosecond photodissociation dynamics of Fe(CO)$_5$ in the gas phase.*
Chemical Physics Letters **267**, 141–148 (1997).

[179] L. Bañares, T. Baumert, M. Bergt, B. Kiefer, and G. Gerber.
*The ultrafast photodissociation of Fe(CO)$_5$ in the gas phase.*
The Journal of Chemical Physics **108**, 5799–5811 (1998).

[180] S. A. Trushin, W. Fuss, K. L. Kompa, and W. E. Schmid.
*Femtosecond Dynamics of Fe(CO)$_5$ Photodissociation at 267 nm Studied by Transient Ionization.*
The Journal of Physical Chemistry A **104**, 1997–2006 (2000).

[181] H. Ihee, J. Cao, and A. H. Zewail.
*Ultrafast Electron Diffraction of Transient [Fe(CO)$_4$]: Determination of Molecular Structure and Reaction Pathway.*
Angewandte Chemie International Edition **40**, 1532–1536 (2001).

[182] P. T. Snee, C. K. Payne, S. D. Mebane, K. T. Kotz, and C. B. Harris.
*Dynamics of Photosubstitution Reactions of Fe(CO)$_5$: An Ultrafast Infrared Study of High Spin Reactivity.*
Journal of the American Chemical Society **123**, 6909–6915 (2001).

[183] P. Portius, J. Yang, X.-Z. Sun, D. C. Grills, P. Matousek, A. W. Parker, M. Towrie, and M. W. George.
*Unraveling the Photochemistry of Fe(CO)$_5$ in Solution: Observation of Fe(CO)$_3$ and the Conversion between 3Fe(CO)$_4$ and 1Fe(CO)$_4$(Solvent).*
Journal of the American Chemical Society **126**, 10713–10720 (2004).

[184] M. Besora, J.-L. Carreón-Macedo, A. J. Cowan, M. W. George, J. N. Harvey, P. Portius, K. L. Ronayne, X.-Z. Sun, and M. Towrie.
*A Combined Theoretical and Experimental Study on the Role of Spin States in the Chemistry of Fe(CO)$_5$ Photoproducts.*
Journal of the American Chemical Society **131**, 3583–3592 (2009).

[185] S. C. Nguyen, J. P. Lomont, M. C. Zoerb, A. D. Hill, J. P. Schlegel, and C. B. Harris.
*Chemistry of the Triplet 14-Electron Complex Fe(CO)$_3$ in Solution Studied by Ultrafast Time-Resolved IR Spectroscopy.*
Organometallics **31**, 3980–3984 (2012).

[186] B. Ahr, M. Chollet, B. Adams, E. M. Lunny, C. M. Laperle, and C. Rose-Petruck.
*Picosecond X-ray absorption measurements of the ligand substitution dynamics of Fe(CO)$_5$ in ethanol.*
Phys. Chem. Chem. Phys. **13**, 5590–5599 (2011).

[187] P. Wernet.
*Mapping chemical bonding of reaction intermediates with femtosecond X-ray laser spectroscopy.*
EPJ Web of Conferences **41**, 05025 (2013).

[188] A. Assion, T. Baumert, M. Bergt, T. Brixner, B. Kiefer, V. Seyfried, M. Strehle, and G. Gerber.
*Control of chemical reactions by feedback-optimized phase-shaped femtosecond laser pulses.*
Science **282**, 919–922 (1998).

[189] M. Bergt, T. Brixner, B. Kiefer, M. Strehle, and G. Gerber.
*Controlling the Femtochemistry of $Fe(CO)_5$.*
The Journal of Physical Chemistry A **103**, 10381–10387 (1999).

[190] J. D. Simon and X. Xie.
*Photodissociation of chromium hexacarbonyl in solution: direct observation of the formation of pentacarbonyl(methanol)chromium.*
The Journal of Physical Chemistry **90**, 6751–6753 (1986).

[191] J. C. King, J. Z. Zhang, B. J. Schwartz, and C. B. Harris.
*Vibrational relaxation of $M(CO)_6$ (M=Cr, Mo, W): Effect of metal mass on vibrational cooling dynamics and non-Boltzmann internal energy distributions.*
The Journal of Chemical Physics **99**, 7595–7601 (1993).

[192] T. Dougherty and E. Heilweil.
*Ultrafast transient infrared absorption studies of $M(CO)_6$ (M=Cr, Mo or W) photoproducts in n-hexane solution.*
Chemical Physics Letters **227**, 19 – 25 (1994).

[193] T. Lian, S. E. Bromberg, M. C. Asplund, H. Yang, and C. B. Harris.
*Femtosecond infrared studies of the dissociation and dynamics of transition metal carbonyls in solution.*
J. Phys. Chem. **100**, 11994–12001 (1996).

[194] J. Z. Zhang and C. B. Harris.
*Photodissociation dynamics of $Mn_2(CO)_{10}$ in solution on ultrafast time scales.*
The Journal of Chemical Physics **95**, 4024–4032 (1991).

[195] J. C. Owrutsky and A. P. Baronavski.
*Ultrafast infrared study of the ultraviolet photodissociation of $Mn_2(CO)_{10}$.*
The Journal of Chemical Physics **105** (1996).

[196] D. A. Steinhurst, A. P. Baronavski, and J. C. Owrutsky.
*Transient infrared spectroscopy of $Mn_2(CO)_{10}$ with 400 nm excitation.*
Chemical Physics Letters **361**, 513 – 519 (2002).

[197] F. W. Vergeer, F. Hartl, P. Matousek, D. J. Stufkens, and M. Towrie.
*First direct observation of a CO-bridged primary photoproduct of $[Ru_3(CO)_{12}]$ by picosecond time-resolved IR spectroscopy.*
Chem. Commun. pp. 1220–1221 (2002).

[198] T. P. Dougherty and E. J. Heilweil.
*Transient infrared spectroscopy of $(\eta^5-C_5H_5)Co(CO)_2$ photoproduct reactions in hydrocarbon solutions.*
The Journal of Chemical Physics **100**, 4006–4009 (1994).

[199] T. P. Dougherty, W. T. Grubbs, and E. J. Heilweil.
*Photochemistry of $Rh(CO)_2(acetylacetonate)$ and Related Metal Dicarbonyls Studied by Ultrafast Infrared Spectroscopy.*
The Journal of Physical Chemistry **98**, 9396–9399 (1994).

[200] E. A. Glascoe, M. F. Kling, J. E. Shanoski, R. A. DiStasio, C. K. Payne, B. V. Mork, T. D. Tilley, and C. B. Harris.
*Photoinduced β-Hydrogen Elimination and Radical Formation with $CpW(CO)_3(CH_2CH_3)$: Ultrafast IR and DFT Studies.*
Organometallics **26**, 1424–1432 (2007).

[201] A. R. Ridley, A. I. Stewart, K. Adamczyk, H. N. Ghosh, B. Kerkeni, Z. X. Guo, E. T. J. Nibbering, C. J. Pickett, and N. T. Hunt.
*Multiple-Timescale Photoreactivity of a Model Compound Related to the Active Site of [FeFe]-Hydrogenase.*
Inorganic Chemistry **47**, 7453–7455 (2008).

[202] T. Jiao, Z. Pang, T. J. Burkey, R. F. Johnston, T. A. Heimer, V. D. Kleiman, and E. J. Heilweil.
*Ultrafast Ring Closure Energetics and Dynamics of Cyclopentadienyl Manganese Tricarbonyl Derivatives.*
Journal of the American Chemical Society **121**, 4618–4624 (1999).

[203] T. T. To, E. J. Heilweil, C. B. Duke, K. R. Ruddick, C. E. Webster, and T. J. Burkey.
*Development of Ultrafast Photochromic Organometallics and Photoinduced Linkage Isomerization of Arene Chromium Carbonyl Derivatives.*
The Journal of Physical Chemistry A **113**, 2666–2676 (2009).

[204] M. Lim, T. A. Jackson, and P. A. Anfinrud.
*Binding of CO to myoglobin from a heme pocket docking site to form nearly linear Fe–C–O.*
Science **269**, 962–966 (1995).

[205] M. Lim, T. A. Jackson, and P. A. Anfinrud.
*Ultrafast rotation and trapping of carbon monoxide dissociated from hemoglobin.*
Nature Struct. Biol. **4**, 209–214 (1997).

[206] J. T. King, E. J. Arthur, C. L. Brooks, and K. J. Kubarych.
*Site-Specific Hydration Dynamics of Globular Proteins and the Role of Constrained Water in Solvent Exchange with Amphiphilic Cosolvents.*
The Journal of Physical Chemistry B **116**, 5604–5611 (2012).

[207] J. T. King and K. J. Kubarych.
*Site-Specific Coupling of Hydration Water and Protein Flexibility Studied in Solution with Ultrafast 2D-IR Spectroscopy.*
Journal of the American Chemical Society **134**, 18705–18712 (2012).

[208] J. Niesel.
*CO release properties and biological activity of manganese tricarbonyl complexes.*
Ph.D. thesis, Ruhr-Universität Bochum (2012).

[209] M. Falk and T. A. Ford.
*Infrared spectrum and structure of liquid water.*
Can. J. Phys. **44**, 1699–1707 (1966).

[210] J. Barrett and A. L. Mansell.
*Ultra-Violet Absorption Spectra of the Molecules $H_2O$, HDO and $D_2O$.*
Nature **187**, 138–138 (1960).

[211] A. Schäfer, H. Horn, and R. Ahlrichs.
*Fully optimized contracted Gaussian basis sets for atoms Li to Kr.*
The Journal of Chemical Physics **97**, 2571–2577 (1992).

[212] F. Neese.
*The ORCA program system.*
Wiley Interdisciplinary Reviews: Computational Molecular Science **2**, 73–78 (2012).

[213] G. L. Geoffroy and M. S. Wrighton.
*Organometallic photochemistry.*
Academic Press, New York [u.a.] (1979).

[214] W. Strohmeier and D. von Hobe.
*Quantenausbeute als Funktion der Wellenlänge bei der photochemischen Bildung von Metallcar-
bonylderivaten.*
Zeitschrift für Physikalische Chemie **34**, 393–400 (1962).

[215] P. J. Giordano and M. S. Wrighton.
*Photosubstitution behavior of dicarbonyl($\eta^5$-cyclopentadienyl)pyridinomanganese and -rhenium
and related complexes.*
Inorganic Chemistry **16**, 160–166 (1977).

[216] W. Strohmeier, D. von Hobe, G. Schönauer, and H. Laporte.
*Einfluss des Zentralatoms und der Donatoren auf die Photochemische Bildung von
Metallcarbonyl-Derivaten.*
Zeitschrift für Naturforschung B: Chemical Science **17**, 502–504 (1962).

[217] M. P. Andersson and P. Uvdal.
*New Scale Factors for Harmonic Vibrational Frequencies Using the B3LYP Density Functional
Method with the Triple-$\zeta$ Basis Set 6-311+G(d,p).*
The Journal of Physical Chemistry A **109**, 2937–2941 (2005).

[218] R. Laenen, T. Roth, and A. Laubereau.
*Novel Precursors of Solvated Electrons in Water: Evidence for a Charge Transfer Process.*
Physics Revue Letters **85**, 50–53 (2000).

[219] W. Huber, R. Linder, J. Niesel, U. Schatzschneider, B. Spingler, and P. C. Kunz.
*A Comparative Study of Tricarbonylmanganese Photoactivatable CO Releasing Molecules (Pho-
toCORMs) by Using the Myoglobin Assay and Time-Resolved IR Spectroscopy.*
European Journal of Inorganic Chemistry **2012**, 3140–3146 (2012).

[220] S. V. C. Vummaleti, D. Branduardi, M. Masetti, M. De Vivo, R. Motterlini, and A. Cavalli.
*Theoretical Insights into the Mechanism of Carbon Monoxide (CO) Release from CO-Releasing
Molecules.*
Chemistry – A European Journal **18**, 9267–9275 (2012).

[221] S. K. Pal, J. Peon, B. Bagchi, and A. H. Zewail.
*Biological Water: Femtosecond Dynamics of Macromolecular Hydration.*
The Journal of Physical Chemistry B **106**, 12376–12395 (2002).

[222] H. Rabitz, R. de Vivie-Riedle, M. Motzkus, and K. Kompa.
*Whither the Future of Controlling Quantum Phenomena?*
Science **288**, 824–828 (2000).

[223] T. Brixner and G. Gerber.
*Quantum control of gas-phase and liquid-phase femtochemistry.*
ChemPhysChem **4**, 418–438 (2003).

[224] S. Weber, M. Barthélemy, and B. Chatel.
*Direct shaping of tunable UV ultra-short pulses.*
Applied Physics B: Lasers and Optics (2009).

[225] S.-H. Shim and M. T. Zanni.
*How to turn your pump–probe instrument into a multidimensional spectrometer: 2D IR and Vis spectroscopies via pulse shaping.*
Physical Chemistry Chemical Physics **11**, 748–761 (2009).

[226] M. Kullmann, S. Ruetzel, J. Buback, P. Nuernberger, and T. Brixner.
*Reaction dynamics of a molecular switch unveiled by coherent two-dimensional electronic spectroscopy.*
Journal of the American Chemical Society **133**, 13074–13080 (2011).

[227] S. Ruetzel, M. Kullmann, J. Buback, P. Nuernberger, and T. Brixner.
*Tracing the Steps of Photoinduced Chemical Reactions in Organic Molecules by Coherent Two-Dimensional Electronic Spectroscopy Using Triggered Exchange.*
Physical Review Letters **110**, 148305 (2013).

[228] P. Tyagi, J. I. Saari, B. Walsh, A. Kabir, V. Crozatier, N. Forget, and P. Kambhampati.
*Two-Color Two-Dimensional Electronic Spectroscopy Using Dual Acousto-Optic Pulse Shapers for Complete Amplitude, Phase, and Polarization Control of Femtosecond Laser Pulses.*
The Journal of Physical Chemistry A **117**, 6264–6269 (2013).

[229] N. Krebs, I. Pugliesi, J. Hauer, and E. Riedle.
*Two-dimensional Fourier transform spectroscopy in the ultraviolet with sub-20 fs pump pulses and 250–720 nm supercontinuum probe.*
New Journal of Physics **15**, 085016 (2013).

[230] P. Nuernberger, G. Vogt, T. Brixner, and G. Gerber.
*Femtosecond quantum control of molecular dynamics in the condensed phase.*
Physical Chemistry Chemical Physics **9**, 2470–2497 (2007).

[231] S. M. Kuebler, K. L. Braun, W. Zhou, J. Cammack, T. Yu, C. K. Ober, S. R. Marder, and J. W. Perry.
*Design and application of high-sensitivity two-photon initiators for three-dimensional microfabrication.*
Journal of Photochemistry and Photobiology A: Chemistry **158**, 163 – 170 (2003).

[232] E. Walker and P. M. Rentzepis.
*Two-photon technology: A new dimension.*
Nature Photonics **2**, 406–408 (2008).

[233] W. R. Zipfel, R. M. Williams, and W. W. Webb.
*Nonlinear magic: multiphoton microscopy in the biosciences.*
Nature Biotechnology **21**, 1369–1377 (2003).

[234] F. Helmchen and W. Denk.
*Deep tissue two-photon microscopy.*
Nature Methods **2**, 932–940 (2005).

[235] A. M. Smith, M. C. Mancini, and S. Nie.
*Bioimaging: Second window for in vivo imaging.*
Nature Nanotechnology **4**, 710–711 (2009).

[236] Z. Zheng, A. Weiner, J. Marsh, and M. M. Karkhanehchi.
*Ultrafast optical thresholding based on two-photon absorption GaAs waveguide photodetectors.*
IEEE Photonics Technology Letters **9**, 493–495 (1997).

[237] H. Hildenbrand.
      *Zwei-Photonen-Anregung mit Nachweis im Infraroten.*
      Bachelor thesis, Julius-Maximilians-Universität Würzburg (2012).

[238] M. Sheik-bahae, A. A. Said, and E. W. V. Stryland.
      *High-sensitivity, single-beam $n_2$ measurements.*
      Optics Letters **14**, 955–957 (1989).

[239] M. Sheik-Bahae, A. Said, T.-H. Wei, D. Hagan, and E. Van Stryland.
      *Sensitive measurement of optical nonlinearities using a single beam.*
      IEEE Journal of Quantum Electronics **26**, 760 –769 (1990).

[240] J. E. Ehrlich, X. L. Wu, I.-Y. S. Lee, Z.-Y. Hu, H. Röckel, S. R. Marder, and J. W. Perry.
      *Two-photon absorption and broadband optical limiting with bis-donor stilbenes.*
      Optics Letters **22**, 1843–1845 (1997).

[241] L. Antonov, K. Kamada, K. Ohta, and F. S. Kamounah.
      *A systematic femtosecond study on the two-photon absorbing D-π-A molecules–π-bridge nitrogen insertion and strength of the donor and acceptor groups.*
      Physical Chemistry Chemical Physics **5**, 1193–1197 (2003).

[242] S.-J. Chung, S. Zheng, T. Odani, L. Beverina, J. Fu, L. A. Padilha, A. Biesso, J. M. Hales, X. Zhan, K. Schmidt, A. Ye, E. Zojer, S. Barlow, D. J. Hagan, E. W. Van Stryland, Y. Yi, Z. Shuai, G. A. Pagani, J.-L. Brédas, J. W. Perry, and S. R. Marder.
      *Extended Squaraine Dyes with Large Two-Photon Absorption Cross-Sections.*
      Journal of the American Chemical Society **128**, 14444–14445 (2006).

[243] J. Moore, P. Hansen, and R. Hochstrasser.
      *A new method for picosecond time-resolved infrared spectroscopy: applications to {CO} photodissociation from iron porphyrins.*
      Chemical Physics Letters **138**, 110 – 114 (1987).

[244] T. P. Dougherty and E. J. Heilweil.
      *Dual-beam subpicosecond broadband infrared spectrometer.*
      Optics Letters **19**, 129–131 (1994).

[245] A. Lukacs, R.-K. Zhao, A. Haigney, R. Brust, G. M. Greetham, M. Towrie, P. J. Tonge, and S. R. Meech.
      *Excited State Structure and Dynamics of the Neutral and Anionic Flavin Radical Revealed by Ultrafast Transient Mid-IR to Visible Spectroscopy.*
      The Journal of Physical Chemistry B **116**, 5810–5818 (2012).

[246] M. J. Nee, R. McCanne, K. J. Kubarych, and M. Joffre.
      *Two-dimensional infrared spectroscopy detected by chirped-pulse upconversion.*
      Opt. Lett. **32**, 713–715 (2007).

[247] J. Treuffet, K. J. Kubarych, J.-C. Lambry, E. Pilet, J.-B. Masson, J.-L. Martin, M. H. Vos, M. Joffre, and A. Alexandrou.
      *Direct observation of ligand transfer and bond formation in cytochrome c oxidase by using mid-infrared chirped-pulse upconversion.*
      Proc. Natl. Acad. Sci. USA **104**, 15705–15710 (2007).

[248] J. M. Anna, M. J. Nee, C. R. Baiz, R. McCanne, and K. J. Kubarych.
      *Measuring absorptive two-dimensional infrared spectra using chirped-pulse upconversion detection.*
      Journal of the Optical Society of America B **27**, 382–393 (2010).

[249] P. Nuernberger, K. F. Lee, A. Bonvalet, L. Bouzhir-Sima, J.-C. Lambry, U. Liebl, M. Joffre, and M. H. Vos.
*Strong Ligand–Protein Interactions Revealed by Ultrafast Infrared Spectroscopy of CO in the Heme Pocket of the Oxygen Sensor FixL.*
Journal of the American Chemical Society **133**, 17110–17113 (2011).

[250] N. Jacquinet-Husson, N. Scott, A. Chédin, L. Crépeau, R. Armante, V. Capelle, J. Orphal, A. Coustenis, C. Boonne, N. Poulet-Crovisier, A. Barbe, M. Birk, L. Brown, C. Camy-Peyret, C. Claveau, K. Chance, N. Christidis, C. Clerbaux, P. Coheur, V. Dana, L. Daumont, M. D. Backer-Barilly, G. D. Lonardo, J. Flaud, A. Goldman, A. Hamdouni, M. Hess, M. Hurley, D. Jacquemart, I. Kleiner, P. Köpke, J. Mandin, S. Massie, S. Mikhailenko, V. Nemtchinov, A. Nikitin, D. Newnham, A. Perrin, V. Perevalov, S. Pinnock, L. Régalia-Jarlot, C. Rinsland, A. Rublev, F. Schreier, L. Schult, K. Smith, S. Tashkun, J. Teffo, R. Toth, V. Tyuterev, J. V. Auwera, P. Varanasi, and G. Wagner.
*The GEISA spectroscopic database: Current and future archive for Earth and planetary atmosphere studies.*
Journal of Quantitative Spectroscopy and Radiative Transfer **109**, 1043 – 1059 (2008).

[251] J. P. Lomont, S. C. Nguyen, and C. B. Harris.
*Ultrafast TRIR and DFT Studies of the Photochemical Dynamics of $Co_4(CO)_{12}$ in Solution.*
Organometallics **31**, 4031–4038 (2012).

[252] D. E. Zelmon, D. L. Small, and D. Jundt.
*Infrared corrected Sellmeier coefficients for congruently grown lithium niobate and 5 mol.% magnesium oxide doped lithium niobate.*
Journal of the Optical Society of America B **14**, 3319–3322 (1997).

# Acknowledgements

Modern natural sciences are far from being a one-man show. Of course, some of the great achievements have been commenced by the initiative of individual people. However, the long way between a first idea and the sound presentation of scientific findings can only be successfully covered by the close teamwork of inquisitive and actively supporting colleagues. In my case, these colleagues are the members of the "Lehrstuhl für Physikalische und Theoretische Chemie 1". I am deeply grateful to all of you. Therefore, at the conclusion of this thesis all that remains for me is to say "thank you" and that I wish you all the best for the future. In particular, I would like to thank:

- Prof. Dr. Tobias Brixner for the confidence he put in me after my diploma thesis, so I had the opportunity to continue working on the IR project in his excellent research group and could even build up a laser laboratory according to my own scientific needs and ideas. With regards to this, I am also thankful that funding was always secured, both for the instrumentation and the staff, which created a high-quality work environment. Owing to his group-leadership, a very good balance has been maintained between motivation and support on the one hand and positive challenges on the other hand. This encourages young scientists to become independently thinking and acting members of a team.

- Prof. Dr. Patrick Nürnberger for his pronounced kindness and great expertise. His unlimited helpfulness combined with his incredibly extensive knowledge concerning our research field made working with him such a pleasant way to improve own abilities and to get better in many ways, which is a very enriching experience. This is why I sincerely feel honored that I became a member of his young research group and that my PhD thesis is reviewed by him. Patrick, I wish you the very best for your future in Bochum. May you reach the objectives you have set yourself and keep on being such a great personality.

- Prof. Dr. Ulrich Schatzschneider for the excellent collaboration within the CORM project, including fruitful discussions and the TDDFT calculations on the compound we investigated.

- Christoph Nagel and Johanna Niesel for the synthesis of the manganese-tricarbonyl CORM and the steady supply of fresh molecules.

- Florian Kanal for the superb teamwork in the course of the CORM project, for thorough proof-reading of this thesis, and for various insights into chemistry, which a physicist would never gain without the help of a well-qualified chemist. Moreover, I am deeply grateful for your warm and friendly nature that also formed the great atmosphere we had in our office. You made the unavoidable experimental set-backs a lot more bearable.

- Dr. Johannes Buback for being a highly capable teammate during long lab nights within the DMA project. His versatile skills concerning LabVIEW have been of inestimable value for the whole research group. In this sense, I also want to thank Andreas Steinbacher for continuing the elaborate work of administrating and developing the VI-Pool, while showing at the same time a great willingness to help every group member in manifold ways.

- Johannes Knorr for proof-reading of this thesis, for his considerate nature, and his very well-structured and organized approach to work, which made the comparative study a smoothly running and successful project.

- Christian Rewitz for proof-reading and commenting on the introduction and summary of this thesis. Furthermore, I appreciate that you shared an office with me from the very beginning till the end of our doctorates. I truly thank you for being a friend by all means.

- Christoph Schwarz for taking care of the workstations. Working without a properly functioning computer is no fun at all. Thanks to you, this happened very rarely.

- Stefan Rützel for his talent as a photographer and for managing the kitty as well as the candy bar and beverage logistics. I enjoy thinking back to our trip to New York and the memorable atmosphere in Harlem.

- Sebastian Schott and Sebastian Götz for undertaking the reference management and the maintenance of the homepage in the future.

- Christian Kramer that he sometimes forgot about his royal descent and gave rise to the "Kramer der Woche" and other cheerfulness. Thanks Prinzregent.

- Dr. Philip Tuchscherer for allowing me to "put you in a good mood" whenever I stopped by at your office.

- Dr. Daniel Wolpert for his contributions to the pump–probe setup.

- Of course, I also want to thank every person hitherto unmentioned that still is or has been a scientific member of the "Lehrstuhl für Physikalische und Theoretische Chemie 1" for diverse input with regard to numerous challenges. Each one of you deserves my sincere gratitude and respect as all of you individually contributed to form our unique working group.

- Jens Giegerich and Christoph Brüning for their assistance to get the DFT calculations started.

- Our secretary Andrea Gehring for maintaining a reliable and accurate administration, which is the backbone of every institute and cannot be valued highly enough.

- The members of the machine and electronic workshop, namely Wolfgang Liebler, Ralf Kohrmann, Katharina Schreckling, Peter Lang, Gerhard Bömmel, Reiner Eck, and Jürgen Zimmermann. Their commitment to find solutions for any kind of mechanical or electronic issue is impressive. Even if the challenge is not totally related to the official duties (thank you Reiner for soldering the carbon brushes of my washing machine).

- The technical assistants Belinda Böhm, Gudrun Mühlrath, Sabine Stahl, and Sabine Fuchs for steady support concerning the working materials and the laser laboratories.

- My dear friends that accompanied me during the past years. When I think of the time we spent together—both inside lecture rooms but likewise apart from everyday university life—I see how lucky I am that we met each other and became friends.

Finally, I want to express my deepest thanks to my family that always has been there for me long before this work began. Their support gave me the opportunity to start studying in Würzburg; their moral backup and encouragement helped me throughout the years to successfully conclude this time. In particular, I owe my most heartfelt gratitude to my beloved wife Gabi for being such a wonderful person. I thank you for your love and affection in good times but likewise when living is hard. Together with you life is beautiful.